Development and Applications of a Transferable Potential Model for Boron Nitride and related compounds

A DPhil Thesis



Angus Heafield

Supervisor: Prof. Mark Wilson

Hertford College

University of Oxford

June 2026

Acknowledgements

First, I would like to thank my supervisor, Mark for his constant support throughout my work. His willingness and availability to discuss any problems which arose and answer any questions I had, no matter how small, were key to my progress and my understanding of my research and its wider implications. I would also like to thank the rest of the Wilson group for their guidance at the start of my work and for helping to push my work through excellent and insightful questions during group meetings. Next, I would like to thank my friends for the countless hours of conversation, jokes and games which helped push me forward especially when the end seemed so far out of sight. Finally, I want to thank my family and especially my parents, for enduring my ramblings trying to explain my work and how it was going. Your endless support and belief has led me to places I never thought I would reach. I would not have been able to get this far without you. I am forever grateful.

Abstract

Boron nitride (BN) exists in a huge range of structures, from crystalline to nanomaterials and disordered. As a result, boron nitride materials have extensive potential applications which take advantage of their remarkable mechanical, chemical, electrical and optical properties. However, whilst significant effort has been made in investigating these materials, much remains unknown, particularly regarding the disordered structures. The work covered in this thesis aims to investigate the structure and properties of boron nitride and related materials through the use of molecular dynamics and Monte Carlo simulations. In particular, a focus is placed on investigating how the atomic charges influence or are influenced by the structure of these materials, by developing a new transferable potential model for these systems in which the charges are allowed to vary.

A variety of crystalline BN structures were modelled using a range of potential models augmented by an electrostatic potential with charges varied systematically. These highlighted how utilising integer charges leads to the unphysical stability of some structures. As such partial atomic charges are required to aptly describe the ionic nature of BN bonds. Methods were developed to generate both two- and three-dimensional amorphous structures allowing for control over the topological (relating to how atomic sites are arranged spatially) and site-based (relating to how atoms occupy the sites in the network) disorder. These methods were employed to study amorphous BN across a range of densities and partial atomic charges showing that site-ordering in these structures is significantly affected by the atomic charges. This demonstrated how a more flexible approach to modelling the electrostatic interactions was required. The fluctuating charge model (FCM) was adapted for network materials and parametrised for BN. The FCM still utilises

point charges to model electron density, however, the magnitude of the charges is able to vary to adapt to the environment. This new potential model was used to show that simple defects can lead to significant changes in atomic charges. It was also shown that amorphous BN nanosheets are arranged into regions of high and low charge. The potential model was expanded to study the formation of domains of BN and C in borocarbonitrides, both topologically ordered and disordered. The charges generated in the FCM for BCN were compared to the results from independent density functional theory-based calculations. It was shown that the size and composition of these domains can have an effect on the charge distributions in these materials. Finally, the FCM was used to investigate how mechanical strain and nanopores can effect the charge distributions in BN nanosheets.

Table of Contents

List of Figures **v**

1 Introduction **1**

2 Background **4**

2.1 The Structures of Boron Nitride 5

2.2 Defects in Boron Nitride 10

2.3 Applications of Boron Nitride 13

2.4 Methods of Modelling Boron Nitride 18

2.4.1 *Ab initio* Methods 18

2.4.2 Molecular Mechanics Methods 19

2.4.3 Other Methods 21

2.5 Polar Bonding in Boron Nitride 22

2.5.1 Determining the Charges in Boron Nitride 24

2.6 Topological and Site Disorder 25

3 Theory **29**

3.1 The Canonical Ensemble 30

3.2 Understanding the Structure of Disordered Materials 31

3.2.1 Pair Distribution Functions (Real Space Functions) . . 32

3.2.2 Structure Factors (Reciprocal Space Functions) 37

3.2.3 The Bhatia-Thornton Formalism 39

3.3 Network Theory and Ring Statistics 42

3.3.1 Node Degree 42

3.3.2 Topological Laws 43

3.3.2.1 Euler's Law 43

3.3.2.2 Lemaître's Law 44
3.3.2.3 Aboav-Weaire Law 46
3.3.3 Atomic and Ring Networks 47
3.4 The Fluctuating Charge Model 47
3.4.1 Calculation of Electronegativities 50
3.4.2 Calculation of Atomic Charges 52

4 Computational Procedures and Methodology 57
4.1 Monte Carlo Simulations 58
4.1.1 The Metropolis Algorithm 58
4.1.2 Bond Switching Monte Carlo 60
4.2 Molecular Dynamics Simulations 63
4.2.1 Algorithmic Details 64
4.2.2 Periodic Boundary Conditions 65
4.2.3 Temperature Control Methods 67
4.2.3.1 Nosé-Hoover Thermostat 68
4.2.3.2 Periodic Velocity Rescaling 70
4.3 Geometric Optimisation and Potential Models 71
4.3.1 Steepest Descent Algorithm 71
4.3.2 Harmonic Potential Models 72
4.3.3 The Tersoff Potential Model 73
4.3.3.1 Application of the Tersoff Potential to Boron Nitride 76

5 Ordered BN Systems and Generating Amorphous Networks 79
5.1 Introduction 79
5.2 Ordered BN Structures 81
5.2.1 2D Lattices 81

5.2.2 3D Crystals 85
5.2.3 Conclusions 88
5.3 Hexagonal Lattice 90
5.4 Controlling disorder in BN networks 93
5.4.1 Site Disordering 93
5.4.2 2D Disordered Systems 96
5.4.3 3D Disordered Systems 103

6 Topological and Site Disorder in Boron Nitride Networks 106
6.1 Introduction 106

7 The Application of a Fluctuating Charge Model for Boron Nitride Networks 120
7.1 Introduction 120

8 Borocarbonitrides 132
8.1 Introduction to Borocarbonitrides 132
8.2 C defects in h-BN 138
8.3 h-BN and Graphene Domains 142
8.3.1 Graphene-h-BN super-ordered arrays 142
8.3.2 Generating irregular domains 143
8.4 Mixed BCN rings 146
8.5 Amorphous BCN 153
8.6 Summary 159

9 Utilizing the Fluctuating Charge Model to Investigate Applications of BN nanosheets 160
9.1 Mechanical Properties 160
9.1.1 Tension 161

9.1.1.1 Strain rate 161
9.1.1.2 Site Disorder 166
9.1.2 Compression 170
9.2 Nanopores 172
9.3 Summary 179

10 Conclusions and Future Work **180**

List of Figures

2.1 Crystal structures of boron nitride: (a) cubic, (b) wurtzite, (c) hexagonal, (d) rhombohedral. Boron and nitrogen atoms are coloured pink and blue respectively. The unit cells for the hexagonal and rhombohedral structures are shown in (c) and (d) to highlight the difference in the stacking patterns. 6

2.2 Structures of example boron nitride nanomaterials: (a) nanosheet, (b) nanotube, (c) fullerene-like nanoparticle. Boron and nitrogen atoms are coloured pink and blue respectively. Figure from ref. [27]. 8

2.3 Example point defects in a BN nanosheet. Boron and nitrogen atoms are coloured pink and blue respectively. 14

2.4 Comparison of 2D networks containing (a) only topological disorder and (b) topological and site disorder. The circled areas in Panel (a) shows regions of high and low topological order. Panel (b) shows the same network with boron and nitrogen atoms coloured pink and blue respectively. The highlighted areas in (b) show regions of topological order which are site ordered and site disordered, as well as the site disorder inherent in topologically disordered regions. 28

3.1 Graphic demonstrating the histogram method for calculating $G(r)$. The dotted lines represent the edges of bins at distance r from the central white atom. The atoms are coloured by the bin they are sorted into. 33

3.2 Example real space structure functions for the same amorphous boron nitride system. The top panel shows the pair distribution function, $G(r)$, with the low and high r limits labelled. The middle panel shows the differential correlation function, $D(r)$, with the low r gradient and the high r limit labelled. The bottom panel shows the radial distribution function, $R(r)$. The highlighted area shows the integration region for the calculation of the nearest-neighbour coordination number. 35

3.3 Example networks based on an amorphous boron nitride monolayer. The nodes in the atomic network are coloured according to their atom type: pink for boron and blue for nitrogen. The nodes in ring network are coloured according to their degree and therefore the number of sides in the ring they are representing: $k < 6$ - purple, $k = 6$ - white, $k > 6$ - green. 48

4.1 Example formation of a Stone-Wales defect in h-BN. A central bond is rotated by 90° resulting in the transformation of 4 six-membered rings into 2 five- and 2 seven-membered rings. . . 62

4.2 Example progression of the employed bond switching algorithm. The hexagonal lattice (a) is thermalised by introducing Stone-Wales defects (b)-(e) until a high energy configuration is reached (f). The system is then "cooled" at a controlled rate (g) until a final configuration is reached potentially containing types of defects which are not normally obtainable from the initial lattice (h). Figure from the doctoral thesis of David Morley [292]. 63

4.3 An example of a two-dimensional periodic system, with a tiling box of length L. 66
4.4 Example 1D charge densities in the Ewald summation. Panel (a) shows the original point charges and the screen distributions. Panel (b) shows the cancelling distribution. Figure taken from [243]. 68

5.1 Ordered 2D BN lattices. Atoms are coloured by type, pink and blue for boron and nitrogen respectively. 83
5.2 Variation of potential energy per formula unit with B-N bond length for a range of potentials and regular 2D lattices. Panels (a) and (b) correspond to different site charges, q. In both panels, line colour corresponds to the potential and the line type corresponds to the lattice type. Key: Red - Kumar *et al* [230], Blue - Albe *et al* [163], Yellow - Sekkal *et al* [164] and Green - Sevik *et al* [166]. Solid Line - Ordered Close Packed, Dotted Line - Disordered Close Packed, Dashed Line - Truncated Square and Dot Dash line - Hexagonal. 84
5.3 Variation of potential energy per formula unit with B-N bond length for a range of potentials and regular 3D crystals. Panels (a) and (b) correspond to different site charges, q. In both panels, line colour corresponds to the potential and the line type corresponds to the lattice type. Key: Red - Kumar *et al* [230], Blue - Albe *et al* [163], Yellow - Sekkal *et al* [164] and Green - Sevik *et al* [166]. Solid Line - Cubic, Dashed Line - Wurtzite and Dot Dash line - NaCl. 87

5.4 Convergence of the Madelung constant, A, for monolayer hexagonal boron nitride, within increasing number of interactions, N, included. 92

5.5 Change in average partial coordination numbers in hexagonal lattices containing 400 B and 400 N over the course of 20000 Monte Carlo steps, for the introduction of site disordering into a ordered system (left) and the reduction of site disordering in a disordered system (right). $\overline{n}^{\mathrm{B}}_{\mathrm{B}} = \overline{n}^{\mathrm{N}}_{\mathrm{N}}$ coloured red and $\overline{n}^{\mathrm{N}}_{\mathrm{B}} = \overline{n}^{\mathrm{B}}_{\mathrm{N}}$ coloured green. 96

5.6 Snapshots of hexagonal lattices containing 400 B and 400 N at varying steps of the two atom label switching Monte Carlo algorithms. (a), (b) - 0 steps, (c), (d) - 100 steps, (e), (f) - 1000 steps, (g), (h) - 20000 steps. (a), (c), (e), (g) show the increasing disorder algorithm. (b), (d), (f), (h) show the decreasing disorder algorithm. Rings are coloured blue if they contain alternating B and N around the entire ring and red otherwise. 97

5.7 The effects of varying topological disorder, represented by the proportion of six-membered rings, p_6, in two-dimensional amorphous BN configurations on site-based disorder, represented by partial coordination numbers, n^{β}_{α}. Points are coloured by partial coordination number: green- α = B/N, β = N/B, blue -α = B, β = B and red - α = N, β = N. 100

5.8 The short-range (Tersoff) potential energy shown as a function of the fraction of hexagons, p_6. Panels (a)-(c) correspond to the potential model parametrisations indicated. In all panels each colour corresponds to different site charges. Key: blue - $|q| = 0$, orange - $|q| = 0.25$, green - $|q| = 0.50$, red - $|q| = 0.75$, purple - $|q| = 1.00$. 102

5.9 Temperature over the course of a melt-quench process for the generation of three dimensional amorphous boron nitride. The colour of the line indicates the different stages of the process: red for melting, orange for equilibration and blue for cooling. . 104

8.1 Three potential BCN monolayer structures. Atoms are coloured according to their type: pink - boron, grey - carbon and blue - nitrogen. Rings are coloured according to their makeup: grey - $B_2C_2N_2$ with no homo-atomic bonds, white - $B_2C_2N_2$ with homo-atomic bonds, blue - $B_3N_3/B_3C_3/C_3N_3$ and red - other. 137

8.2 Charge "heat maps" for C defects in h-BN. Captions describe defect types: C_α is a substitution of atom α with C, V_α is vacancy of atom α and SW is a Stone-Wales defect. Atoms are coloured by their charges: red - more positive and blue - more negative. The edges of atoms are coloured according to their type: pink - boron, grey - carbon, blue - nitrogen. 139

8.2 Charge "heat map" for C defects in h-BN (cont.). 140

8.3 Example hexagonal BC_2N configurations of 800 atoms from the LS-MC approach showing growing domains of C and BN. Captions indicate the number of MC steps. Rings are coloured by their makeup: blue - B_xN_{6-x}, grey - C_6 and red - other. Atoms are coloured by their type: pink - B, grey - C and blue - N. 144

8.4 Change in average partial coordination numbers over the course of 10000 Monte Carlo steps, for the generation of C and BN domains on a hexagonal lattice network of 800 atoms. 145

8.5 Average atomic charge by atom type for hexagonal configurations with a range of C and BN domain sizes, measured using the average C surrounding C partial coordination number, $\overline{n}_{\mathrm{C}}^{\mathrm{C}}$. Points are coloured by atom type: red - B, black - C and blue - N. Error bars show standard deviation of charge distributions. 145

8.6 Three BCN monolayer structures charge "heat maps". Atoms are coloured according to their charge: Red and blue for more positively and negatively charged respectively. The edges of atoms are colour to denote their type: pink - boron, grey - carbon and blue - nitrogen. Rings are coloured according to their makeup: grey - $B_2C_2N_2$ with no homo-atomic bonds, white - $B_2C_2N_2$ with homo-atomic bonds, blue - $B_3N_3/B_3C_3/C_3N_3$ and red - other. 148

8.7 Charge distributions for the BCN_v1 structure calculated using the FCM. Panel (a) shows the charge distributions grouped and coloured by atom type: red - boron, black - carbon and blue - nitrogen. Panels (b) , (c) and (d) show the charge distributions for boron, carbon and nitrogen atoms, respectively, grouped by coordination environments. The lines are coloured by the coordination environment around atom α they represent: red - n_α^{B}, blue - n_α^{N}, black - n_α^{C}. For each colour, the opacity and offset gives the value of n_α^β from 3 to 0 for darkest to lightest. The lines are offset for clarity. 150

8.8 Charge distributions for the BCN_v2 structure calculated using the FCM. Panel (a) shows the charge distributions grouped and coloured by atom type: red - boron, black - carbon and blue - nitrogen. Panels (b) , (c) and (d) show the charge distributions for boron, carbon and nitrogen atoms, respectively, grouped by coordination environments. The lines are coloured by the coordination environment around atom α they represent: red - n_α^{B}, blue - n_α^{N}, black - n_α^{C}. For each colour, the opacity and offset gives the value of n_α^β from 3 to 0 for darkest to lightest. The lines are offset for clarity. 151

8.9 Charge distributions for the BCN_v3 structure calculated using the FCM. Panel (a) shows the charge distributions grouped and coloured by atom type: red - boron, black - carbon and blue - nitrogen. Panels (b) , (c) and (d) show the charge distributions for boron, carbon and nitrogen atoms, respectively, grouped by coordination environments. The lines are coloured by the coordination environment around atom α they represent: red - n_α^{B}, blue - n_α^{N}, black - n_α^{C}. For each colour, the opacity and offset gives the value of n_α^β from 3 to 0 for darkest to lightest. The lines are offset for clarity. 152

8.10 The effects of varying topological disorder in two-dimensional amorphous BC_2N configurations of 800 atoms. Panel (a) shows how site-based disorder, represented by partial coordination numbers, n_α^β, is affected by topological disorder, represented by the proportion of six-membered rings, p_6. Points are coloured by α and β values: blue - α = B, β = B, orange - α = B, β = N, green - α = B, β = C, red - α = N, β = B, purple - α = N, β = N, brown - α = N, β = C, pink - α = C, β = B, grey - α = C, β = N and yellow - α = C, β = C. Panel (b) shows the effect of topological disorder on the atomic charge distribution. Points are coloured by atom type: red - B, black - C and blue - N. Error bars show standard deviation of charge distributions. 154

8.11 Change in average partial coordination numbers over the course of 10000 Monte Carlo steps, for the generation of C and BN domains on a two-dimensional amorphous BC_2N configuration of 800 atoms with $p_6 \approx 0.55$. 156

8.12 Average atomic charge by atom type for two-dimensional amorphous BC_2N configurations of 800 atoms ($p_6 \approx 0.55$) with a range of C and BN domain sizes, measured using the average C surrounding C partial coordination number, $\overline{n}^{C}_{C}$. Points are coloured by atom type: red - B, black - C and blue - N. Error bars show standard deviation of charge distributions. 157

8.13 Average atomic charge by atom type for two dimensional amorphous $(BN)_xC_y$ configurations of 800 atoms ($p_6 \approx 0.55$) with variable chemical compositions. Points are coloured by atom type: red - B, black - C and blue - N. Error bars show standard deviation of charge distributions. 158

9.1 Stress-strain curves for BN nanosheets at a variety of strain rates, applying strain along the zigzag edge. Lines are coloured by strain rate: blue - $2 \times 10^{10}s^{-1}$, orange - $3 \times 10^{10}s^{-1}$, green - $5 \times 10^{10}s^{-1}$, red - $1 \times 10^{11}s^{-1}$ and purple - $5 \times 10^{11}s^{-1}$. . . . 162

9.2 Snapshots of a BN nanosheet under tensile strain with a strain rate of $2 \times 10^{10}s^{-1}$. Strain values of each panel are indicated in the caption. Atoms are coloured by their type: pink - boron and blue - nitrogen. 164

9.3 Average absolute charge-strain curves for BN nanosheets at a variety of strain rates. Lines are coloured by strain rate: blue - $2 \times 10^{10}s^{-1}$, orange - $3 \times 10^{10}s^{-1}$, green - $5 \times 10^{10}s^{-1}$, red - $1 \times 10^{11}s^{-1}$ and purple - $5 \times 10^{11}s^{-1}$. 165

9.4 Stress-strain curves for BN nanosheets with a variety of levels of site disorder, at a strain rate of $10^{11}s^{-1}$. Curves are coloured by level of site disorder, measured using the average number of N surrounding a B, $\overline{n}_B^N$. Key: blue - 3.000, orange - 2.406, green - 2.060, red - 1.815, purple - 1.707, brown - 1.623, pink - 1.598, grey - 1.550 and yellow - 1.507. 167

9.5 Young's modulus for a range of BN nanosheets shown as a function of the site disorder, measured using $\overline{n}_B^N$. 168

9.6 Average absolute charge-strain curves for BN nanosheets with a variety of levels of site disorder, at a strain rate of $10^{11}s^{-1}$. Curves are coloured by level of site disorder, measured using the average number of N round a B, $\overline{n}_B^N$. Key: blue - 3.000, orange - 2.406, green - 2.060, red - 1.815, purple - 1.707, brown - 1.623, pink - 1.598, grey - 1.550 and yellow - 1.507. 169

9.7 Change in buckling amplitude with increasing compressive strain for a h-BN nanosheet. 171

9.8 Snapshots of a BN nanosheet under compressive strain with a strain rate of $1 \times 10^{10}s^{-1}$. Strain values of each panel are indicated in the caption. Atoms are coloured by their type: pink - boron and blue - nitrogen. 172

9.9 Example nanopore geometries in BN nanosheets. Panels (a) and (b) show a triangular and hexagonal pore respectively. Atoms are coloured by their type: pink - boron and blue - nitrogen. 173

9.10 Change in atomic charge surrounding N-terminated triangular pores in BN nanosheets with increasing pore radii. Panels (a) and (b) show charges on B and N atoms respectively. 174

9.11 Comparison of energy difference compared to pristine nanosheet versus radius for a range of N-terminated triangular pore sizes for the mean field approximation (MFA) and the fluctuating charge model (FCM). 175
9.12 Change in atomic charge surrounding hexagonal pores in BN nanosheets with increasing pore radii. Panels (a) and (b) show charges on B and N atoms respectively. 176
9.13 Comparison of energy difference compared to a nanosheet without pores for a range of pore sizes for the ordered and amorphous nanosheets. 178

1 | Introduction

First synthesised in 1842 by W. H. Balmain [1], the study of boron nitride (BN) materials has long been an area of academic interest. Due to their isoelectronic relation to carbon materials, boron nitride materials share many properties with those of their periodic table neighbour. This includes existing as a broad range of structures: crystalline, disordered and nanomaterials. These structures have incredibly varied properties leading to an extensive array of potential applications from those taking advantage of the excellent mechanical properties of BN materials [2, 3] to those utilising their unique electronic and chemical properties [4, 5]. While many of these applications are shared with those of carbon materials, key differences arise between the two due to the presence of the two atom types in boron nitride. This leads to differences in the bonding, structure and disorder of BN materials which are still not fully understood. These differences are particularly prevalent in amorphous boron nitride due to the wide range of boron and nitrogen environments due to the high levels of disorder, both in terms of the topology and site occupancy.

Molecular computer simulations were first carried out in the 1950s [6–8], utilising hard spheres as idealised representations of molecules. Since then, the use of computational models for the study of atomic systems has exploded, becoming a key component of modern chemistry research. Computational models allow for observations of systems at a level of detail and under conditions which are not currently possible with experimental techniques. They also allow for the direct measurement of properties of individual atoms rather than averaging over space and time. This allows for a direct connection between the microscopic and macroscopic properties of a material and therefore

a link between theoretical and experimental work. Computational models are of particular use for studying BN materials, due to the difficulties it presents to experimental techniques. For example, the neutron absorption of B hinders neutron diffraction experiments and the similar sizes of B and N make it hard to distinguish between the two atom types in optical approaches. These problems are most apparent when studying structures lacking long range order, such as amorphous BN. Whilst many of the potential models used to represent the bonding interactions in BN materials have been used to accurately model the properties of the materials, the ionic component of the bonding is often left out. This may not be a problem in ordered systems, where interactions are equal and the ionic component can be included in the strength of the covalent bond. However, in disordered structures or models containing other charged species, the ionic bonding interaction is key to understanding these systems. As such one aim of the present work is to develop a transferable potential model containing the ionic interaction which is able to accurately represent and study the wide range of boron and nitrogen environments present for BN.

The outline of this thesis is as follows. Chapter 2 explores the previous work which was undertaken investigating the range of boron nitride materials, including their structures, applications and methods used to computationally model them. Chapter 3 discusses and derives the key theory which underpins the work in this thesis. This includes the statistical mechanics, network theory and the fluctuating charge model (FCM). Chapter 4 explains the computational methods employed in the work described by this thesis and how they apply to BN networks. Monte Carlo and molecular dynamics simulations are discussed followed by the different potential models used in this work. Chapter 5 is the first results chapter and investigates how a variety of

Tersoff potential parametrisations for BN perform for a variety of crystalline structures. This chapter also investigates methods for generating disordered BN configurations with control over the levels of topological and site disorder. Chapter 6 investigates the modelling of amorphous boron nitride across a range of densities and partial atomic charges. The effect of these properties on the topological and site disordering in these networks is discussed. Chapter 7 introduces the FCM to our potential model for BN. The FCM is used to investigate the effect of defects and larger scale disorder on the charge distribution of BN networks. Chapter 8 expands the potential model to borocarbonitrides. The structure and disorder in BCN nanosheets is investigated as well as the effect these features have on the charge distribution. Chapter 9 contains applications of the FCM to some key properties for the applications of BN nanosheets, namely the mechanical properties and nanopores for chemical separation applications. Chapter 10 contains overall conclusions for the work in this thesis as well as potential directions for future work in this area.

2 | Background

Contents

2.1 The Structures of Boron Nitride 5

2.2 Defects in Boron Nitride 10

2.3 Applications of Boron Nitride 13

2.4 Methods of Modelling Boron Nitride 18

2.4.1 *Ab initio* Methods 18

2.4.2 Molecular Mechanics Methods 19

2.4.3 Other Methods 21

2.5 Polar Bonding in Boron Nitride 22

2.5.1 Determining the Charges in Boron Nitride 24

2.6 Topological and Site Disorder 25

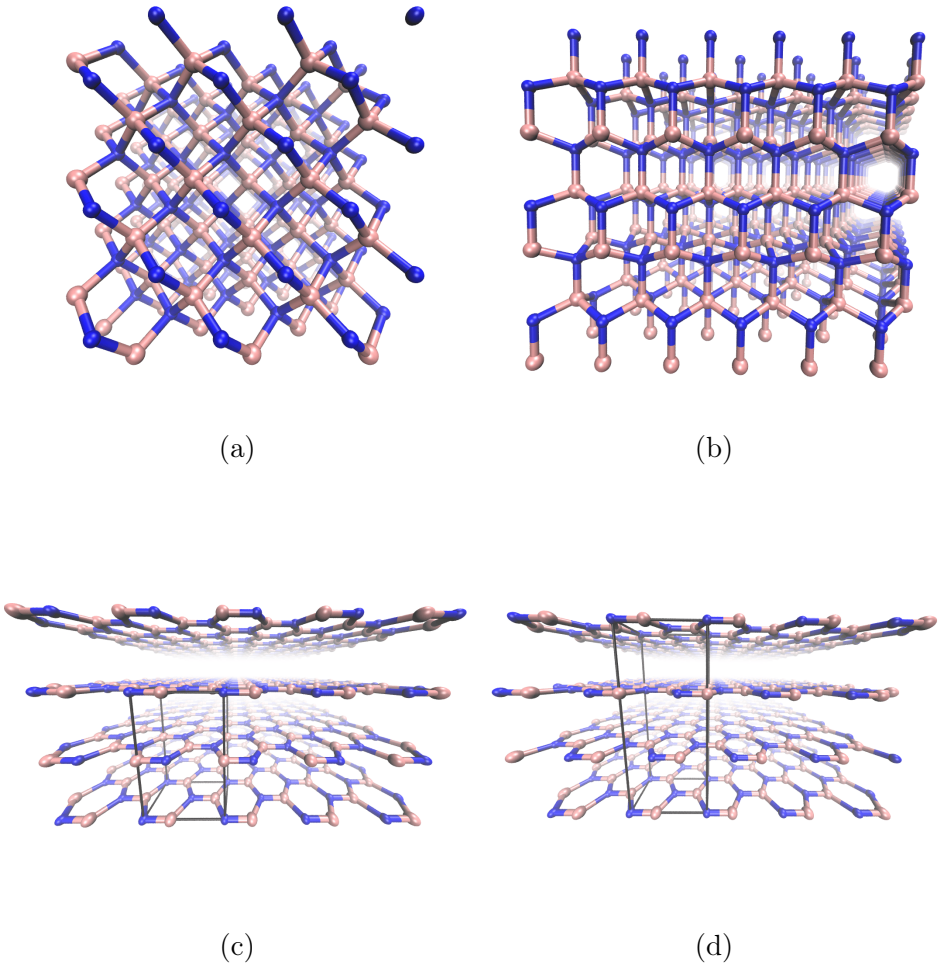
This chapter covers previous work undertaken to investigate boron nitride materials. First, the structures of boron nitride are discussed alongside the methods of synthesis for the structures most relevant to the work in this thesis. Next, the variety of defects formed in BN materials and the wide range of applications of BN materials are explored. This is followed by an analysis of the different methods which have been previously utilised to computationally model BN materials. Finally, two key properties of BN materials for the work in this thesis, the presence of polar bonding and the multiple types of disorder, are examined in more detail.

2.1 The Structures of Boron Nitride

Boron nitride (BN) exists as a wide range of potential structures including crystalline, disordered and nanoscale molecular materials. The crystalline structures of BN can be split into two groups: those containing (i) sp^3 bonding and (ii) sp^2 bonding. Although previously believed to only be formed synthetically, crystalline BN has been discovered to form naturally in the earth's mantle [9].

Cubic boron nitride (c-BN) has a zinc blende structure, analogous to diamond, and is made up of sp^3-bonded boron and nitrogen. Its crystal structure consists of overlapping B and N face-centred cubic lattices [2, 10], as seen in figure 2.1a. The second sp^3-bonded structure is wurtzite boron nitride (w-BN) which is analogous to Lonsdaleite or hexagonal diamond, and is similarly less common. Its structure contains a mixture hexagonal rings in the boat and chair conformations rather than entirely in the chair conformation [11, 12], as seen in figure 2.1b.

Both sp^2-bonded polymorphs of boron nitride are comprised of stacked weakly-interacting monolayers made up of atoms arranged in a hexagonal pattern. The difference between these structures is how the layers are stacked. In hexagonal boron nitride (h-BN), the most stable polymorph of BN [13], the layers are stacked in an AA' arrangement such that each N is above a B in the previous layer and vice versa [14–16], as seen in figure 2.1c. In rhombohedral boron nitride (r-BN) the layers are ordered in an ABC arrangement with half of the atoms aligned with the layer below and the other half sitting above the center of the hexagonal rings [17–19], as seen in figure 2.1d. This difference in stacking can easily be observed by comparing the unit cells of



(a) (b)

(c) (d)

Figure 2.1: Crystal structures of boron nitride: (a) cubic, (b) wurtzite, (c) hexagonal, (d) rhombohedral. Boron and nitrogen atoms are coloured pink and blue respectively. The unit cells for the hexagonal and rhombohedral structures are shown in (c) and (d) to highlight the difference in the stacking patterns.

the two structures. Other stacking patterns have been studied theoretically with some being shown to potentially have lower energy than the AA' stacking of h-BN [20, 21], however these alternative stacking patterns have yet to be synthesised experimentally.

BN can also form nanomaterial structures reminiscent of those formed by carbon. These include zero-dimensional fullerene-like nanoparticles [5, 22, 23], one-dimensional nanotubes (BNNTs) [3, 24, 25] and two-dimensional nanosheets [26]. As shown in figure 2.2, all of these nanomaterials consist only of three-coordinate atoms. However, whilst pristine nanosheets and nanotubes consist of only of hexagonal B_3N_3 rings, due to their curvature, boron nitride fullerene-like particles contain a range of rings sizes. However, unlike the C analogue, the rings in the most common BN fullerene-like particles consist only of even numbers of atoms. This maximises the number of stronger B−N bonds over B−B and N−N bonds and is evident in their more octahedral shape, a result of the more restricted bond angles for four-membered rings[22].

Monolayer boron nitride (m-BN) or boron nitride nanosheets (BNNSs) can be synthesised in a variety of different ways. The methods for this synthesis can be grouped into two main categories: top-down and bottom-up. The top-down approaches all start with h-BN and involve exfoliation of the layers. This can either be mechanically through the use of adhesive tape [26, 28, 29] or ball milling [30, 31], or chemically. The chemical processes are carried out in the liquid state and involves the intercalation of ions between the BN sheets to facilitate their exfoliation by sonication [32–37]. The bottom-up approaches to synthesis involve the formation of the nanosheets by the deposition of atoms or molecules onto a substrate. The most common methods for this are chemical vapour deposition (CVD) [38–42] and physical vapour

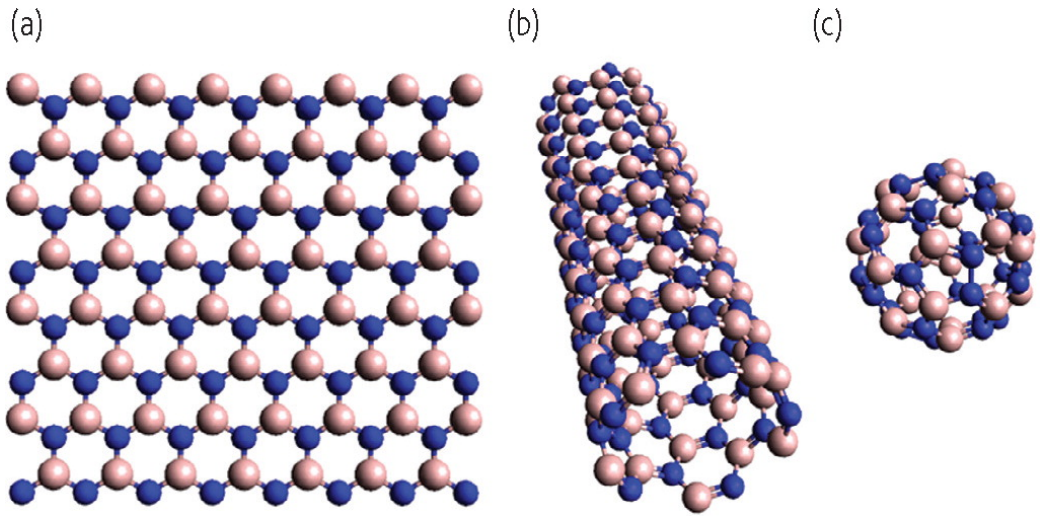


Figure 2.2: Structures of example boron nitride nanomaterials: (a) nanosheet, (b) nanotube, (c) fullerene-like nanoparticle. Boron and nitrogen atoms are coloured pink and blue respectively. Figure from ref. [27].

deposition (PVD) [43–48]. However, atomic layer deposition [49, 50] and molecular beam epitaxy [51–54] have also been used.

Finally, boron nitride can exist in disordered forms. The most common of these structures are turbostratic boron nitride (t-BN) and amorphous boron nitride (a-BN). t-BN has a similar structure to h-BN or r-BN containing stacked layers of sp^2-bonded sheets. However, in t-BN, disorder arises in two aspects of this stacking: rotation and translation. These two dislocations lead to a lack of repeating pattern in the stacking of the layers as well as the layers no longer being strictly parallel, resulting in the opening of pores between the layers [55, 56]. a-BN is most disordered form of boron nitride with no long-range order as a result of the disorder in the local bonding meaning a huge range of potential coordination environments are present [4, 57, 58]. It has been shown that the amorphous structure is made up of mostly sp^2-bonded atoms through x-ray photospectroscopy (XPS) [59] and Raman spectroscopy [4, 58]. As such it is believed that a-BN is made up of intercon-

nected rings of varying sizes, however unlike in the other sp^2-bonded boron nitride structures, these rings are not restricted to two-dimensional layers and so there is further disorder in how the rings are arranged. The structure of all amorphous materials is a hotly debated topic with the two main structural candidates being entirely continuous random networks, first proposed in 1932 by Zachariasen [60] (Z-CRNs), or as containing randomly orientated nanocrystallites, as proposed by Lebedev earlier [61]. It has been recently shown by Ahn *et al.* that disordered BN materials can form structures containing nanocrystallites as well as completely amorphous dependent on the synthetic conditions [62]. Much experimental work has been carried out investigating the synthesis of a-BN. However, the majority of these studies focus on the numerous potential applications of a-BN and the corresponding material properties rather than the underlying structure of the product. As such, the available experimentally-derived structural data for a-BN is relatively sparce. This is potentially due to the poor visibility of B and N to both x-ray and neutron. Hong *et al.* used electron diffraction data to calculate D(r) (as discussed in section 3.2.1) [4]. Whilst a peak at $r = 1.44$Å aligns with the nearest neighbour distance of B-N, the regular decay and spacing of the peaks as well as a peak below $r = 0.5$Å limits the applicability of the data. Much earlier work by Grigoriew and Leciewjewicz [63] included both real-space and reciprocal-space structural functions obtained using x-ray and electron diffraction. Both methods resulted in methods with similarly positioned peaks but with differing intensities. The real-space function, D(r), shows only two sharp peaks demonstrating that the short-ranged order quickly decays by the third coordination sphere. These peaks have maxima between the calculated bond length of sp^2 and sp^3 B-N bonds indicating that both may be present. Monolayer amorphous boron nitride (ma-BN) has also

been theorised [64, 65]. Although it has yet to be created experimentally, the closely related monolayer amorphous carbon (MAC) has been synthesised using electron irradiation of graphene [66, 67] as well as using CVD [68–70]. Due to the similarities between C and BN materials and the majority sp^2-bonding in a-BN, it is very likely that ma-BN will be stable and have a similar structure to that of MAC, with potential differences arising from the presence of less favourable homonuclear B-B and N-N bonds. Zhang *et al.* [64] predict through the use of Monte Carlo simulations, detailed in chapter 4, that ma-BN has a pseudo-CRN structure containing site-disordered, see section 2.6, pseudocrystallites, which is stable at room temperature.

This thesis will start by describing the modelling of the ordered forms of boron nitride before moving to the amorphous forms, as little is known about their structures and so developing an accurate computational model will aid investigations into these structures and therefore their properties and applications.

2.2 Defects in Boron Nitride

Defects can be defined as "a configuration in which an atom (or group of atoms) does not satisfy the structural rules pertaining to the ideal reference system of material."[71] Defects exist in some quantity in all crystalline materials at finite temperature owing to the increased disorder they create and the second law of thermodynamics. Defects can often have a significant effect on the properties of a material, such as changing mechanical properties [72], modifying semiconducting behaviour [73] or increasing reactivity [74], and so understanding the structures and behaviours of defects can be key to understanding how they can be controlled to enable a wide range of

applications.

Defects can be grouped in a variety of different ways. The most wide ranging classification is the dimensionality of the defect. In bulk three dimensional systems, these categories are: 0D or point defects, 1D or linear defects, 2D or planar defects and 3D or volume defects. However, in boron nitide materials, despite existing in all of the ordered structures, defects have been best studied in hBN, mBN and BNNTs. This is due to the unique geometries of these materials allowing defects to be seen directly through the use of microscopy [75–83]. When moving to 2D materials, such as mBN, there are changes in how some defects are classified, for example, in 3D systems grain boundaries and voids (or holes) are 2D and 3D defects respectively, however, in 2D materials they are 1D and 2D defects. This reduction in dimensionality is as a result of it being impossible to define defect edges perpendicular to the layer.

A variety of 1D and 2D defects have been studied in boron nitride. Grain boundaries are among the most common 1D defect, which due to variable ring sizes and orientations have a huge range of structures. Originally through theoretical work [84] and later through the use of microscopy [75–77], h-BN grain boundaries have been shown to contain alternating 5|7-membered rings as well as 4|8-membered rings. However, as neither scanning tunnel or transmission electron microscopy is able differentiate between boron and nitrogen atoms the types of bonds in these boundaries are still debated. By comparison with theoretical band gap data, it has been shown that when grown by CVD the 5|7 boundaries contain alternating B-B and N-N homonuclear bonds and the 4|8 boundaries contain only heteronuclear bonds [75, 77]. However, when h-BN layers are mechanically exfoliated and then irradiated with electrons, the resulting 4|8 boundaries must contain homonuclear B-B

and N-N bonds because of their formation from the pristine lattice. The formation of these boundaries has been explained through gliding of atomic rows [76]. Domain boundaries made up of only 6-membered rings have also been theorised [84]. These boundaries contain homonuclear bonds resulting in the inversion of the lattice ordering. However, as previously mentioned, it is not currently possible to easily image these domain boundaries and so they have not been studied experimentally.

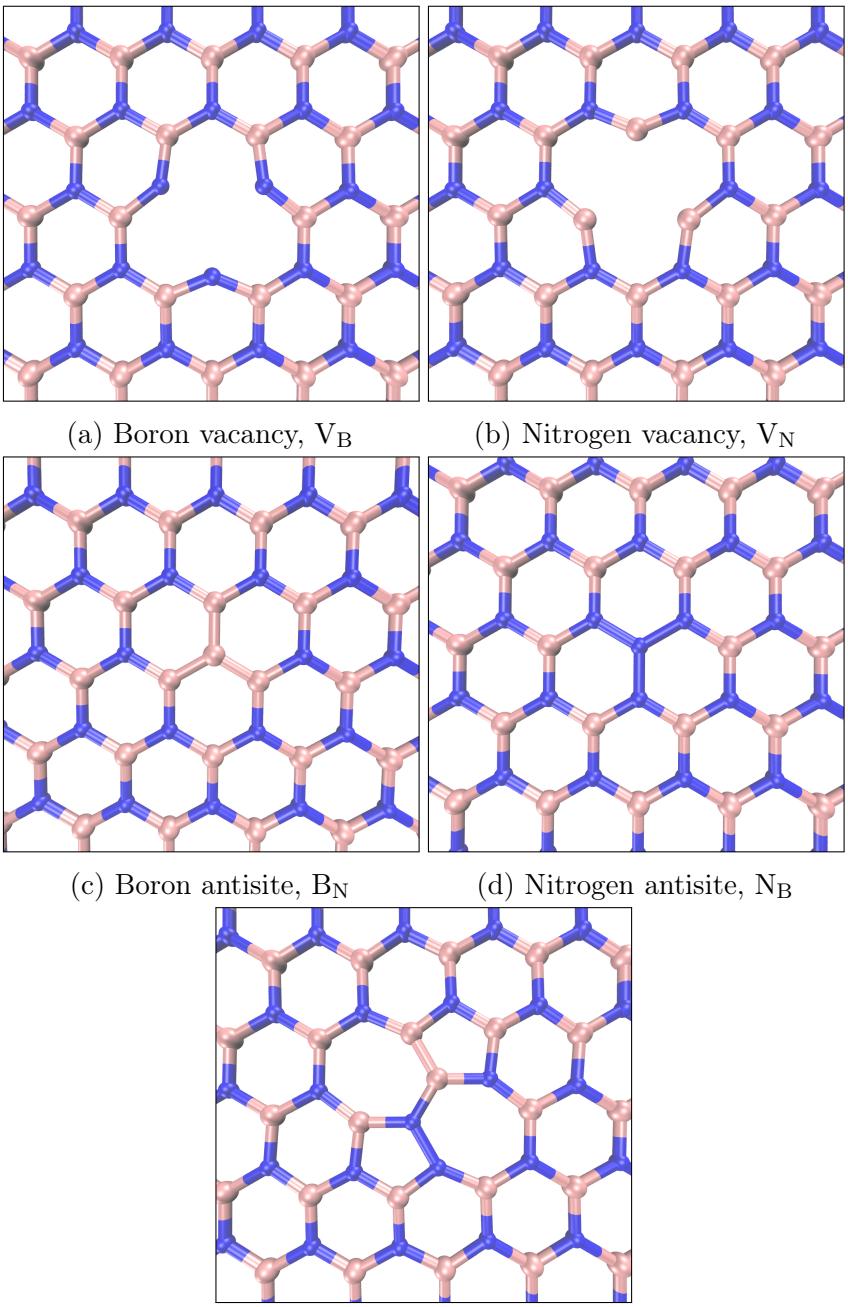
Point or 0D defects can be further classified into intrinsic and extrinsic defects. Intrinsic defects are those containing only atoms already present within the material, examples of these types of defect include vacancies and anti-site defects. Both of these examples have been studied in h-BN. Vacancies involve the removal of small numbers of atoms from the crystal and have been studied both experimentally [78–82] and theoretically [85, 86]. It has been shown that N-terminated triangular vacancies, figure 2.3a, are formed preferentially although B-terminated triangular vacancies, figure 2.3b as well as hexagonal vacancies are also possible. As these vacancies increase in size, they are eventually labelled as holes or pores, a 2D defect type. However, the condition for this crossover is not well defined. Anti-site defects are the replacement of an atom with one of a different type, figures 2.3c and 2.3d. These defects have been studied theoretically in h-BN [86–90], and it has been shown that they are stable and can have a significant effect on thermal and electrical properties of the material, however, it is not currently possible to easily image these defects and so experimental work on these defects has yet to be published. Intrinsic point defects can also involve the rearrangement of the group of atoms. One of the best studied examples of this in h-BN is the Stone-Wales defect [91], figure 2.3e. Originally studied in carbon-based systems, the Stone-Wales defect involves the rotation of a bond

by 90° resulting in the transformation of 4 six-membered rings into 2 five- and 2 seven-membered rings. Much work has been undertaken looking at the effect Stone-Wales defects can have on the properties of h-BN, including their effect on reactivity [92], their role as ultraviolet quantum emitters [93] and how they affect mechanical properties [94]. Furthermore, the different charge states were studied [95], and were shown to have a influence on the configurations and electronic properties of the defect.

Extrinsic defects are those containing atoms not present in the ideal crystal. These impurity atoms can be incorporated in both interstitial and substitutional positions. In h-BN, the majority of studied impurity atoms are incorporated substitiutionally [86, 89, 96, 97]. Some cases of interstitial impurities have been studied, however these are normally accompanied by an adjacent vacancy [86]. The most commonly studied impurity atoms are C and O, however work has been carried out looking at the possibility of Si and S as impurities also. Krivanek *et al.* [83] used annular dark-field electron microscopy to directly image different atom types in h-BN and showed the presence of C and O impurities. It was noted that O substituted only for N atoms and that C atoms were only seen to substitute for a B-N pair. Work has also been carried out by Park *et al.* intentionally inserting C into vacancies in h-BN monolayers using focussed electron beams [98].

2.3 Applications of Boron Nitride

Boron nitride materials have a huge range of potential applications from those taking advantage of their mechanical properties to those using their electrical or chemical properties. Due to the variety in their structures, boron nitride materials often have very different properties and therefore applica-



(a) Boron vacancy, V_B (b) Nitrogen vacancy, V_N

(c) Boron antisite, B_N (d) Nitrogen antisite, N_B

(e) Stone-Wales defect, SW

Figure 2.3: Example point defects in a BN nanosheet. Boron and nitrogen atoms are coloured pink and blue respectively.

tions. Starting with the crystalline forms, c-BN is one of the hardest known materials, second only to diamond [99], and as such has found significant use as a commercial abrasive and in cutting and drilling tools under the trademark Borazon®[100]. These tools are of particular use with ferrous materials which c-BN is inert against unlike diamond [10]. c-BN is also a semiconductor with excellent thermal conductivity which potentially allow it to be used as heat sink in a variety of devices such as LEDs [101].

Due to their layered structure, h-BN and nanosheets have good potential for usage in separation applications. Water purification or desalination involves the removal of pollutants and ions respectively, and is a process of vital importance for the ever increasing population without access to clean fresh water. Lei *et al* showed that porous BN nanosheets have excellent absorbencies for organic solvents, oils and dyes significantly higher than that of the commercially available carbon and BN particles [102]. It was also shown by comparison with pristine nanosheets that the introduction of pores doubled these absorbencies and that through heating, burning or cleaning with solvent, the porous nanosheets can be regenerated allowing for repeated uses. Since then, h-BN and nanosheets have been shown to be adsorbents for a range of ions including Pb^{2+} [103], PO_4^{3-}, NO_3^- and Cr(VI) [104]. A variety of theoretical work has been undertaken investigating the mechanism of water desalination through nanopores in BN nanosheets, including the effect of number of layers [105], pore size [106], edge pattern [107], grain boundaries [108] and functionalisation [109]. Nanopores in BN nanosheets have also been shown to be promising candidates for detection and potential sequencing of single molecules of DNA [110, 111].

h-BN has also shown promise in a variety of electronics applications, owing to its versatile tunable electronic properties. For example, h-BN has been shown

to be a potential candidate for use in supercapacitors [112], lithium batteries [113] and as part of UV emitters and detectors [114]. It has also been used as a excellent substrate for other nanoscale electronic devices owing to its atomic smoothness and lack of dangling bonds [115, 116]. Defects in hexagonal boron nitride have emerged as room temperature quantum emitters, the first two-dimensional material to do so at non-cryogenic temperatures, indicating its potential in nanophotonic devices and sensors [117–119].

Amorphous boron nitride (a-BN) is characterised by its high degree of disorder and as such may have very different properties to the crystalline forms of BN. Hong *et al* demonstrated that a-BN is an excellent candidate for use as a isolation materials for nanoscale electronic interconnects [4]. They demonstrated the growth of a-BN thin films with ultralow dielectric constants, that were able to prevent the diffusion between interconnects whilst being mechanically and electrically robust. a-BN films have been shown to enhance the charge mobility of two-dimensional materials such as graphene [120, 121], MoS_2 and more [122], whilst also acting as a protective barrier. Whilst h-BN has shown promise as a UV detector, the requirement for large single crystal films, only formed under harsh growth conditions, limits its applications. a-BN films have been shown to have similar potential whilst having less intense growth conditions [16, 123, 124]. Wu *et al* also demonstrated the ability for UV detectors based on a-BN films to operate without the need of an external power source, allowing for more sustainable and independent devices [124]. Memristors or resistive switching memories (RSMs) are electrical components which are able to change their resistance based on the charge flowing through them. These devices are able to retain their changed resistance without power and so can be used as potential alternative to flash memory, especially in neuromorphic systems which mimic the human brain.

Memristive devices based on a-BN have been shown to operate via the diffusion of boron vacancies and transition metal defects [125, 126] and are able to achieve high levels of accuracy (90.8%) in pattern recognition neural network simulations [127].

Applications for boron nitride nanomaterials often take advantage of their unique topologies. Fullerenes and nanoparticles have been shown to be effective for the transportation of other species, for example, they have been shown as a potential nanocarriers for drugs to help treat Alzheimer's disease [128] and various forms of cancer [5, 129–131]. BNNTs and nanoparticles have also been shown to be potential mediums for hydrogen storage [132–136]. BNNTs have excellent mechanical properties and thermal conductivity whilst also being electronically insulating [137]. They have, therefore, found success as nano-fillers in a variety of other materials. By incorporating BNNTs into polymers, composites can be created which have the potential to allow for heat dissipation in electronic devices whilst avoiding short circuits [137]. It was shown that BNNT-polymer interactions are much stronger than those in similar CNT polymer composites, which is suggested to be caused by the strong electrostatic interactions present for BNNTs [138] and therefore may further reinforce these structures. BNNTs have also been used as structural reinforcements in metals [139–141], ceramics [142, 143] and glasses [144, 145], showing significant improvements in mechanical properties with only small amounts of incorporated BNNTs. Their superhydrophobicity and mechanical strength has also led to interest in BNNT membranes for water purification. This is due to the high reverse osmosis fluxes they can produce [137], allowing for effective removal of organic pollutants and oil whilst being cleanable and reusable [146, 147]. These properties have also led to work utilising BNNTs for osmotic energy harvesting with currents over two orders

of magnitude greater than those produced by pressure-driven systems [148].

2.4 Methods of Modelling Boron Nitride

2.4.1 *Ab initio* Methods

A wide variety of methods have been used to study boron nitride materials. Among the most complex of these models are *ab initio* methods. One of the most common of these methods is simulations based on density functional theory (DFT). In DFT, many electron systems can be studied by representing the electron density as a spatially dependent functional, which can then by used to determine a wide variety of material properties. Some examples of properties studied using DFT simulations include the mechanical properties of m-BN [149], the adsorption onto m-BN of hydroxides [150] and hydrogen [151], the structure and electronic properties of BN fullerenes [152] and the electronic structure of defects [92, 153].

A less common group of *ab initio* techniques are quantum Monte Carlo (QMC) methods. These approaches involve using Monte Carlo simulations to either solve the Schrödinger equation for a system or model the system by treating the interactions between particles using quantum mechanics. QMC methods have been used to study the cohesive [154] and elastic [155] properties of c-BN as well as the effect of including quantum interactions on c-BN over a range of pressures [156]. QMC has also been used to study similar properties in h-BN [157, 158] as well as the interaction of h-BN with other species. For example, QMC derived potentials have been used to study the wetting of h-BN [159, 160] and the interlayer adhesion between h-BN and graphene monolayers [161].

Whilst *ab initio* methods are excellent at studying the electronic properties of materials, one of their main disadvantages is a relatively long computation time, meaning that only systems of a maximum of a few hundred atoms can be studied in a non-dynamic way. As such to study larger systems ($\geq$ 500 atoms) alternative simulation methods are required.

2.4.2 Molecular Mechanics Methods

Molecular mechanics methods do not traditionally include modelling of the electronic properties of a material. Instead, the Born-Oppenheimer approximation is assumed to be valid allowing for a focus on the nuclear coordinates and treating interactions between atoms using an interatomic potential model. These potential models come in a huge variety of forms but can be grouped by how they are derived. Empirical potentials (EPs) or parametric models are those containing variable parameters whose values are chosen to fit with properties from experimental results or the results of more complex *ab initio* simulations. The most commonly used EP for the study of boron nitride is the Tersoff potential [162], which was first parameterised for cubic boron nitride by Albe *et al* in 1997 [163], since then a variety of parameters for boron nitride structures have been proposed [164–167]. The Tersoff potential is discussed in more detail in subsection 4.3.3. Machine learning potentials (MLPs) are those which employ neural networks to transform inputted atomic coordinates into potential energies. The emergence of MLPs is a much more recent development in literature owing to advances in computational power and the increasing availability of data. MLPs are trained using *ab initio* data and allow for the simulation of large scale systems with accuracy potentially approaching that of *ab initio* calculations.

Both potential types have clear advantages and disadvantages. EPs are de-

signed for a specific system and require significant insight into the domain of materials they apply to, whereas MLPs are very flexible and can essentially fit any atomic energy landscape [168]. However, for a MLP to be accurate, large sets of high quality training data are first required for the potential to learn the system. This *ab initio* training data is becoming more easily obtainable through publicly available databases; however, changes to a system may require a complete retraining of the model, rather than a simple variation of parameters. MLPs may also lack physical interpretability, making it difficult to isolate which physical phenomena are responsible for specific interactions [160]. In contrast, employing a more simple parametrised EP allows for the variation of the model parameters to directly investigate the effect of different interactions on the properties of a material. EPs also allow for the ability to augment the potential with additional levels of complexity which is not possible in more complex MLPs where all interactions are already "baked in".

Molecular dynamics, further discussed in section 4.2, is one of the most common methods for studying condensed matter systems, including boron nitride, using potential models. Molecular dynamics simulations have been used to study many of the properties across the structures of boron nitride, particularly h-BN and its nanosheets. Much work has been undertaken investigating mechanical properties of c-BN [169], h-BN [170–174] , nanosheets [174–179], nanotubes [180, 181] and a-BN [65, 182–184] using both EPs [169–172, 175–182], and MLPs [65, 173, 174, 183, 184]. The interaction of boron nitride materials with other species is another common area of investigation. The interaction of water with h-BN has been studied in relation to both its wetting [160, 185, 186] as well its permeability [107, 108]. These permeability studies also involve modelling the interaction of h-BN with various ions. Molecular dynamics has also been used to investigate defect formation in

h-BN using oxygen irradiation [187].

Potential models can also be employed in Monte Carlo methods, discussed in section 4.1. These method allow for the stochastic modelling of a system, rather than deterministically moving a system along its lines of force. Monte Carlo methods have therefore been used in a range of ways which take advantage of the random nature of the approach. This includes the modelling of the movement of defects in h-BN monolayers [82], the adsorption of hydrogen [188], methane [189] and transition metal complexes [190] onto nanotubes, and for the generation of monolayer amorphous configurations [64, 65].

2.4.3 Other Methods

Whilst *ab initio* and molecular mechanics approaches are the most common methods for modelling boron nitride, semi-empirical and continuum methods have also been employed. Semi-empirical methods typically start from a first principles formalism before introducing approximations allowing for an improvement in their efficiency but a decrease in their accuracy. As such they are between *ab initio* and molecular mechanics methods in terms of both accuracy and speed. To account for these errors produced by these assumptions, parametrisation is introduced which can then be calibrated to fit with experimental data. Semi-empirical approaches have been used to the interaction of BN nanosheets with water [191] and graphene [192], and of BN nanocages with hydrogen [193]. They have also been used to study the electronic properties of both h-BN [194] and c-BN [195].

The continuum approach involves using calculated interaction energies to determine the properties of a model continuous object which is used as an approximation for the atomistic representation. This approach has mainly

been used to calculate mechanical properties of boron nitride materials such as h-BN, c-BN and nanotubes [196–199]. However, Kia *et al* also used it to investigate the encapsulation of both carbon and boron nitride fullerene particles inside carbon and boron nitride nanotubes [200].

2.5 Polar Bonding in Boron Nitride

When studying any system, the nature of the bonding in of key importance to understanding the structure and properties of said material. This is of course particularly evident in materials containing multiple atom types, which naturally have different contributions to bonding interactions. Boron and nitrogen have similar energy orbitals and so form strong covalent bonds. However, due to the electronegativity difference between the two atoms, these covalent bonds have partial ionic character resulting in the electron density in the system being localised closer to the nitrogen. This polar bonding is evident in a large variety of the properties of different boron nitride materials. One of the most obvious pieces of evidence is in the stacking of hexagonal boron nitride. As noted in section 2.1, hexagonal boron nitride is made up of sp^2 bonded layer stacked on top of each other, similar to graphite. In graphite, the layers are arranged in an AB stacking pattern, where each layer is offset to avoid the atoms in the layer below, however, in h-BN, the layers are arranged in a AA' pattern, with atoms positioned directly above each other, despite the interlayer distance being essential the same, $3.30 - 3.35$ Å[201]. The AA' stacking pattern is stabilised in boron nitride by the additional electrostatic force between the alternating boron and nitrogen in each layer which in not present in graphite.

Polar bonding is also evidenced through the comparison of the electronic

conductance of graphene and monolayer h-BN. It has long been shown that layered h-BN is a wide band gap insulator [202] and more recently it has been shown that monolayer h-BN is still an insulator with a band gap of $\sim$ 6eV, although it moves from an indirect to a direct bandgap [203–205]. Whereas, graphene is well known to be a zero band gap semi-conductor or semi-metal [206, 207]. It is clear that this difference is not dependent on their analogous structures but instead the electronegativity difference between B and N resulting in electrons being localised around nitrogen in monolayer h-BN, whilst they are freely delocalised in graphene.

The bonding differences can also been seen in the preferences for different ring sizes. For example, both carbon and boron nitride form nanotubes with sealed ends, however, the geometry of these tips are different. It has been shown that boron nanotubes have a preference to form approximately square closed flat tips over the cone shaped tips formed by carbon nanotubes (as shown in figure 5 of [208, 209]) which is rationalised through the formation of only even-membered rings in BNNTs to ensure an alternating pattern of B and N stabilised by the additional electrostatic contribution to the bonds. However, it has also been demonstrated by Saito *et al* [210] that whilst they are less common, tips containing five- and seven-membered rings do still form despite the less favourable BB or NN bonds inherent in these rings sizes.

Finally, the adsorbtion properties of hexagonal boron nitride also show evidence of the polar bonding in boron nitride. h-BN, similar to graphene, has sp^2-bonding leading to aromatic rings. This means it is an excellent adsorbent for aromatic compounds such as methylene blue [211] or tetracycline [212], both medication. However, the partial ionic character also led to excellent adsorbtion of ions, for example, Karthikeyan *et al* [104] showed that polyaniline-substituted hexagonal boron nitride is an excellent adsorbent of

phosphate, nitrate and chromium ions in aqueous solution owing to the electrostatic attraction between the complex and the ions. Liu *et al* [103] also showed a similar affinity between few-layered boron nitride nanosheets and lead ions again owing to the electrostatic interaction.

2.5.1 Determining the Charges in Boron Nitride

Modelling electron density is a significant computational challenge, therefore a common approximation is modelling these electron clouds as point charges located on atoms. Whilst this approach does not fully capture all the details of the electronic interactions and therefore not accurate enough to model reaction mechanisms or electronic properties, it does allow for the modelling of electrostatic interaction in significantly larger systems. To help better capture the behaviour of systems which contain covalent bonds with ionic character, partial charges are employed. These are point charges with non-integer multiples of e and as such are not entirely physical, but instead allow for the modelling of the increased or decreased electron density present in these polar bonds.

Partial charges for boron nitride structures have been calculated in a variety of ways, with assorted levels of complexity leading to a wide range of results. As seen in table 2.1, the majority of the calculated values fall in between $|q|/e = 0.3$ and $|q|/e = 0.5$ with the most commonly reported value being $|q|/e = 0.3$. Of the results not within this range, most are below $|q|/e = 1.0$ and are physically understandable as representing a polar covalent bond where electrons are not entirely located around either atom. A few values are above $|q|/e = 2.0$ and are therefore representative of the charge transfer of more than 2 electrons from boron to nitrogen indicating ionic bonding rather than polar covalent bonds. It should also be noted that in some cases

the magnitude of the charge on boron is reported as being greater than on nitrogen, which is not physically possible as this would imply that the system is not neutral overall. By looking at the method with which the charges were calculated, it can be seen that, in general, quantum Monte Carlo (QMC) and semi-empirical methods predict lower charge magnitudes than density functional theory (DFT) methods whilst experimental methods produce a range of values.

As mentioned previously, the use of point charges is an approximation and are often calculated by integrating over a region of a calculated charge density. As such, the size of the region chosen can have a significant impact on the magnitude of the resulting point charge value. Therefore, when working with partial charges, it is key to make sure that the values being used are chemically intuitive in relation to the bonding in the studied material.

2.6 Topological and Site Disorder

Due to the multiple types of atom present in boron nitride, there are multiple types of disorder. In materials containing only one type of node, the only type of disorder is topological. This disorder is related to how atoms are arranged in space whilst the type of nodes is irrelevant. The nature of these nodes can vary from single atoms such as in amorphous carbon, both three-dimensional [227–229] and monolayer [67, 69, 70, 230, 231], to bonded units such as SiO_4 in amorphous silica [232–234], or even larger $Ca_3B_2SiO_8$ units in $CaSi_{1/3}B_{2/3}O_{8/3}$[235]. An example of topological disorder in a two-dimensional network material can be seen in figure 2.4a. This example clearly shows areas of high topological order containing only six-membered rings and areas of topological disorder with regions containing many five- and seven-

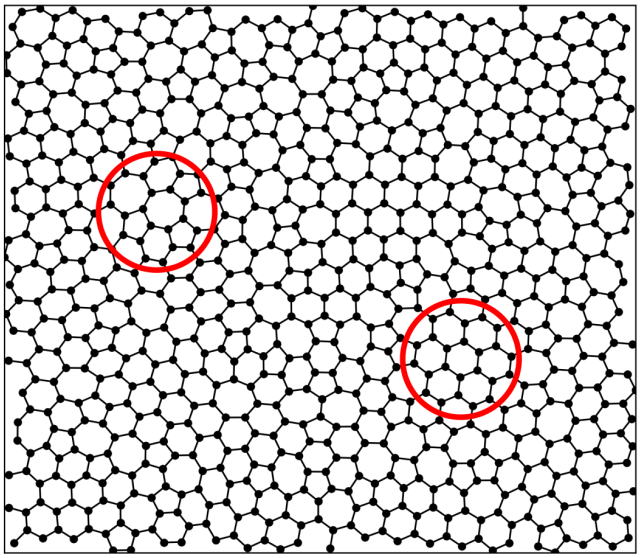
q_B/e	q_N/e	Reference	Method
0.3	-0.3	[194]	Semi-empirical
0.3	-0.3	[213]	Experimental
0.3	-0.3	[214]	DFT
0.30	-0.30	[159]	QMC
0.35	-0.35	[215]	Semi-empirical
0.35	-0.35	[105]	DFT
0.36	-0.36	[160]	QMC
0.42	-0.42	[216]	DFT
0.45	-0.45	[217, 218]	Experimental
0.45	-0.45	[219]	DFT
0.47	-0.47	[95]	DFT
0.50	-0.50	[220]	DFT
0.504	-0.504	[221]	DFT
0.52	-0.52	[222]	DFT
0.61	-0.61	[223]	Experimental
0.907	-0.907	[224]	DFT
1.178	-1.170	[225]	DFT
2.15	-2.15	[219]	DFT
2.7	-1.9	[226]	Experimental

Table 2.1: Previously reported partial atomic charges for h-BN.

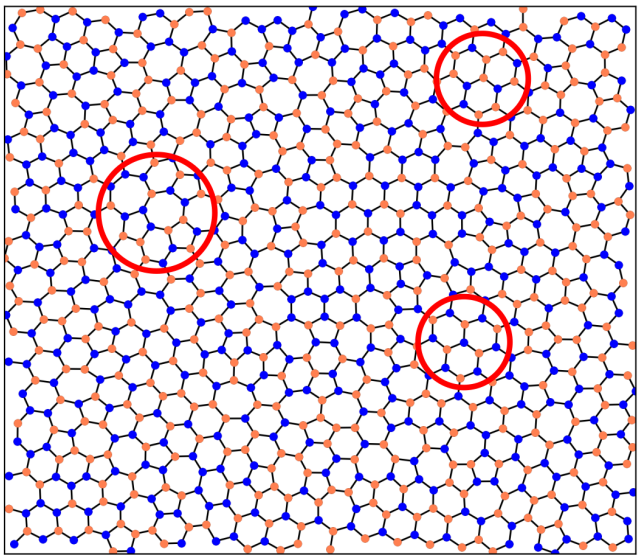
membered rings.

When atoms of different types are allowed to be situated on similar nodes, a second type of disorder is introduced into the material. This site-based or chemical disorder is related to how atoms are arranged on nodes within a network relative to each other. This type of disorder is common in materials containing a mixture of similar atoms, such as gehlenite $Ca_2Al_2SiO_7$ [236] [237], $LiNi_{0.5}Mn_{1.5}O_4$ [238] or lithium argyrodites $LiPS_5X$ [239] [240]. By introducing multiple atom types into our example disordered two-dimensional network, figure 2.4a, we also introduce site-disorder, figure 2.4b. It can be seen that we then have regions which are topologically ordered and site ordered as well as regions which are topologically ordered but site disordered. It can also be seen that there are some links between these two types of disorder. For example in rings containing an odd number of atoms, which must contain homo-atomic bonds which are a source of site disordering and can spread across the network.

Both of these types of disorder also introduce many other types of disorder such as disorder in bond lengths and angles. However, these additional types of disorder have a more minor effect on the overall structure of the material as there is less range in bond lengths and angles and the variations in these properties are often caused by the topological and site disordering.



(a) Topological Disorder



(b) Site Disorder

Figure 2.4: Comparison of 2D networks containing (a) only topological disorder and (b) topological and site disorder. The circled areas in Panel (a) shows regions of high and low topological order. Panel (b) shows the same network with boron and nitrogen atoms coloured pink and blue respectively. The highlighted areas in (b) show regions of topological order which are site ordered and site disordered, as well as the site disorder inherent in topologically disordered regions.

3 | Theory

Contents

3.1 The Canonical Ensemble 30

3.2 Understanding the Structure of Disordered Materials 31

3.2.1 Pair Distribution Functions (Real Space Functions) 32

3.2.2 Structure Factors (Reciprocal Space Functions) . . 37

3.2.3 The Bhatia-Thornton Formalism 39

3.3 Network Theory and Ring Statistics 42

3.3.1 Node Degree 42

3.3.2 Topological Laws 43

3.3.3 Atomic and Ring Networks 47

3.4 The Fluctuating Charge Model 47

3.4.1 Calculation of Electronegativities 50

3.4.2 Calculation of Atomic Charges 52

This chapter discusses and derives some of the key pieces of theory used throughout this work. This includes the underlying statistical mechanics and how this leads into understanding the structure of disordered materials. Next, the basics of network theory are established and how they can be applied to atomic network materials. Finally, the fluctuating charge model is derived and how it can be used to control atomic charges is explained.

3.1 The Canonical Ensemble

The canonical ensemble can be used to describe an ensemble of states of a system containing a fixed number of particles, N, with a fixed volume, V at thermal equilibrium with a heat bath at temperature T. All thermodynamic information about such as system can be obtained through the use of the classical canonical partition function:

$$Q = \frac{1}{N!h^{DN}} \int \int e^{-\beta H(\boldsymbol{r}^N, \boldsymbol{p}^N)} \mathrm{d}\boldsymbol{r}^N \mathrm{d}\boldsymbol{p}^N \tag{3.1}$$

where $\beta = 1/k_B T$, $\boldsymbol{r}^N$ and $\boldsymbol{p}^N$ are positional and momentum coordinates of all atoms in the system respectively, D is the dimensionality of the system and $H(\boldsymbol{r}^N, \boldsymbol{p}^N)$ is the Hamiltonian of the system [241]. The Hamiltonian consists of the kinetic energy of the system, K_N, which is dependent on the momenta of the atoms in the system and the potential energy U_N, which is dependent of the positions of the atoms in the system.

$$\begin{aligned} H(\boldsymbol{r}^N, \boldsymbol{p}^N) &= K_N(\boldsymbol{p}^N) + U_N(\boldsymbol{r}^N) \\ &= \sum_{i=0}^{N} \frac{p_i^2}{2m} + U_N(\boldsymbol{r}^N). \end{aligned} \tag{3.2}$$

Using the explicit form of K_N, the integral over the momenta in the kinetic component of the partition function, Q_T, can be calculated leading to

$$Q(N, V, T) = \frac{1}{\Lambda^{DN} N!} \int e^{-\beta U(\boldsymbol{r}^N)} \mathrm{d}\boldsymbol{r}^N = \frac{1}{\Lambda^{DN} N!} Z(N, V, T) \tag{3.3}$$

where we have defined the de Broglie thermal wavelength, Λ, as

$$\Lambda = \frac{h}{(2\pi m k_B T)^{1/2}} \tag{3.4}$$

and the configurational integral, $Z \equiv Z(N, V, T)$, as

$$Z(N, V, T) = \int e^{-\beta U(\boldsymbol{r}^N)} \mathrm{d}\boldsymbol{r}^N. \tag{3.5}$$

Using this definition for the configurational integral Z we can then obtain an expression for the ensemble average of any quantity $A(\boldsymbol{r}^N)$ which is only dependent on atomic positions as

$$\langle A \rangle = \frac{1}{Z(N, V, T)} \int A(\boldsymbol{r}^N) e^{-\beta U(\boldsymbol{r}^N)} \mathrm{d}\boldsymbol{r}^N. \tag{3.6}$$

The probability of finding system in a given configuration is then

$$P(\boldsymbol{r}^N) \equiv \frac{e^{-\beta U(\boldsymbol{r}^N)}}{Z}. \tag{3.7}$$

3.2 Understanding the Structure of Disordered Materials

The properties of any material are closely related to its structure and so to understand these properties it is first necessary to characterise the structure of said material. Whilst the long range order found in crystalline structure is not present in disordered materials such as liquids or amorphous solids, these materials are not just randomly ordered. Instead, the short range order of these system is quite distinct and often similar to the short range order

found in related crystalline materials [242].

3.2.1 Pair Distribution Functions (Real Space Functions)

One way the structure of these disordered systems can be characterised is through the use of real space atomic position distribution functions. The most commonly used of these is the total pair distribution function, $G(r)$ [243]. By integrating the configurational probability, equation 3.7, across atomic positions and normalising, we can define $G(r)$ as

$$G(r) = \frac{N(N-1)}{n_0^2 Z(N,V,T)} \int e^{-\beta U(\boldsymbol{r}_1,\boldsymbol{r}_2,\ldots,\boldsymbol{r}_N)} \mathrm{d}\boldsymbol{r}_3 \mathrm{d}\boldsymbol{r}_4 \ldots \mathrm{d}\boldsymbol{r}_N \tag{3.8}$$

where n_0 is the average number density of the material. However, this form of the function is not simple to use and so a more convenient definition is as the ratio

$$G(r) = \frac{\rho^{(2)}(\boldsymbol{r}'+\boldsymbol{r},\boldsymbol{r}')}{n_0^2} = \frac{V^2}{N^2}\frac{1}{V}\int \rho^{(2)}(\boldsymbol{r}'+\boldsymbol{r},\boldsymbol{r}')\mathrm{d}\boldsymbol{r}'. \tag{3.9}$$

$\rho^{(2)}(\boldsymbol{r}'+\boldsymbol{r},\boldsymbol{r}')$ is the pair density and can be thought of as the probability density of finding at pair of atoms at separated by r. It can be defined as

$$\rho^{(2)}(\boldsymbol{r}'+\boldsymbol{r},\boldsymbol{r}') = \langle \sum_i^N \sum_{j\neq i}^N \delta(\boldsymbol{r}'+\boldsymbol{r}-\boldsymbol{r}_i)\delta(\boldsymbol{r}'-\boldsymbol{r}_j)\rangle. \tag{3.10}$$

We can then integrate over the delta functions to give an average over the pairs in the system

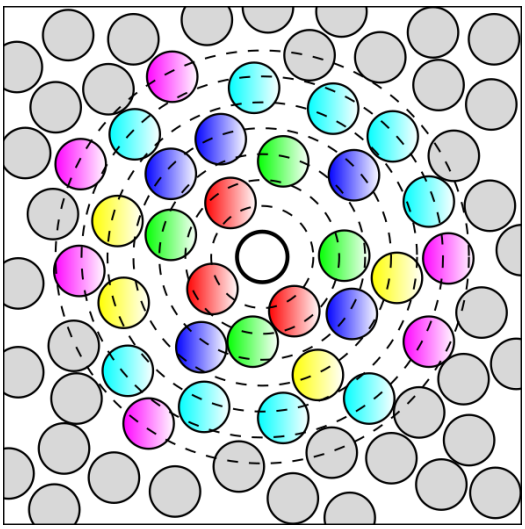


Figure 3.1: Graphic demonstrating the histogram method for calculating $G(r)$. The dotted lines represent the edges of bins at distance r from the central white atom. The atoms are coloured by the bin they are sorted into.

$$G(r) = \frac{V}{N^2}\langle \sum_{i}^{N} \sum_{j \neq i}^{N} \delta(\boldsymbol{r} - \boldsymbol{r}_{ij}) \rangle, \tag{3.11}$$

where $\boldsymbol{r}_{ij} = \boldsymbol{r}_i - \boldsymbol{r}_j$. $G(r)$ can be thought of as the probability of finding an atom at a distance r from another atom in the system relative to randomly distributed atoms at a density ρ. In practice, pair distribution functions are often calculated through the histogram method, as seen in figure 3.1, where each atom is taken in turn and the number of atoms in shells of thickness dr around the central atom at a distance r are counted, $n(r)$, and then normalised using

$$G(r) = \frac{n(r)}{4\pi r^2 \mathrm{d}r n_0}. \tag{3.12}$$

An example $G(r)$ can be seen in figure 3.2.

There are also a variety of other functions in real-space that can be used to

understand the structures of materials [244]. These functions are all closely related to $G(r)$ but can be used to obtain extra information about the system of interest. $D(r)$ is the differential correlation function and is defined as

$$D(r) = 4\pi r n_0[G(r) - 1], \tag{3.13}$$

therefore at low r values (shorter than the first nearest neighbour separation) the gradient is $-4\pi n_0$ and so can be used to calculate n_0 as well as the density, ρ, as seen in figure 3.2. The radial distribution function $R(r)$ is defined as

$$R(r) = 4\pi r^2 n_0 G(r). \tag{3.14}$$

R(r) can be used to calculate coordination number (the average number of neighbouring atoms in a coordination shell) by integration

$$\bar{n} = \int_{r_1}^{r_2} R(r)\mathrm{d}r, \tag{3.15}$$

as demonstrated in figure 3.2.

The functions discussed so far have been defined by summing over all possible atom pairs. However, when studying materials containing multiple types of atom this does not fully capture the structure, as such it can be useful to define partial pair distribution functions, $g_{\alpha\beta}(r)$. The most commonly used definition of these partial function is the Faber-Ziman formalism. Under this formalism, partial pair distribution functions are those containing only contributions from a given type of atomic pair, which by definition sum to give the total or all-atom pair distribution function, $G(r)$ [245]:

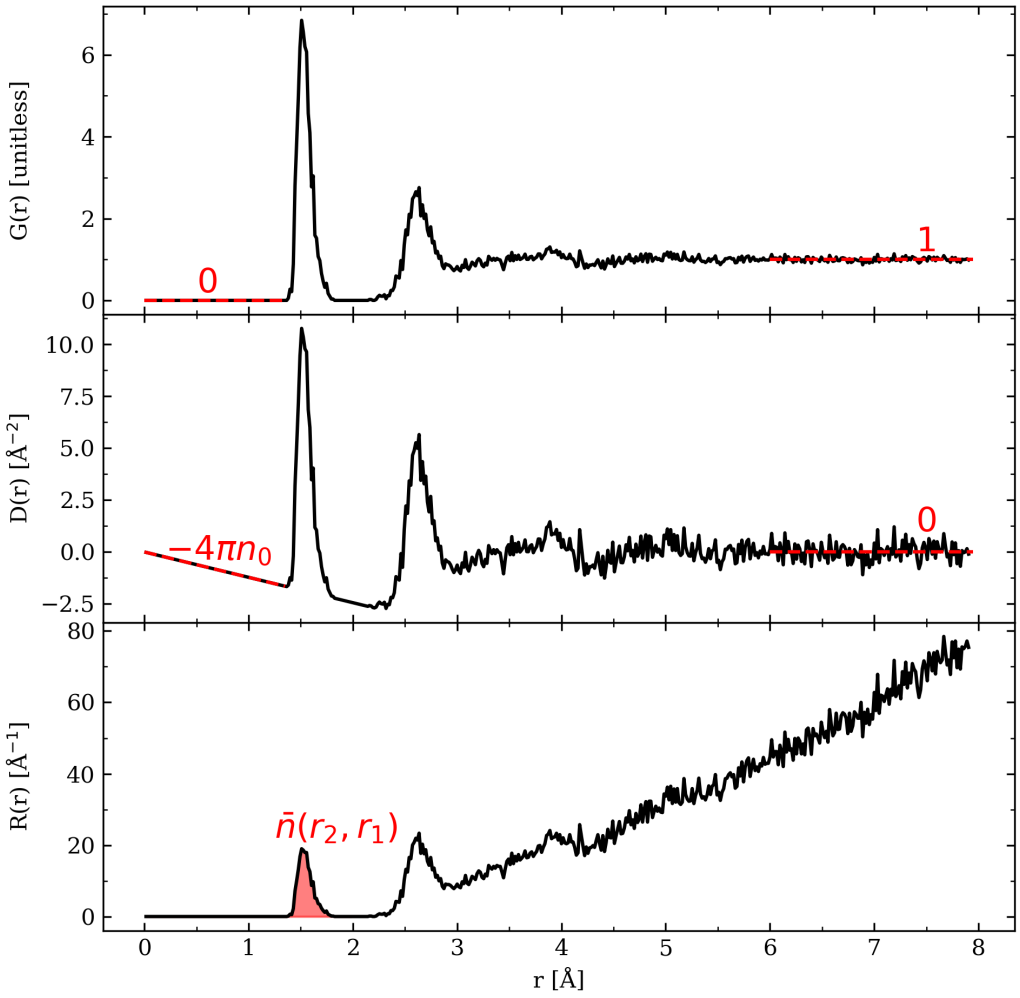


Figure 3.2: Example real space structure functions for the same amorphous boron nitride system. The top panel shows the pair distribution function, $G(r)$, with the low and high r limits labelled. The middle panel shows the differential correlation function, $D(r)$, with the low r gradient and the high r limit labelled. The bottom panel shows the radial distribution function, $R(r)$. The highlighted area shows the integration region for the calculation of the nearest-neighbour coordination number.

$$G(r) = \sum_{\alpha} \sum_{\beta} W_{\alpha\beta} g_{\alpha\beta}(r) \tag{3.16}$$

where $W_{\alpha\beta}$ is the weighting factor associated with the atomic pair of α and β such that $\sum_{\alpha} \sum_{\beta} W_{\alpha\beta} = 1$. $W_{\alpha\beta} = c_{\alpha} c_{\beta} b_{\alpha} b_{\beta}$ where $b_{\alpha(\beta)}$ is a weighting factor for species $\alpha(\beta)$ and can be dependent on the experiment used to measure the function, for example x-ray scattering lengths [244, 246]. These partial functions are also in practice calculated using the histogram method:

$$g_{\alpha\beta}(r) = \frac{n_{\alpha\beta}(r)}{4\pi r^2 \mathrm{d}r n_{\beta}} \tag{3.17}$$

where $n_{\alpha\beta}(r)$ is the number of particles of type β between distances r and $r + dr$ from a particle of type α and $n_{\beta} = c_{\beta} n_0$. We can then use partial pair distribution functions to calculate partial coordination numbers in a similar manner to equation 3.15

$$\overline{n}_{\alpha}^{\beta} = \int_{r_1}^{r_2} 4\pi r^2 n_{\beta} g_{\alpha\beta}(r) \mathrm{d}r. \tag{3.18}$$

$\overline{n}_{\alpha}^{\beta}$ is a mean partial coordination number and is equal to the mean number of atoms of type β around an atom of type α between distances r_1 and r_2. If $r_1 = 0$ and r_2 is equal to the distance of the first trough in the pair distribution function, $\overline{n}_{\alpha}^{\beta}$ is now equal to the mean partial coordination number for the first coordination sphere. Therefore, in a completely site-ordered 3 coordinate system of B and N

$$\overline{n}_{\mathrm{B}}^{\mathrm{N}} = \overline{n}_{\mathrm{N}}^{\mathrm{B}} = 3,$$
$$\overline{n}_{\mathrm{N}}^{\mathrm{N}} = \overline{n}_{\mathrm{B}}^{\mathrm{B}} = 0.$$

In any system, this constraint can be described by

$$\frac{1}{\mathscr{N}} \sum_{\alpha} \sum_{\beta} \overline{n}_{\alpha}^{\beta} = \overline{n}, \tag{3.19}$$

where $\mathscr{N}$ is the number of different types of atom in the system.

It should be noted that these functions can be used to study both two- and three-dimensional systems. However, care needs to be taken when calculating the size of regions used for the histogram method. As these regions are areas rather than volumes in two-dimensional systems meaning that equations 3.12 and 3.17 become

$$G(r) = \frac{n(r)}{2\pi r dr n_0} \tag{3.20}$$

and

$$g_{\alpha\beta}(r) = \frac{n_{\alpha\beta}(r)}{2\pi r dr n_{\beta}} \tag{3.21}$$

respectively. Also, due the change in dimensionality the number density of the system is now defined per unit area and so has units of $\mathrm{Å}^{-2}$ rather than $\mathrm{Å}^{-3}$ meaning that the units for D(r) become $\mathrm{Å}^{-2}$ and R(r) becomes unitless.

3.2.2 Structure Factors (Reciprocal Space Functions)

Another way of understanding the structure of disordered materials is through the use of structure factors. These are functions of wavevectors in reciprocal space and so are able to capture different information about structure than

pair distribution functions. Structure factors are defined as:

$$S(k) = N^{-1}\langle \rho^*(\mathbf{k})\rho(\mathbf{k})\rangle, \tag{3.22}$$

and describe the fluctuations in the Fourier transform of the number density, $\rho(\mathbf{k})$ which is defined as:

$$\rho(\mathbf{k}) = \sum_{i=1}^{N} \exp(-\mathrm{i}\mathbf{k}\cdot\mathbf{r}_i). \tag{3.23}$$

Structure factors can be measured experimentally through the use of diffraction experiments and so are often how structural information is presented in the experimental literature. However, structure factors and pair distribution functions are related through the use of Fourier transforms:

$$S(k) - 1 = \frac{4\pi n_0}{k}\int_0^\infty [G(r) - 1]r\sin(kr)dr \tag{3.24}$$

and

$$G(r) - 1 = \frac{1}{2\pi^2 r n_0}\int_0^\infty [S(k) - 1]k\sin(kr)dk, \tag{3.25}$$

meaning that both reciprocal and real space information can be obtained from diffraction experiments. Due to their reciprocal nature, structure factors are able to represent much longer range structural information, for example, it is possible to see evidence of domains or periodicity in system through small angle scattering [247, 248].

Structure factors can also be broken down into partial functions in much the same way as pair distribution functions whilst still retaining the Fourier relationship between the two functions:

$$S(k) = \sum_{\alpha,\beta} W_{\alpha\beta} S_{\alpha\beta}(k), \tag{3.26}$$

$$S_{\alpha\beta}(k) - 1 = \frac{4\pi n_0}{k} \int_0^\infty [g_{\alpha\beta}(r) - 1] r \sin(kr) dr \tag{3.27}$$

and

$$g_{\alpha\beta}(r) - 1 = \frac{1}{2\pi^2 r n_0} \int_0^\infty [S_{\alpha\beta}(k) - 1] k \sin(kr) dk. \tag{3.28}$$

Partial structure factors can also be defined in terms of Fourier components:

$$S_{\alpha\beta}(k) = \frac{1}{\sqrt{N_\alpha}\sqrt{N_\beta}} \langle \rho_\alpha^*(\mathbf{k}) \rho_\beta(\mathbf{k}) \rangle \tag{3.29}$$

where $\rho_\alpha(\mathbf{k}) = \sum_{i=1}^{N_\alpha} e^{-i\mathbf{k}\cdot\mathbf{r}_i}$. These partial structure factors can also be summed by appropriately weighting them to calculate the total structure factor:

$$F(k) = \sum_{\alpha,\beta} W_{\alpha\beta} (S_{\alpha\beta}(k) - 1) \tag{3.30}$$

3.2.3 The Bhatia-Thornton Formalism

The partial pair distribution functions and structure factors discussed so far have been using the Faber-Ziman formalism [249], which defines the partials by atom pair type. However, there are many other ways in which partial functions could be described. One which is of particular use when studying binary disordered structures, such as a-BN, is the Bhatia-Thornton formalism [250]. Bhatia and Thornton defined a set of partial structure factors, $S_{NN}^{\mathrm{BT}}(k)$,

$S_{CC}^{\mathrm{BT}}(k)$ and $S_{NC}^{\mathrm{BT}}(k)$[1], which describe the distribution of atomic number density, concentration and their correlation respectively. These partials are most easily calculated through a linear combination of the Faber-Ziman partials [251] as follows:

$$S_{\mathrm{NN}}^{\mathrm{BT}}(k) = c_\alpha^2 S_{\alpha\alpha}(k) + c_\beta^2 S_{\beta\beta} + 2c_\alpha c_\beta S_{\alpha\beta}(k) \tag{3.31}$$

$$S_{\mathrm{NC}}^{\mathrm{BT}}(k) = c_\alpha c_\beta (c_\alpha [S_{\alpha\alpha}(k) - S_{\alpha\beta}(k)] - c_\beta [S_{\beta\beta}(k) - S_\alpha(k)]) \tag{3.32}$$

$$S_{\mathrm{CC}}^{\mathrm{BT}}(k) = c_\alpha c_\beta (1 + c_\alpha c_\beta [S_{\alpha\alpha}(k) + S_{\beta\beta}(k) - 2S_{\alpha\beta}(k)]). \tag{3.33}$$

$S_{NN}^{\mathrm{BT}}(k)$ is the number-number partial factor and is able to represent fluctuation in the number density in the system. As this density is not dependent on the types of the atoms, $S_{NN}^{\mathrm{BT}}(k)$ is also independent of the atom types and so in disordered system can be used to study the topological order in the system. Whereas $S_{\mathrm{CC}}^{\mathrm{BT}}(k)$ is the concentration-concentration partial factor which measures only the concentration fluctuations and as such can be used to measure the site or chemical order in the system. Finally, $S_{\mathrm{NC}}^{\mathrm{BT}}(k)$ represents the correlation between the number and concentration fluctuations and so can be used to see if topological sites are favoured by particular atomic species [252]. The total structure factor under the Bhatia-Thornton formalism is expressed as:

$$F(k) = \langle b \rangle^2 S_{\mathrm{NN}}^{\mathrm{BT}}(k) + (b_{\mathrm{M}} - b_{\mathrm{X}})^2 S_{\mathrm{CC}}^{\mathrm{BT}}(k) + 2\langle b \rangle (b_{\mathrm{M}} - b_{\mathrm{X}}) S_{\mathrm{NC}}^{\mathrm{BT}}(k) - (c_{\mathrm{M}} b_{\mathrm{M}}^2 + c_{\mathrm{X}} b_{\mathrm{X}}^2) \tag{3.34}$$

[1]The superscript BT is used to denote the Bhatia-Thornton partial functions to avoid confusion with nitrogen and carbon partial functions under the Faber-Ziman formalism.

where $\langle b \rangle = \sum_\alpha c_\alpha b_\alpha$ is the weighted mean of the appropriate weighting factor.

These definitions for partial functions can also be applied to real space functions again through a linear combination of the Faber-Ziman partials:

$$g_{\mathrm{NN}}^{\mathrm{BT}}(r) = c_\alpha^2 g_{\alpha\alpha}(r) + c_\beta^2 g_{\beta\beta}(r) + 2c_\alpha c_\beta g_\alpha(r) \tag{3.35}$$

$$g_{\mathrm{CC}}^{\mathrm{BT}}(r) = c_\alpha c_\beta [g_{\alpha\alpha}(r) + g_{\beta\beta}(r) - 2g_\alpha(r)] \tag{3.36}$$

$$g_{\mathrm{NC}}^{\mathrm{BT}}(r) = c_\alpha [g_{\alpha\alpha}(r) - g_\alpha(r)] - c_\beta [g_{\beta\beta}(r) - g_\alpha(r)] \tag{3.37}$$

The Bhatia-Thornton formalism also allows for links to thermodynamic quantities, which are strongly dependent on the structure of a material. These quantities can be reached by looking at the low k limits of the partial structure factors:

$$\begin{aligned} S_{\mathrm{NN}}^{\mathrm{BT}}(0) &= n_0 k_{\mathrm{B}} T \chi_T + \delta^2 S_{\mathrm{CC}}^{\mathrm{BT}}(0) \\ S_{\mathrm{CC}}^{\mathrm{BT}}(0) &= k_B T / (\partial^2 G / \partial c_{\mathrm{M}}^2)_{T,p,N} \\ S_{\mathrm{NC}}^{\mathrm{BT}}(0) &= -\delta S_{\mathrm{CC}}^{\mathrm{BT}}(0) \end{aligned}$$

where n_0 is the average number density of the system, T is the absolute temperature, k_{B} is the Boltzmann constant, χ_T is the isothermal compressibility, the dilation factor $\delta = n_0(\nu_{\mathrm{M}} - \nu_{\mathrm{X}})$ where ν_α is the partial molar volume per particle of chemical species α. The charge-charge partial structure factor, for

an ionic system, can be expressed as

$$S_{\mathrm{ZZ}}(k) = \frac{S_{\mathrm{CC}}^{\mathrm{BT}}(k)}{c_{\mathrm{M}} c_{\mathrm{X}}}, \tag{3.38}$$

and must satisfy the Stillinger-Lovett conditions [253]. First, it must be equal to 0 at $k = 0$ i.e. $S_{\mathrm{ZZ}}(0) = 0$, which is an expression of charge neutrality. Secondly, $S_{\mathrm{ZZ}}(k) = \Lambda_D^2 k^2$ for small values of k, where Λ_D is the Debye screening length. Therefore, $S_{\mathrm{CC}}^{\mathrm{BT}}(0) = 0$ must also be true and so $S_{\mathrm{NN}}^{\mathrm{BT}}(0) = n_0 k_{\mathrm{B}} T \chi_T$, allowing for calculation of the isothermal compressibility of a material from its structure factor.

3.3 Network Theory and Ring Statistics

A network is a collection of entities called nodes connected in some way, physical or otherwise, by edges. Networks can be used to represent a huge variety of different things, from geographical or political borders [254] to social interactions [255] and of course chemical species [256] and their reaction pathways [257]. However, what makes network theory so powerful is the ability to study and understand all of these systems with the same underlying mathematics.

3.3.1 Node Degree

One of the easiest ways to characterise a network is through the network degree distribution. First, we define a node's degree, k, as the number of edges connected to the node. Using this we can calculate the probability of

a node having a given degree k,

$$p_k = \frac{V(k)}{V} \tag{3.39}$$

where $V(k)$ is the number of nodes of degree k in a network containing V nodes. This is a normalised set of probabilities such that $\sum_k p_k = 1$. Furthermore these probabilities can be used to calculate the average degree of a node in the network, $\langle k \rangle$:

$$\langle k \rangle = \sum_k k p_k \tag{3.40}$$

which can then be used along side the number of nodes, V, to calculate the number of edges in the system, E:

$$E = \frac{\langle k \rangle}{2} V. \tag{3.41}$$

Since the degree of a node, k, is equal to the number of faces the node is connected to, it is possible to calculate the average ring size of the network, $\langle n \rangle$ (the number of nodes per face) from the average node degree $\langle k \rangle$:

$$\langle n \rangle = \frac{V \langle k \rangle}{F} \tag{3.42}$$

3.3.2 Topological Laws

3.3.2.1 Euler's Law

There are a variety of laws which govern different aspects of the topology of planar networks. Euler's Law links the number of nodes, edges and faces to

a constant dependent of the global topology of the network, χ, through the following expression:

$$V + F - E = \chi, \tag{3.43}$$

By substituting equations 3.41 and 3.42 in to equation 3.43 we can reach:

$$\langle n \rangle = \frac{2\langle k \rangle (1 - \chi/F)}{\langle k \rangle - 2}. \tag{3.44}$$

Whilst equation 3.44 appears simple, it is a very powerful predictive tool allowing us to link the average ring size in the system to the average coordination number. The Euler characteristic, χ, for a two-dimensional periodic system, such as those studied throughout this work, is equal to 0. Therefore, if $\langle k \rangle = 3$ then $\langle n \rangle = 6$. For aperiodic systems, such as real world bulk materials, χ is equal to one, conflicting with the use of a periodic system to model these systems. However, it is noted, in equation 3.44, that as the system size increases χ/F tends towards zero, resulting in a return to the periodic behaviour in sufficiently large systems.

3.3.2.2 Lemaître's Law

The next level of complexity that can be understood about a network is the distribution of its ring sizes. It was demonstrated by Lemaître *et al.* that for 3-coordinate network systems, such as those modelled in this thesis, that the distribution of ring sizes is well described using a maximum entropy distribution. For ring networks this entropy is defined as

$$S = -\sum_n p_n \ln p_n, \tag{3.45}$$

where p_n is the probability of a ring having n sides. This entropy can then be used to calculate p_n for all values of n, after S is assumed to have been maximised according to the constraints of the system. The most obvious constraints are related to those discussed in section 3.3.1, first that the distribution is normalised, $\sum_n p_n = 1$ and second that the mean ring size is fixed $\sum_n np_n = \langle n \rangle$. $\langle n \rangle = 6$ for entirely 3-coordinate systems according to Euler's law, as discussed in section 3.3.2.1. The final constraint takes the form

$$\sum_n \frac{p_n}{n} = \text{constant}, \tag{3.46}$$

and was originally rationalised based on the observation that $A_n = an + b + c/n$, where a, b and c are constants, can be used to well fit the area of a ring of size n, A_n. By applying these constraints through the Lagrange method of undetermined multipliers, the entropy can be maximised to give

$$p_n = \frac{e^{-\lambda_1 n - \lambda_2/n}}{\sum_n e^{-\lambda_1 n - \lambda_2/n}}. \tag{3.47}$$

Whilst the final constraint is in disagreement of the well-known Lewis' Law, which stats A_n is linear in n [258], Lemaître's Law has been shown to hold for a wide range of natural systems [259] and so has found frequent use for understanding the ring distributions of natural systems. Since individual distributions are hard to compare, the variance of the ring size, $\mu_2 = \langle n^2 \rangle - \langle n \rangle^2$, is often used to help summarise.

3.3.2.3 Aboav-Weaire Law

Whilst Euler's and Lemaître's laws allow for an understanding of the average ring size and the distribution of ring sizes in a network, they are unable to describe how these rings are arranged with respect to each other. First investigated by Aboav in 1970 [260] and expanded upon by Weaire in 1974 [261], the Aboav-Weaire law allows for the estimation of the local environment of a ring of size n. The law is most commonly presented as:

$$nm_n = An - A\langle n\rangle + \mu_2 + \langle n\rangle^2, \tag{3.48}$$

but is perhaps more easily understood in the form:

$$m_n = A + \frac{\mu_2 + \langle n\rangle^2 - A\langle n\rangle}{n}, \tag{3.49}$$

where m_n is the mean ring size surrounding a ring of size n. $A = \langle n\rangle(1-\alpha)$, in which α is the Aboav-Weaire parameter used to express the strength of the correlation between ring sizes. μ_2 is the variance of the rings size across the system and has the value $\mu_2 = \langle n^2\rangle - \langle n\rangle^2$. This version of the law has the same general form as the original proposition by Aboav, $m_n = A + B/n$, and can be understood through the $1/n$ relationship, clearly showing that larger rings are on average surrounded by smaller rings.

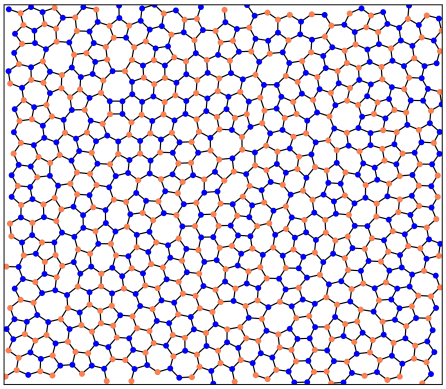
Although the Aboav-Weaire law is empirical in nature, it has been shown to hold for a range of natural network forming materials, such as epithelial cells both in plants [262] and animals [263], colloids [264] and foams [265].

3.3.3 Atomic and Ring Networks

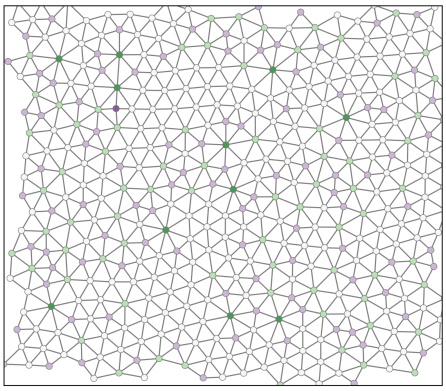
As previously mentioned, networks can also be used to represent molecules or materials, where atoms are represented as node and bonds are represented by edges. This allows for an atom's degree to represent the number of atoms bonded to it and therefore its coordination number. Therefore, in an amorphous graphene network, such as the one seen in figure 2.4, where every atom is sp^2-bonded, the node degree is 3. However, network theory can be utilised further when studying two-dimensional amorphous networks as they can also be inverted such that the rings in these networks are represented by nodes with any bond-sharing ring nodes being connected by edges. A ring in network theory is defined as closed series of sequentially connected nodes and edges without overlap, however for the rest of this thesis all rings referred to will be primitive rings, which are rings that cannot be decomposed into two smaller rings [266]. This then allows us to represent these two-dimensional amorphous networks in three different ways, as seen in figure 3.3, an atomic network, a ring network and a dual network. As mentioned in section 2.6, the number of non-six-membered rings can be used to represent the level of topological disorder and therefore this method is of particular use as the node degree of these ring nodes is equal to the number of atoms in the ring. Allowing us to use p_k, equation 3.39, to calculate the proportion of rings at each ring size in the network, otherwise known as the ring statistics.

3.4 The Fluctuating Charge Model

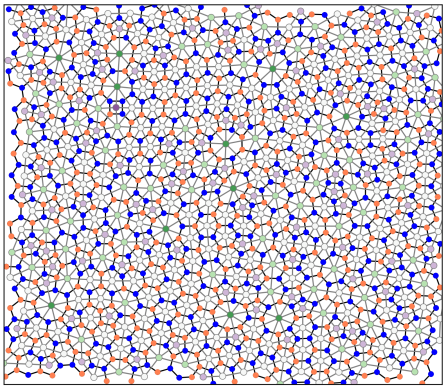
Atomic charge distributions are vital to successful calculations of electrostatic energies and therefore simulations of structures and therefore properties dependent on these energies, such as those studying solvation or hydrogen



(a) Atomic network



(b) Ring Network



(c) Dual Network

Figure 3.3: Example networks based on an amorphous boron nitride monolayer. The nodes in the atomic network are coloured according to their atom type: pink for boron and blue for nitrogen. The nodes in ring network are coloured according to their degree and therefore the number of sides in the ring they are representing: $k < 6$ - purple, $k = 6$ - white, $k > 6$ - green.

bonding. One of the biggest approximations in many molecular dynamics simulations is that of pairwise additive potentials [267]. This approximation can often be very effective when studying molecular species in which potentials can be adjusted to fit with *ab initio* or experimental results, however for nanoscale systems, such as liquids, biomolecules or disordered solids, many-body interactions can have a much more significant impact on the structure and properties. For example, it has been noted that the dipole moment of water varies from 1.85D in the gas phase to ∼2.5D [268] in the liquid phase and that varying the density and temperature of water also has a significant effect on its dipole moment [269]. It has also been shown that some common ions such as O_2^{2-} and S_2^{2-} are stable in crystals such as Li_2O_2 [270] and Li_2S_2 [271] but unstable in vacuum [272]. As such, the introduction of a potential model which allows for the response of atomic charges to environmental changes is essential in more accurate modelling of systems in which interactions spread further than the molecular scale.

First introduced in 1991 by Rappé and Goddard [273], the fluctuating charge model (FCM) has been used to understand a wide range of systems. Originally small peptides and polymer fragments [273] were studied, but since then the FCM has been used to model water [274], ionic liquids and crystals containing a variety of polyatomic anions: CN^- [275], NO_3^- [267] and CO_3^{2-} [276, 277], as well as variety of transition metal complexes, both inorganic [278] and organic [279, 280], and organic chromophores [281].

The FCM allows for the variation of charges using an electronegativity equilibration method through which atomic electronegativities are calculated based on an atom's charge as well as the electronegativities of its neighbours. This results in areas of differing electronegativities based on their environments which then results in the electrons in the system moving from

areas of low electronegativity to areas of high electronegativity in order to equilibrate the electrochemical potential of the electrons at each site. This section follows the derivation of the site electronegativities as laid out by Rappé and Goddard [273] and then looks at how the atomic charges can be calculated and vary with the electronegativities [274].

3.4.1 Calculation of Electronegativities

First we start from a neutral reference point and consider the energy of atom α as a function of its charge, q_α. We can express this in the form of a Taylor expansion as follows:

$$E_\alpha(q) = E_{\alpha^0} + q_\alpha \left(\frac{\partial E}{\partial q}\right)_{\alpha^0} + \frac{1}{2} q_\alpha^2 \left(\frac{\partial^2 E}{\partial q^2}\right)_{\alpha^0} + ... \tag{3.50}$$

where subscript α^0 is used to indicate the neutral reference point. We can then use this to obtain expressions for the positive and negatively singularly charged ions as follows

$$E_\alpha(+1) = E_{\alpha^0} + \left(\frac{\partial E}{\partial q}\right)_{\alpha^0} + \frac{1}{2} \left(\frac{\partial^2 E}{\partial q^2}\right)_{\alpha^0}, \tag{3.51}$$

$$E_\alpha(-1) = E_{\alpha^0} - \left(\frac{\partial E}{\partial q}\right)_{\alpha^0} + \frac{1}{2} \left(\frac{\partial^2 E}{\partial q^2}\right)_{\alpha^0}, \tag{3.52}$$

where we have only included up to the second order terms. We then note that by taking the sum and the difference of these expressions, we can separate out the derivatives. It can then be seen that these are equal to the definitions for the absolute electronegativity [282] and hardness [283] of atom A:

$$\left(\frac{\partial E}{\partial q}\right)_{\alpha^0} = \frac{1}{2}(IP + EA) = \chi^0_\alpha \tag{3.53}$$

$$\left(\frac{\partial^2 E}{\partial q^2}\right)_{\alpha^0} = (IP - EA) = J^0_{\alpha\alpha} = 2\eta^0_\alpha \tag{3.54}$$

where IP is ionisation potential of α, EA is the electron affinity of α, χ^0_α is electronegativity of α, η^0_α is the hardness of α and $J^0_{\alpha\alpha}$ is the coulomb repulsion between two electrons in the σ_α orbital, also known as the self-coulomb integral. We can then insert these definitions into equation 3.50 to give:

$$E_\alpha(q) = E_{\alpha^0} + \chi^0_\alpha q_\alpha + \frac{1}{2} J^0_{\alpha\alpha} q^2_\alpha. \tag{3.55}$$

Now that we have an expression for the energy of an atom in terms of atomic data, we can move to look at how this leads to electronegativities and therefore an atomic charge distribution. The obvious step is to calculate the energy of all atoms in the system as a function of their charges. To do this, we need to include the interatomic electrostatic energy, $\sum_{\alpha<B} q_\alpha q_\beta J_{\alpha\beta}$, where $J_{\alpha\beta}$ is the coulombic interaction between unit charges on atoms α and β ($J_{\alpha\beta}$ depends on $r_{\alpha\beta}$). This leads to a total electrostatic energy of

$$E(q_1 ... q_N) = \sum_\alpha (E_{\alpha^0} + \chi^0_\alpha q_\alpha + \frac{1}{2} q^2_\alpha J^0_{\alpha\alpha}) + \sum_{\alpha<\beta} q_\alpha q_\beta J_{\alpha\beta}. \tag{3.56}$$

If we assume that $J_{\alpha\alpha}(r) \to J^0_{\alpha\alpha}$ as $r \to 0$, equation 3.56 can then be rewritten as

$$E(q_1...q_N) = \sum_{\alpha}(E_{\alpha^0} + \chi^0_\alpha q_\alpha) + \frac{1}{2}\sum_{\alpha,\beta} q_\alpha q_\beta J_{\alpha\beta}. \tag{3.57}$$

To go from energy as a function of all charges to an electronegativity we take the derivative with respect to q_α, leading to

$$\chi_\alpha(q_1...q_N) = \frac{\partial E}{\partial q_\alpha} = \chi^0_\alpha + \sum_{\beta} J_{\alpha\beta} q_\beta \tag{3.58}$$

or

$$\chi_\alpha(q_1...q_N) = \chi^0_\alpha + J^0_{\alpha\alpha} q_\alpha + \sum_{\beta\neq\alpha} J_{\alpha\beta} q_\beta \tag{3.59}$$

where χ_α is the electronegativity of atom A as a function of the charges on all the atoms and all atomic positions through J_{AB}. This expression can then be simplified further when dealing with molecular species [267, 276] to give

$$\chi_{i\alpha} = \chi^0_{i\alpha} + J^0_{\alpha\alpha} q_{i\alpha} + \sum_{\beta\neq\alpha} J_{\alpha\beta} q_{i\beta} + \sum_{j\neq i}\sum_{\beta} \frac{q_{j\beta}}{r} \tag{3.60}$$

where i indicates atom α is in molecule or ion i. In this form the 2nd and 3rd terms containing $J^0_{\alpha\alpha}$ and $J_{\alpha\beta}$ control the intramolecular contributions whilst the fourth term assumes that atoms outside of the molecule or ion i interact with atom α as a point charge and therefore controls the intermolecular atom-atom interactions.

3.4.2 Calculation of Atomic Charges

To reach an equilibrium charge distribution, two sets of constraints must be applied to the system. First, since the system is at equilibrium, all atomic chemical potentials must be equal,

$$\chi_1 = \chi_2 = ... = \chi_N, \tag{3.61}$$

and secondly the sum of all charges must be constant, as no ions or electrons are being added or removed from the system. This charge conservation constraint can be defined in one of two ways. First, the charge of entire system is constant but the charge of individual molecules may vary,

$$\sum_{i=1}^{N_{molec}} \sum_{\alpha=1}^{N_{atom}} q_{i\alpha} = q_{\text{tot}}, \tag{3.62}$$

or that the charge on each molecule must be constant. Therefore for each molecule or ion i

$$\sum_{\alpha=1}^{N_{atom}} q_{i\alpha} = q_{\text{tot},i}. \tag{3.63}$$

This leaves us with N simultaneous equations which can be solved to reach an equilibrium self consistent set of charges any given structure. Originally, these equations were solved by Rappé and Goddard for systems with experimentally measured geometries [273], however as the model has evolved it has been applied to study dynamic systems. Therefore, Rick *et al* developed a method for calculating how the charges "move" with changing electronegativities [274]. To enforce these constraints, the method of undetermined multipliers is used to give the following expressions for the above constraints respectively:

$$L_1 = \sum_{i=1}^{N_{molec}} \sum_{\alpha=1}^{N_{atom}} \frac{1}{2} m_\alpha \dot{r}_{i\alpha}^2 + \sum_{i=1}^{N_{molec}} \sum_{\alpha=1}^{N_{atom}} \frac{1}{2} M_q \dot{q}_{i\alpha}^2 - E[(q),(r)] - \lambda \left(\sum_{i=1}^{N_{molec}} \sum_{\alpha=1}^{N_{atom}} q_{i\alpha} - q_{\text{tot}} \right) \tag{3.64}$$

and

$$L_2 = \sum_{i=1}^{N_{molec}} \sum_{\alpha=1}^{N_{atom}} \frac{1}{2} m_\alpha \dot{r}_{i\alpha}^2 + \sum_{i=1}^{N_{molec}} \sum_{\alpha=1}^{N_{atom}} \frac{1}{2} M_q \dot{q}_{i\alpha}^2 - E[(q),(r)] - \sum_{i=1}^{N_{molec}} \lambda_i (\sum_{\alpha=1}^{N_{atom}} q_{i\alpha} - q_{\mathrm{tot},i}) \tag{3.65}$$

where m_α is the mass of atom α, M_q is a fictitious charge "mass", and the λ are the Lagrange multipliers. If we then follow the standard undetermined multipliers method and differentiate by the degrees of freedom we can see that the nuclear positional degrees of freedom follow the standard equations of motion

$$m_\alpha \ddot{r_{i\alpha}} = -\frac{\partial E[(q),(r)]}{\partial r_{i\alpha}} \tag{3.66}$$

and the charges evolve in time according to a similar set of equations

$$\begin{aligned} M_q \ddot{q_{i\alpha}} &= -\frac{\partial E[(q),(r)]}{\partial q_{i\alpha}} - \lambda_i \\ &= -\chi_{i\alpha} - \lambda_i \end{aligned} \tag{3.67}$$

where λ_i depends on the charge constraint we have used. If the total charge is a constant of motion, as is the case in all systems where the number of electrons is constant i.e. no ionisation has occurred and the total number of atoms has stayed constant, then

$$\sum_{i=1}^{N_{molec}} \sum_{\alpha=1}^{N_{atom}} \ddot{q}_{i\alpha} = 0. \tag{3.68}$$

Alternatively, if the total charge on each molecule is a constant of motion,

then for each molecule or ion i we can say

$$\sum_{\alpha=1}^{N_{atom}} \ddot{q}_{i\alpha} = 0. \tag{3.69}$$

We can then obtain expressions for λ through the substitution of equation 3.67 into equations 3.68 and 3.69, to show that λ is equal to the negative average of the electronegativity over the entire system or molecule/ion i respectively

$$\lambda = -\frac{1}{N_{molec}N_{atom}} \sum_{i=1}^{N_{molec}} \sum_{\alpha=1}^{N_{atom}} \tilde{\chi}_{i\alpha} \tag{3.70}$$

$$\lambda_i = -\frac{1}{N_{atom}} \sum_{\alpha=1}^{N_{atom}} \tilde{\chi}_{i\alpha}. \tag{3.71}$$

Substitution of equations 3.70 and 3.71 into equation 3.67 gives our equation of motion for the charges in the system in terms of the electronegativities in the system

$$\ddot{q}_{i\alpha} = -\frac{1}{M_q}(\tilde{\chi}_{i\alpha} - \chi_{i,avg}) \tag{3.72}$$

where $\chi_{i,avg}$ is calculated by averaging over the entire system or each molecule depending on the charge constraint applied. The charge "mass" M_q controls the "motion" of the charge in much the same way as mass controls the nuclear motions. As such to ensure that the nuclear motion and electronic "motion" are separate, the charge mass should be small enough that the charges adapt rapidly to changes in the nuclear motion and remain at their equilibrium values, whilst being large enough to allow reasonable time steps in simulation.

Whilst, in theory, the nuclear and electronic degrees of freedom are completely separate, in practice, this is not the case. Although the frequency of the nuclear vibrational modes is much lower than those of the charges (relatively), there is still a non-zero energy transfer between the two, reflecting the small overlap in resonant frequencies. If not accounted for this will lead to a slow transfer of energy from the nuclear modes to the charge modes resulting in a gradual decrease in the system temperature and a gradual increase in the "temperature" associated with the charge. This increase in "temperature" will lead the charge values straying further and further from their equilibrium values. A simple way on controlling this is through the use of a thermostat to ensure that the charge modes stay "cold". The thermostat chosen for this purpose throughout the work in this thesis is the Nosé-Hoover [284, 285], as discussed in section 4.2.3.1. The parameters for this thermostat as well as the charge "mass" were adapted from previous work utilizing the FCM for similar atoms, C and O [276], to ensure they match the dynamics of BN systems.

4 | Computational Procedures and Methodology

Contents

4.1 Monte Carlo Simulations 58

4.1.1 The Metropolis Algorithm 58

4.1.2 Bond Switching Monte Carlo 60

4.2 Molecular Dynamics Simulations 63

4.2.1 Algorithmic Details 64

4.2.2 Periodic Boundary Conditions 65

4.2.3 Temperature Control Methods 67

4.3 Geometric Optimisation and Potential Models . . 71

4.3.1 Steepest Descent Algorithm 71

4.3.2 Harmonic Potential Models 72

4.3.3 The Tersoff Potential Model 73

This chapter derives and discusses the computational methods employed throughout the work detailed in this thesis. This includes detailing Monte Carlo and molecular dynamics simulations before moving onto discussing how these approaches can be applied to structures in this work. Finally, the potential models used throughout the work in this thesis are discussed including how the Tersoff potential has been applied to BN materials.

4.1 Monte Carlo Simulations

Monte Carlo simulations involve the exploration of a problem stochastically rather than in a predetermined manner. These methods were first described by Metropolis and Ulam in 1949 [286] and have since become an invaluable tool to help solve problems across a range of disciplines [287]. In the physical sciences, Monte Carlo methods can be used to solve the Schrödinger equation for complex systems [13], explore phase spaces allowing for the calculation of thermodynamic averages of equilibrium properties [288] as well as studying the behaviour of non-equilibrium systems such as for the growth of disordered systems [64, 65]. In this thesis, Monte Carlo methods are used for the generation of amorphous configurations. The general theory is presented here and expanded on in the relevant chapter.

4.1.1 The Metropolis Algorithm

When selecting random numbers from a distribution, importance sampling is often used so that regions which make the largest contribution to the final result are concentrated on rather than evaluating all possible configurations, many of which will have near-zero contribution to the final result [243]. One of the most commonly used forms of importance sampling is the Metropolis algorithm [6]. The Metropolis algorithm gives a method to determine the transition probability $\pi(o \rightarrow n)$ of moving from an old configuration o to a new trial configuration n which is only a small random displacement from o following a Markov chain [241].

First, we consider a system at equilibrium, meaning that the number of trial moves accepted leaving o to n must be equal to the number of accepted trial

moves moving to o from n. We can then write this condition as a relationship between the probabilities of being in a states o and n, $P(o)$ and $P(n)$, and the transition probabilities between o and n, $\pi(o \to n)$ and $\pi(n \to o)$:

$$P(o)\pi(o \to n) = P(n)\pi(n \to o). \tag{4.1}$$

The transition probabilities can then be deconstructed into the two main parts of a Monte Carlo move, namely generating a trial move and accepting a trial move, giving

$$\pi(o \to n) = \alpha(o \to n) \times acc(o \to n) \tag{4.2}$$

where $\alpha(o \to n)$ is the probability of generating a random trial move with leads from o to n and $acc(o \to n)$ is the probability of then accepting said trial move. If the probability of generating trial moves is equal in both directions, $\alpha(o \to n) = \alpha(n \to o)$, we can then rewrite equation 4.1 as

$$P(o) \times acc(o \to n) = P(n) \times acc(n \to o). \tag{4.3}$$

This expression can be applied to any Monte Carlo system. To apply it to a NVT ensemble, we then include equation 3.7 as an expression for $P(o)$ and $P(n)$. This lead to a relationship between the acceptance probabilities and energies of the states

$$\frac{acc(o \to n)}{acc(n \to o)} = \frac{P(n)}{P(o)} = e^{-\beta[U(n)-U(o)]}. \tag{4.4}$$

There are many choices for $acc(o \to n)$ which satisfy the above condition,

however, the original choice by Metropolis *et al* [6] appears to be the most efficient strategy for sampling of a configurational space [241] and so is the most commonly used:

$$acc(o \to n) = \begin{cases} \frac{P(n)}{P(o)}, & \text{if } P(n) < P(o) \\ 1, & \text{if } P(n) \geq P(o) \end{cases} = \begin{cases} e^{-\beta[U(n)-U(o)]}, & \text{if } U(n) < U(o) \\ 1, & \text{if } U(n) \geq U(o) \end{cases} \tag{4.5}$$

where the cases are chosen such that $acc(o \to n)$ is never greater than 1. If we then include this choice into equation 4.2 we get the final transition probability as

$$\begin{aligned} \pi(o \to n) &= \begin{cases} \alpha(o \to n), & P(n) \geq P(o) \\ \alpha(o \to n)[\frac{P(n)}{P(o)}], & P(n) < P(o) \end{cases} \\ \pi(o \to o) &= 1 - \sum_{n \neq o} \pi(o \to n). \end{aligned} \tag{4.6}$$

Using these transition probabilities, we can then summarise the Metropolis algorithm as shown in Algorithm 1.

4.1.2 Bond Switching Monte Carlo

Bond switching Monte Carlo methods are among the most commonly used computational models to study amorphous materials. First introduced in 1985 by Wooten, Winer and Weaire [289] to study amorphous Si and Ge. The general approach for bond switching algorithms involves the generation of continuous random networks (CRNs) through Monte Carlo moves

Algorithm 1 General Metropolis algorithm

Create system in initial state, o, and calculate its potential energy, $U(o)$
for each step **do**
  Generate a trial move and the resulting trial state, n
  Calculate potential energy of trial state, $U(n)$
  Generate random number, x, between 0 and 1
  if $x \leq e^{-\beta[U(n)-U(o)]}$ **then**
    Accept trial move and update state of system
    $o \leftarrow n$
    $U(o) \leftarrow U(n)$
  end if
end for

which involve the local rearrangement of bonds. The structures are relaxed after each step to ensure that the results are able to model experimental results with high accuracy. Although originally developed to model three-dimensional amorphous system, the method can easily be adapted to study two-dimensional system, including monolayer amorphous carbon (MAC) or amorphous graphene [230] and amorphous bilayers [234, 290]. A basic outline of an algorithm used is as follows:

1. Generate original crystalline lattice
2. Heat the structure to high temperature and introduce a large number of random moves
3. Allow to cool to specified temperature at controlled rate accepting moves according to the Metropolis criteria, equation 4.5

This approach is an example of simulated annealing, which is a commonly used extension to the Metropolis algorithm. Simulated annealing is often used to ensure that global minima are reached when performing optimisation calculations [291]. However, in the case of the bond switching algorithm, simulated annealing is instead used as it allows for the formation of defect

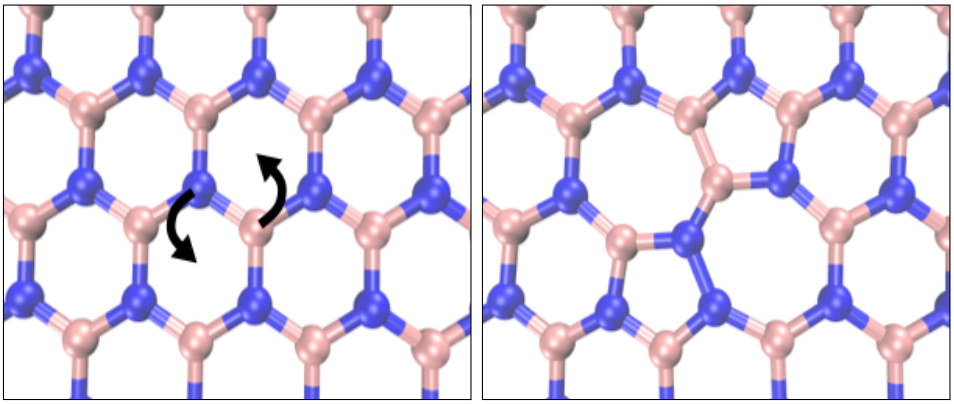


Figure 4.1: Example formation of a Stone-Wales defect in h-BN. A central bond is rotated by 90° resulting in the transformation of 4 six-membered rings into 2 five- and 2 seven-membered rings.

patterns which would not be obtainable through a standard Metropolis algorithm.

For 3-coordinate two dimensional atomic systems, the Monte Carlo move used is the Stone-Wales defect [91]. This defect involves the rotation of a bond through 90°, leading to two edge-sharing rings containing the bond reducing in ring size from n to $n-1$ whilst the two rings at either end of the bond increase in ring size from n to $n+1$, as seen in figure 4.1. This transformation lead to the mean ring size in the system as well as the coordination number staying constant. After each transformation, a geometric optimisation is performed to minimise the energy of the system and ensure it remains physically reasonable, details of this process can be found in section 4.3. As more defects are introduced into the system, the topological disorder increases and eventually leads to more diversity in ring sizes. An example progression of the simulated annealing bond switching Monte Carlo algorithm is shown in figure 4.2. Panels (a) to (f) show the increasing levels of disorder as an increasing number of Stone-Wales defects are introduced into the system. Panels (g) and (h) show the cooling process

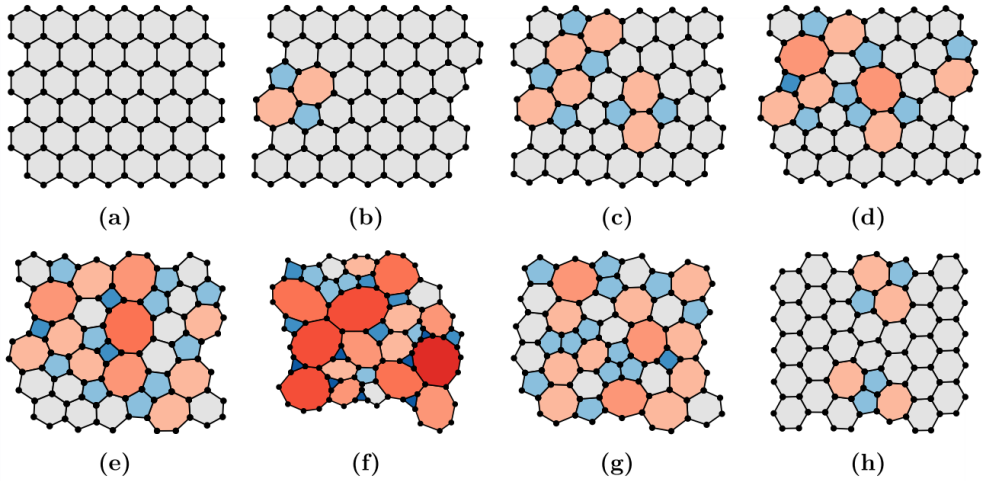


Figure 4.2: Example progression of the employed bond switching algorithm. The hexagonal lattice (a) is thermalised by introducing Stone-Wales defects (b)-(e) until a high energy configuration is reached (f). The system is then "cooled" at a controlled rate (g) until a final configuration is reached potentially containing types of defects which are not normally obtainable from the initial lattice (h). Figure from the doctoral thesis of David Morley [292].

eventually leading to a configuration potentially containing defects types not obtainable through a standard bond switching algorithm.

4.2 Molecular Dynamics Simulations

Molecular dynamics simulations are used to follow the evolution of systems through the use of the classical equations of motion and an interaction potential. This methodology dates back to 1957 when Alder and Wainwright used it to study the phase transition of a hard sphere system [7]. Since then, molecular dynamics simulation has been used to study an extensive range of systems from biomolecules [293] and polymers [294] to crystalline [171] and amorphous solids [184, 295], and interfaces [108].

4.2.1 Algorithmic Details

All molecular dynamics simulations follow the same general approach as set out in the algorithm 2.

Algorithm 2 General Molecular Dynamics Algorithm

```
Read in simulation conditions
Initialise system by giving all particles their starting positions and velocities according to conditions
for each step do
    Use interaction potential to calculate forces on all atoms
    Integrate equations of motion using calculated forces
    Update atomic positions and velocities
    Increase time by Δt
    Sample system
end for
```

The slowest step for the majority of molecular dynamics simulations is the calculation of the forces. This is because even when using the simplest pairwise additive potential, the contribution to the force between a particle i and all of its neighbours must be evaluated. This means that for a system containing N particles there are $N(N-1)/2$ distances which need to be considered, leading to the time taken for evaluation of the forces scaling as N^2 [241]. This scaling only increases as more complex potentials are used. For example, the Tersoff potential [162], used throughout this work and discussed later in this chapter, includes a 3-body angular term which causes the time to scale as N^3.

The other main step in each loop is the integration of the equations of motion. This can be performed in a variety of ways, the method used in simulations studied in this thesis is the velocity-Verlet algorithm [296]. This approach is preferred over the original Verlet algorithm [297] as it allows for more exact calculation of the velocities and therefore more accurate kinetic energies. A

brief description of the algorithm, where $r_i(t), v_i(t)$ and $a_i(t)$ represent the position, velocity and acceleration of particle i at time t respectively, is as follows [243] :

1. Calculate new atomic positions using

$$r_i(t + \Delta t) = r_i(t) + v_i(t)\Delta t + \frac{1}{2}a_i(t)\Delta t^2 \tag{4.7}$$

2. Derive $a_i(t + \Delta t)$ from the forces on atom i using interaction potential and $r_i(t + \Delta t)$

3. Calculate new atomic velocities using

$$v_i(t + \Delta t) = v_i(t) + \frac{1}{2}[a_i(t) + a_i(t + \Delta t)]\Delta t \tag{4.8}$$

4.2.2 Periodic Boundary Conditions

Due to computational efficiency being dependent on the number of atoms in the system, computational simulations often contain significantly fewer atoms than the real world systems that they are modelling. This can cause the results of the simulation to not accurately represent the properties of the bulk material. For example, a much greater proportion of the atoms in the system will reside at the surface in the simulation than in the real material. Therefore these atoms will experience a vastly different potential than those imbedded within the material due to a lack on interaction. The most common way of combating this problem is through the use of a periodic boundary condition, which involves the tiling of the simulation box in space, as shown in figure 4.3. This effectively removes the material's surface meaning that all atoms in the simulation are now modelling part of an infinitely large bulk

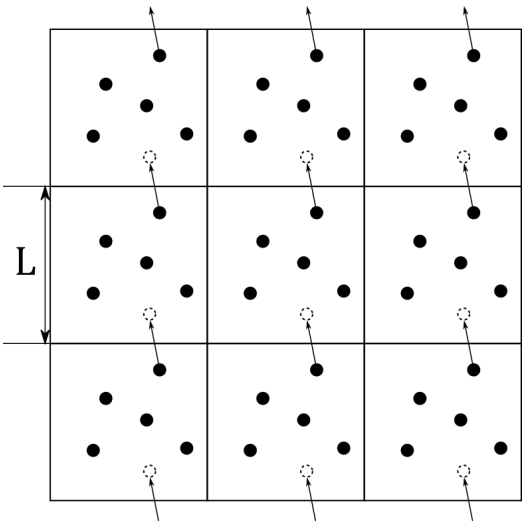


Figure 4.3: An example of a two-dimensional periodic system, with a tiling box of length L.

material. Whilst periodic boundary conditions can allow for the modelling of bulk materials, it is important to check whether the periodic simulation box is large enough to full encompass the interactions and phenomenons being studied to ensure that the macroscopic system is being accurately modelled.

Due to the infinite number of atoms in a system employing a periodic boundary condition, it is no longer possible to simply sum over all atomic interactions to calculate the potential energy of the system. For short-range interaction potentials, such as those used to represent chemical bonds, this sum can be restricted to a manageable number of terms by applying a cutoff distance, above which the interaction potential is zero. However, for long-range (greater than $L/2$) interactions, in particular the Coulombic interaction, this truncation is not possible. Therefore, alternate methods for considering the interactions of a charge with all other charges within its own box as well as the periodic images is required.

The Ewald summation is a technique employed in this work which allows

for the efficient calculation of large numbers of electrostatic interactions over long distances by splitting the interaction into more easily calculable real-space and reciprocal-space parts [243]. The key premise of the Ewald method is the introduction of charge distributions of equal magnitude but opposite sign surrounding each point charge in the system, as shown in figure 4.4a. These charge distributions are typically chosen to be Gaussian, as in this work, however, other distributions are possible. The introduction of these distributions screens the interactions between the point charges and those outside of the charge distributions. This makes the screened interactions short range. These short-range interactions can then be summed across the periodic box and their images.

Next, a second set of charge distributions is added, with the same shapes and the same sign as the original charges, as shown in figure 4.4b. This distribution cancels out the screening distributions returning the overall potential back to that of the original set of charges. This cancelling distribution can be summed in reciprocal-space through the use of a Fourier transform of each distribution. This total is then converted back to real-space and combined with the real-space sum for the screened charges. Finally, the total currently includes the interaction of the cancelling distribution at $\boldsymbol{r}_i$ with itself with must be subtracted. This leaves a total expression containing the real-space screening sum plus the reciprocal-space cancelling sum minus the self-term.

4.2.3 Temperature Control Methods

When molecular dynamics simulations are carried out under a canonical ensemble three key variables must be controlled throughout, namely the number of atoms in the system, the volume of the system and the temperature. Whilst the number of atoms N and the volume V can be easily fixed, tem-

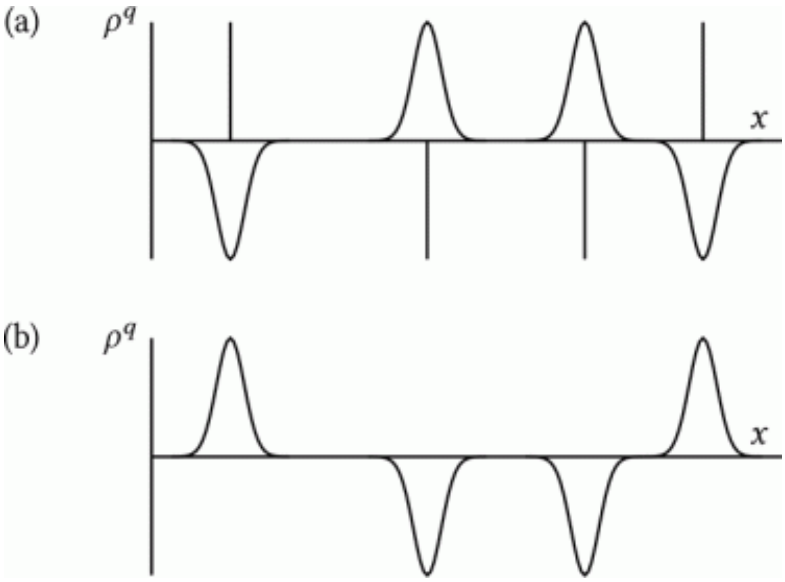


Figure 4.4: Example 1D charge densities in the Ewald summation. Panel (a) shows the original point charges and the screen distributions. Panel (b) shows the cancelling distribution. Figure taken from [243].

perature T is closely related the motion of the atoms in the system and so controlling it is a more complex endeavour. Two approaches are taken in this work so solve this problem: the Nosé-Hoover thermostat and periodic velocity rescaling.

4.2.3.1 Nosé-Hoover Thermostat

First introduced in 1984 by Nosé [284] and later expanded upon by Hoover [285], the Nosé-Hoover thermostat is one of the most commonly used methods for temperature control in molecular dynamics simulations. By introducing an additional degree of freedom to each atom, the simulated system is able to "interact" with an external system allowing for the temperature to respond in a more physical way, reminiscent of a heat bath. This is implemented through the use of a thermodynamic friction coefficient, ξ, which modifies the equations of motions to:

$$\dot{\boldsymbol{r}}_i = \frac{\boldsymbol{p}_i}{m_i} \tag{4.9}$$

$$\dot{\boldsymbol{p}}_i = -\frac{\partial U(\boldsymbol{r}^N)}{\partial \boldsymbol{r}_i} - \xi \boldsymbol{p}_i \tag{4.10}$$

with ξ evolving in time according to

$$\dot{\xi} = [\frac{K}{\langle K \rangle} - 1]/\tau^2. \tag{4.11}$$

K is the total kinetic energy of the system and $\langle K \rangle = \frac{3}{2} N k_B T$ where T is the desired temperature of the system. τ is the characteristic time scale of the system which governs the rate at which fluctuations are dampened out, and should be chosen to roughly match the physical timescales of the motions in the system [298].

Due to the changes in the equations of motion required by the Nosé-Hoover thermostat, modifications to the velocity-Verlet algorithm are also required [241]. Equations 4.7 and 4.8 become:

$$r_i(t + \Delta t) = r_i(t) + v(t)\Delta t + \frac{1}{2}[a_i(t) - \xi(t)v_i(t)]\Delta t^2 \tag{4.12}$$

$$v_i(t + \Delta t) = v(t) + \frac{1}{2}[a_i(t) - \xi(t)v_i(t) + a_i(t + \Delta t) - \xi(t + \Delta t)v_i(t + \Delta t)]\Delta t \tag{4.13}$$

respectively. Whilst evaluating $r_i(t + \Delta t)$ comes with no new major challenges, the updated evaluation of $v_i(t+\Delta t)$ is more complicated as $v_i(t+\Delta t)$ is on both the left- and right-hand sides of the equation, and so cannot be exactly integrated. As such a predictor-corrector scheme is implemented where the value at a half time step is estimated first and then corrected.

4.2.3.2 Periodic Velocity Rescaling

Periodic velocity rescaling is one of the simplest ways of controlling temperature and involves using the relationship between the kinetic temperature of the system $\mathcal{T}$ and the atomic velocities to generate a scaling factor to enforce the total kinetic energy, K, of the system to be equal to the average kinetic energy, $\langle K \rangle = \frac{3}{2} N k_B T$, for the required temperature, T. In each rescaling step, the atomic velocities are adjusted using:

$$v_i^{\text{new}} = v_i^{\text{old}} \lambda, \tag{4.14}$$

where

$$\lambda = \sqrt{\frac{K}{\langle K \rangle}} = \sqrt{\frac{\mathcal{T}}{T}}. \tag{4.15}$$

Whilst the Nosé-Hoover thermostat allows for more accurate control of a system's temperature, its reliance on a "friction" and "momentum" based approach often leads to oscillations in the temperature. When the system is already at a temperature close to the desired temperature, these oscillations are small and so have negligible effect on the results. However, when the system is at a temperature significantly greater than the desired temperature, such as at the start of a cooling process, these oscillations are large and much longer lasting. The size of these oscillations can result in the system being notably below its desired temperature for a significant period of time meaning that the final structure may not truly reflect the chosen temperature. As such, periodic velocity rescaling is used in the work described in this thesis for the initial cooling period of a melt-quench approach to ensure the temperature of the system is always above or close to the desired temperature.

4.3 Geometric Optimisation and Potential Models

Geometric optimisation is a vital step when simulating the structures of molecules or materials, and is applied throughout this thesis during both Monte Carlo and molecular dynamics simulations to ensure that systems are arranged in a stable configuration at an energy minimum. The optimisation of a non-linear function to find a global minimum, such as finding the most stable structure of a system using a potential model, is famously complex, often requiring repeated local optimisations which can lead to the system being trapped in a local minimum [299]. This thesis is concerned with the study of disordered materials which are by nature metastable states and so the finding of local minima in the potential energy surface is fortunately the desired outcome.

4.3.1 Steepest Descent Algorithm

One of the most commonly used approaches for geometric optimisation, and the one applied throughout simulations in this thesis, is the steepest descent algorithm. This algorithm is based on the observation that moving down a negative gradient for a continuous function will lead to a decrease in the value of the function [300]. The steepest descent algorithm takes an iterative approach to minimisation by taking repeated steps along the direction of the most negative gradient until the energy of the system converges according to a predefined condition. A general version of the algorithm is shown in Algorithm 3.

In molecular dynamics simulations, the simplest way to ensure the system

Algorithm 3 Steepest Descent Algorithm

```
while not converged do
    Calculate potential energy of system
    Determine negative gradient i.e. forces on atoms
    Move atoms along lines of force
    Check convergence
end while
```

is always following direction of the most negative gradient in the potential energy is to monitor the total kinetic energy of the system. If there is a decrease in kinetic energy then the system is now moving up a gradient in the potential energy and so the velocity of all atoms is set to zero to ensure movement towards the minimum in the next timestep. However, as Monte Carlo simulations do not study the dynamics of the systems, more care must be taken when defining the steps which atoms take along the lines of force. As such, an optimum step distance is determined by performing a one-dimensional minimisation along the line of force [301]. One benefit of Monte Carlo simulations is that Monte Carlo moves in the Metropolis algorithm are inherently localised and so when optimising the geometry of a structure only the local region needs to be relaxed significantly speeding up the process. In this work, a distance of 5 bond lengths is used to determine the size of the local region.

4.3.2 Harmonic Potential Models

Bond switching Monte Carlo simulations require geometric optimisation after every trial move before the energy of the new and old configurations are compared. Therefore, to ensure that the simulations are time-efficient, a simple potential model is used to model the bond distances and angles. In this work, harmonic potentials are used in both cases. The bond lengths are

modelled through the uses of harmonic springs connecting each node with its nearest neighbours. The energy of moving these bonds from their equilibrium length is given by

$$U_{ij} = \frac{1}{2}k_r(r_{ij} - r_0)^2, \tag{4.16}$$

where k_r is the bond force constant, taken as 0.8 in this work, r_{ij} is the distance between nodes i and j and r_0 is the equilibrium bond distance. r_0 is dependent on the system and for the boron nitride system studied is taken to be 1.42 Å. Control over the angles uses a potential of a similar form, which is used to approximate a three body term:

$$U_{ijk} = \frac{1}{2}k_\theta[\cos(\theta_{ijk}) - \cos(\theta_0)]^2, \tag{4.17}$$

where k_θ is the angle force constant, taken in this work as 0.2, θ_{ijk} is the angle between nodes i, j and k and θ_0 is the ideal bond angle of the system, which for a hexagonal net is $\pi/3$. These simple models are able to relax the configuration into a physically feasible geometry, however, they are not tailored for a specific system and so may not be entirely accurate. As such, after an amorphous network is generated using the Monte Carlo simulation, relaxation with a potential designed to more accurately model the system of interest using molecular dynamics is required.

4.3.3 The Tersoff Potential Model

In 1988, Tersoff proposed a new potential model for the study of covalent systems [162], and developed parameters for silicon [162] and carbon [302], with applications to their amorphous forms. It was later expanded to model multicomponent systems [303] and has since been used to study a range of covalent systems and their properties [304–306], including boron nitride [108,

163, 164, 166, 169, 177, 179–181, 307–310]. The form of the Tersoff potential is as follows:

$$E_{\text{Tersoff}} = \sum_i E_i = \frac{1}{2}\sum_{i \neq j} V_{ij},$$
$$V_{ij} = f_C(r_{ij})[a_{ij} f_R(r_{ij}) + b_{ij} f_A(r_{ij})]. \tag{4.18}$$

Here the bond energy V_{ij} between atoms i and j can be split up into 5 terms. Firstly, we have the repulsive and attractive pair potentials, $f_R(r_{ij})$ and $f_A(r_{ij})$ respectively. Next, $f_C(r_{ij})$ is a cutoff function used to limit the range of the potential allowing for a significant boost in computational efficiency of the potential. Finally, a_{ij} and b_{ij} control the repulsive and attractive terms. Whilst a_{ij} consists only of terms to limit the range of $f_R(r_{ij})$, b_{ij} is more complex. b_{ij} can be though of a measure of the bond order, which is assumed to be a function of the coordination numbers of i and j, as atoms with many neighbours form weaker bonds. As such b_{ij} is a function of not just bond lengths but also bond angles.

The two pair potentials employed have similar forms:

$$f_R(r) = Ae^{-\lambda_1 r} \tag{4.19}$$
$$f_A(r) = -Be^{-\lambda_2 r} \tag{4.20}$$

where the parameters A, B, λ_1 and λ_2 are parameters determined for the system. The cutoff function $f_C(r_{ij})$ has the form

$$f_C(r) = \begin{cases} 1 & r < R - D \\ \frac{1}{2} - \frac{1}{2}\sin\left[\frac{\pi}{2}\frac{r-R}{D}\right] & R - D < r < R + D \\ 0 & r > R + D \end{cases} \tag{4.21}$$

which is a smooth cutoff between 1 and 0 in a small range $2D$ around R. R is chosen to include only the shell of nearest neighbours. a_{ij} has the form

$$\begin{aligned} a_{ij} &= (1 + \alpha^n \eta_{ij}^n)^{-1/(2n)}, \\ \eta_{ij} &= \sum_{k(\neq i,j)} f_C(r_{ik}) e^{\lambda_3^3 (r_{ij} - r_{ik})^3}, \end{aligned} \tag{4.22}$$

with α chosen to be sufficiently small that $a_{ij} \approx 1$ unless η_{ij} is exponentially large. However, in nearly all cases, including every set of parameters used in this work, α is equal to zero and so $a_{ij} = 1$. The form of b_{ij} was originally chosen by Tersoff to be

$$\begin{aligned} b_{ij} &= (1 + \beta^n \zeta_{ij}^n)^{-1/(2n)}, \\ \zeta_{ij} &= \sum_{k(\neq i,j)} f_C(r_{ik}) g(\theta_{ijk}) e^{\lambda_3^3 (r_{ij} - r_{ik})^3} \\ g(\theta) &= 1 + \frac{c^2}{d^2} - \frac{c^2}{d^2 + (h - \cos\theta)^2}. \end{aligned} \tag{4.23}$$

In this form ζ_{ij} is an effective coordination number, which counts the number of other bonds to atom i. This can then modified through the exponential to vary bond strength if one bond is much longer than the other, however, in many cases $\lambda_3 = 0$ and so this is ignored. ζ_{ij} is also modified to include an angular dependence. This is implemented through $g(\theta)$, allowing certain bond angles to be favoured. Within $g(\theta)$, h controls the optimal angle, c

controls strong the angular dependence is and d controls how sharp the range of angles is.

4.3.3.1 Application of the Tersoff Potential to Boron Nitride

The Tersoff potential has been adapted to model a variety of boron nitride systems. In 1997, Albe *et al.* developed parameters for the BB, BN and NN interactions based on *ab initio* DFT calculations within the local-density approximation of a variety of crystal structures [163]. In 1998, Sekkal *et al.* developed parameters for the BN interactions specific to c-BN adapted from Tersoff's original C parameters [302]. These parameters were used to study the thermodynamic properties of c-BN as well as the liquid state of boron nitride [164]. In 2011, Sevik *et al.* developed parameters for the study of low-dimensional boron nitride nanostructures such as nanosheets and nanotubes. These parameters were fitted to structural, mechanical and dynamical properties of h-BN nanostructures and the model was then used to study the thermal conductivities of the nanostructures [166]. This work was followed up in 2012 in a paper by Kınacı *et al.* where the parameters were expanded to work for systems containing C as well as B and N. This model was then used to study the thermal conductivity of a variety of graphene-h-BN superlattices [167]. Tables 4.1 and 4.2 show the parameters from the discussed literature which have been adapted for use with the form of the Tersoff potential used in simulations in this thesis.

Further work has been undertaken by Los *et al.* to extend the Tersoff potential to more accurately model boron nitride [311]. This extension involves the inclusion of an additional term alongside b_{ij} to modify the bond order. This term is dependent on the nearest neighbours and their chemical identities. Whilst the BN extended Tersoff potential (BN-ExTeP) has been used to ac-

curately model many structures of BN and their properties [4, 64, 187, 312], the lack of an electrostatic component in the potential means that the variable bond order does not result in a physically meaningful charge or electron density on each atom. As such, its use for the study of interactions between BN materials and charged or polarisable species is potentially limited.

	CC[230]	BB[163]	BN[163]	NN[163]	BN[164]	BN[166]
A/E_h	51.214	51.614	163.93	109.47	51.214	50.714
B/E_h	12.742	43.114	132.79	94.209	12.745	12.495
λ_1/a_0^{-1}	1.8457	1.1839	1.5867	1.4972	1.8352	1.8881
λ_2/a_0^{-1}	1.1705	1.0994	1.4734	1.3903	1.1748	1.1637
λ_3/a_0^{-1}	0	0	1.0544	0	0	0
β	$1.5724\ x10^{-7}$	$1.6000x10^{-6}$	$1.1134x10^{-5}$	0.019251	$1.5742x10^{-5}$	$1.2572x10^{-7}$
c	38049	0.52629	1029.9	17.796	38049	25000
d	4.3484	$1.5870x10^{-3}$	12.380	5.9484	4.3484	4.3484
h	-0.57058	0.50000	-0.54130	0	-0.57058	-0.89000
α	0	0	0	0	0	0
n	0.72751	3.9929	0.36453	0.61844	0.72751	0.72751
R/a_0	3.685	3.7795	3.7795	3.7795	3.685	3.685
D/a_0	0.283	0.18897	0.18897	0.18897	0.37795	0.094486

Table 4.1: Tersoff parameters for BN and C adapted from work by Kumar *et al* [230], Albe *et al* [163], Sekkal *et al* [164] and Sevik *et al* [166].

	BB	BN	BC	NN	NC	CC
A/E_h	50.71440646	50.714	50.963	50.71440646	50.963	51.324
B/E_h	12.49476954	12.495	12.5605	12.49476954	14.243	15.802
λ_1/a_0^{-1}	1.88810428	1.88881	1.86688	1.88104289	1.86688	1.8457
λ_2/a_0^{-1}	1.163660687	1.2166	1.16715	1.163660687	1.16715	1.17049
λ_3/a_0^{-1}	0	0	0	0	0	0
β	1.25724e-7	1.5742e-7	1.5742e-7	1.25724e-7	1.5742e-7	1.5742e-7
c	25000	25000	38049	25000	38049	38049
d	4.3484	4.3484	4.3484	4.3484	4.3484	4.3484
h	-0.89	-0.89	-0.93	-0.89	-0.93	-0.93
α	0	0	0	0	0	0
n	0.72751	0.72751	0.72751	0.72751	0.72751	0.72751
R/a_0	3.685	3.685	3.685	3.685	3.685	3.59048
D/a_0	0.09449	0.09449	0.18897	0.09449	0.18897	0.18897

Table 4.2: Tersoff Parameters for BCN adapted from Kınacı *et al* [167].

5 | Ordered BN Systems and Generating Amorphous Networks

Contents

5.1 Introduction 79

5.2 Ordered BN Structures 81

5.2.1 2D Lattices 81

5.2.2 3D Crystals 85

5.2.3 Conclusions 88

5.3 Hexagonal Lattice 90

5.4 Controlling disorder in BN networks 93

5.4.1 Site Disordering 93

5.4.2 2D Disordered Systems 96

5.4.3 3D Disordered Systems 103

5.1 Introduction

The Tersoff potential, as discussed in section 4.3.3, is the most commonly used potential model for the study of boron nitride materials, and has been parametrised for a range of BN structures. However, whilst these potentials have been used to accurately model the properties of these structures, they are not wholly representative of the bonding in these systems. In some parametrisations, the interactions between different atomic pairs are treated differently whilst in others they are treated equally. However, despite the electronegativity difference of the atoms and the evidence for a polarised

bond, as discussed in section 2.5, in all versions of the Tersoff potential, the bonding is treated as entirely covalent. In ordered systems containing only one type of B-N bond, this is not a problem as the electrostatic interaction can be included in the strength of the covalent bond. However, for disordered materials containing a wide range of environments or materials interacting with other charged or polarisable species, the site charges and electrostatic interactions may be key for accurate modelling. One of the simplest ways of representing a polar bond is by assigning partial charges to the atoms. These charges can then be incorporated into the model by augmenting the pair potential with the standard electrostatic interaction energy for point charges. Since the Tersoff potential is the most frequently used potential for BN, it was chosen to represent the covalent interaction in our simulations, leading to a total potential energy of:

$$E = E_{\text{Tersoff}} + \frac{1}{2}\sum_{i \neq j} \frac{q_i q_j}{r_{ij}}, \tag{5.1}$$

where E_{Tersoff} is the same as discussed in section 4.3.3, q_i anq q_j are the site charges on atoms i and j and r_{ij} is the distance between atoms i and j. This chapter investigates how the different parametrisations of the Tersoff potential perform for different ordered lattice types, with a range of atomic charges. Following this, the effect of introducing disorder into a system are investigated and finally methods for generating fully amorphous structures are discussed.

5.2 Ordered BN Structures

As discussed in section 4.3.3, there are three sets of parameters which have been derived to model BN structures through the use of an unmodified Tersoff potential. To investigate how each of the potentials performed in a range of environments, a variety of regular lattices were modelled in both two and three dimensions using BN bond lengths from $0.9r_{\mathrm{BN}}$ to $1.7r_{\mathrm{BN}}$ where r_{BN} was chosen to be 1.442 Å based on experimentally derived lattice constants [313]. Other values for the BN bond length in h-BN between 1.44 Å and 1.45 Å have been quoted in the literature [314–316]. The total potential energy of these structures was calculated with and without the use of site charges, using all three BN Tersoff parametrisations. These structures were also modelled using the C parameters used by Kumar *et al* [230] to study amorphous graphene for comparison.

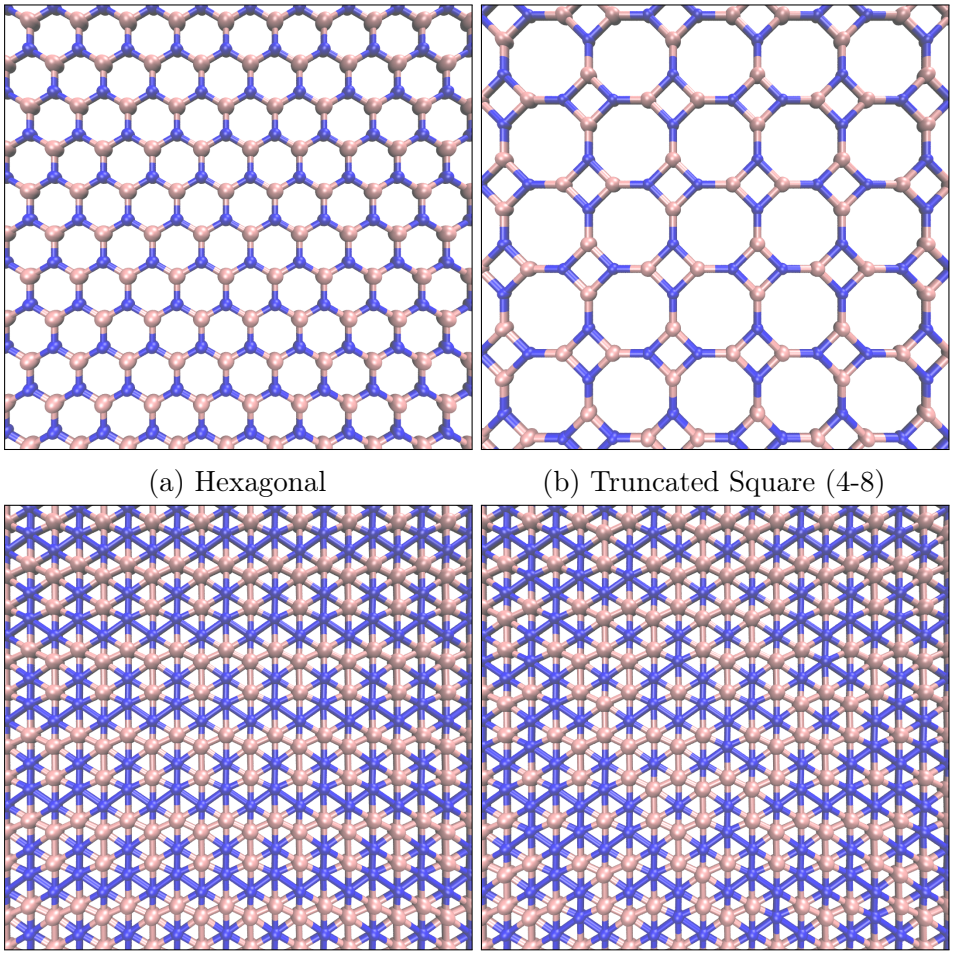
5.2.1 2D Lattices

The two-dimensional lattices modelled included hexagonal, truncated square and close packed with ordered and disordered B and N placement, as show in figure 5.1. The hexagonal lattice was chosen as it is the most common form of BN while the truncated square or 4-8 lattice allows for investigation into the effect of other ring sizes and therefore bond angle whilst preserving the site ordering in the system. The close packed network allows for investigation into the effect of coordination number on the system. Due to the close packed network being composed of only 3-membered rings, completely alternating site ordering is not possible. As such we have modelled a site ordered configuration which attempts to maximise the number of BN interactions and a site disordered network in which an equal number of B and N were randomly

assigned to the network nodes. Figure 5.2 shows how the potential energy of these various two dimensional regular lattices change with an increasing B-N bond length, at different site charges. Energies were calculated using simulations containing 800, 1200 and 784 atoms for the hexagonal, close packed and truncated square lattices respectively. All four structures employed periodic boundary conditions in the x and y directions.

The difference between the various potentials can be observed through the overall shape of the curves. The Kumar *et al* [230] and Sekkal *et al* [164] potentials have very similar shapes across all four structures, with the Sekkal potential resulting in a slightly less stable structure across all bond lengths. This agrees with the observation that the parameters for the Kumar and Sekkal potentials are similar: both are based on Tersoff's original parameters for C [302]. The Sevik *et al* [166] potential also has a somewhat similar shape to the Kumar potential however the wells in the Sevik curves are deeper with steeper walls across all structures to varying degrees. This difference is smallest for the hexagonal lattice for which the parameters were derived. It can also be seen that the truncated square or 4-8 lattice is much closer in energy for the Sevik potential that the Kumar or Sekkal potentials; this is likely caused by lower value of c in the parametrisation which results in a weaker angular dependence. Whilst the Albe *et al* potential [163] does result in energies of the same order of magnitude to the other parametrisations, the shape of the curves are quite different across all structures; in particular, there is a significant overlap between the hexagonal and truncated square curves which is not present in any of the other potentials. It can also be seen that the well depth for each structure calculated using the Albe potential is very similar, unlike the other BN parametrisations.

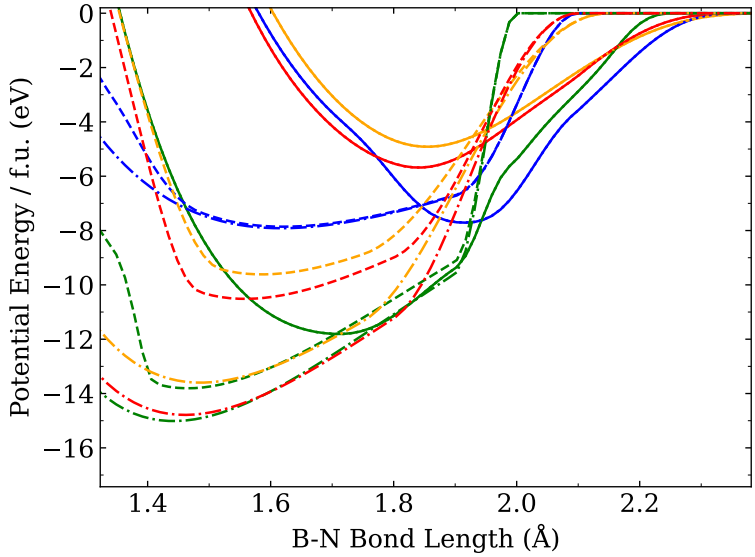
The most obvious change on increasing the atomic charge is an increase in



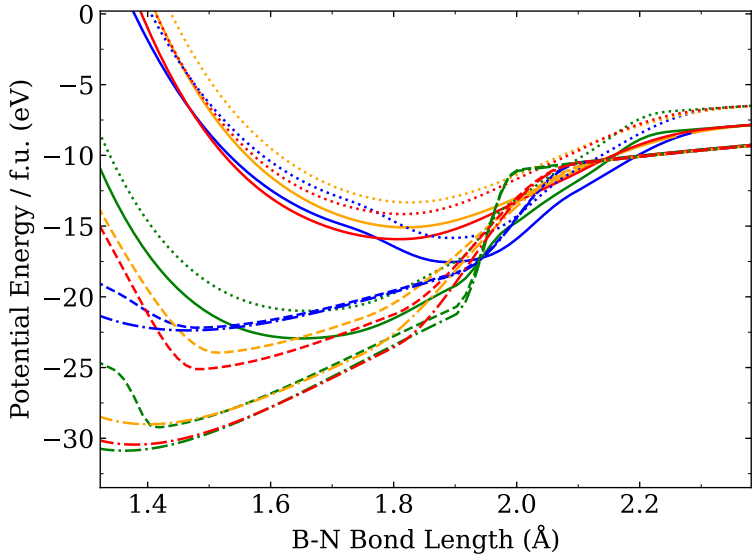
(a) Hexagonal (b) Truncated Square (4-8)

(c) Close Packed, site ordered (d) Close Packed, site disordered

Figure 5.1: Ordered 2D BN lattices. Atoms are coloured by type, pink and blue for boron and nitrogen respectively.



(a) $|q/e| = 0$



(b) $|q/e| = 1.0$

Figure 5.2: Variation of potential energy per formula unit with B-N bond length for a range of potentials and regular 2D lattices. Panels (a) and (b) correspond to different site charges, q. In both panels, line colour corresponds to the potential and the line type corresponds to the lattice type. Key: Red - Kumar *et al* [230], Blue - Albe *et al* [163], Yellow - Sekkal *et al* [164] and Green - Sevik *et al* [166]. Solid Line - Ordered Close Packed, Dotted Line - Disordered Close Packed, Dashed Line - Truncated Square and Dot Dash line - Hexagonal.

the coulombic attraction between atoms leading to all of the curves moving down and becoming the interactions becoming more favourable. However, this increase in attraction is not equal for each structure: the hexagonal and truncated square curves shift by a greater amount than the close packed curves. This difference is caused by the difference in the number of atoms per ring in each structure. In the case of hexagonal and truncated square, all the rings contain an even number of atoms allowing for an alternating pattern of B and N, and therefore all of the shortest distance coulombic interactions are attractive, resulting in a more favourable coulombic energy. In the case of close packed, the rings contain an odd number of atoms and so each ring must contain at least one repulsive interaction as a result of a homo-atomic bond, resulting in a less favourable coulombic energy. There is also a difference in the shift between the ordered and random close packed structures. The ordered structure has an increased amount of B-N interactions and so has a greater increase in stability than the randomly arranged structure. This is an example of topological vs site based order as both have the same underlying topological network but due to the different arrangement of B and N on this network, there is a difference in the energies.

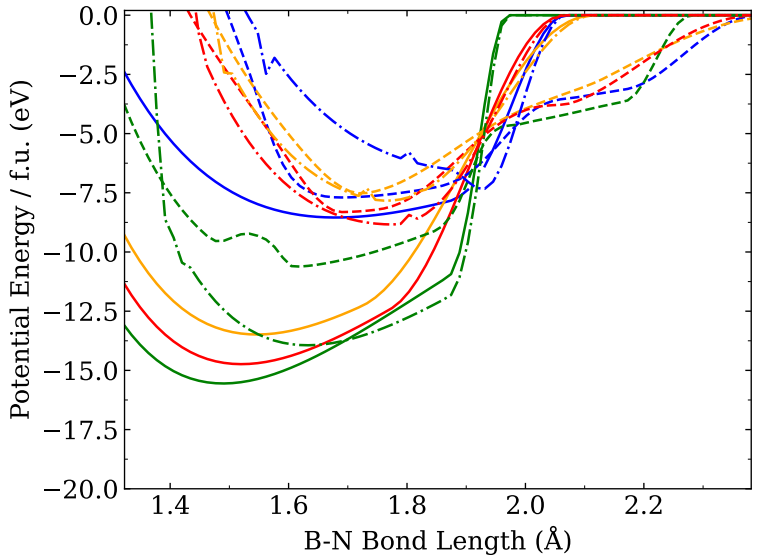
5.2.2 3D Crystals

The three dimensional crystals studied were the cubic, wurtzite and NaCl structures. The cubic and wurtzite structures are well known for BN, as discussed in section 2.1. While the NaCl structure is not an experimentally realised form of BN, its inclusion allows for the investigation of a structure containing different bond angles and coordination numbers. It also acts as a comparison for the stable cubic and wurtzite structures with an experimentally unstable structure. Figure 5.3 shows how the potential energy of

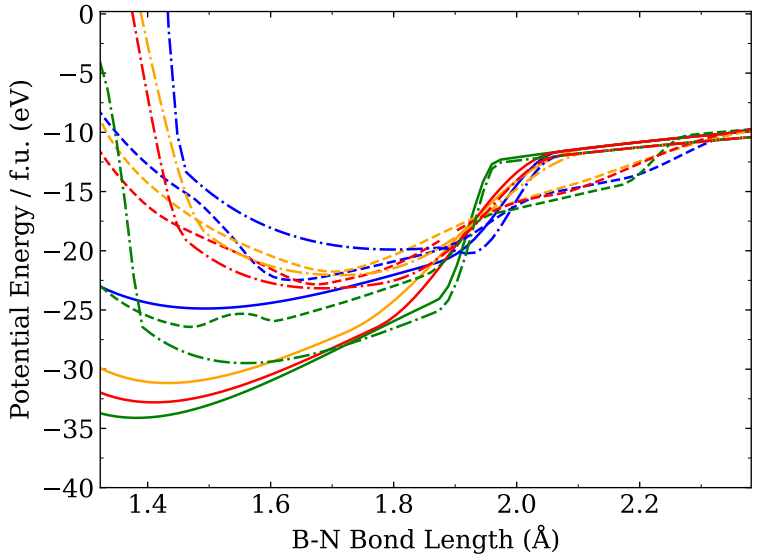
these various three dimensional regular crystal structures change with an increasing B-N bond length, at different site charges. Energies were calculated using simulations containing 1000 atoms for the cubic and NaCl structures and 972 atoms for the wurtzite structure. All three structures employed periodic boundary conditions in three dimensions.

Similar to the two dimensional lattices, clear differences between the Tersoff potential parametrisations can be seen by looking at the shapes of the curves. Once again, the Sekkal and Kumar potentials show very similarly shaped curves for all three of the crystals studied, due to the two parametrisations both being based on the original parameters proposed by Tersoff. Whilst the Sevik potential shows a cubic curve of a similar shape to the Kumar and Sekkal potentials, its curves for the wurtzite and NaCl are quite different. The most obvious difference is that these two structures have much deeper potential wells, especially the NaCl crystal which is shown to be significantly more stable than the wurtzite structure across a wide range of bond lengths and even the cubic structure at some bond lengths. The wurtzite curve for the Sevik potential is also quite irregular with a peak in the curve between bond lengths of 1.5 Å and 1.6 Å. The Albe potential results in curves with different shapes to the other potentials. For the four coordinate structures, the Albe potential results in wells with much flatter bottoms, particularly for wurtzite. The curve for the NaCl structure also predicts a greater most stable bond length than the three other potentials. It is also noted that the three structures also result in minimum energies which are much closer for the Albe potential than any of the other potentials.

By comparing panels (a) and (b) of figure 5.3, the effect of introducing site charges and a electrostatic interaction to the potential has on the potential energies of the 3D crystal structures. Similar to the 2D lattices, the main



(a) $|q/e| = 0$



(b) $|q/e| = 1.0$

Figure 5.3: Variation of potential energy per formula unit with B-N bond length for a range of potentials and regular 3D crystals. Panels (a) and (b) correspond to different site charges, q. In both panels, line colour corresponds to the potential and the line type corresponds to the lattice type. Key: Red - Kumar *et al* [230], Blue - Albe *et al* [163], Yellow - Sekkal *et al* [164] and Green - Sevik *et al* [166]. Solid Line - Cubic, Dashed Line - Wurtzite and Dot Dash line - NaCl.

effect is an overall increase in the stability of all the crystals across all bond lengths. This is caused by the crystal structures studied only being made up of B-N bonds, rather than any homo-atomic bonds. This additional attractive component in the potential also leads to a slight decreases in the most stable bond length for all structures. These effects appear to be equal across all three crystal structures. Interestingly this has no effect on the peak in the well of the wurtzite curve for the Sevik potential.

5.2.3 Conclusions

Table 5.1 shows the minimum energies for each of the curves in figure 5.3 along with the difference between the values for the site charges, $|q/e| = 0$ and $|q/e| = 1$. By comparing the energy minima for the all different structures studied, it can be seen that for $|q/e| = 0$, the 2D hexagonal lattice is the most stable for the Sekkal and Kumar. It is of particular interest that this is not the case for the Sevik potential which was parametrised for nanostructures containing the hexagonal structure. When grouping the structures by dimensionality, it can be seen that of the 2D structures, hexagonal is the most stable whilst cubic is the most stable 3D structure. Due to its short range, the Tersoff potential is not able to describe the interlayer interactions present in the structure of h-BN and as such the full layered h-BN lattice cannot be simulated without the introduction of a second potential. However, the stability of the singular h-BN layer agrees with the fact that h-BN is the most commonly synthesised structure of BN. From these energy minima we can also see which of the different structures are most affected by the inclusion of an electrostatic potential. In general, it can be seen that the three dimensional structures experience greater stabilisation than the two dimensional ones. This is caused by the greater coordination numbers re-

Potential	Dimensions	Crystal Structure	$E_{\text{min},q=0}$	$E_{\text{min},q=1}$	ΔE_{min}
Albe	2D	Hexagonal	-7.9146	-22.373	14.458
		Close Packed	-7.7100	-17.550	9.8400
		Close Packed (disordered)	-7.7040	-15.841	8.1370
		Truncated Square	-7.8581	-22.182	14.324
	3D	Cubic	-8.5437	-25.878	17.334
		Wurtzite	-7.6976	-22.477	14.7794
		NaCl	-7.3331	-20.220	12.887
Sekkal	2D	Hexagonal	-13.598	-29.008	15.410
		Close Packed	-4.9140	-15.095	10.181
		Close Packed (disordered)	-4.9140	-13.327	8.4130
		Truncated Square	-9.6133	-23.952	14.339
	3D	Cubic	-13.485	-31.170	17.685
		Wurtzite	-7.5204	-21.759	14.239
		NaCl	-7.8307	-22.054	14.223
Sevik	2D	Hexagonal	-15.011	-30.877	15.866
		Close Packed	-11.805	-22.941	11.136
		Close Packed (disordered)	-11.805	-20.996	9.1910
		Truncated Square	-13.807	-29.223	15.416
	3D	Cubic	-15.553	-34.109	18.556
		Wurtzite	-10.616	-26.436	15.820
		NaCl	-13.939	-29.487	15.548
Kumar	2D	Hexagonal	-14.787	-30.447	15.660
		Close Packed	-5.680	-15.925	10.245
		Close Packed (disordered)	-5.680	-14.152	8.4720
		Truncated Square	-10.515	-25.105	14.590
	3D	Cubic	-14.737	-32.802	18.065
		Wurtzite	-8.3140	-22.846	14.532
		NaCl	-8.8395	-23.170	14.331

Table 5.1: Table of minimum potential energies for the curves show in figures 5.2 and 5.3. All energy values are given per formula unit of the structure and in units of eV. The highlighted cells show the lowest energy crystal structure at each atomic charge, q, value.

sulting in more favourable short range electrostatic interactions. It can also be seen that introducing a charge of $|q/e| = 1$ to each atom leads to the cubic structure becoming the most stable structure for all potentials. This is unphysical and therefore demonstrates the requirement for the use of partial charges.

5.3 Hexagonal Lattice

The hexagonal lattice is the most stable form of BN, as seen in table 5.1, and so was studied in more depth. Madelung constants are simple numbers which are often used to help study ionic crystals. These values represent all the electrostatic interactions of a given atom with all other atoms in the crystal. As such they are most commonly used to the approximation of cohesive energies and so they can be used predictively to assign crystal structures to materials. However, they have also be used for a variety of other applications such as the determination of optical phonon modes [317] and as a method of sensing phase transitions and amorphisation [318]. Whilst the bonding in boron nitride materials is only partially ionic, as discussed in section 2.5, calculating a Madelung constant allows for a direct calculation of the ionic component of the total potential energy. By taking the origin to the coordinates of the reference atom, the Madelung constant, A, can be written as:

$$A = \sum_{i}^{N} \frac{Z_i}{(r_i/r_0)} \tag{5.2}$$

where r_i is the distance between the reference atom and atom i, r_0 is the bond length, and Z_i is the charge on atom i divided by e in relation to the reference

atom. If the charges on both atoms are the same sign then Z_i is positive and if they are different signs then Z_i is negative. Assuming all atoms are in the same coordination environment and have the same magnitude of charge, A can then be used to calculate the total Coulombic interaction using:

$$U_{\text{Coulomb}} = \frac{N}{2}\frac{|Z|e^2}{4\pi\epsilon_0 r_0}A. \tag{5.3}$$

where N is the total number of atoms, $|Z|$ is the magnitude of charge on the atoms and $4\pi\epsilon_0 = 1.112 \times 10^{-12}$ C^2/(J $\cdot$ m) is the permittivity of free space. As seen in equation 5.2, A is calculated using a series and so its accuracy is dependent on the number of interactions, N, considered in the sum. To ensure accuracy when calculating a value for a two dimensional hexagonal BN lattice, we gradually increased the number of interactions considered until the result converged to within an accuracy of 5 decimal places, as seen in figure 5.4. This leads to a value of 1.54223 by calculating the interaction of the reference atom with $\sim 1.6 \times 10^9$ other atoms.

Using a bond length, r_0, of 1.442 Å and a charge magnitude, $|Z|$, of 1, we can calculate a coulombic lattice energy of -15.639 eV per formula unit. This is in excellent agreement with the ΔE_{min} values seen in table 5.1 for the hexagonal lattice using the Sekkal, Sevik and Kumar potentials and good agreement with the value for the Albe potential. The differences between these values and the Madelung value is likely caused by the inclusion of an additional electrostatic potential leading to a change in the most stable bond length. This is more evident by looking at how the potential energy changes for a fixed bond length. Table 5.2 shows the potential energies for the hexagonal lattice using the Kumar potential at a fixed bond length of 1.442 Å for a range of site charges from 0 to 1. By taking the difference

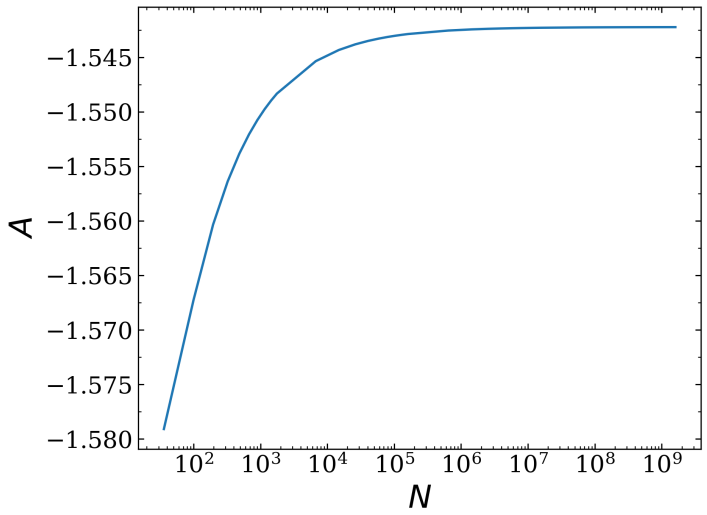


Figure 5.4: Convergence of the Madelung constant, A, for monolayer hexagonal boron nitride, within increasing number of interactions, N, included.

between the ordered values for $|q|/e = 0$ and 1, we get a value of 15.63 eV per formula unit which is near identical to the value calculated using the Madelung constant, verifying its usage. This value for the Madelung constant of monolayer h-BN has since been verified by Vanhinsbergh [319] and Piggott [320] who calculated values of 1.54306 and 1.54246 using molecular dynamics simulations of BN nanotubes and h-BN nanosheets respectively.

q/e	Ordered /eV	Disordered /eV
0.00	-14.685	-14.685
0.25	-15.663	-14.900
0.50	-18.595	-15.630
0.75	-23.482	-17.056
1.00	-30.315	-19.517

Table 5.2: Potential energy per formula unit of a hexagonal lattice of 800 atoms with perfectly ordered and disordered BN calculated using molecular dynamics across a range of ionic charges, q, using a BN bond length of 1.42 Å

5.4 Controlling disorder in BN networks

Amorphous BN materials contain both topological and site disordering, as discussed in section 2.6. However, these two types of disorder can have very different effects on the properties of a material. As such being able to separate out the contributions from each of these types of disorder is potentially key to understanding the structure and properties of these amorphous BN materials.

5.4.1 Site Disordering

Whilst BN materials containing high levels of only site disordering are unlikely to form in the real world, they can be generated computationally and allow for investigation into the effects of solely site ordering on the materials. Site disorder can be quantified most simply through the use of partial coordination numbers, n_α^β, which is equal to the number of atoms of type β bonded to an atom of type α. These coordination numbers can be defined on an atom by atom basis, however, for quantifying the site disorder in a whole system the mean value, $\overline{n}_\alpha^\beta$, is more suitable. These values can be calculated either by integrating the real space structural functions, as seen in equation 3.18, or by simply averaging over the atomistic coordination numbers.

Generating site disordered configurations can be carried out in a variety of ways. The simplest of these is by simply randomly assigning half of the atoms in a system to be B and half to be N. This process was applied to hexagonal lattices, resulting in configurations with $\overline{n}_\mathrm{B}^\mathrm{B} = \overline{n}_\mathrm{B}^\mathrm{N} = \overline{n}_\mathrm{N}^\mathrm{B} = \overline{n}_\mathrm{N}^\mathrm{N} = 1.5$. This implies that the configuration are at the greatest possible amount of site disordering as there is an equal chance of an atom being bonded to B or N. If $\overline{n}_\mathrm{B}^\mathrm{B}, \overline{n}_\mathrm{N}^\mathrm{N} > \overline{n}_\mathrm{B}^\mathrm{N}, \overline{n}_\mathrm{N}^\mathrm{B}$ then a configuration contains atoms of the same type

congregating, whereas $\overline{n}_{\mathrm{B}}^{\mathrm{B}}, \overline{n}_{\mathrm{N}}^{\mathrm{N}} < \overline{n}_{\mathrm{B}}^{\mathrm{N}}, \overline{n}_{\mathrm{N}}^{\mathrm{B}}$ implies atoms are more likely to be bonded to other types of atoms. By calculating the energy of these generated configurations in the same way as discussed in section 5.3, we can see in table 5.2 there is an increasing difference between the ordered and disordered energies as $|q|/e$ is increased. This is another example of both systems having the same topological network but different atoms occupying each site leading to a difference in energy, showing that site disorder could have a potential effect on the properties of boron nitride structures.

Generating configurations by randomly assigning atomic labels gives no control over the level of disorder in the resulting structure. To enable investigation into how changing levels of site disorder affect materials, more complex methods which allow for control over the amount of site disordering in a structure are required. This can be achieved in one of two ways, either disorder is gradually introduced into ordered systems or disordered systems are gradually ordered. Both of these methods can be employed through the use of a Monte Carlo algorithm, as described in section 4.1. By using a Monte Carlo algorithm we are able to introduce disorder stochastically whilst monitoring the amount of site disorder through $\overline{n}_{\mathrm{B}}^{\mathrm{N}}$ allowing the process to be cut off at the desired value. In both of these two cases the Monte Carlo move is the swapping of the atomic labels on two randomly chosen atoms. A new $\overline{n}_{\mathrm{B}}^{\mathrm{N}}$ is calculated after each swap and compared to the previous value. The acceptance condition then depends on where disorder is being added to the configuration or removed. For increasing site disorder, the Monte Carlo move is accepted if the value of $\overline{n}_{\mathrm{B}}^{\mathrm{N}}$ has decreased whereas for decreasing site disorder the Monte Carlo move is accepted if the value of $\overline{n}_{\mathrm{B}}^{\mathrm{N}}$ has increased. The outline of this algorithm is shown in algorithm 4.

These two methods were tested on systems containing 400 B and 400 N by

Algorithm 4 Atomic label swapping Monte Carlo algorithm

```
Read in initial configuration state, o
Calculate initial n̄_B^N(o) value
while desired level of disorder is not met do
    Randomly select two atoms, a and b
    if atom a and atom b have the same atomic labels then
        Continue to next iteration of loop
    end if
    Create trial configuration state, n, with the atomic labels of atoms a
and b swapped
    Calculate n̄_B^N(n) value for trial state, n
    if n̄_B^N(n) for trial state meets acceptance condition then
        Accept trial move and update state of system
        o ← n
        n̄_B^N(o) ← n̄_B^N(n)
    end if
end while
```

inputting the most ordered and most disordered configurations into the two algorithms respectively and allowing the algorithm to run until the value of $\overline{n}_{\mathrm{B}}^{\mathrm{N}}$ had converged. As shown in figure 5.5, both increasing and decreasing disorder algorithms converge after approximately 20000 steps to a value of ~ 2.5 for $\overline{n}_{\mathrm{B}}^{\mathrm{B}}$ and $\overline{n}_{\mathrm{B}}^{\mathrm{N}}$ respectively. The inability for either of these algorithms to reach a value of 3.0 is caused by the formation of domains within the structures. Whilst the increasing disorder algorithm is able to quickly reach a state of high disorder continuing past this leads to the formation of domains of entirely B and N, as seen in figure 5.6. These domains must connect at some point which leads to the formation of B-N bonds meaning that $\overline{n}_{\mathrm{B}}^{\mathrm{B}}$ can never reach 3.0. While these structures could have interesting properties caused by these domains, they are also likely to be very unstable due to the majority of the bonds being homo-atomic. For the decreasing disorder algorithm the domains which form differ by an inversion of the ordering. When these domains meet, this difference results in the formation of homo-

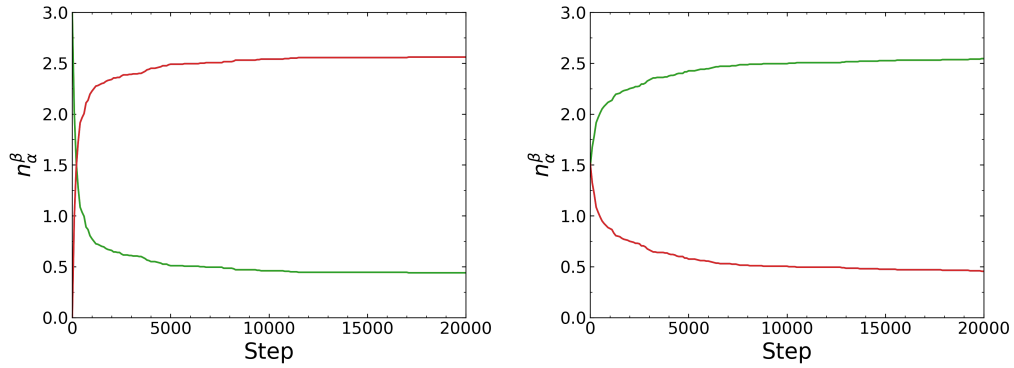


Figure 5.5: Change in average partial coordination numbers in hexagonal lattices containing 400 B and 400 N over the course of 20000 Monte Carlo steps, for the introduction of site disordering into a ordered system (left) and the reduction of site disordering in a disordered system (right). $\overline{n}_{\mathrm{B}}^{\mathrm{B}} = \overline{n}_{\mathrm{N}}^{\mathrm{N}}$ coloured red and $\overline{n}_{\mathrm{B}}^{\mathrm{N}} = \overline{n}_{\mathrm{N}}^{\mathrm{B}}$ coloured green.

atomic bonds, as show in figure 5.6. As mentioned in section 2.2, whilst these types of domain boundary have not been studied experimentally due to difficulty in distinguishing between types of atom so similar in size, they have been studied theoretically [84]. To improve these two methods further and allow them to converge on $\overline{n}_{\mathrm{B}}^{\mathrm{B}}$ and $\overline{n}_{\mathrm{B}}^{\mathrm{N}}$ values of 3 would require one of two potential modifications. Either the Monte Carlo move would have to be modified to allow for the switching of the atomic labels for more than one pair of atoms at once or a probability based acceptance condition would have to be implemented which would allow for some "uphill" moves to be accepted. Both of these methods would significantly increase the number of steps required for the result to converge.

5.4.2 2D Disordered Systems

One of the most common approaches for generating simulation configurations containing topological disorder is through the repeated introduction of site defects. For two-dimensional hexagonal networks such as graphene, silica

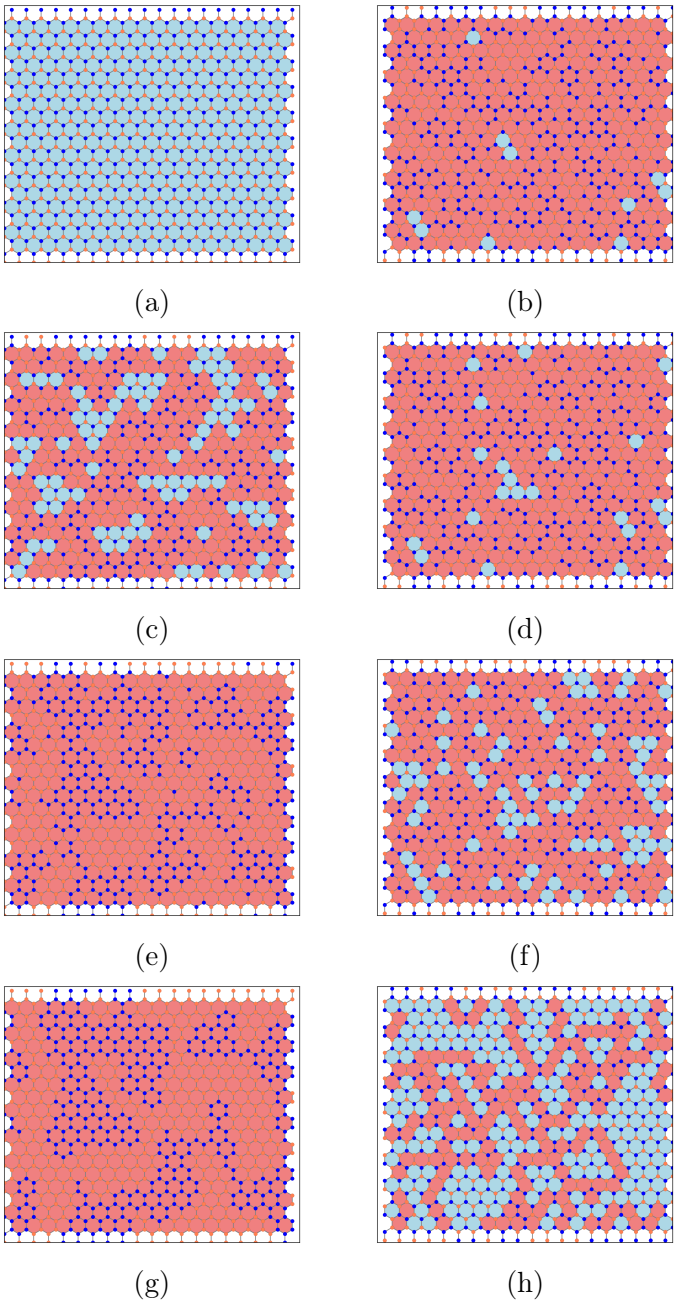


Figure 5.6: Snapshots of hexagonal lattices containing 400 B and 400 N at varying steps of the two atom label switching Monte Carlo algorithms. (a), (b) - 0 steps, (c), (d) - 100 steps, (e), (f) - 1000 steps, (g), (h) - 20000 steps. (a), (c), (e), (g) show the increasing disorder algorithm. (b), (d), (f), (h) show the decreasing disorder algorithm. Rings are coloured blue if they contain alternating B and N around the entire ring and red otherwise.

bilayers and h-BN monolayers, the site defect of choice is the Stone-Wales rotation, which involves the rotation of a bond by 90° resulting in the two rings containing the bond decreasing in size by one atom and the 2 rings at the ends of the bond increasing in size by one atom. Introducing these defects is achieved through the use of a simulated annealing bond-switching Monte Carlo algorithm, as discussed in section 4.1.2. This approach allows for control over the amount of topological disorder in the system through the use of a Monte Carlo "temperature". This "temperature" controls the rate at which unfavourable moves are accepted in the standard Metropolis algorithm. When the simulated annealing approach is introduced this "temperature" is varied. After an initial high "temperature" period used to introduce a high amount of disorder into the system, the "temperature" is gradually reduced to a specified value. By controlling the rate of "cooling" and the final "temperature" value the final amount of topological disorder in the system can also be controlled. The use of a simulated annealing approach is also an improvement over the standard Metropolis algorithm as it allows for the formation of defect arrangements which would not form during the run of a bond switching algorithm using a constant Monte Carlo "temperature".

Whilst the bond switching algorithm is an effective way of controlling topological disorder, its use of only a simple harmonic potential model means it is unable to differentiate between different types of atom. As such after the system has been "heated" the atom types in the system are thoroughly site disordered. One way of solving this would be through the introduction of a more complex potential model into the Monte Carlo algorithm. However, as each step of the algorithm requires a geometric optimisation, a more complex potential model would significantly reduce the efficiency of the method. Therefore to ensure that the final configurations have a much more physically

rational amount of site ordering, the disorder reducing atomic label swapping Monte Carlo algorithm is employed. Following this, the configurations are relaxed using a molecular dynamics-based steepest descent algorithm, in which the atomic forces are modelled using the Tersoff potential augmented with a coulombic interaction as described in section 5.1.

To investigate how the Tersoff potentials perform for systems containing a wide range of disorder, 2D amorphous systems were generated using a range of final Monte Carlo "temperatures" from 10^0 K to $10^{-3.5}$ K. It should be noted that while these "temperatures" behave in a similar way to real temperatures (i.e. increasing temperature leads to increased disorder), they are not directly related and are only used to control the acceptance rate of unfavourable moves. The level of topological disorder within these systems can be measured using the ring statistics of the system, specifically the proportion of rings in the system that are 6-membered, p_6. Whilst the resulting networks contain a range of ring sizes, only p_6 is required to describe the distribution of rings, as the Monte Carlo process is entropically driven. Therefore the configuration generated will have ring statistics following a maximum entropy distribution. As such the value of p_6 is directly related to the width of the distribution according to Lemaître's Law, see section 3.3.2.2. The hexagonal lattice is completely topologically ordered and has a p_6 value of 1, therefore as p_6 decreases the amount of disordered increases. After the systems were relaxed, the coulombic and Tersoff potential energies of the systems were calculated. The coulombic energy followed the same trends for all 3 potentials and was constant across all values of p_6, increasing in magnitude as q increased. This lack of change with p_6 is unexpected as in general a decreasing value of p_6 means there is an increase in the number of odd-membered rings, assuming the system is not made up of only even membered rings.

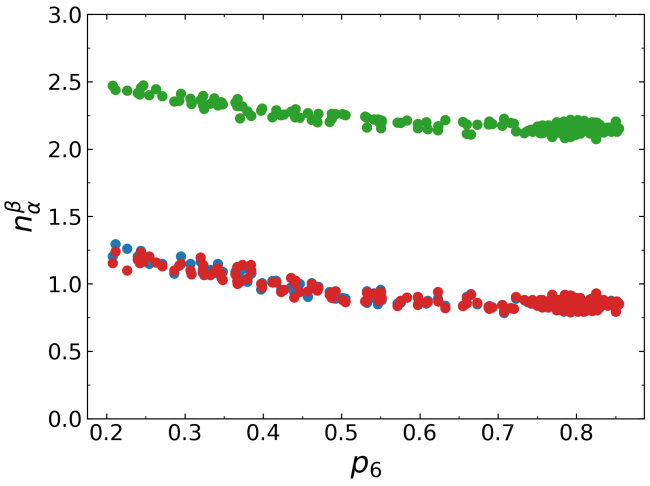
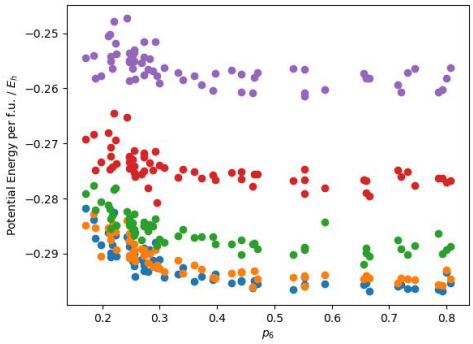


Figure 5.7: The effects of varying topological disorder, represented by the proportion of six-membered rings, p_6, in two-dimensional amorphous BN configurations on site-based disorder, represented by partial coordination numbers, n_α^β. Points are coloured by partial coordination number: green- $\alpha = \mathrm{B/N}$, $\beta = \mathrm{N/B}$, blue -$\alpha = \mathrm{B}$, $\beta = \mathrm{B}$ and red - $\alpha = \mathrm{N}$, $\beta = \mathrm{N}$.

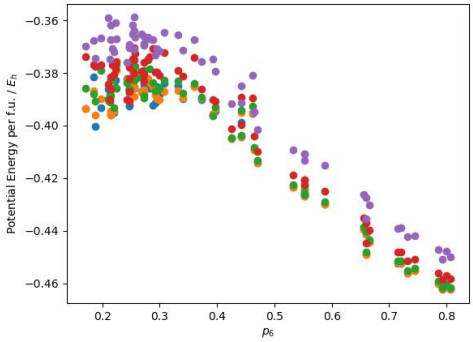
These odd-membered rings force a homo-atomic B-B or N-N interaction and so an increased number of these rings should lead to a smaller magnitude of coulombic energy. However, as seen in figure 5.5, the process of reducing the site disorder is not perfect and leaves some rings containing homo-atomic bonds. Therefore, it is possible that when this process is applied to the more topologically disordered networks that homo-atomic bonds are generated instead of fully site-ordered even-membered rings leading to a roughly constant number of homo- and hetero-atomic bonds for networks across all p_6 values. This can be seen more simply by comparing the level of topological order, p_6 with the level of site-based disorder, $\overline{n}_{\mathrm{B}}^{\mathrm{N}}$, as shown in figure 5.7. This figure shows how all partial coordination numbers decreases equally as p_6 increases due to the decreasing total coordination number, showing the ratio of hetero- and homo-atomic bonds stays roughly constant across all levels of topological disorder.

Since the Tersoff potential energy is dependent on the bond angles as well as the bond length, it varies with p_6 as seen in figure 5.8. All three potentials show an expected increase in stability as p_6 increases. This is caused by the average bonds angles and lengths becoming closer to the optimum values for the system, 1.442 Å and 120°, as the proportion of 6-membered rings increases . This increase in stability is more prominent in the systems using the Sekkal and Sevik potentials (figures 5.8b and 5.8c) which each have change in potential energy of $\sim$0.075 E_h per formula unit, or $\sim$2 eV per formula unit, compared to the system using the Albe potential (figure 5.8a) which only has a change of $\sim$0.00625 E_h per formula unit, or $\sim$0.17 eV per formula unit. This can be further understood by comparison with figure 5.2, where the well for the hexagonal lattice modelled using the Albe potential can be seen to be much flatter and much difference between the hexagonal and truncated square lattices is much smaller for the Albe potential than either the Sekkal or Sevik potentials. This shows that the Albe potential is more lenient to variation in bond length and angle.

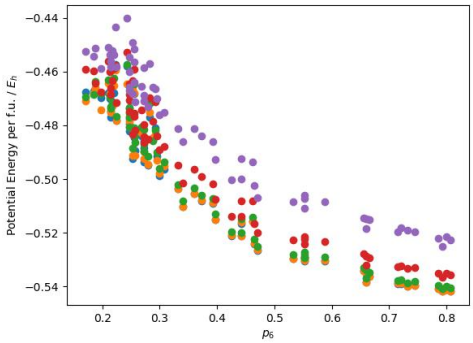
The three potentials also show different behaviour for configurations with p_6 values below $\sim$0.35. The systems using the Albe and Sevik potentials become increasingly less stable as p_6 decreases whereas the system using the Sekkal potential appears to plateau. This difference may be caused by how the system relaxes when there is high amounts of disorder. The Albe and Sevik potentials may cause ring sizes which deviate even more from the average to become more numerous leading to the increase in energy, whereas the Sekkal potential may cause the formation of other defect types which stabilise the system. It can also be seen in figure 5.8 for all 3 potentials that as charge, q, increases the Tersoff potential energy becomes less favourable. This is likely caused by the increasing charge leading to shorter BN bond lengths



(a) Albe [163]



(b) Sekkal [164]



(c) Sevik [166]

Figure 5.8: The short-range (Tersoff) potential energy shown as a function of the fraction of hexagons, p_6. Panels (a)-(c) correspond to the potential model parametrisations indicated. In all panels each colour corresponds to different site charges. Key: blue - $|q| = 0$, orange - $|q| = 0.25$, green - $|q| = 0.50$, red - $|q| = 0.75$, purple - $|q| = 1.00$.

and longer BB and NN bond lengths distorting the rings in the systems away from the ideal shapes.

A few variations of the relaxation process were also carried out for comparison. Firstly, the relaxation was carried out without the use of the $\overline{n}_B^N$ maximisation algorithm. This resulted in systems which had similar Tersoff potential energies to those shown in figure 5.8, however the coulombic potenial energy was significantly less negative as a result of the increased number of homo-atomic interactions. This could also be considered as an example of topological *vs* site based order, as the similar Tersoff energies could suggest a similar underlying network. Secondly, the relaxation was carried out without the use of a 2D constraint. This resulted in movement out of the plane which varied with both charge and p_6. As p_6 decreased, the average movement out of the plane increased, this is caused by the non-6-membered rings having significant ring strain which is relieved by the rings bending out of the plane. This movement out of the plane also decreased as the charge increased caused by the shorter BN bond lengths.

5.4.3 3D Disordered Systems

Whilst the levels of disorder can be controlled fairly simply in two dimensional systems, the same is not true for three dimensional systems. Since there is no simple Stone-Wales equivalent for the cubic BN structure, it is more complex to introduce topological disorder using a Monte Carlo algorithm. As such an alternate method for generating three dimensional disordered configurations is required. The melt-quench method involves the heating of an initial crystalline material to very high temperatures to ensure it is melted resulting in high levels of disordered followed by rapid cooling to ensure that the final structure retains this disorder. This process is commonly used

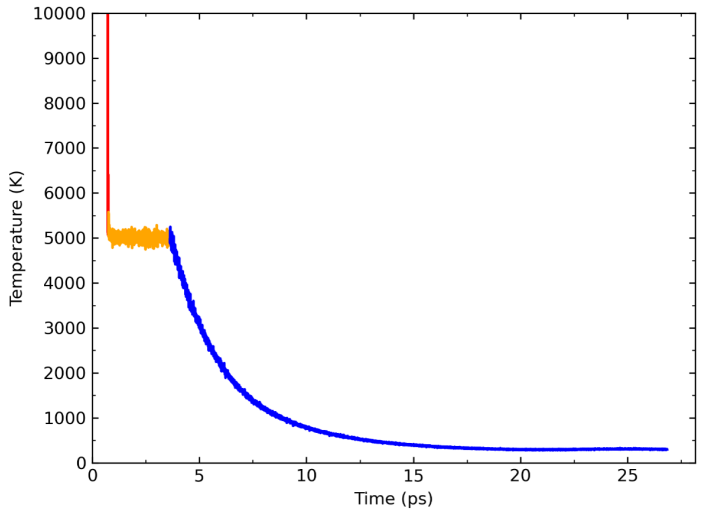


Figure 5.9: Temperature over the course of a melt-quench process for the generation of three dimensional amorphous boron nitride. The colour of the line indicates the different stages of the process: red for melting, orange for equilibration and blue for cooling.

to form non-crystalline metal and alloys structures as well as amorphous structures like glasses. Whilst the melt-quench method has yet to be used to form disordered boron nitride materials, its simplistic nature and the lack of by-products allows for fairly easy computational modelling.

The melt-quench procedure used to generate three-dimensional amorphous boron nitride in this work utilises molecular dynamics with a periodic boundary condition in all three dimensions. The interatomic forces were calculated using the Tersoff potential augmented with a coulombic interaction as described in section 5.1. The procedure is show in figure 5.9. A cubic boron nitride structure containing 1000 atoms is generated at the desired density by varying the bond length and periodic box dimensions. This structure is then rapidly heated to 10^5K over a period of 60.472 fs. The temperature was controlled using periodic velocity rescaling, as described in section 4.2.3.2,

with a rescaling step every 0.242 fs. This initial heating period is significantly above the melting point of both cubic and hexagonal boron nitride, which has been calculated to be between 3000K and 4000K depending on the pressure applied [321]. Due to this high temperature, high levels of disorder are rapidly introduced into the system. Next, the system is rapidly cooled to 5000K and held at this temperature for a period of 242 fs, with the temperature again being controlled using periodic velocity rescaling every 0.242 fs, to equilibrate and form an accurate liquid boron nitride structure. This temperature was chosen as it is greater than the melting point by enough to ensure the system is still liquid whilst being low enough temperature to allow the potential models to dictate the structure, rather than the kinetic energy dominating. The liquid state is then cooled to 300K using a Nosé-Hoover thermostat with a relaxation time, τ, of 120.944 fs as the temperature control, as discussed in section 4.2.3.1. The Nosé-Hoover thermostat is used when cooling the structure from the liquid to the amorphous state as it provides more accurate and gradual control over the temperature, ensuring that the system cools down in a realistic manner reminiscent of being connected to a temperature bath. A variety of amorphous structures with the same density can be generated by allowing the liquid state to equilibrate for differing lengths of additional time before it is cooled down.

6 | Topological and Site Disorder in Boron Nitride Networks

6.1 Introduction

In chapter 5, we introduced methods for generating amorphous configurations of boron nitride in both two and three dimensions. Two dimensional amorphous boron nitride has the potential to have very useful properties, however, it has yet to be synthesised and so currently there is no experimentally derived structural data available. Whilst three dimensional amorphous boron nitride has been studied extensively, much of the work published investigates its properties rather than its underlying structure. Little to no work has been published looking at how ionicity has an effect on the structure of these amorphous systems. As such in this chapter we utilise the potential model and methods for generating three dimensional amorphous materials discussed in chapter 5 to investigate how varying atomic charges can have an effect on the structure of amorphous materials and assess how well a fairly simple potential model and generation method perform in comparison to experimental and more complex simulation structural results. The work contained in this chapter has been published in the Journal of Physics: Condensed Matter [322].

OPEN ACCESS
IOP Publishing
Journal of Physics: Condensed Matter
J. Phys.: Condens. Matter **37** (2025) 045101 (13pp)
https://doi.org/10.1088/1361-648X/ad882d

Topological and site disorder in boron nitride networks

Angus Heafield* and **Mark Wilson**

Department of Chemistry, Physical and Theoretical Chemistry Laboratory, University of Oxford, South Parks Road, Oxford OX1 3QZ, United Kingdom

E-mail: angus.heafield@chem.ox.ac.uk and mark.wilson@chem.ox.ac.uk

Received 17 June 2024, revised 3 October 2024
Accepted for publication 17 October 2024
Published 11 November 2024

Abstract

Amorphous boron nitride (a-BN) is modelled over a wide range of densities using a relatively simple potential model augmented with site charges. The local topology (defined, for example, through the total nearest-neighbour coordination number), appears near-constant across a wide range of densities and site charges. Furthermore, *total* scattering and *total* pair distribution functions also show few changes as a function of either density or site charge. Variation of the site charges directly controls the level of site (rather than topological) disorder meaning that although total pair functions may be near-constant, the underlying partial contributions may be very different. Direct contact is made with both experiment and (more recent) density-functional theory-based modelling work.

Keywords: amorphous boron nitride, molecular dynamics, pair distribution function, site disorder

1. Introduction

Boron nitride (BN) is a significant material showing potentially useful mechanical and thermal properties. Furthermore, the material may be manipulated into a wide range of environments, including into thin films [1, 2], low-dimensional nanotubes [3–5] and buckyballs [6, 7]. The crystalline phase diagram is relatively well-understood showing graphite-like (h-BN) and diamond-like (c-BN) structures at low and high pressure respectively [8, 9]. Melting points are typically high, with $T_m \sim 3000$ K. Key differences with respect to carbon are observed. For example, the hexagonal (BN) layers in h-BN sit in an eclipsed geometry in which the B atoms sit above the N and vice versa rather than being staggered as in graphite, a difference attributed to electrostatic interactions [10, 11]. In the disordered (here meaning liquid, glassy or amorphous) states BN can be considered near-analogous to carbon, for example forming structures dominated by three- and four-coordinate sites. In addition, BN shows a wide range of low-dimensional fullerene-like and nanotubular structures. As a result BN displays a range of structures which may vary with preparation conditions including film thickness and density. However, even seemingly simple data (for example, the number density) is relatively hard to obtain and highly dependent upon the formation conditions. For example, a major focus is in synthesising relatively thin films of amorphous BN which leads to a potentially wide range of densities [12].

Experimental information regarding the structure of disordered BN is relative sparse, reflecting a difficulty in synthesis coupled with the poor visibility of the constituent atoms to both x-rays and neutrons. Modelling efforts have focussed mainly on the application of density-functional theory (DFT)-based approaches [13–18]. Whilst these provide potentially invaluable insight, it is clear that the structures generated vary significantly in terms of the detail of the calculation.

* Author to whom any correspondence should be addressed.

Original Content from this work may be used under the terms of the Creative Commons Attribution 4.0 licence. Any further distribution of this work must maintain attribution to the author(s) and the title of the work, journal citation and DOI.

© 2024 The Author(s). Published by IOP Publishing Ltd

In some sense the structures adopted by BN mirror those for elemental carbon in that the local coordination environments are dominated by a mix of 3- and 4-coordination. The key difference, of course, lies in the presense of two types of atom, potentially allowing for a distribution of local coordination environments which differ in terms of the different chemical identities. From a chemistry perspective, the 'limits' are clear. At one limit, for a given coordination number, each possible nearest-neighbour environment is equally likely and hence observed with a frequency given by simple statistics. This corresponds to the case in which the B-B, N-N and B-N interactions are identical. At the other extreme the network structure is highly ordered, with N atoms surrounding B atoms and vice versa. From a bonding perspective, the former corresponds to a covalent limit with equal bond energies, whilst the latter is the ionic limit in which electrostatic interactions are dominant. For BN covalent interactions are expected to dominate. However, the electronegativity difference between the B and N atoms leads to a small (but potentially significant) charge separation. In the limit that the B and N atoms occupy sites on a given network then the problem becomes one of topological and site disorder. Here we understand topological disorder as being the result of disorder in the atom coordinates and connectivities, as manifested in, for example, ring size distributions or coordination numbers, whereas site disorder reflects the arrangement of the individual atom identities onto the network topology.

Overall, therefore, the available structural information, both from experiments and simulation models, is both sparse and relatively unfocussed in the sense that many different densities have been studied with systems formed under a wide range of conditions (which here means both in a thermodynamic/kinetic sense but also in terms of the detail of the DFT calculation). Furthermore, a comparison of the most common published structural metric, the total pair distribution function (TPDF—$G(r)$), shows that these appear relatively similar *despite* clear differences in the system conditions and/or models.

The key objective of this study is to investigate the evolution of structure in a-BN as the density is systematically varied to help fill in the gaps in the sparse structural data currently available. This is carried out through the use of a 'simple' carbon-like atomistic model which allows for detailed insight into how the structure is affected by factors such as the degree of ionicity. An understanding of how such simple models transfer between different (chemically-related) systems is key if potentially significant systems, such as B/C/N mixtures, are to be successfully exploited.

In this paper we utilise a relatively simple carbon-like atomistic model. Simpler models can help 'unpick' system properties on by breaking down the fundamental interactions. Here, we utilise a simple Tersoff potential to account for the 2- and 3-body terms and add an electrostatic term to account for the electronegativity difference between B and N. The use of a relatively simple model allows us to, firstly, attempt to rationalise the available published structural information and, secondly, to perform calculations in which the system density and site charges are systematically modified.

The paper is organised as follows. Section 2 describes the background (and hence motivation) for the present work, incorporating a clarification of the nomenclature used throughout and a summary of previous work. Section 3 describes the potential model used. Section 4 contains the key results, divided into real and reciprocal space. Section 5 contains a discussion which links the present work into previous modelling and experimental work. Section 6 draws conclusions.

2. Background

2.1. Nomenclature

To attempt to circumvent potential confusion we adopt the standard nomenclature as described in Fischer *et al* [19] and Keen [20]. The total pair distribution function (TPDF) is defined as,

$$G(r) = \sum_{\alpha}\sum_{\beta} c_\alpha c_\beta b_\alpha b_\beta g_{\alpha\beta}(r), \tag{1}$$

where $g_{\alpha\beta}(r)$ is the partial pair distribution function for the atom pair $\alpha\beta$, and $b_{\alpha(\beta)}$ is the appropriate weighting factor for species $\alpha(\beta)$ (e.g. a scattering length in order to obtain a neutron-weighted TPDF). The *differential correlation function*, denoted $D(r)$, is then simply related to $G(r)$ via

$$D(r) = 4\pi n_0 r\{G(r) - 1\}, \tag{2}$$

where n_0 is the total number density. As a result, the gradient of $D(r)$ at low r (i.e. at length-scales shorter than the nearest-neighbour separation, at which $G(r) = 0$) is simply $-4\pi n_0$.

The total structure factor can be expressed in terms of fluctuations in the number density and concentration as suggested by Bhatia and Thornton [21] such that,

$$\begin{aligned} F(k) = {} & \langle w(k)\rangle^2 \left[S^{\mathrm{BT}}_{\mathrm{NN}}(k) - 1\right] \\ & + c_{\mathrm{M}}c_{\mathrm{X}}\left[w_{\mathrm{M}}(k) - w_{\mathrm{X}}(k)\right]^2 \left\{\left[S^{\mathrm{BT}}_{\mathrm{CC}}/c_{\mathrm{M}}c_{\mathrm{X}}\right] - 1\right\} \\ & + 2\langle w(k)\rangle\left[w_{\mathrm{M}}(k) - w_{\mathrm{X}}(k)\right] S^{\mathrm{BT}}_{\mathrm{NC}}(k), \end{aligned} \tag{3}$$

where $S^{\mathrm{BT}}_{\mathrm{NN}}(k)$, $S^{\mathrm{BT}}_{\mathrm{CC}}(k)$ and $S^{\mathrm{BT}}_{\mathrm{NC}}(k)$ represent the BT number-number, concentration-concentration and number-concentration partial structure factors, respectively. $w_\alpha(k)$ represents either the X-ray form factor (which is $k-$dependent) or the $k-$independent neutron scattering length species α. The weighted mean is $\langle w(k)\rangle = c_{\mathrm{M}}w_{\mathrm{M}}(k) + c_{\mathrm{X}}w_{\mathrm{X}}(k)$. The respective low-$k$ limits of these partial structure factors are related to thermodynamic properties (see, for example, [22]). For example, the limit for $S^{\mathrm{BT}}_{\mathrm{NN}}(k)$ may be written as,

$$S^{\mathrm{BT}}_{\mathrm{NN}}(0) = n_0 k_{\mathrm{B}} T\chi_T + \delta^2 S_{\mathrm{CC}}(0), \tag{4}$$

where T is the absolute temperature, k_{B} is the Boltzmann constant, χ_T is the isothermal compressibility, and the dilation

factor $\delta = n_0\,(v_{\rm M} - v_{\rm X})$ where v_α is the partial molar volume per particle of chemical species α.

For an ionic system, the charge-charge partial structure factor $S_{ZZ}(k) = S^{\rm BT}_{\rm CC}(k)/c_{\rm M}c_{\rm X}$ satisfies the Stillinger–Lovett [23] conditions (i) $S_{ZZ}(0) = 0$, which expresses charge neutrality, and (ii) $S_{ZZ}(k) = \Lambda_{\rm D}^2 k^2$ in the small-k region, where $\Lambda_{\rm D}$ is the Debye screening length given by

$$\Lambda_{\rm D}^{-2} = \frac{4\pi n_0}{k_{\rm B}T\varepsilon}\sum_\alpha c_\alpha\,(Z_\alpha e)^2\,, \tag{5}$$

$\varepsilon \equiv 4\pi\,\varepsilon_{\rm r}\varepsilon_0$, $\varepsilon_{\rm r}$ is the dimensionless relative dielectric constant, ε_0 is the vacuum permittivity, and $Z_\alpha e$ is the charge on ion α [24]. Hence $S^{\rm BT}_{\rm CC}(0) = S^{\rm BT}_{\rm NC}(0) = 0$ and $S^{\rm BT}_{\rm NN}(0) = n_0 k_{\rm B} T\chi_T$.

The respective BT partial structure factors can be Fourier transformed to give the corresponding partial pair distribution functions. For example, $S^{\rm BT}_{\rm NN}(k)$ transforms as

The number-number partial pair-distribution function is given by the Fourier transform

$$g^{\rm BT}_{\rm NN}(r) - 1 = \frac{1}{2\pi^2 n_0\, r}\int_0^\infty {\rm d}k\,k\,\left[S^{\rm BT}_{\rm NN}(k) - 1\right]\sin(kr)\,. \tag{6}$$

Equivalent expressions relate the concentration-concentration partial pair-distribution function $g^{\rm BT}_{\rm CC}(r)$ to $\left[S^{\rm BT}_{\rm CC}(k)/c_{\rm M}c_{\rm X} - 1\right]$ and the number-concentration partial pair-distribution function $g^{\rm BT}_{\rm NC}(r)$ to $S^{\rm BT}_{\rm NC}(k)/c_{\rm M}c_{\rm X}$.

In addition, the Bhatia-Thornton partial pair distribution functions can also be defined by direct reference to the partial pdfs,

$$\begin{aligned}
g^{\rm BT}_{\rm NN}(r) &= c_{\rm A}^2 g_{\rm AA}(r) + c_{\rm B}^2 g_{\rm BB}(r) + 2c_{\rm A}c_{\rm B}g_{\rm AB}(r)\,,\\
g^{\rm BT}_{\rm CC}(r) &= c_{\rm A}c_{\rm B}\left[g_{\rm AA}(r) + g_{\rm BB}(r) - 2g_{\rm AB}(r)\right],\\
g^{\rm BT}_{\rm NC}(r) &= c_{\rm A}\left[g_{\rm AA}(r) - g_{\rm AB}(r)\right] - c_{\rm B}\left[g_{\rm BB}(r) - g_{\rm AB}(r)\right].
\end{aligned} \tag{7}$$

2.2. Summary and rationalisation of previous work

Grigoriew and Leciejewicz [25] present both x-ray and electron diffraction for thin films (at thicknesses of ~1μm and 15–20 nm for the x-ray and electron diffraction studies respectively). Both $k-$space (total scattering functions) and real space (differential correlation functions) are shown. No densities are quoted in [25] but the low$-r$ gradients of $D(r)$ (figures 3 abd 4 in [25]) give values of $\rho \sim 1.99$ gcm^{-3} and $\rho \sim 1.84$ gcm^{-3} for the x-ray and electron diffraction studies respectively assumed taken at room temperature. Hong *et al* [26] generate amorphous thin films (~3 nm thick) with densities in the range $\rho = 2.1 - 2.3$ gcm^{-3} and show an experimentally-determined differential correlation function, $D(r)$, obtained via electron diffraction (figure SI2) backed up with molecular dynamics simulations on the Si/BN interface using an empirical potential.

The disordered systems have been modelled using varying 'levels' of density-functional theory (DFT) [13–18]. Hinojosa-Romero *et al* [18] generate two amorphous systems at densities of $\rho = 2.04$ gcm^{-3} and $\rho = 2.80$ gcm^{-3}. McCulloch *et al* [16] generate amorphous structures at room temperature at densities of $\rho = 2.0$ gcm^{-3} and $\rho = 3.0$ gcm^{-3}. The authors show the obtained 'reduced density functions' (albeit with no ordinate axis scale). Kaya *et al* [17] build a gaussian approximation potential (GAP) by reference to DFT calculations, mainly to study mixtures of BN and C, although they generate pure amorphous BN with density $\rho = 2.1$ gcm^{-3}. Durandurdu performed extensive DFT simulations (mostly) on disordered BN under a range or conditions, from amorphous ($\rho = 2.042$ gcm^{-3}) under ambient conditions [13, 15], liquid ($\rho = 2.07$ gcm^{-3}) [13], and amorphous under pressure ($\rho = 2.042 - 4.439$ gcm^{-3}) [14].

To attempt to help visualise and rationalise the DFT-generated real space data, Figure 1 shows a subset of the raw data obtained [13–18]. Figure 1(a) shows the raw $D(r)$ data. Figure 1(b) shows the corresponding $G(r)$ data. The $G(r)$ data from Durandurdu [13] is generated using the published partial pdfs (figure 2 in [13]). The $G(r)$ data from Kaya [17] is scaled on the ordinate axis by a factor of 2.61 to produce a limit of $G(r) \longrightarrow 1$ as $r \longrightarrow \infty$. The data from Hinojosa-Romero *et al* [18] is taken directly from figures 1 and 3 in [18]. The data from McCulloch *et al* [16] is labelled as a 'reduced density function' (figure 4 in [16]). However, the low$-r$ gradients do not appear to correspond to the quoted densities. We have, therefore, generated $G(r)$ from the published functions and rescaled these to give the $G(r) = 0$ at the $r = 0$ limit. Figure 1(c) shows the final TPDFs obtained from DFT under a variety of conditions with the corrected functions from McCulloch *et al* shown for comparison. All the functions show a first peak (at $r_1 \sim 1.5$ Å) corresponding to the first coordination shell and a second peak (at $r_2 \sim 2.6$ Å) corresponding to the formation of a next-nearest-neighbour length-scale. Significant oscillations to high r are present which are more visible in $D(r)$ (figure 1(b)). The spatial extent of these high$-r$ oscillations is difficult to assess given the relatively small system sizes employed throughout. Some further observations are as follows. The 'transformation' from the liquid to amorphous states, studied by Durandurdu, has the expected effect on the TPDFs, with the latter showing significantly stronger peaks both on a nearerst- and next-nearest-neighbour length-scales. In addition, any effect of the differences in densities employed in these simulations appears near-impossible to 'unpick' without additional systematic simulations.

3. Potential models and methods

Amorphous BN (a-BN) was modelled at a range of densities from $\rho = 1.7$ to 3.0 gcm^{-3} using molecular dynamics simulations within the *NVT*-ensemble. The system energy and associated forces between atoms were calculated using a Tersoff potential [27] as parameterised for BN in [28] to which a Coulombic term was added to account for the electronegativity difference between boron and nitrogen and to investigate the effect of ionicity on the disordered structure. This results

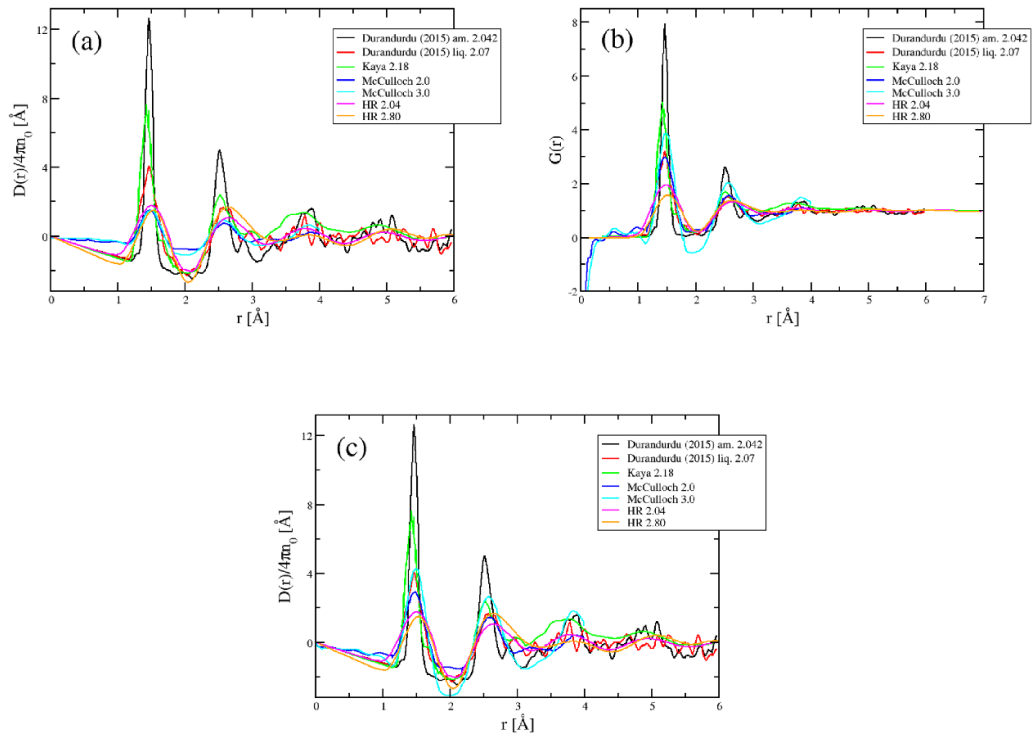


Figure 1. Comparison of the real-space data published from density-function theory (DFT)-based simulations [13–18]. Panel (a) shows the raw $D(r)$ data (from the references as indicated in the caption). Panel (b) shows the resulting $G(r)$ functions generated as discussed in the text. Panel (c) shows $D(r)$ functions with the data from [16] manipulated to give the required low$-r$ gradient (see main text).

in total potential energy of

$$E = E_{\text{Tersoff}} + \frac{1}{2}\sum_{i\neq j}\frac{q_i q_j}{r_{ij}}$$

$$E_{\text{Tersoff}} = \sum_i E_i = \frac{1}{2}\sum_{i\neq j} V_{ij}$$

$$V_{ij} = f_C(r_{ij})\left[a_{ij} f_R(r_{ij}) + b_{ij} f_A(r_{ij})\right]$$

where

$$f_R(r) = A\exp(-\lambda_1 r)$$

$$f_A(r) = -B\exp(-\lambda_2 r)$$

$$f_C(r) = \begin{cases} 1 & r < R-D \\ \frac{1}{2} - \frac{1}{2}\sin\left[\frac{\pi}{2}\frac{r-R}{D}\right] & R-D < r < R+D \\ 0 & r > R+D \end{cases}$$

$$a_{ij} = \left(1+\alpha^n \eta_{ij}^n\right)^{-1/(2n)}$$

$$\eta_{ij} = \sum_{k(\neq i,j)} f_C(r_{ik})\exp\left[\lambda_3^3 (r_{ij}-r_{ik})^3\right]$$

$$b_{ij} = \left(1+\beta^n \zeta_{ij}^n\right)^{-1/(2n)}$$

Table 1. Potential parameters used in the Tersoff potential applied in the present work, taken from Sekkal *et al* [28].

A (eV)	1393.6
B (eV)	346.7
λ_1 (Å^{-1})	3.468
λ_2 (Å^{-1})	2.220
λ_3 (Å^{-1})	0
n	0.72 751
h	-0.57 058
α	0
β	1.5725 x 10^{-7}
c	38 049
d	4.384
R (Å)	1.95
D (Å)	0.20

$$\zeta_{ij} = \sum_{k(\neq i,j)} f_C(r_{ik})\, g(\Theta_{ijk})\exp\left[\lambda_3^3 (r_{ij}-r_{ik})^3\right]$$

$$g(\Theta) = 1 + \frac{c^2}{d^2} - \frac{c^2}{d^2 + (h-\cos\Theta)^2}.$$

The parameters for the Tersoff potential were taken from Sekkal *et al* [28], see table 1, who previously used them to model c-BN as well as liquid BN between T =6000 K and 8000 K. These parameters were originally based on the carbon parameters found in [27] due to the similarities between boron nitride and carbon, and so treat all interactions in the system as equivalent. The short-range Tersoff parameters are,

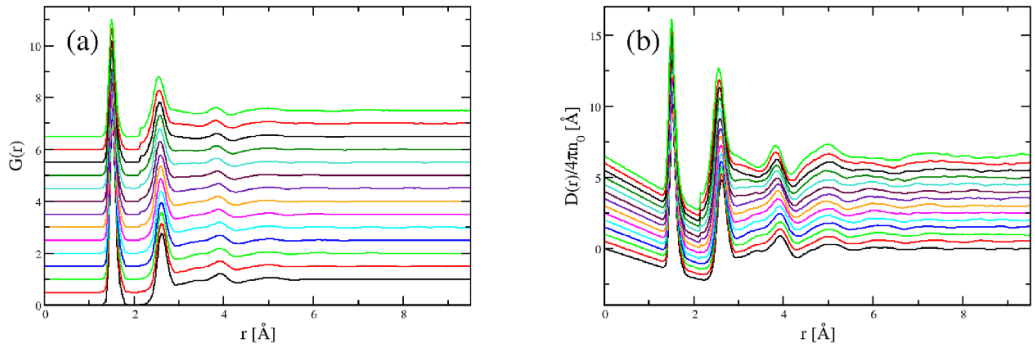


Figure 2. $G(r)$ (panel (a)) and $D(r)$ (panel (b)) functions obtained at $T = 300$ K from $\rho = 1.7$ gcm^{-3} to $\rho = 3.0$ gcm^{-3} (bottom to top, functions are offset along the abscissa for clarity.

naturally, strictly only applicable for the $|q| = 0$ case (i.e. zero site charges). As a result, in order to retain *exactly* the same mean average nearest-neighbour separation, it is likely that these short-range parameters should be modified. For example, if increasing the site charge increases the number of unlike charge nearest-neighbour interactions, it is likely that the mean average nearest-neighbour separation will decrease and hence require a concomitant increase in the appropriate short-range interactions. However, a central remit on the present work is to investigate how the variation of site charges may affect both topological and site disorder. As a result, the short-range interaction terms are kept as simple as possible and hence retained as constant throughout with the subsequent nearest-neighbour separations monitored to identify any major changes in length-scale.

The a-BN systems were generated thought a melt-quench procedure. A timestep of $\Delta t = 12$au ($\equiv$0.29fs) was used throughout. Starting with a c-BN simulation cell containing 1000 atoms at a range of densities, the system was heated to $T = 10^5$K for 0.725 ps to introduce disorder. Next, the system was rapidly cooled to $T = 5000$ K and then allowed to equilibrate at this temperature for 2.9 ps. Finally the system was allowed to cool to 300 K over 23.221 ps using a Nosé-Hoover thermostat, with a relaxation time, τ, of 14.5 ps.

4. Results

The results are presented by those in real and reciprocal space. The real space functions are considered first as the majority of data to date has been presented in this form.

4.1. Real space

Figure 2 shows (a) $G(r)$ and (b) $D(r)$ for the $q = 0$ (uncharged) model as a function of system density, ρ, for $\rho = 1.7 - 3.0$gcm^{-3} in steps of $\Delta\rho = 0.1$gcm^{-3}. The overall shapes of both $G(r)$ and $D(r)$ appear largely invariant across the range of densities studied, implying that any changes in structure may be relatively minor. The first peak position, corresponding to the nearest-neighbour length-scale, remains essentially invariant with density, although the area under the peak changes, corresponding to a change in coordination number from $\bar{n}_{\rm tot} = 2.91 - 3.32$ across the density range studied (see below). The second peak, corresponding to the next-nearest-neighbour length-scale, moves to shorted length-scale with increasing density, shifting from $r_2 \sim 2.62$ Å at $\rho = 1.7$ gcm^{-3}, to $r_2 \sim 2.55$ Å at $\rho = 3.0$ gcm^{-3}. There is also significant 'filling in' on a length-scale of $r \sim 3 - 3.5$ Å (which is more clear in $D(r)$—figure 2(b)). This implies that the densification is driven by changes in structure beyond the nearest-neighbour length-scale.

Figure 3 shows the TPDFs at an example density of $\rho = 2.0$ gcm^{-3} for the site charges (units of e) of $|q| = 0, 0.5, 1.0$. The functions are shown at high temperature ($T = 5000$K, in the liquid state) and at low temperature ($T = 300$K, in the quenched amorphous state). Modifying the site charges within this range appears to have a relatively small effect on the shape of these functions, again implying a relatively small change in the *topological* structure. The effect of reducing temperature is clear and expected in that the first and second peaks are more intense at lower temperature and these functions show significant structure to significantly longer range. Both the first and second peaks shift to lower r at the charge increases, although the ratio of these two peak positions remains approximately constant concomitant with a small decrease in the B-N nearest-neighbour coordination number (see below).

Figure 3 highlights that there appears to be relatively little change in overall structure on modifying the atom charges. However, the TPDF (and the related differential correlation function) is constructed from the three underlying partial pdfs (equation (1)). Figure 4 shows the breakdown of $G(r)$ into the three partial pdfs for $\rho = 2.0$ gcm^{-3} with site charges $|q| = 0, 0.5, 1.0$ respectively. At first glance it can clearly be seen that, as expected, increasing the site charge lead to changes in the partial pdfs with unlike interactions becoming more favourable. However, as depicted in figure 3, this has very little effect on the TPDF. Figures 3 and 4 also highlight the effectiveness of retaining the short-range (Tersoff) parameters whilst systematically varying the site charges (as discussed

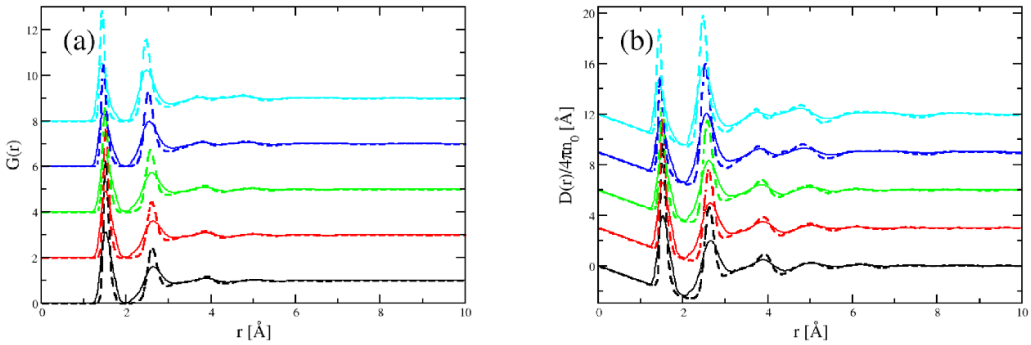


Figure 3. $G(r)$ (panel (a)) and $D(r)$ (panel (b)) functions for $\rho = 2$ gcm^{-3} obtained at $T = 2000$ K (solid lines) and $T = 300$ K (dashed lines) and for site charges of $|q/e| = 0, 0.25, 0.5, 0.75, 1.0$ (shown offset along the abscissa for clarity with increasing charge).

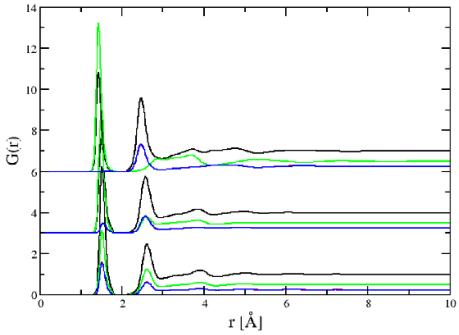


Figure 4. Panel (a) shows the $G(r)$ function (black line) and its breakdown into the three underlying partial contributions (red-BB, green-BN, blue-NN). The functions are shown for $\rho = 2$ gcm^{-3} and $T = 300$ K and for site charges of $|q/e| = 0, 0.25, 0.5, 0.75, 1.0$ (shown offset along the abscissa for clarity with increasing charge).

in section 3). There is a small reduction in the mean average nearest-neighbour length-scale, from $\bar{r}_1 \sim 1.513$ Å at $|q| = 0$ to $\bar{r}_1 \sim 1.430$ Å at $|q| = 1.0$, a reduction of around 5%. The low and high q functions show the significant limits. At $q = 0$ the interactions between atom pairs are all equivalent (at least for the highly simplified representation adopted here) and so $g_{\mathrm{BN}} \equiv g_{\mathrm{NB}} \equiv g_{\mathrm{BB}} \equiv g_{\mathrm{NN}}$. As a result, the first peak in $G(r)$ is comprised of contributions from all three partials. For $q = 1$ the effect of imposing the charges on the atoms is clear as the system adopts structure typical of those dominated by electrostatic interactions and hence displaying significant charge ordering. As a result, the first peak in $G(r)$, at $r_1 \sim 1.5$ Å, is comprised entirely of contributions from g_{BN} and g_{NB}, whilst the second peak, at $r_2 \sim 2.6$ Å, is composed of contributions *almost* entirely from g_{NN} and g_{BB}, which retain their symmetrical relationship. For the intermediate $|q/e| = 0.5$ case the presence of site charges breaks the $g_{\mathrm{BN}} \equiv g_{\mathrm{NN}}$ (or g_{BB}) symmetry and so the first peak in $G(r)$ is dominated by g_{BN} but with significant contributions from both g_{BB} and g_{NN}. Repeating the key observation from figures 2 and 3, the *total* PDF, $G(r)$, appears near-invariant with both site charge and density (within the relatively wide ranges chosen here).

Figure 5 shows the change in mean nearest-neighbour coordination number, $\bar{n}^{\beta}_{\alpha}$, over a range of both densities and site charges. The total mean coordination number, $\bar{n}_{\mathrm{tot}}$, remains approximately fixed at $\bar{n}_{\mathrm{tot}} \sim 3 - 3.4$ across the density range studied. The contributions from $\bar{n}^{\mathrm{N}}_{\mathrm{B}}$, $\bar{n}^{\mathrm{B}}_{\mathrm{B}}$, $\bar{n}^{\mathrm{N}}_{\mathrm{N}}$, and $\bar{n}^{\mathrm{B}}_{\mathrm{N}}$ vary systematically as the site charge is increased, with the unlike contributions ($\bar{n}^{\mathrm{N}}_{\mathrm{B}}$ and $\bar{n}^{\mathrm{B}}_{\mathrm{N}}$) systematically increasing with site charge with a concomitant reduction in the like contributions ($\bar{n}^{\mathrm{B}}_{\mathrm{B}}$ and $\bar{n}^{\mathrm{N}}_{\mathrm{N}}$). At $q/e = 0$ the different partial coordination numbers are equivalent, whilst at $q/e = 1$ the total coordination number is dominated by the unlike coordination environments. To help visualise these differences, figure 6 shows molecular graphics 'snapshots' of the amorphous networks at a fixed density of $\rho = 2.0$ gcm^{-3} at site charges of $|q/e| = 0$, 0.5 and 1.0. As the site charge increases there is a clear visual increase in the number of unlike coordination environments.

The implication of the above analysis is that the basic *topology* of the BN network remains effectively invariant with atom charge, but there is a difference in terms of how the B and N atoms are arranged. There appears to be an effective *site disorder* which is controlled by the magnitude of the site charges. As a result, a more 'natural' method for breaking down the total pair distribution function (or total scattering function in $k-$space) is as described by Bhatia and Thornton [21]. In this formalism the total functions are expressed in terms of those which depend on the chemical (C) and topological (N) ordering [22]. As a result, the real space function, $g^{\mathrm{BT}}_{\mathrm{NN}}(r)$, effectively describes the global network structure, whilst $g^{\mathrm{BT}}_{\mathrm{CC}}(r)$ describes any chemical ordering on the network described by $g^{\mathrm{BT}}_{\mathrm{NN}}(r)$. $g^{\mathrm{BT}}_{\mathrm{NC}}(r)$ reveals information regarding the correlation between a given network site and its

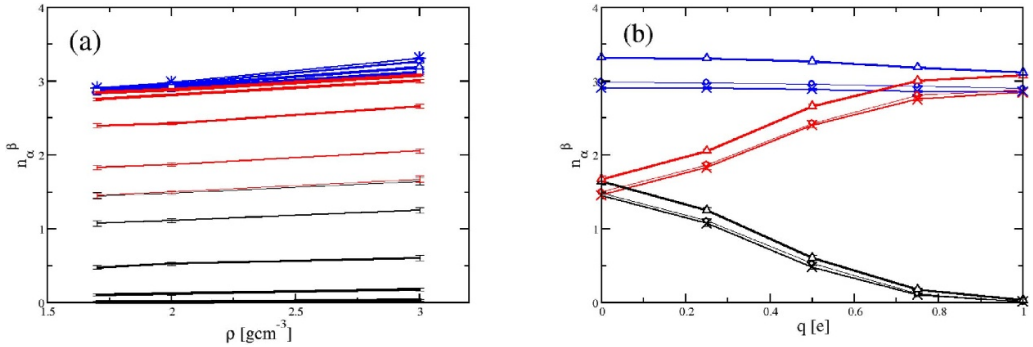


Figure 5. Panel (a) shows the mean coordination numbers as a function of the density charge. Key: Panel (b) shows the mean coordination numbers as a function of the site charge. Key: black line—$\bar{n}_{\mathrm{B}}^{\mathrm{B}}$, green line—$\bar{n}_{\mathrm{N}}^{\mathrm{N}}$, red line—$\bar{n}_{\mathrm{B}}^{\mathrm{N}}$, blue line—$\bar{n}_{\mathrm{tot}}$.

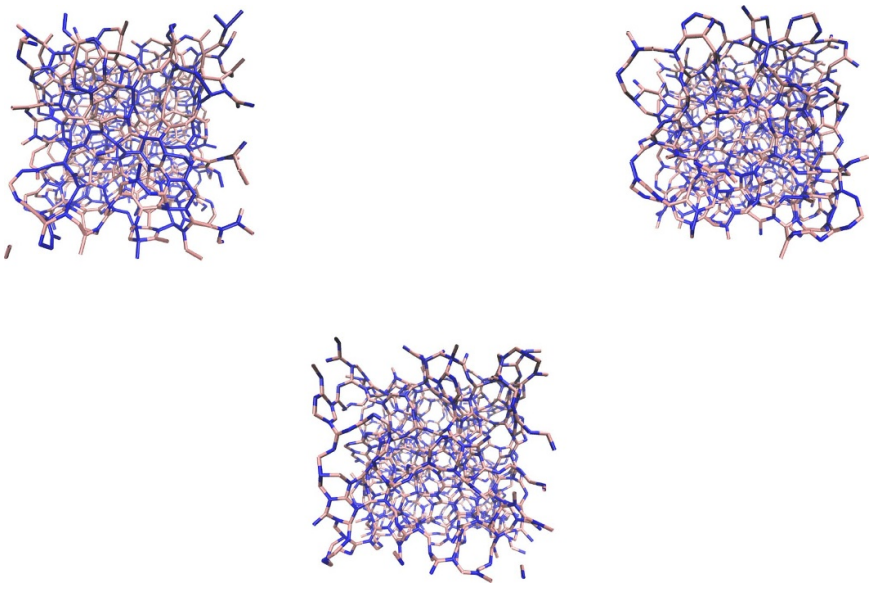


Figure 6. Molecular graphics 'snapshots' for amorphous configurations obtained at a fixed density of $\rho = 2.0$ gcm^{-3} for (top left) $|q/e| = 0$, (top right) $|q/e| = 0.5$, (bottom) $|q/e| = 1.0$. In all cases blue represents the N atoms and pink the B atoms.

occupancy by a particular chemical species [29, 30]. Figure 7 shows the real space BT functions for $\rho = 2.0\mathrm{gcm}^{-3}$ over a range of site charges. $g_{\mathrm{NN}}^{\mathrm{BT}}(r)$ (figure 7(a)) appears almost invariant to the site charges whilst $g_{\mathrm{CC}}^{\mathrm{BT}}(r)$ (figure 7(b)) shows a large systematic change in the intensities of both the first and second peaks, consistent with relatively small changes in network topology coupled with greater coulombically-driven site ordering as the site charges are increased. $g_{\mathrm{NC}}^{\mathrm{BT}}(r)$ (figure 7(c)) shows very little intensity, indicative of the great similarity of the coordination sites whether B- or N-centred.

4.2. Reciprocal space

The figures introduced in section 4.1 highlight how any topological differences (either as a function of density or site charge) appear difficult to detect to real space. Figure 8 shows the BT functions $S_{\mathrm{NN}}^{\mathrm{BT}}(k)$ and $S_{\mathrm{CC}}^{\mathrm{BT}}(k)$ for $T = 300$K over a range of densities. $S_{\mathrm{NN}}^{\mathrm{BT}}(k)$ is shown for $|q/e| = 0$ and 1, whilst $S_{\mathrm{CC}}^{\mathrm{BT}}(k)$ is shown for $|q/e| = 1$ only (as $S_{\mathrm{CC}}^{\mathrm{BT}}(k) = 0$ for all k for $|q/e| = 0$ (see below). Overall, although there are slight changes in all three functions they all remain mostly invariant to the changing density. This indicates that both the topological structure and the site ordering appear to be approximately constant on increasing density. For both $|q/e| = 0$ and 1 $S_{NN}^{BT}(k)$ shows a small shift to high k in the peak at $k \sim 2\text{Å}^{-1}$ as the density increases. The peak also increases in intensity and becomes sharper as the density increases. The peak at $k \sim 5$ Å^{-1} appears near-invariant with density at both site charges shown. At both of these site charges there is an increase in intensity at low k, indicative of changes in the $k \longrightarrow 0$ limit. The low k limit in $S_{\mathrm{NN}}^{\mathrm{BT}}(k)$ is related to the isothermal compressibility, χ_T, via

$$S_{\mathrm{NN}}^{\mathrm{BT}}(0) = n_0 k_{\mathrm{B}} T \chi_T, \tag{8}$$

where n_0 is the number density. $S_{\mathrm{CC}}^{\mathrm{BT}}(k)$ appears to change very little with density. Furthermore, for that function the low k limit $S_{\mathrm{CC}}^{\mathrm{BT}}(0)$, tends to zero, consistent with overall electroneutrality for charged systems [23]. Figure 9 shows the BT functions $S_{\mathrm{NN}}^{\mathrm{BT}}(k)$ and $S_{\mathrm{CC}}^{\mathrm{BT}}(k)$ for $T = 300$K at

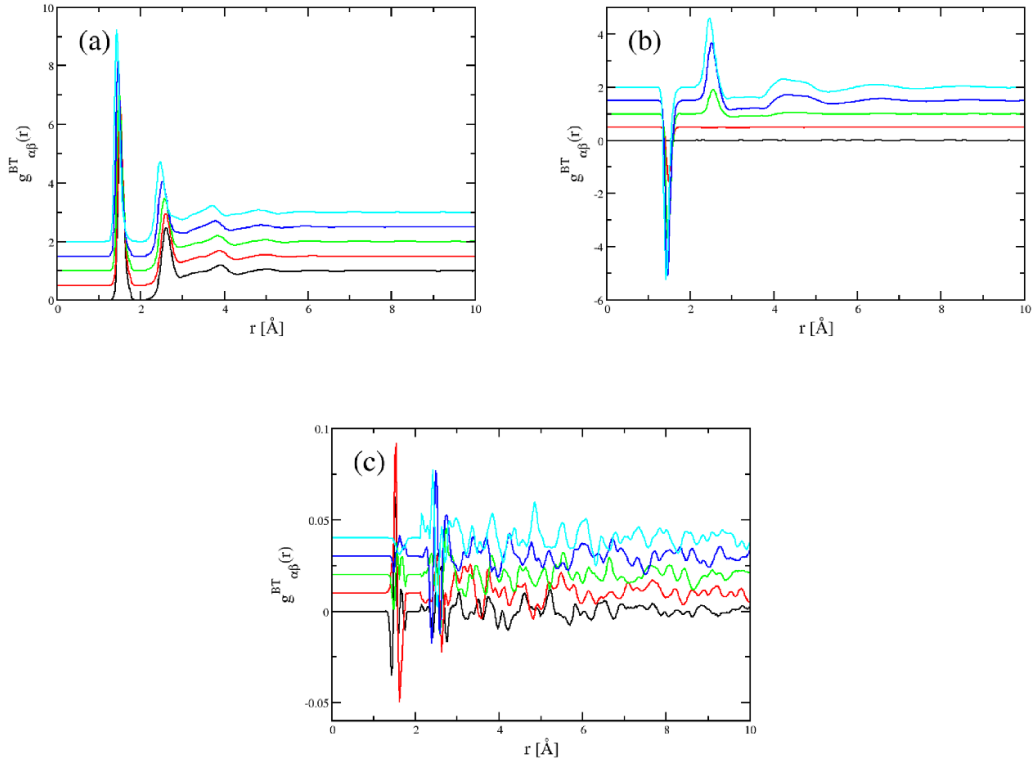


Figure 7. Bhatia-Thornton pair distribution functions for $T = 300$ K and $\rho = 2.0$ gcm^{-3} and for site charges of $|q/e| = 0, 0.25, 0.5, 0.75, 1.0$ (shown offset along the abscissa for clarity with increasing charge). Panels (a)–(c) show $g_{\mathrm{NN}}(r)$, $g_{\mathrm{CC}}(r)$, and $g_{\mathrm{NC}}(r)$ respectively.

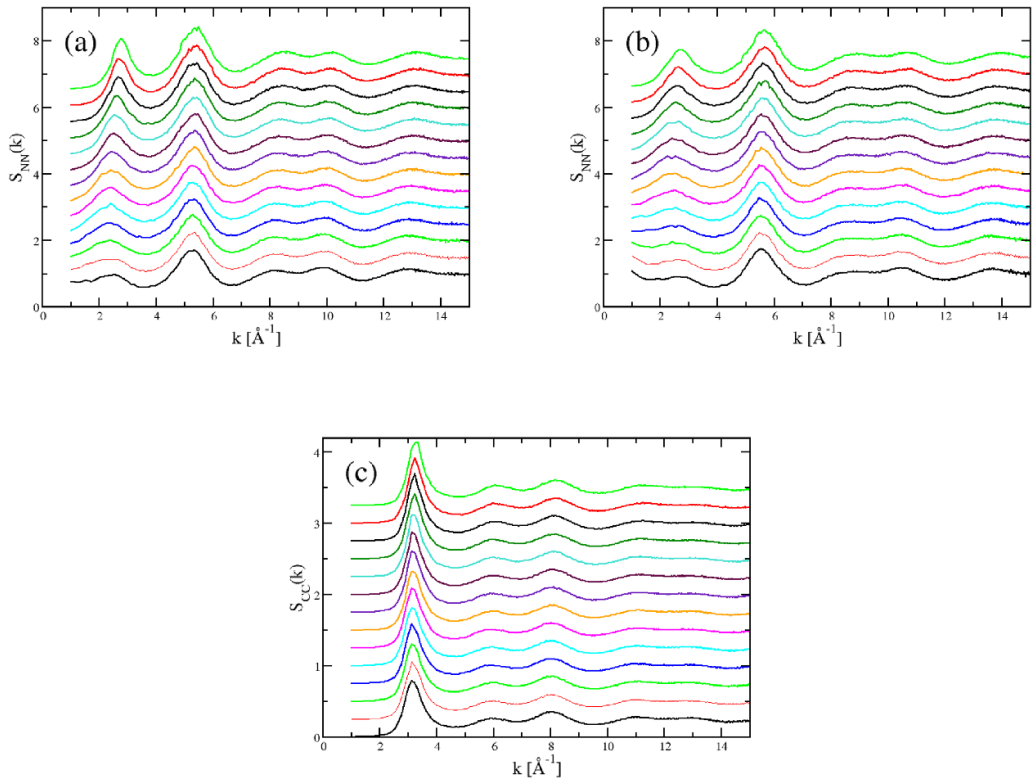


Figure 8. Panels (a) and (b) show $S_{\mathrm{NN}}(k)$ obtained at $T = 300$ K and $\rho = 1.7 - 3.0$ gcm^{-3} (offset along the abscissa for clarity). Panel (a) is for site charge $|q/e| = 0$ and panel (b) is for site charge $|q/e| = 1.0$. Panel (c) shows $S_{\mathrm{CC}}(k)$ under the same conditions for site charge $|q/e| = 1.0$.

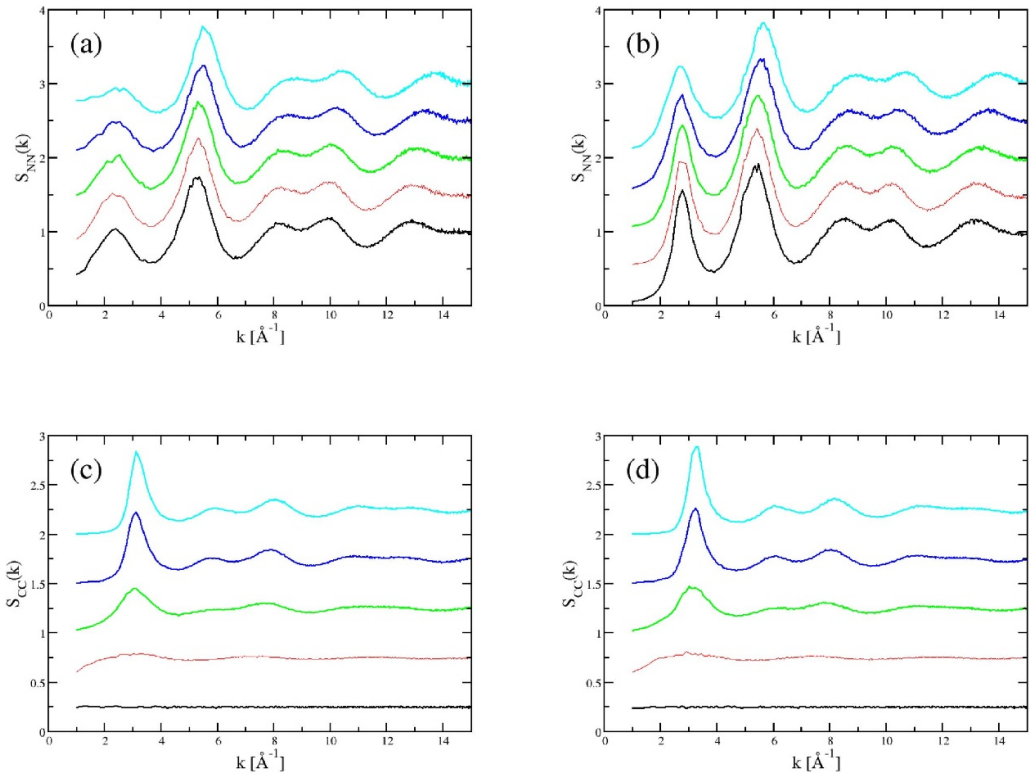


Figure 9. Bhatia-Thornton structure factors obtained for (panels (a) and (c)) $\rho = 2.0$ gcm^{-3} and (panels (b) and (d)) $\rho = 3.0$ gcm^{-3} and for site charges of $|q/e| = 0, 0.25, 0.5, 0.75, 1.0$ (shown offset along the abscissa for clarity with increasing charge). Panels (a) and (b) show $S_{\mathrm{NN}}(k)$ whilst panels (c) and (d) show $S_{\mathrm{CC}}(k)$.

$\rho = 2.0$gcm^{-3} and 3.0gcm^{-3} for a range of site charges. At the lower density the change in $S^{\mathrm{BT}}_{\mathrm{NN}}(k)$, in particular at low k, is clear. At both densities the expected changes in $S^{\mathrm{BT}}_{\mathrm{CC}}(k)$ are observed as the network becomes more charge ordered as the magnitude of the site charges increase. To highlight the change in the low$-k$ limits in $S^{\mathrm{BT}}_{\mathrm{NN}}(k)$, figure 10 shows the isothermal compressibility, χ_T, calculated from equation (8) by performing a linear fit to the low k region of $S^{\mathrm{BT}}_{\mathrm{NN}}(k)$ plotted against k^2 and extracting the $k \longrightarrow 0$ limit. Compressibility of amorphous materials is of particular interest as there are a wide range of behaviours observed for different materials. Some amorphous systems, such as alkali borates and silicates, behaviour in a similar manner to more crystalline structures, decreasing compressibility with increasing pressure [31]. Whist others, such as amorphous silica, behave somewhat anomalously, becoming softer on compression [32]. In addition, the compressibility represents a key material property and so an understanding as to how this behaves as key model parameters are systematically varied, is important, Furthermore, the compressibility potentially represents a useful property which may be investigated experimentally in a number of different ways. Such investigations could be significant given the uncertainty in the published densities and their potential dependence upon the synthesis pathway. At all site charges there is a systematic reduction in χ_T as the density increases. At high density the compressibilities are approximately independent of density. At lower densities, however, the compressibility increases significantly as the site charge is increased. The effect is seen more clearly in figure 10(b) which shows χ_T as a function of the site charge for a range of densities. The figures indicate that, for $\rho \gtrsim 2.5$ gcm^{-3}, the isothermal compressibility shows a relatively small density dependence which is approximately independent of site charge. For $\rho \lesssim 2.5$ gcm^{-3}, the increase in χ_T as the density falls appears much more dramatic at higher site charges. Since the basic network topologies appear similar, the long-range electrostatic interactions driving the site ordering are effectively softening the networks.

5. Discussion

The above analysis indicates that the topological disorder appears largely invariant across the density range studied but there is variation in the level of site disorder with the model partial charges. In the discussion we attempt to place the current results in context by comparison to previous DFT-based simulation results and by comparison to the results of diffraction experiments. There is also a more general discussion to attempt to bring the work together.

5.1. Relationship to previous DFT calculations

The analysis presented above is consistent with a network whose local topology appears near-invariant across a surprisingly wide range of densities and site charges. As much of

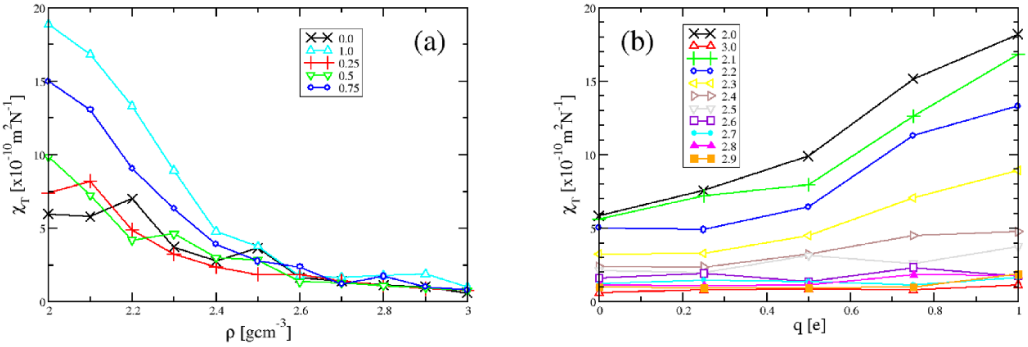


Figure 10. Isothermal compressibilities, χ_T, calculated from a fit of the low k region of $S^{\mathrm{BT}}_{\mathrm{NN}}(k)$ plotted against k^2 and extrapolated to find the $k \longrightarrow 0$ limit then applying equation (8). Panel (a) shows χ_T as a function of the mass density shown over a range of site charges (as indicated in the legend) whilst panel (b) shows the reverse (with the mass densities indicated in the legend in gcm^{-3}).

Table 2. Summary of previous modelling work using density-functional theory (DFT) - based methods. The columns list the respective temperatures and densities used in the stated references. The final column notes any other applied conditions.

Reference	ρ(gcm^{-3})	T(K)	Detail
Hinojosa-Romero *et al* [18]	2.04	300	
	2.80	300	
McCulloch *et al* [16]	2.0	300	
	3.0	300	
Kaya *et al* [17]	2.18	300	
Durandurdu [13]	2.042	300	
	2.07	3300	
Durandurdu [14]	2.042	300	$p = 0$ (compressed)
	3.403	300	$p = 60$GPa
	4.439	300	$p = 200$GPa
	2.521	300	$p = 0$ (decompressed)
Durandurdu [15]	3.083	300	

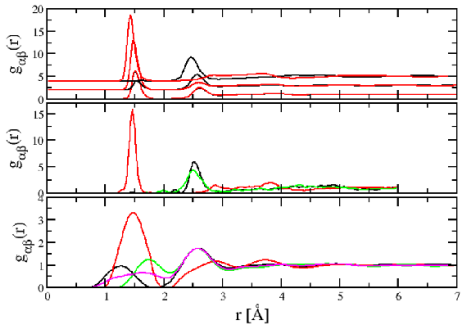


Figure 11. Partial pair distribution functions obtained from DFT-based simulations compared with those obtained in the present work. The lower and middle panels show the DFT-based functions obtained at $\rho = 2.041$ gcm^{-3} and $T = 300$ K from [18] and [13] respectively. The three sets of curves shown in the upper panel correspond to site charges (from bottom to top) of $|q/e| = 0, 0.5, 1.0$. In all cases the key is: red line—$g_{\mathrm{BN}}(r)$, black line—$g_{\mathrm{NN}}(r)$, green line—$g_{\mathrm{BB}}(r)$. For the lower curves the magenta line shows the mean average of $g_{\mathrm{BB}}(r)$ and $g_{\mathrm{NN}}(r)$. Note the difference in ordinate scales in the three panels.

the previous simulation work has been performed using DFT-based approaches, it is worth discussing these (often seemingly quite different) results and placing them in the context of the results derived here. Table 2 summarises the mass densities and temperatures considered in previous work. The spread in densities studied reflects the dispersion in observed experimental values. Comparison of figures 1 and 3 shows that positions of peaks in the current work match well with the previously published result. The small change in the peak positions on varying density and site charge fit well within the bounds of peaks positions shown in the existing literature. The peak heights across all site charges and densities in the current work most closely match with the work of Durandurdu [13] (in both the amorphous and liquid states) and Kaya *et al* [17]. The peak heights which match most closely are those for site charges of $|q/e| = 0.25$ and 0.5. The peaks obtained elsewhere appear to be shorter and broader, indicating a similar average number of closest neighbours but spread of a wider range of bond lengths. Figure 11 shows a direct comparison of the PRDFs obtained from DFT simulations at $\rho = 2.042$ gcm^{-3} and $T = 300$K (from [18] and [13] respectively) along with the like (BB) and unlike (BN) functions obtained for site charges of $|q/e| = 0, 0.5, 1.0$. The DFT functions from [18] show a first peak with the largest contribution from the unlike PRDF but with significant contributions from both $g_{\mathrm{BB}}(r)$ and $g_{\mathrm{NN}}(r)$. In this case the first peaks in the latter two functions are distinct, with the former at lower r. The results from [18] most closely resemble those here with $|q/e| = 0.5$ but with much broader peaks, however due to the interactions being treated differently the BB and NN peaks are at different distances. This distinction is not present in the current work as the BB and NN interactions are considered equivalent for simplicity, as discussed in section 3. The NN peak is particularly interesting as it is at an even shorter distance than the BN peak, despite the repulsive ionic character, it is possible that this could be a result of a NN bond being more covalent in character than a BN or BB bond. To help compare with the present simplified model (which retains a symmetry between the N-N and B-B interactions) the figure also shows the mean average of $g_{\mathrm{BB}}(r)$ and $g_{\mathrm{NN}}(r)$. In contrast, the functions from [13] show a first peak in $G(r)$ which is almost entirely dominated by the unlike $g_{\mathrm{BN}}(r)$ contribution. In terms of the current model, therefore, the latter corresponds to site charges of $|q/e| = 1.0$ whilst the former is nearest site charges of $|q/e| = 0.5$. The difference in the DFT outcomes could be simply a function of the 'level'

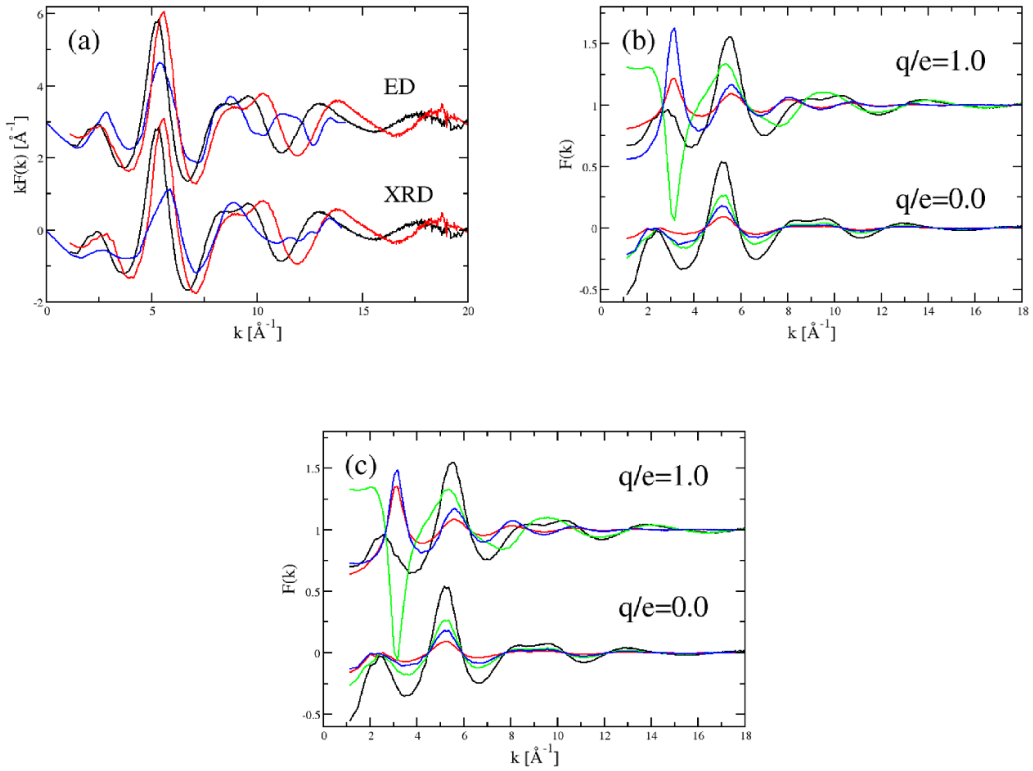


Figure 12. Panel (a) shows the experimental total scattering function, $kF(k)$, obtained from both x-ray and electron (blue lines) diffraction and compared to simulation data obtained for $\rho = 2.0$ gcm^{-3} and $T = 300$ K with site charges of $|q/e| = 0.0$ (black lines) and $|q/e| = 1.0$ (red line). Panels (b) and (c) shows the total x-ray and electron scattering functions (black lines) for with site charges of $|q/e| = 0.0$ (lower figures) and $|q/e| = 1.0$ (upper figures) along with the respective breakdowns into the x-ray and electron-weighted contributions from the NN (blue lines), BB (red lines) and BN (green lines) atom pairs.

of the theory applied in each case. Massobrio *et al* [33], for example, show how the use of a local density approximation (LDA) and a generalised gradient approximation (GGA) affect the structure of liquid $GeSe_2$. In that case the use of a gradient-corrected methodology allowed the atom centres to adopt a more ionic character (see, for example, the electron densities in figure 2 in [33]). The key point, therefore, is that relatively subtle differences in the details of the DFT calculations can greatly affect the ionicity which is a possible explanation of the differences described above.

5.2. Comparison to experimental diffraction data

Figure 12(a) shows the direct comparison of the total scattering functions (from [25]) obtained by both x-ray and electron diffraction to those generated in the present work for $|q/e| = 1$ and $|q/e| = 0$ respectively. The respective total scattering functions are obtained from the partial structure factors via

$$F^{(a)}(k) = \sum_{\alpha}\sum_{\beta} c_\alpha c_\beta f_\alpha^{(a)}(k) f_\beta^{(a)}(k)\left[S_{\alpha\beta}(k) - 1\right], \qquad (9)$$

where $f_{\alpha(\beta)}^{(a)}(k)$ is the electron scattering function $a = e$ or x-ray form factor $a = X$ for species $\alpha(\beta)$. These can be calculated using high level quantum mechanical methods (as tabulated in [34–36]). The differences in the two experimentally-determined curves reflect the respective weightings of the underlying partial structure factors. The two total scattering functions calculated in the present work show a similar peak structure, in particular in the positions of the first three peaks at $k \sim 2.5$ Å^{-1}, $k \sim 5$ Å^{-1}, and $k \sim 8$ Å^{-1} respectively. The model functions show similar peak structure to the experimental total scattering functions including the shoulder in $k \sim 8$ Å^{-1} for electron diffraction. However differences appear at higher k values, particular in comparison to the electron diffraction data, where there is a peak at $k \sim 12$ Å^{-1} which is not present in either the high or low site charge scattering factors from the current work. The intensity of the some of the peaks is also different, with the $k \sim 2.5$ Å^{-1} peak being more intense in the ED results than the current results and less intense in the XRD results than the current results. The $k \sim 5$ Å^{-1} peak is less intense for both sets of experimental results whilst the $k \sim 8$ Å^{-1} peak is of a similar intensity to the current results for both experimental results. The function obtained using a site charge of $|q/e| = 1$ shows a shift to higher k with respect to the zero charge model. To further understand the differences, Figures 12(b) and (c) show the breakdown of the total scattering x-ray scattering functions and electron diffraction functions into the respective weighted partial structure factor contributions for both the $|q/e| = 0$ and $|q/e| = 1$ site charge models. For $|q/e| = 0$ the respective contributions from the three partials are only different because of their different scattering

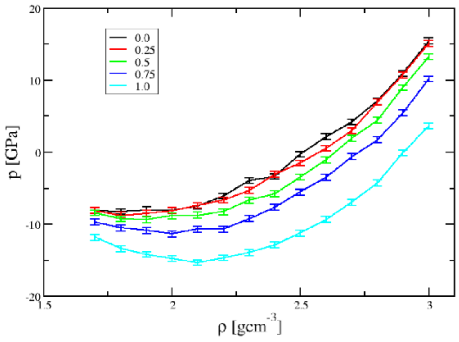


Figure 13. The pressure exherted by the simulation cell determined along the $T = 300$ K isotherm, as a function of density, and determined for the five site charges studied here (as indicated in the legend as $|q/e|$).

lengths. For $|q/e| = 1$ the underlying partial structure factors are very different, typical of those for a charge-ordered system, for example, showing strong destructive interference in the BB, NN and BN functions at $k \sim 3$ Å^{-1}, but sum to give very similar total scattering functions.

5.3. General discussion

The above analysis shows that the topological structure of the amorphous BN appears to change very little across a wide density range. The additional of site charges to the model thus controls the site ordering in a given topology. As an example of the effect of these changes, figure 13 shows the pressures (determined along the T =300 K isotherm determined across the five values of the site charge investigated here. The change in curvature as the charge increases (which is related to the bulk modulus) is clear. Figure 13 also highlights the presence of so-called anomalous thermodynamic behaviour (see, for example, [37]) with the minimum (corresponding to $\left(\frac{\partial P}{\partial \rho}\right)_{T,q} = 0$) strengthening as the charge increases. Such behaviour is observed for related systems such as Si and BeF_2 (see, for example, [38] and references therein). The behaviour of the isothermal compressibility shows two key trends, as a function of density and site charge. As the density increases the network becomes less compressible (higher bulk modulus) as would be expected. The behaviour with site charge is more subtle, with the systems becoming more compressible (lower bulk modulus) as the site charge increases, with the change becoming more significant as the density is reduced highlighting the effect of increases nearest-neighbour charge ordering as the site charges are increased. The range of compressibilities determined here correspond to bulk moduli in the range $B_0 \sim 2 - 17$GPa. This compares to a value of $B_0 = 36.5$GPa for h-BN (the graphitic crystalline analogue) [39] which is around 10% of the values observed for the higher coordinate blende and wurtzite polymorphs ($B_0 \sim 400$GPa [40]). The observation that the compressibilites are relatively small across a wide density range is consistent with the wide range of densities observed experimentally. It is clearly possible to form the (thermodynamically metastable) amorphous state over a wide density range with very little energetic penalty.

6. Conclusions

In this paper the structure of amorphous boron nitride has been investigated across a wide density range using a relatively simple potential model. Augmenting the potential model with site charges (whose values can be systematically varied) controls the level of site disorder although the topological order appears near-constant across the a (large) range of densities and site charges studied. The compressibilities are low across the density range studied consistent with the observation that the material may be readily formed over a large density range. The work highlights the potential significant role of (relatively small) site charges in controlling the site ordering. We expect these effects to become more significant when modelling surfaces and thin films due to the presense of a wider range of local coordination environments compared to the bulk amorphous material studied here. We further anticipate that the work presented here will form a basis for key future investigations, including detailed studies as to how different conditions affect the structure of a-BN, for example, temperature, the presence of ionic materials, or the presence of different charge states. The general model framework could also be applied to a variety of other materials such as B/C/N mixtures and other amorphous III-V compounds.

Data availability statements

All data that support the findings of this study are included within the article (and any supplementary files).

Acknowledgments

This paper conforms to the RCUK data management requirements

ORCID iDs

Angus Heafield https://orcid.org/0009-0001-1537-6591
Mark Wilson https://orcid.org/0000-0003-4599-7943

References

[1] Rand M J and Roberts J F 1968 *J. Electrochem. Soc.* **115** 423
[2] Shi Y *et al* 2010 *Nano Lett.* **10** 4134
[3] Chopra N G, Luyken R J, Cherrey K, Crespi V H, Cohen M L, Louie S G and Zettl A 1995 *Science* **269** 966
[4] Golberg D, Bando Y, Tang C and Zhi C 2007 *Adv. Mater.* **19** 2413
[5] Golberg D, Bando Y, Huang Y, Terao T, Mitome M, Tang C and Zhi C 2010 *ACS Nano* **4** 2979
[6] Golberg D, Bando Y, Stéphan O and Kurashima K 1998 *Appl. Phys. Lett.* **73** 2441–3
[7] Oku T, Kuno M, Kitahara H and Narita I 2001 *Int. J. Inorg. Mater.* **3** 597
[8] Wells A F 1984 *Structural Inorganic Chemistry* (Clarendon)
[9] Mueller U 1993 *Inorganic Structural Chemistry* (Wiley)
[10] Cotton F, Wilkinson G, Murillo C A and Bochmann M 1999 *Advanced Inorganic Chemistry* (Wiley)
[11] Greenwood N and Earnshaw A 1997 *Chemistry of the Elements* (Butterworth-Heinemann)

[12] A number of key references in this area are ascribed to 'Private Communication'
[13] Durandurdu M 2015 *J. Non-Cryst. Solids* **427** 41
[14] Durandurdu M 2016 *Phil. Mag.* **96** 1950
[15] Durandurdu M 2019 *J. Am. Ceram. Soc.* **103** 973
[16] McCulloch D G, McKenzie D R and Goringe C M 2000 *J. Appl. Phys.* **88** 5028
[17] Kaya O, Colombo L, Antidormi A, Lanza M and Roche S 2023 *Nanoscale Horiz.* **8** 361
[18] Hinojosa Romero D, Valladares A, Valladares R M, Rodrigues I and Valladares A A 2024 *Sci. Rep.* **14** 7949
[19] Fischer H E, Barnes A C and Salmon P S 2006 *Rep. Prog. Phys.* **69** 233
[20] Keen D A 2001 *J. Appl. Cryst.* **34** 172
[21] Bhatia A B and Thornton D E 1970 *Phys. Rev.* B **2** 3004
[22] Salmon P S 1992 *Proc. R. Soc.* Lond. A **437** 591
[23] Stillinger Jr F H and Lovett R 1968 *J. Chem. Phys.* **48** 3858
[24] Salmon P S 2006 *J. Phys.: Condens. Matter* **18** 11443
[25] Grigoriew G and Leciejewicz J 1989 *Thin Solid Films* **172** L75
[26] Hong S *et al* 2020 *Nature* **582** 511
[27] Tersoff J 1988 *Phys. Rev.* B **37** 6991
[28] Sekkal W, Bouhafs B, Aourag H and Certier M 1998 *J. Phys.: Condens. Matter* **10** 4975
[29] $g_{NC}^{BT} = 0$ for an ideal solution
[30] Here we adopt the nomenclature $g_{\alpha\beta}^{\mathrm{BT}}(r)$, where $\alpha\beta$ =NN, CC or NC, in order to avoid confusion with the Faber-Ziman partial functions which involve the nitrogen atoms
[31] Weir C E Shartsis L 1955 *J. Am. Ceram. Soc.* **38** 299
[32] Walker A M, Sullivan L A, Trachenko K, Bruin R P, White T O H, Dove M T, Tyer R P, Todorov I T and Wells S A 2007 *J. Phys. Condens. Matter* **19** 275210
[33] Massobrio C, Pasquarello A and Car R 1999 *J. Am. Chem. Soc.* **121** 2943
[34] Peng L M Ren G, Dudarev S L Whelan M J 1996 *Acta. Cryst.* **52** 257
[35] Peng L M 1998 *Acta. Cryst.* **54** 481
[36] Cromer D and Waber J T 1974 *International tables for x-ray Crystallography* (Kynoch Press)
[37] Debenedetti P 1997 *Metastable Liquids.* (Princeton University Press)
[38] Fijan D and Wilson M 2023 *Phil. Trans. R. Soc.* A **381** 20220336
[39] Solozhenko V and Peun T 1997 *J. Phys. Chem. Solids* **58** 1321
[40] Shimada K, Sota T and Suzuku K 1998 *J. Appl. Phys.* **84** 4951

7 | The Application of a Fluctuating Charge Model for Boron Nitride Networks

7.1 Introduction

In chapter 6, we investigated the effect of increasing ionicity on the structure and properties of amorphous boron nitride. It was shown that modelling the nature of the bonding using relatively small site charges, between $|q/e| = 0$ and 1, has a potentially significant effect on these materials. However, throughout the previous work in this thesis, these site charges have always been assumed to be static and independent of their environment. While this assumption may be appropriate when simulations are static and all atomic environments are identical throughout the structure, it is unlikely to still hold when modelling the dynamic properties of systems or those containing varied atomic environments. As such a more flexible approach may be required.

In this chapter, we introduce the fluctuating charge model (FCM), as discussed in section 3.4, to our potential model for boron nitride. Under the FCM electron density is still modelled through the use of site charges, however these charges are allowed to vary with their environment. This allows for a compromise between static charges and modelling full electron density wave functions. This chapter details how the FCM was adapted for application to network materials and a comparison of its results with those of more complex density functional theory (DFT) simulations, before moving to applying the new potential model to disordered BN structures. The work contained in this chapter has been published in The Journal of Chemical Physics [323].

The Journal of Chemical Physics ARTICLE pubs.aip.org/aip/jcp

The application of a fluctuating charge model for boron nitride networks

Cite as: J. Chem. Phys. 164, 024705 (2026); doi: 10.1063/5.0311291
Submitted: 8 November 2025 • Accepted: 22 December 2025 •
Published Online: 13 January 2026

View Online Export Citation CrossMark

Angus Heafield[a] and Mark Wilson

AFFILIATIONS

Physical and Theoretical Chemistry Laboratory, Department of Chemistry, University of Oxford, South Parks Road, Oxford OX1 3QZ, United Kingdom

[a]Author to whom correspondence should be addressed: angus.heafield@chem.ox.ac.uk

ABSTRACT

A fluctuating charge model (FCM) is developed to consider two-dimensional networks of boron nitride. In the FCM, the charge on each atom site is controlled by parameters linked to the atom's electronegativity and the interactions with other atoms (the coordination environment). The charge held on each atom site is a strong function of the local (first shell) coordination environment. The site charges are shown to be in excellent agreement with those extracted from independent density-functional theory-based calculations. The behavior of the site charges is investigated as a function of the network topology and site disorder. In the first case, specific defects (both site and topological) are introduced, and the spatial "decay" of the local charge to bulk values is assessed. In the second, highly disordered (amorphous) networks are generated, and the distribution of site charges is studied as a function of the degree of topological and site disorder (characterized by the fraction of six-membered rings and mean boron–nitrogen coordination numbers, respectively). Domains of high and low charges are observed to form across a wide range of topological disorder.

© 2026 Author(s). All article content, except where otherwise noted, is licensed under a Creative Commons Attribution (CC BY) license (https://creativecommons.org/licenses/by/4.0/). https://doi.org/10.1063/5.0311291

13 January 2026 13:55:09

I. INTRODUCTION

Boron nitride (BN) is considered a promising material due to its unique thermal, electronic, and mechanical properties with a wide range of potential applications, including water purification,[1,2] UV photodetection,[3] and structural reinforcements.[4] BN has been well-studied in three main crystalline forms: hexagonal (h-BN),[5] cubic (c-BN),[6] and wurtzite (w-BN),[7] as well as a range of synthetic structures, such as thin films,[8] nanotubes,[9] fullerene-like nanoparticles,[10] and a range of amorphous states.[11] These structures are reminiscent of their carbon analogs but with the potential additional complexity of the existence of charge separation as a result of the two different atomic species with differing electronegativities. This charge separation leads to a variety of differences in structure and properties between BN and C materials, such as h-BN favoring AA′ stacking over the AB stacking favored by graphite and h-BN having a bandgap of ~6 eV (an insulator within layers[12]), while graphite has no bandgap (a conductor within layers[13]).

The existence of two elements allows different types of defects, such as boron or nitrogen vacancies, or boron/nitrogen anti-site defects, that is, boron taking the place of a nitrogen in the lattice or vice versa. In addition, the topological disorder may be introduced. The topological disorder relates to the locations of atoms in a network structure, while site-based disorder is related to how the different types of atoms occupy those sites.

We have previously found that systematically varying the charge separation, such that the *magnitude* of the charge on each site is fixed, in amorphous BN systems leads to changes in partial structure factors and radial distribution functions, while the corresponding total functions remain near-constant, indicating that there is a change in the site-based disorder, while the topological disorder remains fairly constant.[14] However, it is likely that the site charge varies according to the environment of a given atom rather than all atoms having the same charge. It is possible that this distribution of charge throughout a system could also help understand properties such as its permeability for charged species, such as, for example, ions in water desalination[15] or DNA sequencing.[16] In addition, the charge distribution may affect the movement of defects through the network.[17,18] However, establishing the precise values of the site charges remains problematic. *Ab initio* calculations suggest charges of magnitude $|q| \sim 0.25 - 0.50e$.[19] Furthermore, site charges inferred from density-functional-based calculations appear

© Author(s) 2026

to depend heavily on the details of the applied model, while the effect of using different charges is hard to resolve from experimental diffraction data.[14,20,21]

The fluctuating charge model, FCM, allows for the variation of charge on each site throughout a classical molecular dynamics simulation. By assigning each site an effective electronegativity, which is a function of the atom identity and its local environment, charge can move between sites depending on changes in the environment. The FCM has been used previously to model the charges on isolated molecular species, such as polyatomic anions, for example, CN^-,[22] NO_3^-,[23,24] and CO_3^{2-},[25,26] uncovering complex ordering on multiple length-scales, for example, low-dimensional chains in Na_2CO_3.[25] In this paper, we apply the FCM to much larger BN networks, allowing for the investigation into how the topological and site disorder affect the charge distributions in these systems.

The aim of this paper is to develop a model to investigate how the charge distribution in BN is affected by both topological and site disorder. We will develop and apply a fluctuating charge model to a range of two-dimensional configurations, ranging from the ideal crystalline structures to defective crystals, clusters, and disordered (amorphous) environments. The cluster calculations allow for direct comparison with the results of independent electronic structure calculations, which help validate our model parameterization. This paper is arranged as follows: The FCM is introduced, and the parameterization is established. The charges obtained are then compared to independent *ab initio* results across a range of clusters containing B, C, and N atoms. Pure BN networks are then considered, first via the introduction of specific defects leading to site and/or topological disorder, and then to highly disordered (amorphous) networks. The results are brought together in discussions, and conclusions are drawn.

II. METHODS

In this section, we will review the basis of the fluctuating charge model (FCM). We first show how the model can be modified to account for the lack of well-defined molecules, how the charge can be modified dynamically, and how the model is parameterized. We then move on to describe the methods employed to study the networks, both in terms of their generation and their dynamic evolution.

A. The fluctuating charge model (FCM) applied to continuous networks

The following derivations are based on the work of Ribeiro and Almeida,[23] Rappé and Goddard,[27] and Rick *et al.*:[28]

1. The basic model

The energy of an atom A can be expressed as a function of the atomic charge, q_A, in terms of the deviation from a neutral state, A_0,

$$E_A(q_A) = E_{A_0} + q_A\left(\frac{\partial E}{\partial q_A}\right)_{A_0} + \frac{1}{2}q_A^2\left(\frac{\partial^2 E}{\partial q_A^2}\right)_{A_0} + \cdots. \tag{1}$$

By substituting $q_A = +1, 0$, and -1 into Eq. (1) and including only terms up to the second order, the following expressions for the energy of the neutral atom and the mono-charged ions are obtained:

$$E_A(+1) = E_{A_0} + \left(\frac{\partial E}{\partial q_A}\right)_{A_0} + \frac{1}{2}\left(\frac{\partial^2 E}{\partial q_A^2}\right)_{A_0}, \tag{2}$$

$$E_A(0) = E_{A_0}, \tag{3}$$

$$E_A(-1) = E_{A_0} - \left(\frac{\partial E}{\partial q_A}\right)_{A_0} + \frac{1}{2}\left(\frac{\partial^2 E}{\partial q_A^2}\right)_{A_0}. \tag{4}$$

Equations (2)–(4) can then be used to obtain expressions for the first and second derivatives of the energy with respect to the charge,

$$\left(\frac{\partial E}{\partial q_A}\right)_{A_0} = \frac{1}{2}(IP + EA) = \chi_A^0 \tag{5}$$

and

$$\left(\frac{\partial^2 E}{\partial q_A^2}\right)_{A_0} = (IP - EA) = J_{AA}^0, \tag{6}$$

where $IP = E_A(+1) - E_A(0)$ is the ionization potential of atom A, $EA = E_A(0) - E_A(-1)$ is the electron affinity of atom A, χ_A^0 is the electronegativity of atom A in a neutral reference,[29] and J_{AA}^0 is the hardness parameter of atom A in a neutral reference.[28,30] Equations (5) and (6) can then be inserted into Eq. (1), again including only terms up to the second order, to reach an expression for the energy of atom A, using physically understandable parameters,

$$E_A(q_A) = E_{A_0} + \chi_A^0 q_A + \frac{1}{2}J_{AA}^0 q_A^2. \tag{7}$$

To calculate the optimal charge distribution in a system with more than one atom, the inclusion of the interatomic electrostatic energy, $\sum_{A<B} q_A q_B J_{AB}$, is required, where J_{AB} is the Coulombic interaction between unit charges on atoms A and B, which is dependent on r_{AB}, the distance between atoms A and B. This leads to a total electrostatic energy for a system of N atoms,

$$E(q_1 \ldots q_N, r_1 \ldots r_N) = \sum_A \left(E_{A_0} + \chi_A^0 q_A + \frac{1}{2}q_A^2 J_{AA}^0\right) + \sum_{A<B} q_A q_B J_{AB}. \tag{8}$$

Taking the derivative of Eq. (8) with respect to q_A leads to an expression for the electronegativity of atom A in the system of N atoms,

$$\chi_A(q_1 \ldots q_N, r_1 \ldots r_N) = \chi_A^0 + J_{AA}^0 q_A + \sum_{B\neq A} J_{AB} q_B. \tag{9}$$

For molecular systems, Eq. (9) can then be further divided by considering the J_{AB} term for intermolecular interactions as taking the form of the interaction between point charges, $1/r_{AB}$,[23] giving

$$\chi_{iA}(q_1 \ldots q_N, r_1 \ldots r_N) = \chi_{iA}^0 + J_{AA}^0 q_{iA} + \sum_{B\neq A} J_{AB} q_{iB} + \sum_{j\neq i}\sum_B \frac{q_{jB}}{r_{AB}}, \tag{10}$$

where $\chi_{iA}(q_1 \ldots q_N, r_1 \ldots r_N)$ is the electronegativity of atom A in molecule i.

In treating molecular systems, the breakdown in terms of intra- and inter-molecular interactions is clear. As a result, the charge may fluctuate across a given molecule with the clear constraint that the overall charge on that molecule is fixed. In a network system, the

13 January 2026 13:55:09

© Author(s) 2026

overall system charge remains fixed; however, a length-scale needs to be identified over which the charge is allowed to effectively move. To apply the FCM to a continuous network, this length-scale is imposed by treating only atoms within a specified cutoff as allowing charge transfer, preventing charge from being transferred across longer (non-physical) distances. Equation (10) is modified as

$$\chi_A = \chi_A^0 + J_{AA}^0 q_A + \sum_{B\neq A} F_c(r_{AB}) J_{AB} q_B + \sum_{B\neq A} (1 - F_c(r_{AB}))\frac{q_B}{r_{AB}}, \quad (11)$$

where $F_c(r)$ is the cutoff complementary error function, which varies from 0 to 1,

$$F_c(r_{AB}) = \frac{1}{2}\,\mathrm{erfc}(\xi(r_{AB} - r_c)).$$

The parameter ξ is used to control how steep the cutoff is, and r_c is the cutoff radius and is the value of r for which $F_c(r)$ is equal to 0.5. A complementary error function was chosen to be modified due to its smooth and integrable nature for all values of r_{AB}, allowing for simple calculation of the forces on the charges and for the ease with which the shape of the function can be adjusted with only two parameters.

2. The movement of charge

For a system to be at equilibrium, all atomic chemical potentials must be equal. This leads to $(N-1)$ constraints on the atomic chemical potentials, or electronegativities, such that

$$\chi_1 = \chi_2 = \cdots = \chi_N. \quad (12)$$

An additional constraint arises from the requirement for charge conservation,

$$q_{tot} = \sum_{A=1}^{N} q_A, \quad (13)$$

which leads to N simultaneous equations, which can then be solved for a given structure to reach a self-consistent equilibrium set of charges. To allow for the study of dynamic systems, Rick *et al.*[28] developed a method to allow charges to evolve in time in parallel to the atom motion (a Car–Parrinello method[31]). The constraints are treated using the undetermined multipliers method, giving

$$L = \sum_{A=1}^{N_{atom}} \frac{1}{2} m_A \dot{r}_A^2 + \sum_{A=1}^{N_{atom}} \frac{1}{2} M_q \dot{q}_A^2 - E(q_1 \ldots q_N, r_1 \ldots r_N) - \lambda\left(\sum_{A=1}^{N_{atom}} q_A - q_{tot}\right), \quad (14)$$

where m_A is the mass of atom A and M_q is a fictitious charge "mass" with units of energy time^2/charge^2. Solving by the standard approach leads to the following expression:

$$M_q \ddot{q}_A = -\frac{\partial E[(q),(r)]}{\partial q_A} - \lambda = -\tilde{\chi}_A - \lambda, \quad (15)$$

showing the charges evolving in time in parallel to the atomic degrees of freedom. It is then possible to solve for λ as the total charge is fixed, such that

$$\sum_{A=1}^{N_{atom}} \ddot{q}_A = 0. \quad (16)$$

Substitution of Eq. (15) into Eq. (16) gives

$$\lambda = -\frac{1}{N_{atom}} \sum_{A=1}^{N_{atom}} \tilde{\chi}_A = -\chi_{avg}, \quad (17)$$

which can then be substituted back into Eq. (15) to give a final equation of motion,

$$\ddot{q}_A = -\frac{1}{M_q}(\tilde{\chi}_A - \chi_{avg}). \quad (18)$$

The fictitious mass, M_q, is chosen such that the charge "motion" is rapid (by comparison to the atomic motion), which allows the charges to remain at their equilibrium (adiabatic) values. In reality, although the energy transfer between the (relatively) low frequency atomic vibrational modes and the high frequency modes associated with the charges is small (reflecting the small overlap in resonant frequencies), it is not zero. As a result, if uncorrected, then energy would (slowly) transfer between the atomic modes and the (necessarily cold) charge modes, which will lead to both a decrease in the system temperature and an increase in the temperature associated with the charge motion, the latter of which corresponds to the charges becoming more detached from the required adiabatic surface. A simple way to control this (slow) energy transfer (and employed here) is to utilize Nosé–Hoover thermostats to maintain the temperature of the respective atomic and charge degrees of freedom.[32,33]

3. Parameterization

The parameters for the FCM used in this work, as shown in Table I, were adapted from those previously used to model the charges for C and O in Ref. 25. While parameters have been proposed for a range of atoms, including N,[27] these parameters were calculated for individual atoms, and so additional *ab initio* calculations are required for their application to molecules. Due to the similarity in electronegativity difference and bonding between C–O and B–N, it is believed that these parameters will also provide a good model for the charges in BN systems. The hardness parameters, J_{BB}^0

TABLE I. Parameters for the FCM for BN and C. All values are quoted in atomic units.

χ_B^0	0.200
χ_N^0	0.321
χ_C^0	0.261
J_{BB}^0	1.297
J_{NN}^0	1.474
J_{CC}^0	1.385
J_{BB}	0.226
J_{BN}	0.290
J_{NN}	0.226
J_{BC}	0.290
J_{NC}	0.290
J_{CC}	0.226

13 January 2026 13:55:09

© Author(s) 2026

and J^0_{NN}, were adjusted to give an average absolute charge, $\overline{|q|}$, in h-BN of 0.31e, in line with previous *ab initio* calculations,[19] to allow for a meaningful comparison.

B. Methodology

Two-dimensional amorphous BN configurations were generated through the use of Monte Carlo simulations. First, topological disorder was introduced into a hexagonal network of 800 atoms through the use of a bond-switching algorithm as described in Refs. 34 and 35. The Monte Carlo move for this algorithm is the creation of a Stone–Wales defect by rotating a selected bond by 90°. This results in two rings increasing in size by one and two rings decreasing in size by one; for example, four 6-membered rings become two 5-membered rings and two 7-membered rings. To ensure a wide distribution of ring sizes, simulated annealing was utilized, wherein all Monte Carlo moves are initially accepted and then the system is "cooled down" by reducing the probability of accepting unfavorable moves. By controlling the probability of accepting moves, we are able to control the level of topological order in the system. For the configurations studied in this work, the initial thermalization was carried out over 1000 steps, followed by 10 000 steps for the "cooling" process. The networks generated are entropically driven, meaning that the resulting distributions of ring sizes follow a maximum entropy distribution. As a result, a fraction of a single ring size, usually taken as the fraction of six-membered rings, p_6, is all that is required to define the distribution since this will relate directly to the width of the distribution (Lemaître's law[36]).

The bond-switching algorithm controls the network topology and so does not take into account the identities of the atoms at each site. As a result, the bond-switching is followed by a second Monte Carlo procedure to control the site-ordering. This second algorithm involves assigning atomic identities at random to the sites and then swapping atom pairs at random. The local coordination environment is a key indicator of the level of site disorder; for example, using the mean nearest-neighbor coordination number, $\overline{n}^{\beta}_{\alpha}$, which gives the mean average number of atoms of type β in the first coordination shell of an atom of type α. Therefore, in ideal h-BN, a site-ordered three-coordinate system, $\overline{n}^{N}_{B} = \overline{n}^{B}_{N} = 3$ and $\overline{n}^{N}_{N} = \overline{n}^{B}_{B} = 0$. In the second MC procedure, the only accepted moves are those that result in an increase in the number of B–N nearest-neighbors ($\overline{n}^{N}_{B} = \overline{n}^{B}_{N}$ increases). MC moves are performed until $\overline{n}^{N}_{B} (= \overline{n}^{B}_{N})$ reaches a fixed value.

Finally, the systems were geometrically relaxed through the use of a steepest descent algorithm. The forces on the atoms were calculated using a Tersoff potential[37] parameterized for low-dimensional BN[38] and BN-C[39] nanostructures, augmented with the FCM for the electrostatic interaction. The molecular dynamics simulations were carried out in the N, V, T canonical ensemble at 300 K, controlled using a Nosé–Hoover thermostat. The time step was set to be 1 fs, and periodic boundary conditions were applied in the x–y plane.

III. RESULTS

A. Comparison to density-functional theory-based calculations

In order to assess the validity of our (physically motivated) parameterization, a comparison is made to the site charges obtained from recent DFT-based calculations.[40] DFT calculations were performed as described in Ref. 41 on seven two-dimensional clusters, all containing 252 atoms, of which 36 are H atoms placed on the cluster extremities to retain full (three) coordination of the B, C, and N atoms. The number of C atoms was varied from 0 (i.e., all BN) to 216 (all C) with the total number of B, N, and C atoms fixed at 216. Configurations are labeled as BN (the ideal BN lattice) or C_n, where n is the number of C atoms in the configuration, with the remaining $(216 - n)$ atoms being BN. Each configuration can be characterized in terms of both the stoichiometry (the number of B, N, and C atoms) and the local coordination environments. All sites are three-coordinate, and so the local environment can be characterized ideally by the identity of the central atom and the three nearest-neighbors. For example, the ideal BN lattice will contain B–N_3 and N–B_3 units only. Calculations were performed as described in Refs. 40 and 41, with an analysis of the site charges performed as in Ref. 41. Site charges are extracted at the MDC-q level. Analogous calculations were performed using the FCM as parameterized above, but using a periodically repeating lattice rather than the isolated cluster. Figure 1 shows an example C_{24} cluster (containing 24 C atoms) used in the DFT calculations and the periodic analog used in the FCM calculations. In both panels, the charges are highlighted via the coloring of the sites.

Figure 2 shows the distribution of site charges for the B, N, and C atoms determined for the seven cluster stoichiometries

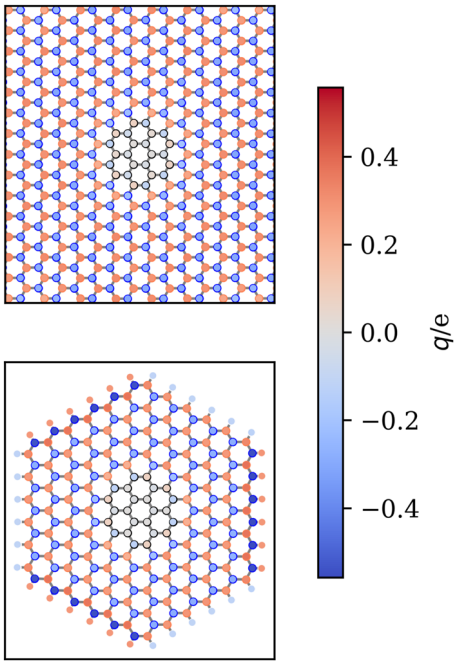


FIG. 1. Example charge "heat maps" obtained from the fluctuating charge model (top, using a periodic cell) and density-functional theory calculations (bottom, using a cluster) for systems containing 24 C atoms per cell. In both panels, the degree of red and blue corresponds to the size of the positive and negative charges, respectively. In the lower panel, the smaller circles around the edge represent the H atoms required to charge-balance the cluster. In both panels, the circle circumferences are colored red, blue, or black to indicate B, N, or C atoms, respectively.

13 January 2026 13:55:09

© Author(s) 2026

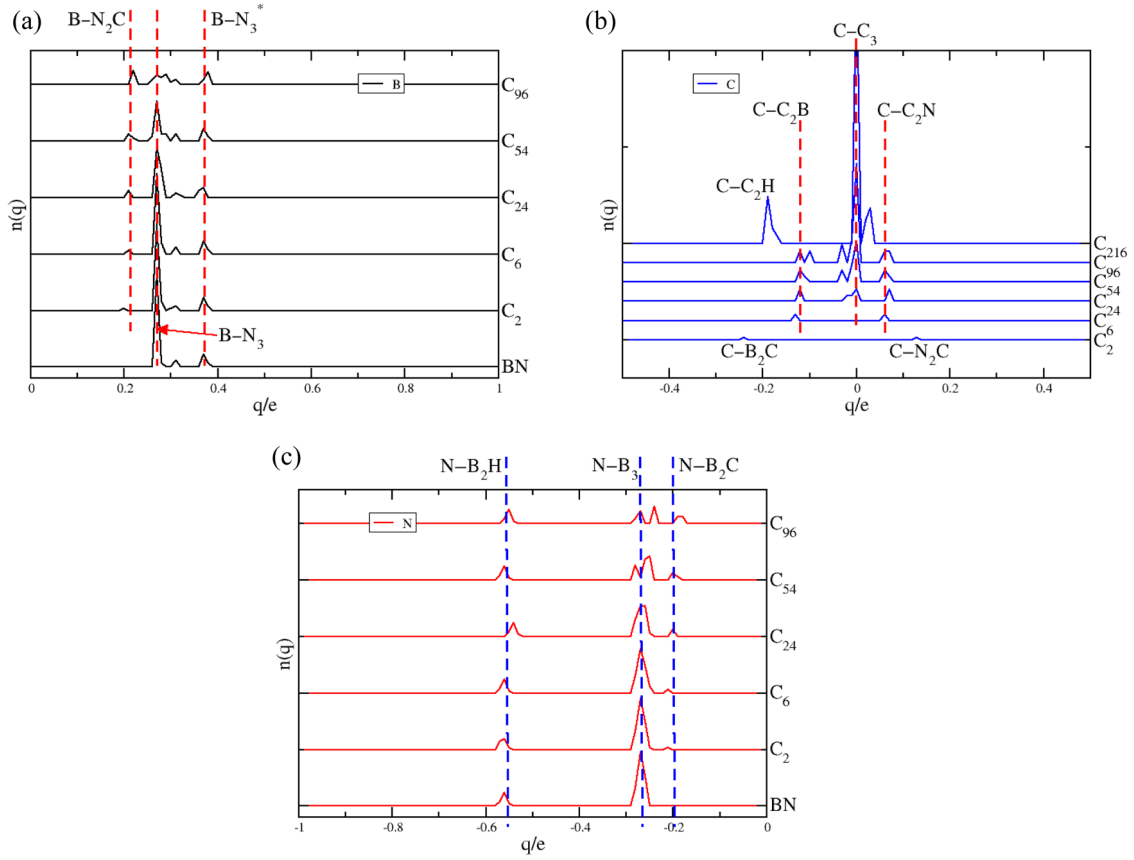


FIG. 2. Distribution of site charges obtained using density-functional theory.[41] Panels (a), (b), and (c) show the charges on the B, C, and N atoms, respectively, with the cluster composition shown on the right hand side of each panel. The vertical dashed lines are a guide to the eye and are labeled with the respective local coordination environments. The peaks labeled "B–N_3^*" in panel (a) refer to the B atoms on the edge of the cluster, which are surrounded by N atoms that are themselves nearest-neighbors to the outer H atoms.

considered, split into three panels according to atom identity. For the C atom sites, the pure BN configuration is omitted, while for the B and N sites, the pure C configuration is similarly omitted. The most significant conclusion to draw from these figures is that the charge on a given site appears to be a *strong* function of the *local* (nearest-neighbor) coordination environment. For the C atom, for example, the C_6 to C_{96} configurations show clear peaks attributable to the C–C_2B, C–C_3, and C–C_2N local coordination environments. The C_2 configuration shows peaks attributable to the C–B_2C and C–N_2C environments, while the C_{216} configuration shows peaks attributable to the C–C_3 and C–C_2H environments. Similarly, the B atom sites show peaks associated with B–N_3, B–N_2C, and B–N_2H environments, while the N atoms show the equivalent N–B_3, N–B_2C, and N–B_2H environments. In addition, a small number of B atoms show a large charge, which is the result of the next-nearest neighbors in which they are surrounded by three N atoms, but those N atoms are nearest-neighbors to the outer H atoms [labeled B-N_3^* on panel (a)]. Table II lists the mean charges and standard deviations on each site, averaged over all configurations containing those sites. In the cluster used for the DFT calculations, H atoms sit at the extremities in order to preserve charge neutrality. As a result, the DFT configurations contain both N–B_2H and B–N_2H local coordination environments.

To consider the effect of the local coordination environment on the atom charge, a careful nomenclature is required. For example, the environment about an atom of type α, surrounded by a maximum of two atom types, β and γ, may be characterized either in terms of n_α^β or n_α^γ, for which $n_\alpha^\beta + n_\alpha^\gamma = 3$. A consistent nomenclature is required to define a site α having a coordination $n_\alpha^{\beta,\gamma}$, where the numerical value is the number of atoms of type β surrounding site α (the remaining atoms being of type γ), and to order the superscripts with the most electronegative element first (i.e., $\chi_\beta > \chi_\gamma$).

Figure 3 shows the evolution of the site charge as a function of the local environment for both the DFT and FCM calculations, with the charges determined as the mean values averaged over the seven configurations studied. The error bars show the standard deviations resulting from this averaging. The figure highlights the clear dependence of, and trends in, the site charges on the local coordination environment. In addition, the relatively small standard deviations indicate that the site charges are very strongly dependent on the *local* coordination environment and not on the overall

13 January 2026 13:55:09

© Author(s) 2026

TABLE II. Mean charges and the associated standard deviations of atom site charges obtained from density-functional theory, arranged by coordination environment as indicated in the first column. The charges are averaged across all configurations containing those local environments.

Site coordination	$\bar{q}/e$	σ_q/e
B–N_3	0.298 24	0.042 14
B–N_2C	0.217 61	0.004 90
B–N_2H	0.289 60	0.018 49
C–B_2C	−0.247 36	N/A
C–C_2B	−0.119 84	0.007 64
C–N_2C	0.137 08	N/A
C–C_2N	0.069 87	0.004 38
C–C_2H	−0.190 09	0.006 14
C–C_3	−0.000 52	0.013 62
N–B_3	−0.270 76	0.009 31
N–B_2C	−0.200 45	0.010 42
N–B_2H	−0.562 38	0.008 81
H–B	−0.105 08	0.006 57
H–C	0.162 69	0.003 66
H–N	0.292 18	0.005 18

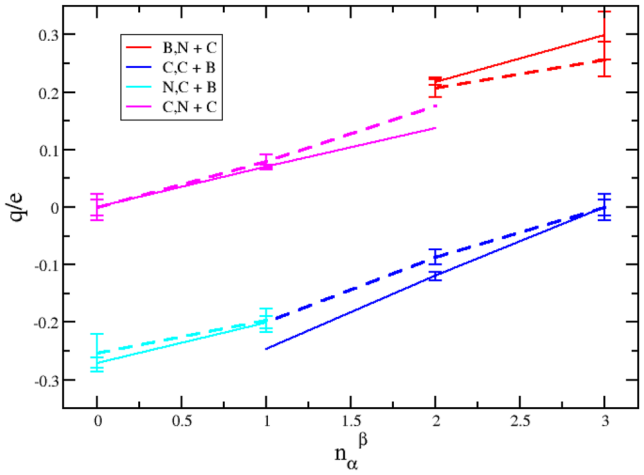


FIG. 3. Mean site charges shown as a function of the nearest-neighbor coordination environment, n_α^β. The solid and dashed lines show the results from the density-functional theory and fluctuating charge model calculations, respectively. The error bars for the DFT results reflect the differences in site charges across different stoichiometries as extracted from Fig. 2.

stoichiometry and any differences in ordering beyond the nearest-neighbor length-scale. It is clear that the FCM site charges are very close to those obtained from DFT, recalling that the FCM was *not* parameterized using the DFT values. As would be expected physically, the magnitude of the site charges becomes larger as a greater number of atoms with a larger electronegativity difference are added.

Table III shows the comparison of the nearest-neighbor atom separations for the BN, BC, NC, and CC pairs obtained from both the DFT and FCM for three example configurations: C_{24}, C_{54}, and C_{96}. The agreement in the bond lengths is close throughout, with the only significant differences observed for the BC distances (of ~7%). For comparison, the BN, NC, and CC bond lengths show differences of ~ 1%, ~ 2%, and ~ 1%, respectively.

TABLE III. Nearest-neighbor atom separations for the BN, BC, NC, and CC pairs obtained from both the DFT and FCM for three example configurations: C_{24}, C_{54}, and C_{96}.

	r_{BN}/Å		r_{BC}/Å		r_{NC}/Å		r_{CC}/Å	
C_n	DFT	FCM	DFT	FCM	DFT	FCM	DFT	FCM
24	1.433	1.447	1.441	1.535	1.441	1.415	1.439	1.425
54	1.432	1.446	1.435	1.538	1.436	1.412	1.441	1.424
96	1.432	1.442	1.438	1.540	1.438	1.405	1.436	1.425

B. Network properties

In this section, the FCM is applied to two-dimensional networks containing different amounts of disorder. Two dimensional networks are studied as they allow for a clear separation of site and topological disorder while retaining connections with recent experimental insights.[20,21] Three "classes" of disorder are introduced and studied. In the first, site disorder is introduced by switching B and N sites, thus introducing homopolar bonds (here, N–N and B–B) while retaining the ideal total mean coordination number of three. The degree of disorder can be characterized, at the simplest level, by a mean local coordination number, such as $\bar{n}_B^N$. In the second, vacancies are created in the ideal lattice, while in the third, topological disorder is introduced via bond-switching.

1. Site disorder

Figure 4 shows the effect of varying the cutoff parameter (Sec. II A 1) for an ideal hexagonal lattice with varying degrees of site disorder, characterized by $\bar{n}_B^N$. Considering first the ideal ordering hexagonal lattice (for which $\bar{n}_B^N = 3$), the effect of the length-scale over which the charge transfers directly is clear. The curve shows characteristic "jumps" in the charge on the central atom as a result of consecutive shells of neighboring atoms coming into range. Below the nearest-neighbor length-scale (denoted $r_{\alpha\beta}^{(1)}$), the atoms adopt charges driven by their bare respective electronegativities (i.e., there are no interactions with other atoms). For $r_{\alpha\beta}^{(1)} < r < r_{\alpha\beta}^{(2)}$ (i.e., between the first and second nearest-neighbor length-scales in the ideal hexagonal lattice, with $r_{\alpha\beta}^{(2)} = \sqrt{3} r_{\alpha\beta}^{(1)} \sim 2.4$Å), the nearest-neighbor interactions lead to greater charge separation. For $r_{\alpha\beta}^{(2)} < r < r_{\alpha\beta}^{(3)}$ (i.e., $r_{\alpha\beta}^{(3)} = 2 r_{\alpha\beta}^{(1)} \sim 2.8$Å), the second nearest-neighbors (which, in the ideal lattice, are like charges) lead to a reduction in the mean site charge.

Figure 4 highlights the effect of introducing site disorder. The disorder is introduced by randomly swapping pairs of B and N atoms in a fixed lattice, and the degree of site disorder is characterized by the mean B–N coordination number, $\bar{n}_B^N$, for which $1.5 \leq \bar{n}_B^N \leq 3$, where the lower and upper limits represent the maximum disorder and ideal order, respectively. For ~ 1.4Å < r_{cut} < 2.4Å (i.e., for atoms in the nearest-neighbor coordination shell), as the degree of disorder increases, the effect of the nearest-neighbor and

13 January 2026 13:55:09

© Author(s) 2026

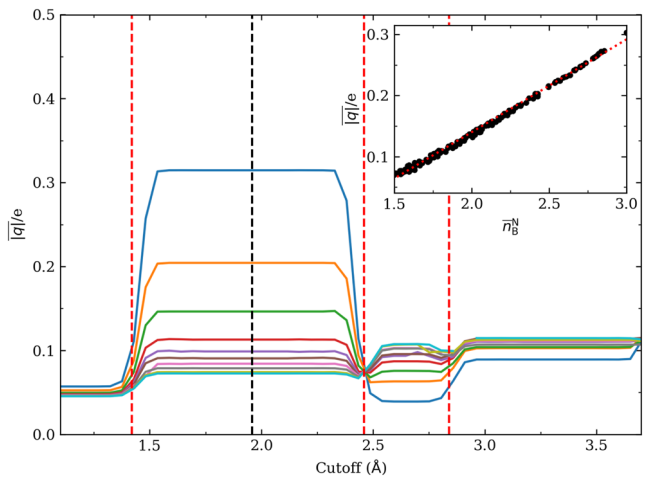


FIG. 4. (Main panel) Mean average site charge, $|\bar{q}|$, shown against the cutoff radius employed for the fluctuating charge model as described in the text. The site charges are shown for a range of site disorders on an ideal hexagonal lattice. Looking along the black vertical dashed line, corresponding to $r_{cut} = 1.96$Å, from bottom to top, $\bar{n}_B^N = 1.505, 1.507, 1.550, 1.598, 1.623, 1.707, 1.815, 2.060, 2.406, 3.000$. The inset shows the mean average site charge, $|\bar{q}|$, as a function of $\bar{n}_B^N$ for a fluctuating charge model cutoff of $r_{cut} = 1.96$Å (corresponding to the vertical black dashed line in the main panel). The red vertical dashed lines show the length-scales associated with successive coordination shells ($r_{\alpha\beta}^{(1)} = 1.4$Å, $r_{\alpha\beta}^{(2)} = \sqrt{3}r_{\alpha\beta}^{(1)} \sim 2.4$Å, $r_{\alpha\beta}^{(3)} = 2r_{\alpha\beta}^{(1)} \sim 2.8$Å).

next-nearest-neighbor interactions diminishes. The inset to the figure shows the mean site charge as a function of the mean coordination number with a cutoff intermediate between the first and second shells (i.e., including the interactions with the neighboring atoms only). The mean site charge shows a near-linear dependence on the local coordination number.

2. Defects

The analysis in Secs. III B 1 and III B 2 indicates how the site charge appears to be a strong function of the nearest-neighbor coordination environment. In this section, we consider the effect on the site charges of the introduction of specific defects. Three types of defects are considered: anti-site, vacancy, and Stone–Wales rotation. Figures 5(a)–5(c) show the examples of ideal hexagonal nets with a single defect. In panel (a), the B atom replaces an N (an anti-site defect); in panel (b), a single N atom is removed; and panel (c) shows a single Stone–Wales rotation. In all cases, the area of the hexagonal net is fixed at that for the energy minimum of the ideal net. The ideal defect is generated, and the atom positions are relaxed using a steepest descent algorithm. To highlight the effect of the site charges on the presence of the defects, Fig. 6 shows the evolution of the site charges as a function of distance away from the central defect site. Figure 6 shows the difference in charge on the site α, $|\Delta q_1| = |q - \bar{q}_{bulk}|$, with respect to the site charge at large distances from the defect (i.e., the bulk values in the ideal hexagonal lattice).

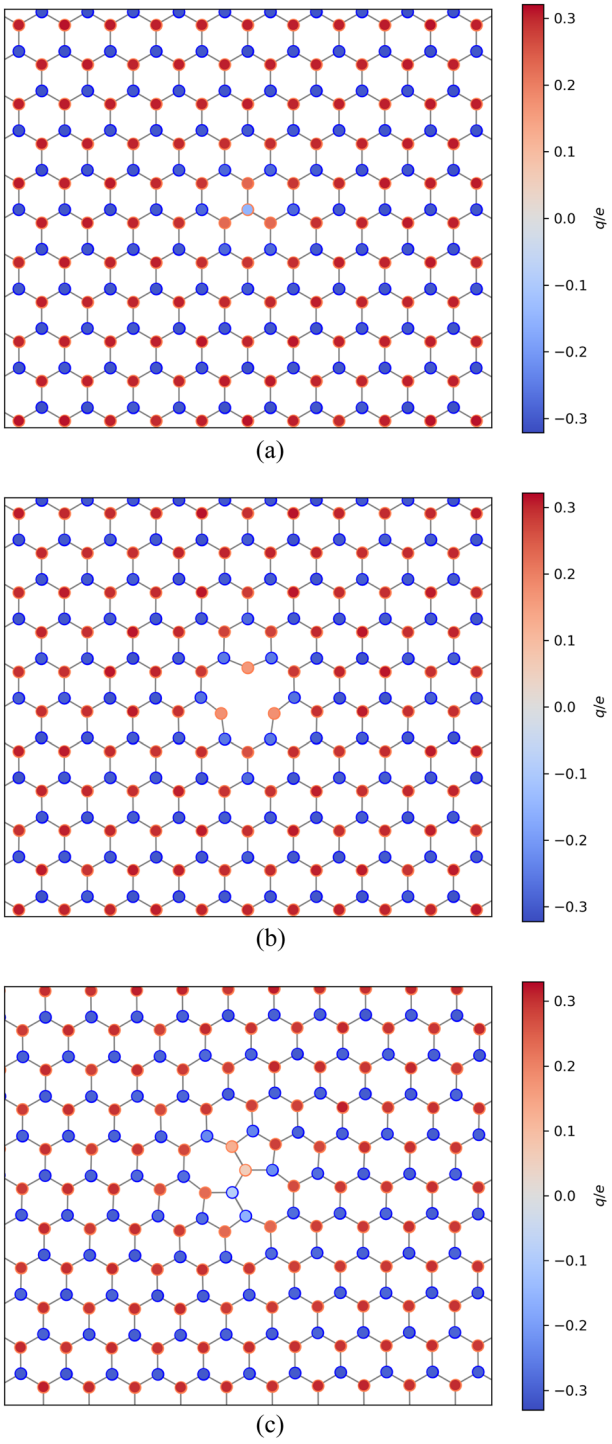


FIG. 5. Charge "heat maps" for three types of defects in an ideal hexagonal lattice. (a) A boron anti-site defect, (b) a nitrogen vacancy, and (c) a Stone–Wales defect. In all panels, the degree of red and blue corresponds to the size of the positive and negative charges, respectively. The circle circumferences are colored red or blue, which indicate B or N atoms, respectively.

13 January 2026 13:55:09

© Author(s) 2026

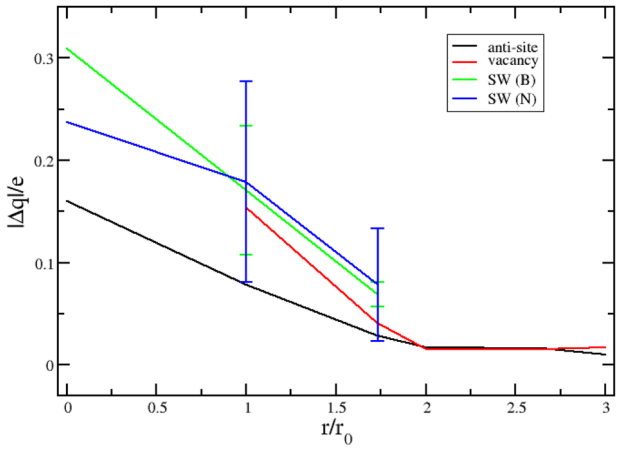


FIG. 6. Magnitudes of the mean site charge differences as a function of distance away from the defect for the B anti-site (black line), N vacancy (red line), and Stone–Wales defect with respect to the B and N atoms (green and blue lines, respectively). The distance is shown relative to the ideal B–N nearest-neighbor separation, r_0.

For the anti-site defect, the central B atom (which has replaced an N atom) adopts a small *negative* charge, reflecting the nearest-neighbor coordination environment of three B atoms (which adopt positive charges, but smaller than those observed in the bulk environments). The site charge "relaxes" to the bulk values by around $r/r_0 \sim 2$ (i.e., by the third coordination shell). For the N vacancy, the nearest-neighbor B atoms again adopt a smaller positive charge than for the bulk equivalents, with the charges again effectively reaching their bulk values by the third coordination shell with $r/r_0 \sim 2.6$. For the SW defect, we can consider the charges at a distance with respect to either the B or N atoms in the bond, which has been switched. Note that the presence of topological disorder almost certainly links to site disorder (unless the network retains only even-membered rings). In both cases, the charge decays to the bulk value by $r/r_0 \sim 3$.

3. Topological disorder

Figure 7(a) shows the examples of the distribution of site charges on the B and N atoms "colored" by the fraction of six-membered rings, p_6, with $p_6 = 0.35, 0.50, 0.65$, and 0.80. The distribution of charges appears near-independent of the degree of topological disorder. Note that a small fraction of atoms (of the order of 2%–4%) adopt the opposite charge to that suggested by their formal valence. The charge distributions highlighted in Fig. 7(a) can be further colored in terms of the local coordination environment. Figure 7(b) shows an example breakdown of the charges on the B and N atoms for a configuration with $p_6 = 0.5625$ and $\overline{n}_B^N = 2.19$ and highlights the clear separation of charge based on local environment as displayed in Fig. 3. It is clear that the strong dependence of the site charge on the *local* coordination environment identified in Secs. III B 1 and III B 2 in more idealized structures persists into more disordered states.

Figure 8 shows the three example amorphous configurations, which display different levels of disorder as quantified by the fraction of six-membered rings, $p_6 = 0.37$, 0.56, and 0.82, respectively.

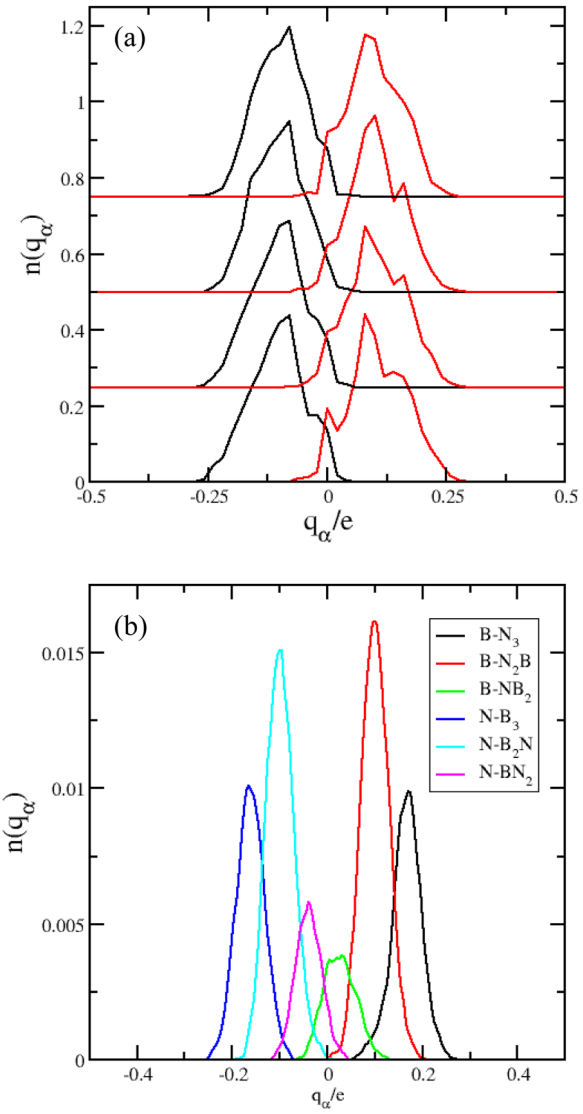


FIG. 7. (a) Distribution of site charges on the B (red lines) and N (black lines) atoms for disordered networks at four different levels of disorder as characterized by the fraction of six-membered rings, p_6, from bottom to top, $p_6 = 0.35, 0.50, 0.65, 0.80$. Successive distributions are offset along the abscissa for clarity. (b) An example charge distribution for the amorphous network with $p_6 = 0.5625$ broken down in terms of the local coordination environment as indicated in the legend.

Panel (a) shows the charge map for $p_6 = 0.56$, with the atom colors indicating the degree of positive or negative charge on those sites (i.e., highly positively charged B atoms appear more red, and highly negatively charged N atoms appear more blue). Panels (b), (c), and (d) show an alternative representation for $p_6 = 0.37$, 0.56, and 0.82, respectively, with the intensity of the color indicating a deviation of the absolute charge from the mean value, $\Delta q_2 = |q| - \overline{|q|}$. It appears visually that there are regions of relatively high and low charges, spread over groups of atoms, across all levels of topological disorder. To attempt to characterize these regions, partial structure factors

13 January 2026 13:55:09

© Author(s) 2026

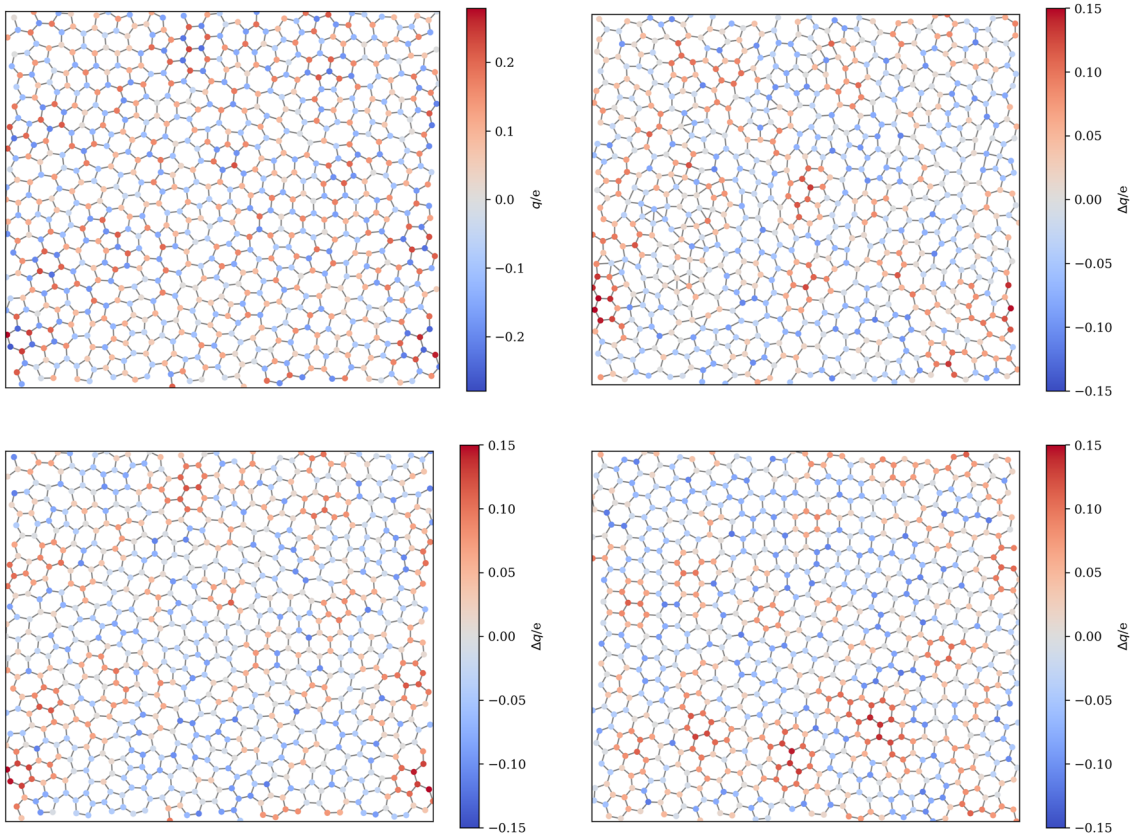


FIG. 8. Charge "heat maps" for three example configurations with a range of p_6 values. The top-left panel shows a configuration with $p_6 = 0.5628$, and the atoms are colored based on their partial charges, q, with the degree of red and blue indicating more positive and negative charges, respectively. The top-right, bottom-left, and bottom-right panels show the configurations with $p_6 = 0.3659$, 0.5628, and 0.8241. The atoms in these panels are colored based on their Δq values, $\Delta q = |q| - \overline{|q|}$, with the degree of red and blue indicating more positive and negative values, respectively.

are constructed, which are colored by the magnitude of the charges on each site. The distribution of charge magnitudes is divided into high and low charges using the distributions of the type shown in Fig. 7. The 20% of the atoms with the highest charge magnitudes are labeled "high" (h), and the remaining 80% are labeled "low" (l). Partial structure factors and radial distribution functions are extracted from these two groups of configurations, for example,

$$S^{Q}_{\alpha\beta}(k) = \langle A^{*}_{\alpha}(k).A_{\beta}(k)\rangle, \tag{19}$$

where $A_\alpha(k) = \frac{1}{\sqrt{N_\alpha}}\sum_i e^{i\mathbf{k}\mathbf{r}_i}$ is the Fourier component, and α and β refer to the high and low charge atoms, respectively. Figures 9(a) and 9(b) show $S^{Q}_{\alpha\beta}(k)$ for $\alpha\beta = hh, hl, ll$ calculated over two p_6 domains, $0.3 < p_6 < 0.4$ and $0.7 < p_6 < 0.8$. The effect of increasing the level of disorder (reducing p_6) is clear in all three partial structure factors. The functions at high p_6 show significantly sharper peaks, and some clearly coalesce to form single peaks at low p_6. Similar changes have been observed in two dimensional networks of amorphous carbon.[42] To help understand the distribution of charge in the networks, Figs. 9(a) and 9(b) show the analogous partial structure factors obtained by assigning the "h" and "l" labels at random (rather than by charge magnitude). As a result, the three partial structure factors become equivalent and differ only in the fluctuations due to the small number of sites labeled "h." The most striking difference between the different functions is in $S^{Q}_{hh}(k)$, which shows significant intensity at low k, indicative of the formation of nanodomains of the sort shown in Fig. 8. Analogous partial radial distribution functions can also be defined. Figures 9(c) and 9(d) show $g^{Q}_{\alpha\beta}(r)$ for $\alpha\beta = hh, hl, ll$ [the analogs of the structure factors shown in panels (a) and (b)] again colored in terms of site charge and at random. The greater ordering at high p_6 is again clear in terms of sharper peaks and oscillations persisting to significantly higher r. More significantly, here the formation of the charge domains is evident, most clearly in $g^{Q}_{hh}(r)$, which shows significantly greater intensity in both the first and second peaks.

To focus a little more on these domains, Fig. 10 shows $S^{Q}_{hh}(k)$ calculated over six different ranges of p_6 using the labeling by charge [panel (a)] and at random [panel (b)]. The greater ordering as p_6 increases is again clear across both sets of functions. For the charge-labeled functions [panel (a)], the low k intensity shows a small increase as p_6 increases. An approximate measure of the spatial extent of the charge domains can be extracted by relating the low

13 January 2026 13:55:09

© Author(s) 2026

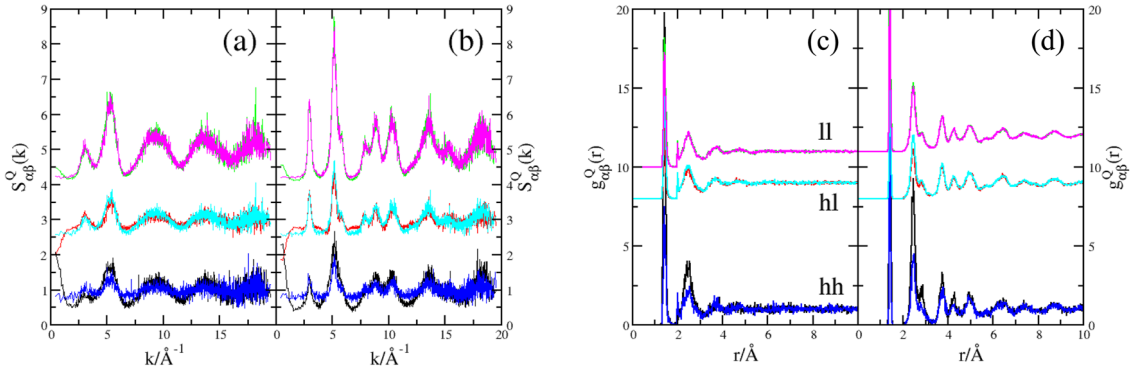


FIG. 9. Panels (a) and (b) show the structure factors, $S^{Q}_{\alpha\beta}(k)$, colored in terms of high and low charges (labeled "h" and "l," respectively, as discussed in the main text). The black, red, and green lines show $S^{Q}_{hh}(k)$, $S^{Q}_{hl}(k)$, and $S^{Q}_{ll}(k)$, respectively. The blue, cyan, and magenta lines show the equivalent functions but with the atoms labeled at random as described in the text. Successive functions are offset along the abscissa axis for clarity. Panels (c) and (d) show the corresponding partial radial distribution functions, which employ the same color scheme as panels (a) and (b).

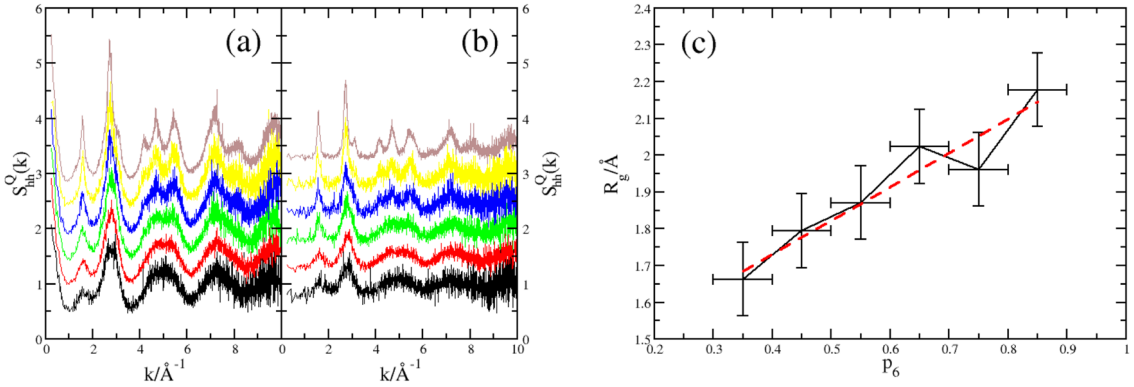


FIG. 10. Panels (a) and (b) show the structure factor, $S^{Q}_{hh}(k)$, colored in terms of high charge as described in the main text. In both panels, successive functions are determined at different levels of disorder as characterized by the fraction of six-membered rings, p_6. Successive functions are offset along the abscissa axis for clarity. From bottom to top, $0.3 < p_6 < 0.4$, $0.4 < p_6 < 0.5$, $0.5 < p_6 < 0.6$, $0.6 < p_6 < 0.7$, $0.7 < p_6 < 0.8$, and $0.8 < p_6 < 0.9$. Panel (a) shows the effect of coloring the sites by high charge, while panel (b) shows the analogous functions generated by selecting the same fraction of sites at random. Panel (c) shows the effective radius of the domain size as a function of the fraction of six-membered rings determined from the low $-k$ gradient as described in the text.

k gradient to an effective radius of gyration (i.e., by plotting the low k regime against k^2 and extracting the gradient). Figure 10(c) shows the change in domain radius as a function of p_6, highlighting the weak increase in domain size as the level of disorder is reduced.

IV. DISCUSSION

The results presented here show how the charge held by each atom can fluctuate as a function of the atom's environment. In the present work, a relatively simple network system (BN) has been chosen. The environment here is effectively synonymous with network disorder, which is present here in the form of both site and topological disorder. It is clear that the charge separation, resulting from the difference in electronegativities of the two atomic species, is both significant and highly dependent on the local coordination environment. While using fixed (mean field) values for the charges is possible, it is likely to lead to significant errors, in particular where there are high levels of disorder (either pure site or topological/site disorder). These errors are likely more significant in systems such as BN, in which the charge *magnitudes* are relatively small and, hence, the effect of the (local) environment is potentially more important.

Future work will focus on a number of key extensions. The formation of large pores in these systems is of general interest, as these thin films can act as filters (for example, in desalination). The implication of the present work is that the charge present on atoms sitting on the pores may be significantly different from those in the bulk, with clear implications for properties such as ion transport. Adding a third atom type (for example, carbon to form BCN composites) introduces additional significant complexity with the potential formation of superlattices in which the carbon atoms effectively remain demixed, forming domains. The potential changes in charge indicate that the addition of intercalated atoms or molecules may alter the charge distribution in a significant manner. In

13 January 2026 13:55:09

© Author(s) 2026

addition, it is likely that similar charge separation effects will be observed in three-dimensional networks and in BN nanotubes and fullerenes.

V. CONCLUSIONS

In this paper, a fluctuating charge model (FCM) has been developed to study a key network material, BN. In the FCM, the charge on each atomic site is controlled by the atom's electronegativity plus terms that are linked to the interactions with the surrounding environment. As a result, charges can deviate from their typical (mean field) values. The results presented here show how the introduction of simple defects, both in terms of site and topological disorder, leads to significant changes in site charge. In addition, in highly disordered (amorphous) systems, the network is arranged into regions of relatively high and low charges, with the size of the charge domains a weak function of the degree of topological disorder. The distribution in charge is likely most significant in systems such as BN in which the typical mean charge magnitudes are relatively small.

ACKNOWLEDGMENTS

This paper conforms to the RCUK data management requirements.

AUTHOR DECLARATIONS

Conflict of Interest

The authors have no conflicts to disclose.

Author Contributions

Angus Heafield: Conceptualization (equal); Data curation (equal); Formal analysis (equal); Investigation (equal); Methodology (equal); Project administration (equal); Software (equal); Supervision (equal); Validation (equal); Visualization (equal); Writing – original draft (equal); Writing – review & editing (equal). **Mark Wilson**: Conceptualization (equal); Data curation (equal); Formal analysis (equal); Investigation (equal); Methodology (equal); Project administration (equal); Supervision (equal); Validation (equal); Visualization (equal); Writing – original draft (equal); Writing – review & editing (equal).

DATA AVAILABILITY

The data that support the findings of this study are available from the corresponding author upon reasonable request.

REFERENCES

[1] L. Liu, Y. Liu, Y. Qi, M. Song, L. Jiang, G. Fu, and J. Li, Sep. Purif. Technol. **251**, 117409 (2020).
[2] X. Davoy, A. Gellé, J. C. Lebreton, H. Tabuteau, A. Soldera, A. Szymczyk, and A. Ghoufi, ACS Omega **3**, 6305 (2018).
[3] Y. Li, J. Guo, W. Zheng, and F. Huang, Appl. Phys. Lett. **117**, 023504 (2020).
[4] J. Reif, T. N. Narayanan, D. P. Hashim, N. Sakhavand, R. Shahsavari, R. Vajtai, and P. M. Ajayan, Adv. Funct. Mater. **23**, 5624 (2013).
[5] A. E. Naclerio, P. R. Kidambi, A. E. Naclerio, and P. R. Kidambi, Adv. Mater. **35**, 2207374 (2023).
[6] C. B. Samantaray and R. N. Singh, Int. Mater. Rev. **50**, 313 (2005).
[7] T. Liu, Y. Li, J. He, K. Zhang, Y. Hu, X. Chen, C. Wang, X. Huang, L. Kong, and J. Liu, J. Mater. Sci. **54**, 5366 (2019).
[8] M. J. Molaei, M. Younas, and M. Rezakazemi, ACS Appl. Electron. Mater. **3**, 5165 (2021).
[9] T. Xu, K. Zhang, Q. Cai, N. Wang, L. Wu, Q. He, H. Wang, Y. Zhang, Y. Xie, Y. Yao, and Y. Chen, Chem. Eng. J. **431**, 134118 (2022).
[10] D. V. Shtansky, K. L. Firestein, and D. V. Golberg, Nanoscale **10**, 17477 (2018).
[11] S. M. Sattari-Esfahlan, S. Mirzaei, M. J. Josline, J. Y. Moon, S. H. Hyun, H. Jang, and J. H. Lee, Nano Convergence **12**, 22 (2025).
[12] C. Elias, P. Valvin, T. Pelini, A. Summerfield, C. J. Mellor, T. S. Cheng, L. Eaves, C. T. Foxon, P. H. Beton, S. V. Novikov, B. Gil, and G. Cassabois, Nat. Commun. **10**, 2639 (2019).
[13] K. S. Novoselov, A. K. Geim, S. V. Morozov, D. Jiang, Y. Zhang, S. V. Dubonos, I. V. Grigorieva, and A. A. Firsov, Science **306**, 666 (2004).
[14] A. Heafield and M. Wilson, J. Phys.: Condens. Matter **37**, 045101 (2024).
[15] M. Zahoor, P. M. Ismail, S. Khan, M. Bououdina, M. Haneef, J. Akbar, E. Ahmed, C. Zeng, and S. Ali, "Hexagonal boron nitride for water desalination and wastewater treatment," in *Hexagonal Boron Nitride: Synthesis, Properties, and Applications* (Elsevier, 2024), pp. 457–482, ISBN: 9780443188435.
[16] L. Zhang and X. Wang, Nanomaterials **6**, 111 (2016).
[17] A. Zobelli, C. P. Ewels, A. Gloter, and G. Seifert, Phys. Rev. B **75**, 094104 (2007).
[18] N. Alem, R. Erni, C. Kisielowski, M. D. Rossell, P. Hartel, B. Jiang, W. Gannett, and A. Zettl, Phys. Status Solidi RRL **5**, 295 (2011).
[19] L. Chkhartishvili, S. Dekanosidze, N. Maisuradze, M. Beridze, and R. Esiava, East.-Eur. J. Enterp. Technol. **3**, 50 (2015).
[20] A. Govind Rajan, M. S. Strano, and D. Blankschtein, J. Phys. Chem. Lett. **9**, 1584 (2018).
[21] L. Susana, A. Gloter, M. Tencé, and A. Zobelli, ACS Nano **18**, 7424 (2024).
[22] M. C. C. Ribeiro and L. C. J. Almeida, J. Chem. Phys. **110**, 11445 (1999).
[23] M. C. C. Ribeiro and L. C. J. Almeida, J. Chem. Phys. **113**, 4722 (2000).
[24] M. C. Wilding, M. Wilson, M. C. C. Ribeiro, C. J. Benmore, J. K. R. Weber, O. L. G. Alderman, A. Tamalonis, and J. B. Parise, Phys. Chem. Chem. Phys. **19**, 21625 (2017).
[25] M. Wilson, M. C. C. Ribeiro, M. C. Wilding, C. Benmore, J. K. R. Weber, O. Alderman, A. Tamalonis, and J. B. Parise, J. Phys. Chem. A **122**, 1071 (2018).
[26] M. C. Wilding, F. Demmel, and M. Wilson, J. Phys. Chem. A **129**, 1890 (2025).
[27] A. K. Rappe and W. A. Goddard III, J. Phys. Chem. **95**, 3358 (1991).
[28] S. W. Rick, S. J. Stuart, and B. J. Berne, J. Chem. Phys. **101**, 6141 (1994).
[29] R. S. Mulliken, J. Chem. Phys. **2**, 782 (1934).
[30] R. G. Parr and R. G. Pearson, J. Am. Chem. Soc. **105**, 7512 (1983).
[31] R. Car and M. Parrinello, Phys. Rev. Lett. **55**, 2471 (1985).
[32] S. Nosé, J. Chem. Phys. **81**, 511 (1984).
[33] W. G. Hoover, Phys. Rev. A **31**, 1695 (1985).
[34] D. Ormrod Morley and M. Wilson, J. Phys.: Condens. Matter **30**, 50LT02 (2018).
[35] D. Ormrod Morley, A. Thorneywork, R. Dullens, and M. Wilson, Phys. Rev. E **101**, 042309 (2020).
[36] A. Gervois, J. P. Troadec, and J. Lemaitre, J. Phys. A: Math. Gen. **25**, 6169 (1992).
[37] J. Tersoff, Phys. Rev. Lett. **61**, 2879 (1988).
[38] C. Sevik, A. Kınacı, J. B. Haskins, and T. Çağın, Phys. Rev. B **84**, 085409 (2011).
[39] A. Kınacı, J. B. Haskins, C. Sevik, and T. Çağın, Phys. Rev. B **86**, 115410 (2012).
[40] E. M. O'Sullivan, N. Grobert, and M. Swart, J. Phys. Chem. C **129**, 638 (2024).
[41] M. Swart, P. T. V. Duijnen, and J. G. Snijders, J. Comput. Chem. **22**, 79 (2001).
[42] A. Kumar, M. Wilson, and M. F. Thorpe, J. Phys.: Condens. Matter **24**, 485003 (2012).

13 January 2026 13:55:09

© Author(s) 2026

8 | Borocarbonitrides

Contents

8.1 Introduction to Borocarbonitrides 132

8.2 C defects in h-BN 138

8.3 h-BN and Graphene Domains 142

8.3.1 Graphene-h-BN super-ordered arrays 142

8.3.2 Generating irregular domains 143

8.4 Mixed BCN rings 146

8.5 Amorphous BCN 153

8.6 Summary 159

This chapter includes a brief introduction to borocarbonitride (BCN) materials before investigating a variety of the potential topologically ordered structures of these materials as well as C defects in h-BN using the FCM introduced in chapter 7. The potential structure of a variety of amorphous BCN materials containing both topological and site disorder are also investigated. The work in this chapter is being adapted for future journal publication.

8.1 Introduction to Borocarbonitrides

Owing to the similarities between carbon and boron nitride materials, such as only a 2% difference in their lattice constants [324], much work has been undertaken investigating materials containing all three types of atom, generally named borocarbonitrides, $B_xC_yN_z$. It has been shown that due to the similarities in the bonding in C and BN materials that it is possible

for these borocarbonitrides to be stable in a wide range of structures and stoichiometries [325, 326].

As the dominant form of sp^3-bonded carbon and boron nitride, the cubic structure is the basis for the most common structures of three dimensional BCN materials. Whilst a variety of methods have been attempted for the synthesis of crystalline BCN materials, the most consistently achieved crystalline products have been produced through the use of the high temperature and high pressure, HTHP method. The first reported synthesis of a crystalline hybrid of diamond and c-BN was in 1981 when Badzian compressed graphitic $B_xC_yN_z$ under 14 GPa at 3300K [327]. Since then a wide range of conditions have been employed to achieve a wide range of stoichiometries [326, 328]. While the most studied compositions contain equal amounts of boron and nitrogen, some studies also discuss the synthesis of materials with different amounts of each element [329–331]. The structure of these BCN structures has been analysed through the use of XRD to verify their cubic nature and through XPS to show that B, C and N are all bonded to each other, however, the nature of this site ordering is still unknown. Little work has been performed investigating the applications of cubic BCN structures. However, due to its excellent thermal stability exceeding diamond and hardness surpassing cubic boron nitride [326], it is believed cubic BCN compounds may find applications in high-speed cutting and milling.

While some work has been carried out on sp^3-bonded BCN structures, the majority of studies focus on the range of potential sp^2-bonded BCN structures. These structures can be split into two main categories: those with chemical bonds between C and B/N and those without. Due to the layered nature of sp^2-bonded structures of both carbon and boron nitride, it is possible for structures to be formed containing all three types of atom

without formal chemical bonds by stacking these layers. These structures are most commonly created through the mechanical stacking of layers which have been exfoliated from the bulk layered material. This stacking process can be carried out in a range of ways, which can be divided into two main categories: wet and dry transfer techniques. Wet transfer techniques involve flakes being exfoliated onto sacrificial polymer layers which can then be dissolved after the flakes are aligned. Dry transfer techniques utilise viscoelastic or adhesive polymer layers to pick up the exfoliated flakes [332]. One of the reasons these materials are of interest is the weak interlayer van der Waals forces allow for arbitrary rotational alignment between the layers, which due to the close match in lattice constants results in moiré superlattices with exotic properties such as superconductivity [333, 334].

In-plane BCN heterostructures are those containing all three types of atom within a single sp^2-bonded layer, reminiscent of graphene or monolayer BN. As such these materials contain bonds between C and B/N similar to the cubic BCN structures described above. However, due to the two dimensional nature of these structures it is possible to control and observe the ordering of the elements on the underlying hexagonal lattice. The structure of these BCN nano-sheets can be grouped into two categories based on their site ordering. These groups are those containing domains of graphene and h-BN, termed simple structures and those containing mixed BCN rings, termed complex structures. The synthetic precursors and conditions are highly influential to which category the resulting structure falls into. Utilizing pyrolysis or the molten salt method, a range of precursors can be heated to temperatures from 600 to 1250°C. These precursors then breakdown to form more reactive species such as B_2O_3 and NH_3 which then react with a source of C such as activated charcoal self-assembling into BCN nano-sheets

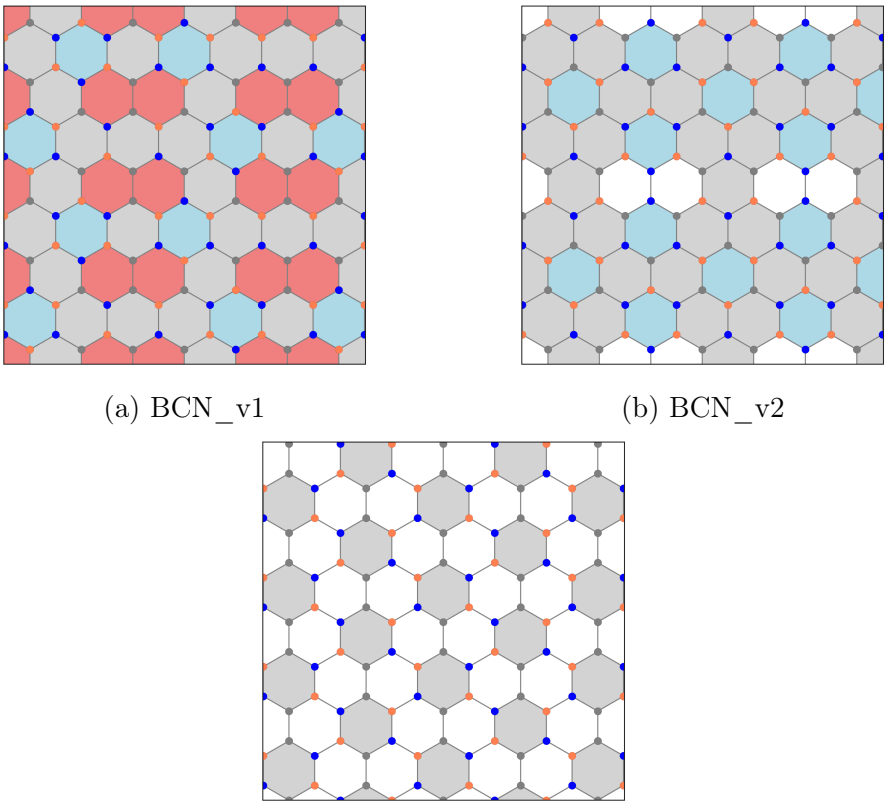
[335]. This approach offers little control over the resulting site ordering of the system and so likely forms structures containing high levels of mixed BCN rings. Deposition approaches such as CVD and PVD offer more control over how the nano-sheets are grown. Precursors containing B, C and N can all be introduced simultaneously to form nano-sheets containing all three elements mixed together, however it is also possible for the different species to be introduced sequentially allowing for separated domains to be grown. Examples of this domain formation include the growth of self-assembling graphene-h-BN super-ordered arrays [336], domains of C grown inside holes left by temperature-triggered etching of h-BN [337] and domains of controlled shape grown by patterning with photoresist [338]. These domains have been grown up to centimetre-scale [336] allowing for easy visualisation, however in the case of mixed ring systems this visualisation is not possible and little is known about their ordering.

Theoretical studies have been carried out investigating the stability of various potential configurations for the ordering in a BCN monolayer. The most commonly studied structures are those with composition with equal parts B, C and N. The initial simulations on these structures were carried out by Beniwal *et al.* following their work synthesising a BCN monolayer using bis-BN-cyclohexane, $B_2N_2C_2H_{12}$ as a precursor [339]. Therefore, their proposed structures reflected this and were built using $B_2C_2N_2$ rings as a building block. Three main structures were proposed, as shown in figure 8.1. Of these three structures, BCN_v1 was shown to agree best with the experimental analysis whilst BCN_v3 was shown to be the most stable structure. These three structures have since been the subject of multiple subsequent papers investigating their mechanical and thermal properties [340–343].

Extensive work has also been performed investigating the wide range of struc-

tures and synthesis methods for BCN nanotubes. Due to the similarity in the bonding between nanotubes and hexagonal BCN materials, both contain layers of sp^2-bonded atoms, there are many similarities in the ways B, C and N atoms are structured throughout the materials. This has lead to the synthesis of BCN nanotubes with mixed B, C and N rings [344], co-axial C and BN nanotubes [345] and C nanotubes with flakes of BN attached [346]. The range of structures for these nanotubes has found potential applications taking advantage of many of their varied properties. These applications include as energy dissipating devices [346], nanocables [345] and supercapcitors [347].

Amorphous BCN has been synthesised through a range of methods including solid state reactions [348, 349], physical vapour depositions [350–356] and ball milling [357, 358]. It has been shown to have excellent mechanical properties, which, along with other properties such as band-gap can be controlled through the ratios of boron, carbon and nitrogen as well as the conditions used for synthesis [354, 355]. However, little in known about the structure of these materials. Many experimental papers identify peaks in XPS, Raman and UV spectra attributable to a wide range of bond types and environments including sp^2 and sp^3 bonds, but very few theoretical papers modelling these structures have been published. Duranduru has modelled amorphous BCN with compositions of BC_2N [359] and BC_4N [360, 361] whilst Ivashchenko *et al.* modelled samples with compositions of the form BC_xN_{1-x} for $x = 0, 0.25, 0.5, 0.75$ and 1 [362]. In both cases, *ab initio* molecular dynamics methods were employed. In both works, a mixture of sp^2 and sp^3 bonding is present. In Durandurdu's initial works the configurations show clear layers with some bonds between them whilst in the work by Ivashchenko *et al.* no clear layers are present. Since then Durandurdu has investigated



(a) BCN_v1 (b) BCN_v2

(c) BCN_v3

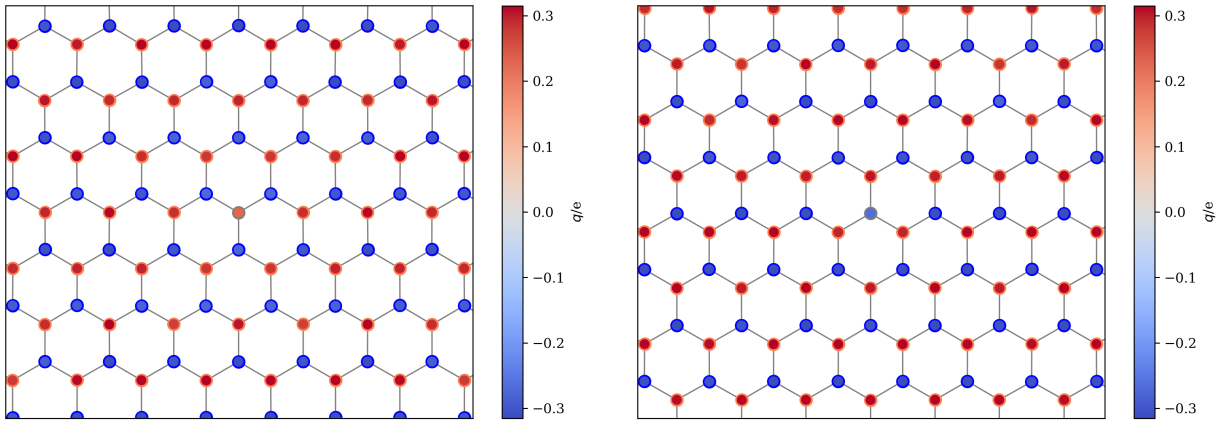
Figure 8.1: Three potential BCN monolayer structures. Atoms are coloured according to their type: pink - boron, grey - carbon and blue - nitrogen. Rings are coloured according to their makeup: grey - $B_2C_2N_2$ with no homo-atomic bonds, white - $B_2C_2N_2$ with homo-atomic bonds, blue - $B_3N_3/B_3C_3/C_3N_3$ and red - other.

a potential pressure-induced phase transformation of the amorphous BC_4N structure which leads to a significant increase in the percentage of sp^3 bonds, with the average coordination number moving from ~ 3.0 for all types of atom to $3.54 - 3.83$ depending the type of atom.

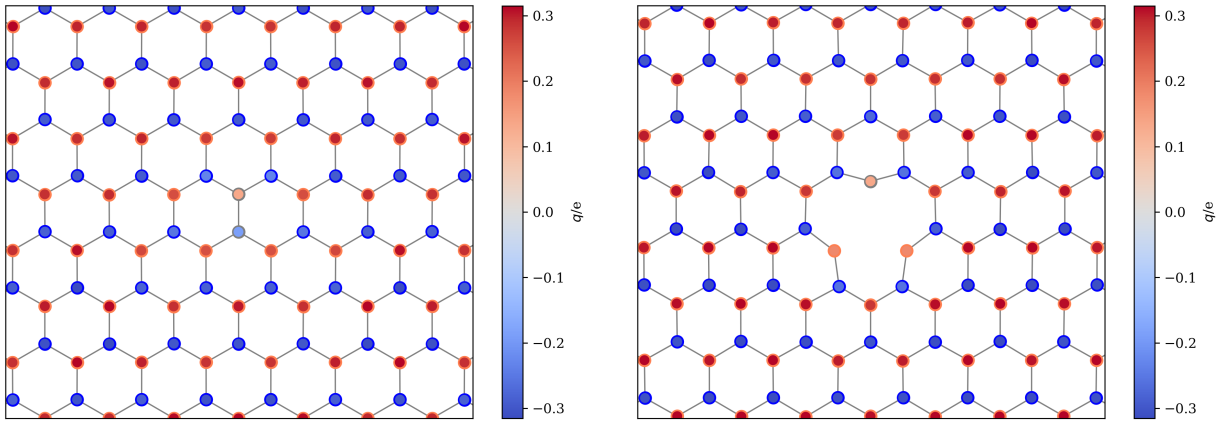
8.2 C defects in h-BN

As discussed in section 2.2, some of the most commonly studied extrinsic defects in h-BN are those containing C substitutions. Whilst work has been undertaken investigating individual substitutions of B and N for C, C_B and C_N [86, 89, 98], a variety of other defects forms which combine multiple types of defects have also been the investigated. These defects have been of particular interest due to their potential as sites for single-photon emission [96, 97]. While this activity would require more complex methods to accurately model, defects also have significant effects on a variety of other properties which cannot be easily modelled with more complex techniques. As such, finding ways to model these defects and their site charges using simpler methods is important to understanding the effects of these defects on the properties of h-BN.

Figure 8.2 shows charge "heat maps" for a variety of well-studied C defects in h-BN obtained using the application of the fluctuating charge model, as discussed in section 3.4 and as applied to intrinsic h-BN defects in chapter 7. Panels (a) and (b) shows the simple substitution defects in which C atoms replaces a B atom, C_B, a N atom, C_N. From these it can once again be seen that the local environment has a significant effect on an atom's charge. In the C_B defect, the C atom takes on a positive charge of 0.227e whilst in the C_N defect the C takes on a negative charge of -0.267e. While these values are still less than the overall average charge values for the network, they are significantly closer values than those observed in the intrinsic substitutional or antisite defect studied in chapter 7, $q(N_B)$ = 0.087e and $q(B_N)$ = -0.149e. Panel (c) shows a dual substitution defect in which a pair of B and N are replaced by two C, C_BC_N. The inclusion of an additional C results in the

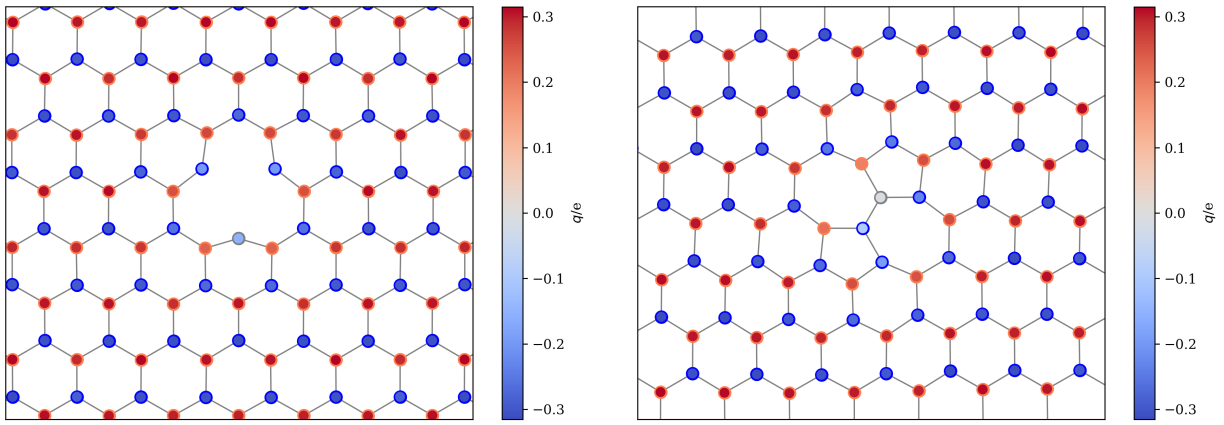


(a) C_B (b) C_N

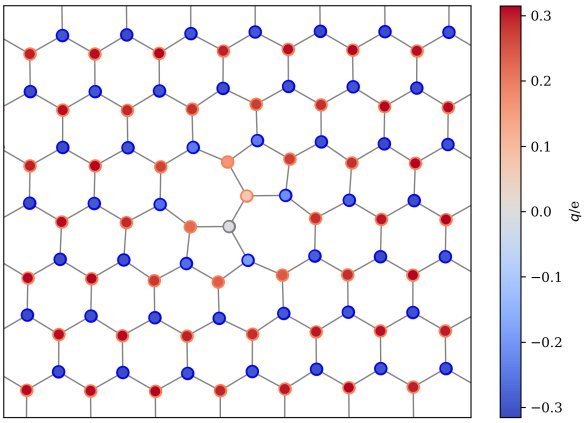


(c) C_BC_N (d) V_NC_B

Figure 8.2: Charge "heat maps" for C defects in h-BN. Captions describe defect types: C_α is a substitution of atom α with C, V_α is vacancy of atom α and SW is a Stone-Wales defect. Atoms are coloured by their charges: red - more positive and blue - more negative. The edges of atoms are coloured according to their type: pink - boron, grey - carbon, blue - nitrogen.



(e) V_BC_N (f) SWC_B



(g) SWC_N

Figure 8.2: Charge "heat map" for C defects in h-BN (cont.).

reduction of the charge on both atoms compared to the single substitution defect, with the C−N_2C having a charge of 0.134e and the C−B_2C having a charge of -0.188e. This trend is expected as increasing the amount of C-C bonds reduces the polarity of the bonds resulting in the charge being less localised.

Panels (d)-(g) show more complex defects in which the substitution of a B or N for a C is combined with another type of defect. Panels (d) and (e) show defects in which the substitution defects is combined with a neighbouring vacancy. As in the case of the V_N and V_B defects studied in chapter 7, the vacancy results in a drop in the magnitude of charge of the surrounding atoms. In the case of the carbons, the site charges were 0.135e and -0.154e for the V_NC_B and the V_BC_N defects respectively. Interestingly, the introduction of a substitutional defect lessens the reduction of the charge for the other atoms neighbouring the vacancy. Without a C substitution, the B atoms neighbouring a N vacancy have a charge of ∼0.17e but with a C substitution they have a charge of ∼0.18e. This can also be seen in a reduced capacity for N atoms neighbouring a B vacancy which have charges of ~ -0.194e and -0.197e, without and with C substitution. The structure of these defects can be compared to structures calculated for these defects using simulations based on density functional theory (DFT) [96]. Whilst we also predict that the N-N distance increases in the V_BC_N defect, for the V_NC_B defect, DFT calculations predict a reduction in the B-B distance. This reduction is believed to be caused by an additional bonding interaction between B atoms surrounding a vacancy which is not accounted for in the potential model for this work.

Panels (f) and (g) show variation on the Stone-Wales defect in which one of the atoms in the rotated bond have been substituted with a C, SWC_B and SWC_N. These defects have been shown to be more stable than the standard

Stone-Wales defect in h-BN by replacing the B-B or N-N bond formed on rotation with a B-C or C-N bond [363]. As such disordered BCN structures may contain a higher concentration of these defects than the standard BN Stone-Wales defect. Using the FCM, this stabilisation can be seen by looking at the charge on the B bonded to the C in the SWC_B defect, panel (f), or on the N bonded to C in the SWC_N defect, panel (g). In both cases, there is a greater magnitude of charge than in the equivalent atom of the standard Stone-Wales defect. The B in the SWC_B defect goes from 0.128e to 0.192e and the N in the SWC_N defect goes from -0.158e to -0.188e. These charges result in greater electrostatic attraction stabilising the defect.

8.3 h-BN and Graphene Domains

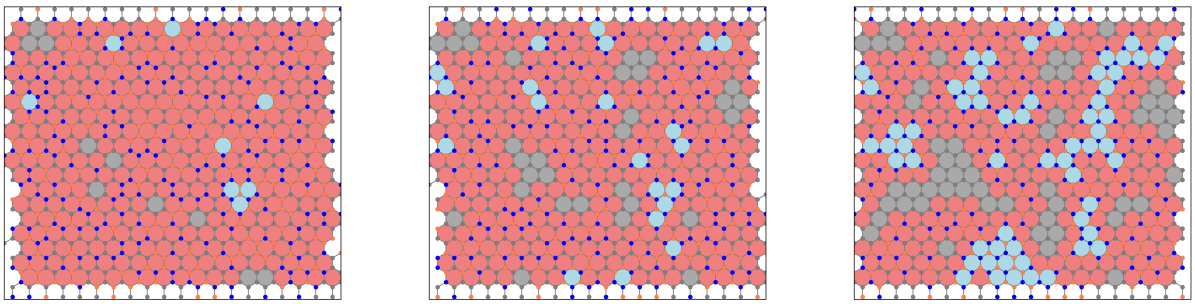
8.3.1 Graphene-h-BN super-ordered arrays

Graphene-h-BN super-ordered arrays are examples of two-dimensional hexagonal BCN structures which contain ordered hexagonal domains of graphene and h-BN. These structures have been grown experimentally using CVD on a liquid Cu surface with controllable domain size. First, graphene arrays are grown and then surrounded by h-BN [336]. The ordered nature of the final arrays is believed to be caused by the electrostatic force between the charges on the terminating regions of h-BN. Due to the edge atoms being either B or N, these regions have a positive or negative charge which guides the motion of each of the units into a regular arrangement. Theoretical work has also been carried out on these systems including using DFT to investigate the electronic structure and potential as catalysts for these materials [364]. Recall that chapter 7 contained the comparison of FCM results for a range of these graphene-h-BN super-ordered arrays with these DFT results.

8.3.2 Generating irregular domains

Whilst BCN domains of regular size and ordering may be promising candidates for integrated electronics or catalysis, it is unlikely that domains formed by less precise synthesis methods will be reminiscent of this. As such developing methods to generate and model these irregular domains will be important for understanding the properties of these materials. By expanding on the methods introduced in section 5.4 and employed in chapter 7, an atom label swapping Monte Carlo (LS-MC) approach was developed to order atoms on a network to result in the formation of carbon and boron nitride domains. As discussed in section 4.1, Monte Carlo methods are stochastic in nature and therefore do not generate regular domains. Instead the domains are grown by initially randomly assigning atomic labels in the desired ratios. Next, Monte Carlo moves are generated by randomly swapping a pair of atomic labels. The swap is then accepted if the move results in an increase in the number of B-N bonds. This process lead to C atoms gradually being moved next to each other resulting in the growth of a domain, as seen in figure 8.3.

Figure 8.4 shows the change in partial coordination numbers over 10000 Monte Carlo steps for a BC_2N system containing 800 atoms. From this the formation of domains of C and BN can clearly be seen with $\overline{n}_{\mathrm{C}}^{\mathrm{C}}$ increasing whilst the values of $\overline{n}_{\mathrm{C}}^{\mathrm{B}}$ and $\overline{n}_{\mathrm{C}}^{\mathrm{N}}$ decrease indicating C atoms are becoming increasingly bonded with other C atoms. The formation of BN domains can also be seen through the similar behaviour of the $\overline{n}_{\mathrm{B}}^{\mathrm{N}}/\overline{n}_{\mathrm{N}}^{\mathrm{B}}$ and the $\overline{n}_{\mathrm{B}}^{\mathrm{C}}/\overline{n}_{\mathrm{N}}^{\mathrm{C}}$ values. However, due to the presence of multiple atom types in the BN domains, similar to entirely BN nanosheets, site disorder is still present in the final domains. This is a result of the two possible entirely site ordered con-



(a) 0 (b) 1000 (c) 10000

Figure 8.3: Example hexagonal BC_2N configurations of 800 atoms from the LS-MC approach showing growing domains of C and BN. Captions indicate the number of MC steps. Rings are coloured by their makeup: blue - B_xN_{6-x}, grey - C_6 and red - other. Atoms are coloured by their type: pink - B, grey - C and blue - N.

figurations, which grow simultaneously, resulting in boundaries which must contain homo-atomic bonds, as shown by the non-zero values of $\overline{n}^{\mathrm{B}}_{\mathrm{B}}$ and $\overline{n}^{\mathrm{N}}_{\mathrm{N}}$.

Figure 8.5 shows how the charges calculated for LS-MC configurations using the FCM vary with domains size. As shown in figure 8.4, there is a clear correlation between the partial coordination numbers and the size of domains, as such the average partial coordination number of C surrounding C, $\overline{n}^{\mathrm{C}}_{\mathrm{C}}$, was used to quantify domain size. It can be seen in figure 8.5 that as the domains grow there are trends in the charge distributions, more specifically the average charge and the width of the distributions. On increasing domain size, the average magnitude of charge increases for both B and N whilst that of C stays at approximately $\overline{q}/\mathrm{e}{=}0$. This is caused by the increase in the number of more polar BN bonds formed in favour of less polar BC or CN bonds. The average charge on C roughly stays constant as a roughly equal amount of BC bonds, where C is negatively charged, and CN bonds, where C is positively charged, are being replaced with CC bonds where C is neutral as seen in the coincident $n^{\mathrm{B}}_{\mathrm{C}}$ and $n^{\mathrm{N}}_{\mathrm{C}}$ lines in figure 8.4. It can also be seen

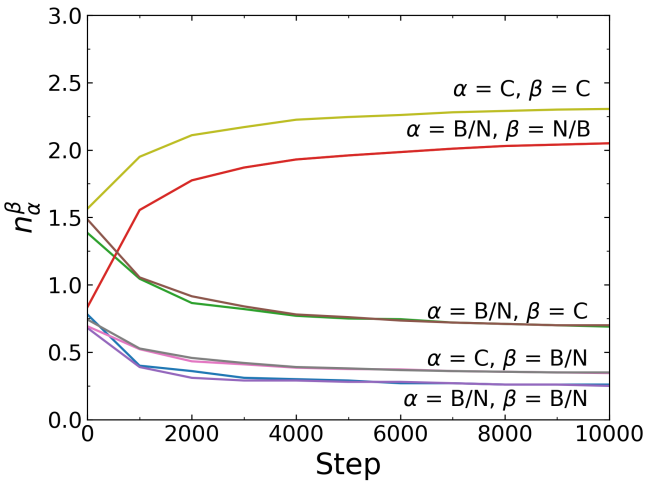


Figure 8.4: Change in average partial coordination numbers over the course of 10000 Monte Carlo steps, for the generation of C and BN domains on a hexagonal lattice network of 800 atoms.

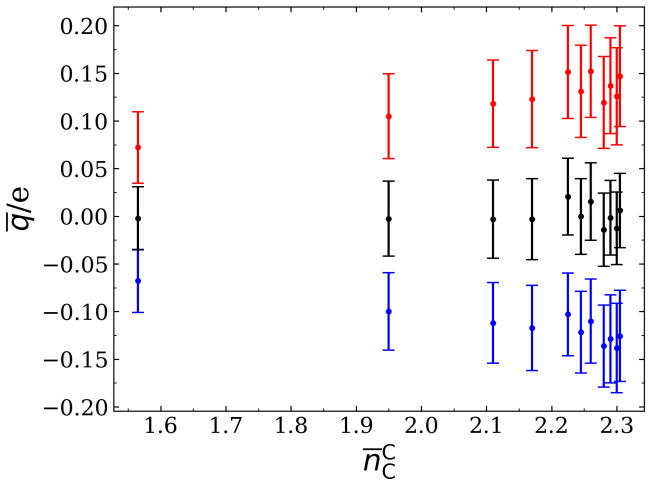


Figure 8.5: Average atomic charge by atom type for hexagonal configurations with a range of C and BN domain sizes, measured using the average C surrounding C partial coordination number, $\overline{n}_C^C$. Points are coloured by atom type: red - B, black - C and blue - N. Error bars show standard deviation of charge distributions.

that on increasing domain size for all three types of atom there is an increase in the width of the charge distributions represented by the increase in the standard deviation. This trend can be explained by a change in the variety of coordination environments. In the most disordered configurations, at the start of the LS-MC process, all coordination environments are equally likely and so there is not a majority of any type of charged atom. In the more ordered configurations, later in the LS-MC process, there are more atoms in domains, however, there is still a significant proportion of atoms on the edge of these domains or not in the domains which will have a different charge to those buried in the domains. This leads to an overall wider distribution. As these domains get even larger, the width of the distributions will begin to shrink again, as shown in figure 2 in chapter 7, due to the proportion of atoms not in domains shrinking.

8.4 Mixed BCN rings

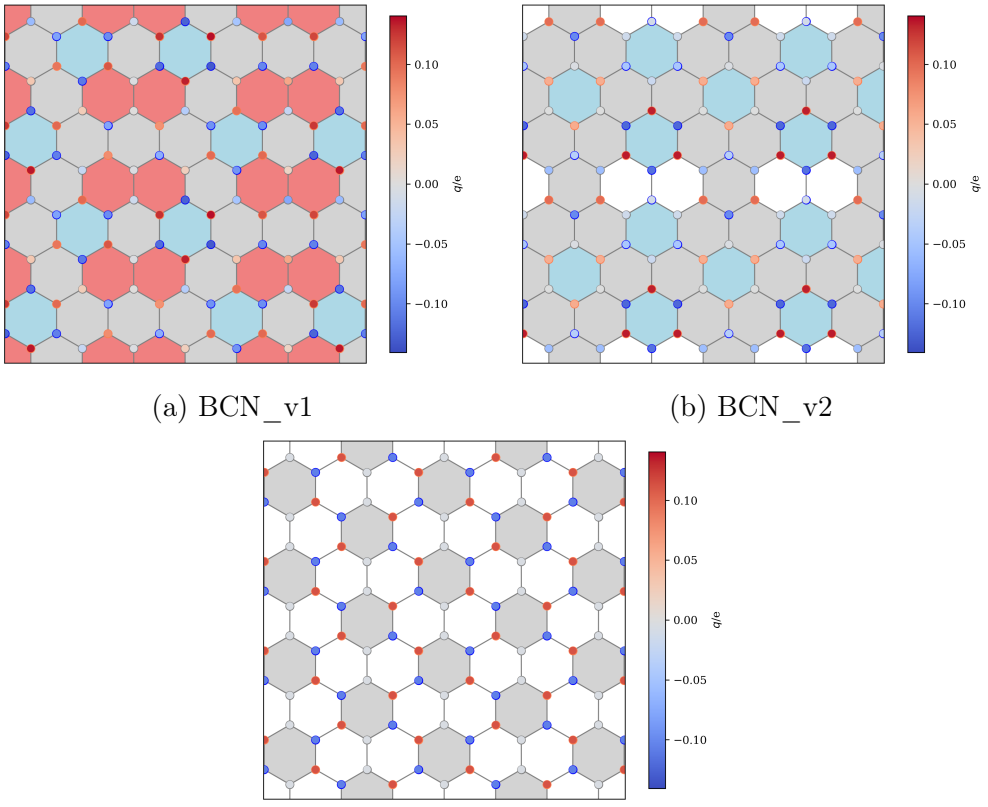
As discussed in section 8.1, the majority of theoretical work investigating in-plane BCN heterostructures containing mixed BCN rings focus on three structures, named BCN_v1, BCN_v2 and BCN_v3, as seen in figure 8.1. Whilst a variety of other structures have been proposed in the original work by Beniwal *et al.* [339], as well as other works since [365–367], many of these structures contain features which are significantly less stable, such as high fractions of homo-atomic bonds or non-six-membered rings. As such, for the aid of comparison with the most literature, the BCN_v1, BCN_v2 and BCN_v3 structures will be the focus of this section.

Figure 8.6 shows charge "heat maps" for the three structures with charges calculated utilising the FCM. These charge "heat maps" show only a few of

the repeating units which make up each structure. These systems were each modelled using 840 to 960 atoms depending on the structure. From these figures it can be seen how the atomic charges are affected by the local environment as well as the longer range interactions. For example, in BCN_v1, the repeating unit contains two B_3N_3 rings with each B bonded to two N and a C, and each N bonded to two B and a C. However, despite the similarities of the charges on these atoms are not equal. This is caused by the bonded C atoms taking on charges which are either the opposite sign or the same sign to the charges of the atoms in the B_3N_3 ring. This results in the charges in the ring becoming greater in magnitude or being reduced in magnitude respectively. This effect is then further reinforced if it is the same for each atom of the ring, and could potentially be representative of electron density being drawn to or from N or B through the bonded C atoms.

The effect of environment on charge can also be seen by looking at the profiles of the charge distributions for BCN_v1, as shown in figure 8.7. Whilst the overall peaks for B and N, shown in panel (a), appear as singular peaks, by breaking them down according to coordination environment, panels (b), (c) and (d), the multiple environments become clearer. However, due to the multiple sites with very similar bonding described above, the peaks are fairly broad, implying the charge density is constantly shifting. The difference in atomic hardness can also be seen by comparing the width of each of the B peaks with its N equivalent. For the B environments, the peaks are more spread out showing that the N is more resistant to the changes in its charge.

Figures 8.8 show the charge distributions for the BCN_v2 structure. For the BCN_v2 structure, there are a two main notable features to the charge distributions. First, unlike the other two structures, the B and N charge distributions have quite different shapes. Second, the distribution for C has



(a) BCN_v1

(b) BCN_v2

(c) BCN_v3

Figure 8.6: Three BCN monolayer structures charge "heat maps". Atoms are coloured according to their charge: Red and blue for more positively and negatively charged respectively. The edges of atoms are colour to denote their type: pink - boron, grey - carbon and blue - nitrogen. Rings are coloured according to their makeup: grey - $B_2C_2N_2$ with no homo-atomic bonds, white - $B_2C_2N_2$ with homo-atomic bonds, blue - $B_3N_3/B_3C_3/C_3N_3$ and red - other.

a significant negatively charged peak but no positively charged peak. Both of these features can be rationalised by inspecting the BCN_v2 structure. The presence of a N-N bond as well as a N bonded to two negatively charged C atoms in the unit cell results in the distribution being shifted to closer to q/e = 0. These structural features also link to the shape of the C distribution. The negative charge on the C atoms are caused by their bonds to two B atoms. The lack of positively charged C peak despite the presence of C atoms bonded to two N atoms is due to these N atoms being fairly low charge due to the N-N bond previously discussed.

The charge distribution for the BCN_v3 structure, seen in figure 8.9, is much simpler than either of the other structures. This is caused by its highly symmetric nature. This results in there being only one local environment, for each atom type, both in the first coordination sphere as well as in the more extended structure. As such, each atom type has only a singular sharp peak.

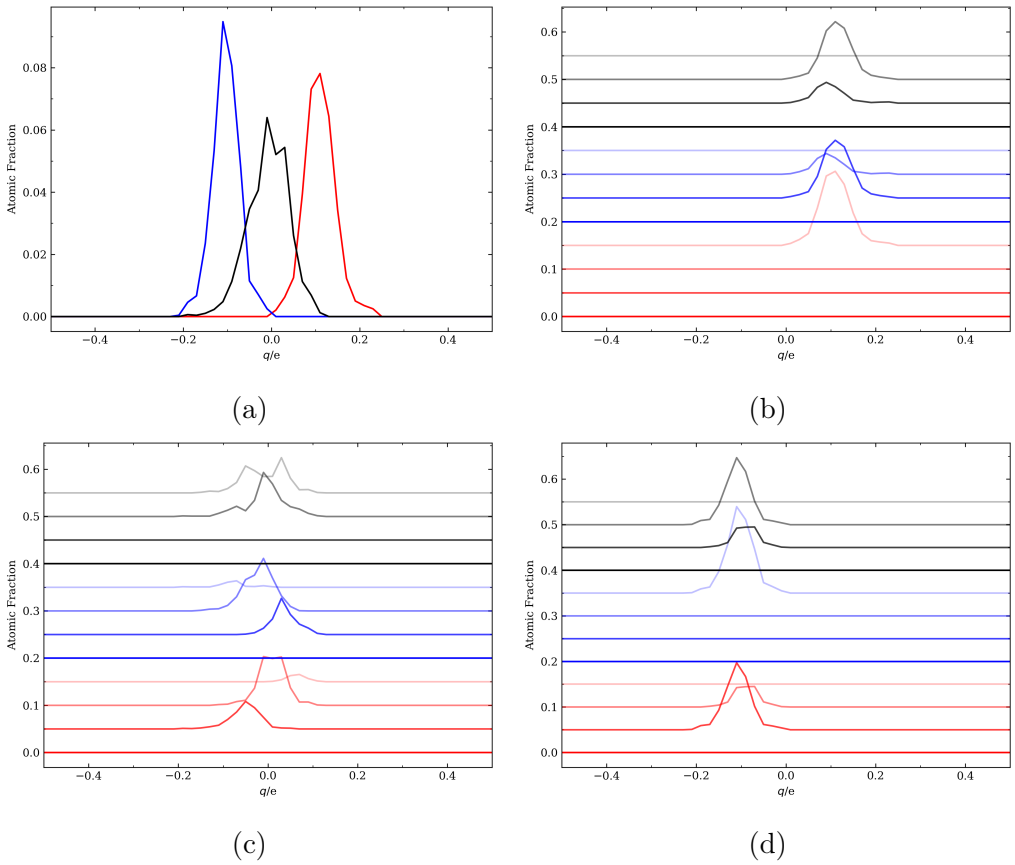


Figure 8.7: Charge distributions for the BCN_v1 structure calculated using the FCM. Panel (a) shows the charge distributions grouped and coloured by atom type: red - boron, black - carbon and blue - nitrogen. Panels (b) , (c) and (d) show the charge distributions for boron, carbon and nitrogen atoms, respectively, grouped by coordination environments. The lines are coloured by the coordination environment around atom α they represent: red - n_α^{B}, blue - n_α^{N}, black - n_α^{C}. For each colour, the opacity and offset gives the value of n_α^β from 3 to 0 for darkest to lightest. The lines are offset for clarity.

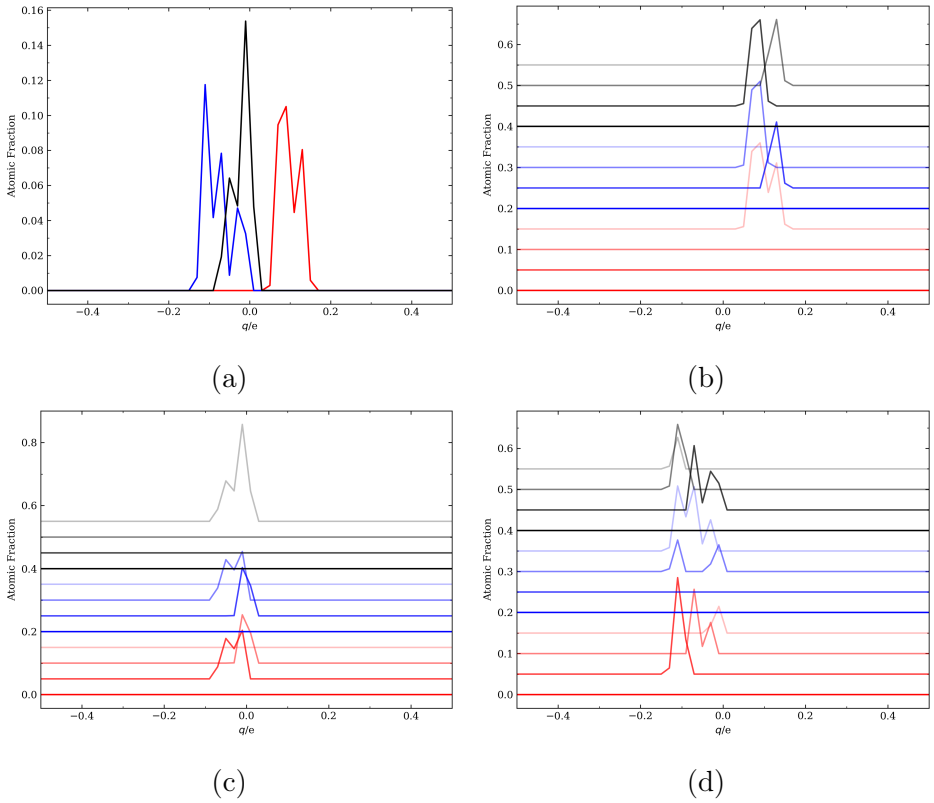


Figure 8.8: Charge distributions for the BCN_v2 structure calculated using the FCM. Panel (a) shows the charge distributions grouped and coloured by atom type: red - boron, black - carbon and blue - nitrogen. Panels (b) , (c) and (d) show the charge distributions for boron, carbon and nitrogen atoms, respectively, grouped by coordination environments. The lines are coloured by the coordination environment around atom α they represent: red - n_α^{B}, blue - n_α^{N}, black - n_α^{C}. For each colour, the opacity and offset gives the value of n_α^β from 3 to 0 for darkest to lightest. The lines are offset for clarity.

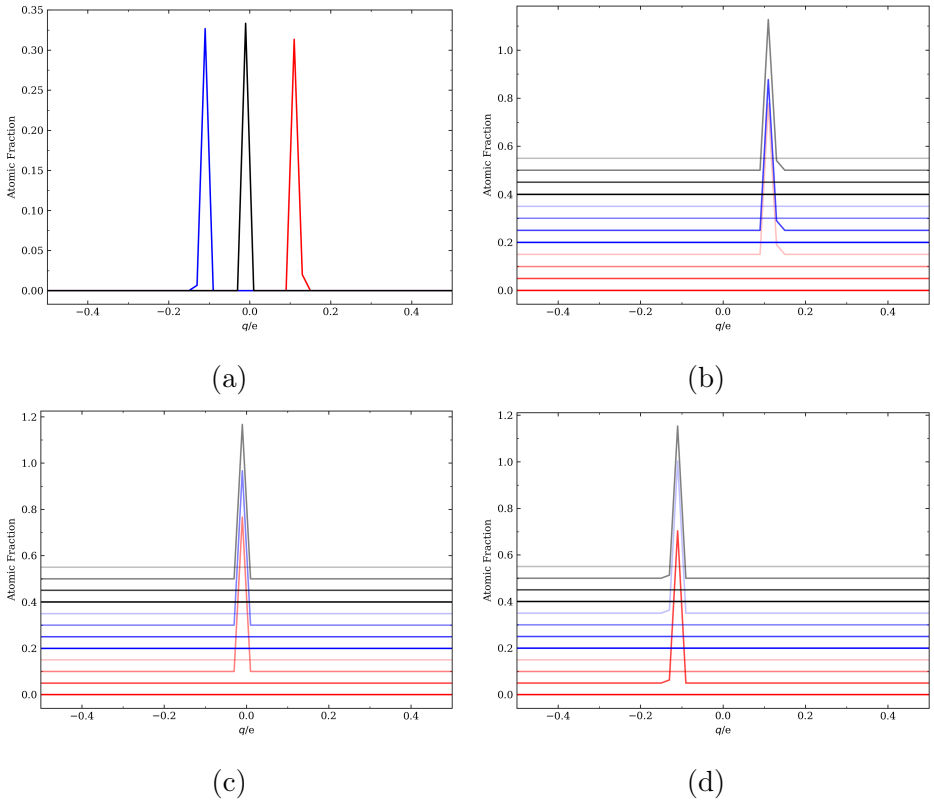
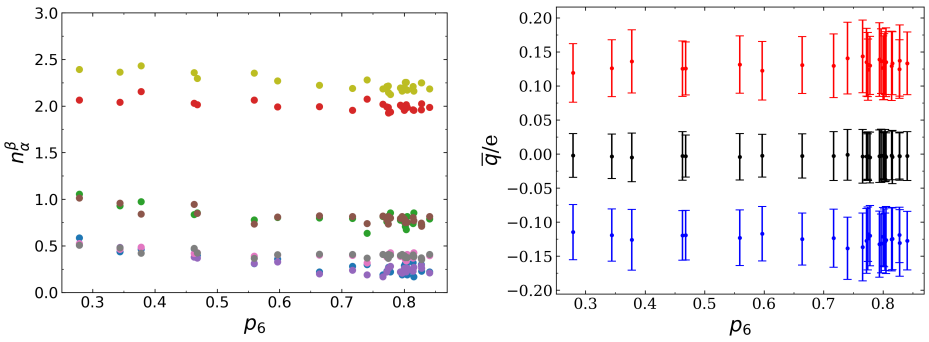


Figure 8.9: Charge distributions for the BCN_v3 structure calculated using the FCM. Panel (a) shows the charge distributions grouped and coloured by atom type: red - boron, black - carbon and blue - nitrogen. Panels (b) , (c) and (d) show the charge distributions for boron, carbon and nitrogen atoms, respectively, grouped by coordination environments. The lines are coloured by the coordination environment around atom α they represent: red - n_α^{B}, blue - n_α^{N}, black - n_α^{C}. For each colour, the opacity and offset gives the value of n_α^β from 3 to 0 for darkest to lightest. The lines are offset for clarity.

8.5 Amorphous BCN

Two-dimensional amorphous BCN configurations were generated using the methods discussed in section 5.4. Starting from a hexagonal lattice, topological disorder is introduced by the repeated creation of Stone-Wales defects. The defects are introduced through a simulated annealing bond-switching Monte Carlo algorithm, discussed in section 4.1.2, which allows for the level of disorder to be controlled through the use of a Monte Carlo "temperature". Next, the level of site disorder is controlled through the use of the atom label swapping Monte Carlo discussed in sections 5.4 and 8.3.2. For amorphous BN systems an equal amount of B and N atoms are required to ensure overall charge neutrality, as such, only one possible chemical composition with half the atoms being B and half being N is possible. Whilst this balance of B and N is still required in amorphous BCN systems, the addition of C means that there is a range of chemical compositions maintaining the charge neutrality, which can be studied. The resulting amorphous configurations are then relaxed using molecular dynamics in which the atomic interactions were modelled using a Tersoff potential, parametrised for BCN by Kınacı *et al* [167] (as shown in table 4.2), augmented with point charge electrostatic interactions. The point charges for these interactions are calculated using the fluctuating charge model (FCM). This section will investigate how varying the topological and site disorder as well as the chemical composition affects the charge distributions of these networks.

Figure 8.10 shows how the site-disorder, panel (a), and charge distributions, panel (b) vary for a two-dimensional amorphous BC_2N configurations of 800 atoms with a range of levels of topological disorder from $p_6 \approx 0.29$ to 0.85. By comparing panel (a) to a similar figure for two-dimensional BN config-



(a) (b)

Figure 8.10: The effects of varying topological disorder in two-dimensional amorphous BC_2N configurations of 800 atoms. Panel (a) shows how site-based disorder, represented by partial coordination numbers, n_α^β, is affected by topological disorder, represented by the proportion of six-membered rings, p_6. Points are coloured by α and β values: blue - α = B, β = B, orange - α = B, β = N, green - α = B, β = C, red - α = N, β = B, purple - α = N, β = N, brown - α = N, β = C, pink - α = C, β = B, grey - α = C, β = N and yellow - α = C, β = C. Panel (b) shows the effect of topological disorder on the atomic charge distribution. Points are coloured by atom type: red - B, black - C and blue - N. Error bars show standard deviation of charge distributions.

urations, figure 5.7, the effects of introducing C become evident. First, the trend of decreasing coordination numbers on increasing p_6 appears to be reduced. This is due to the decrease being split over a greater number of partial coordination numbers, 9 in BCN configurations compared to 4 in BN configurations. Secondly, it can be seen that whilst there is a slight decrease in the $n_{\mathrm{B/N}}^{\mathrm{N/B}}$ values, there is a significantly greater reduction in the $n_{\mathrm{B/N}}^{\mathrm{B/N}}$ values across all levels of topological disorder. This shows that during the atomic label swapping Monte Carlo process C atoms are being used to preferentially reduce the number of BB and NN interactions over BN interactions. The calculated charge distributions for these configurations, as shown in figure 8.10(b), are fairly consistent across all values of p_6. When compared to distributions calculated for similar amorphous BN configurations, such as those studied in chapter 7, the average charges for B and N are very similar with a magnitude of ~ 0.125e. However, the amorphous BCN configurations have smaller standard deviations, ~ 0.04e compared to ~ 0.06e for amorphous BN configurations. This is likely caused by the previously mentioned decrease in both BB/NN and BN interactions and the increase in B/N and C interactions. This change may result in less highly charged atoms as the B/N and C bond is less polar than a BN bond and less lowly charged atoms as it is more polar than a BB or NN bond, therefore reducing the overall spread of charges.

Figure 8.11 shows the change in partial coordination numbers for a two-dimensional amorphous BC_2N configuration of 800 atoms with $p_6 \approx 0.55$ over the course of 10000 steps of an atomic label swapping Monte Carlo simulation. By comparing with figure 8.4, a similar figure for a topologically ordered system, we can see that both structures result similar values for each partial coordination number. This is indicative of domains of similar size be-

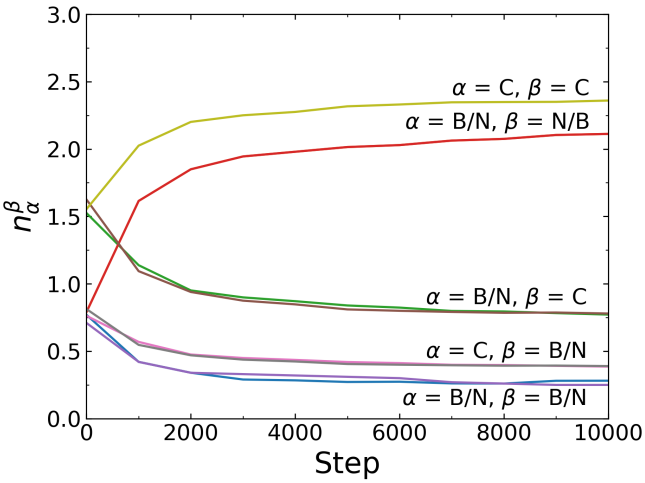


Figure 8.11: Change in average partial coordination numbers over the course of 10000 Monte Carlo steps, for the generation of C and BN domains on a two-dimensional amorphous BC_2N configuration of 800 atoms with $p_6 \approx 0.55$.

ing formed in each structure, and therefore topological disorder having little effect on the domain size. This is in agreement with recent work performed by Durandurdu [359] who simulated amorphous BC_2N using an *ab initio* potential model and a melt-quench approach, showing that a layered structure is formed. By investigating the coordination environments of each atom type, it was shown that C was more likely to be bonded to C and that B and N were most likely to be bonded to each other, demonstrating the formation of C-rich and BN-rich domains, like those generated using our atom label swapping Monte Carlo approach.

Figure 8.12 shows how the charge distributions of amorphous BC_2N configurations vary with domain size. Similar to figure 8.5, this domain size is measured using the average C-C partial coordination number. As with the topologically ordered BC_2N systems, there is a gradual increase in the magnitude of the charge on the B and N atoms, however, for the amorphous system this trend is slightly smoother. It is possible that the topological

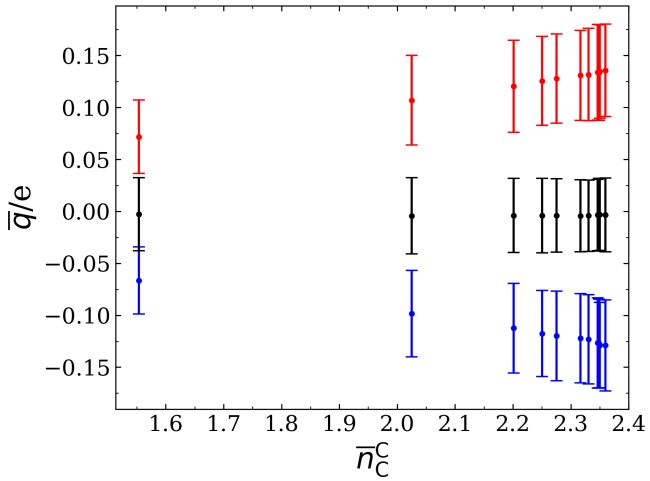


Figure 8.12: Average atomic charge by atom type for two-dimensional amorphous BC_2N configurations of 800 atoms ($p_6 \approx 0.55$) with a range of C and BN domain sizes, measured using the average C surrounding C partial coordination number, $\overline{n}^{C}_{C}$. Points are coloured by atom type: red - B, black - C and blue - N. Error bars show standard deviation of charge distributions.

defects such as odd-membered rings allow for more fluid transition between domains resulting in fewer anomalous regions of site-ordering. There is also an increase in the standard deviation as the domain sizes increase; however, this is less pronounced for the amorphous configurations. This is again potentially indicative of fewer anomalous regions of site-ordering potentially caused by topological disorder.

Figure 8.13 shows how the charge distributions calculated using the FCM vary with the chemical composition of amorphous $(BN)_xC_y$ configuration at a set level of topological disorder, $p_6 \approx 0.55$. Overall for intermediate compositions, from $\sim 20\%$ to $\sim 70\%$ C, there is little variation in either the average charge or the standard deviation. However, at both extremes, this changes. At high percentages of C, there is a gradual decrease in both the average charge for B and N as well at the standard deviation for all three

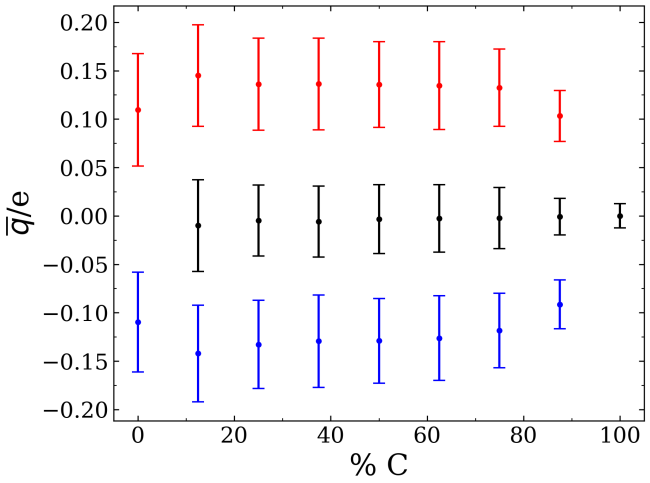


Figure 8.13: Average atomic charge by atom type for two dimensional amorphous $(BN)_xC_y$ configurations of 800 atoms ($p_6 \approx 0.55$) with variable chemical compositions. Points are coloured by atom type: red - B, black - C and blue - N. Error bars show standard deviation of charge distributions.

atom types. This is likely caused by the BN-rich domains becoming smaller resulting in an increase in the number of less polar BC and NC interaction over BN interaction. This results in less charge separation and narrower distributions as the variety of local coordination environments reduces. At low percentages of C, there is a slight increase in average charge at $\sim 10\%$ C before a decrease towards 0% C. There is also a slight increase in the standard deviation of the charge distributions as the percentage of C decreases below $\sim 20\%$. The increase in standard deviation is likely caused by the lack of C resulting in a greater number of both BN site-ordered regions as well as BN site-disordered regions. This leads to more highly and lowly charged atoms and therefore a wider distribution. The change in the average charge is a bit more subtle and is likely caused by where the C atoms are situated. At low concentrations of C, it may be possible for the C atoms mostly occupy sites which would otherwise result in the formation of a BB or NN bond. This

would lead to a slight increase in charge as the BC and NC bonds are still slightly polar. However, as the concentration of C decreases further, there is no longer enough C atoms to fill these sites leading to the less favourable BB and NN bonds being formed and reduction in the average charge.

8.6 Summary

This chapter has focused on the development of methods for the generation of configurations for various BCN materials and the application of the fluctuating charge model to these materials. The results in this chapter demonstrate how charge distributions in these materials are affected by the nature of the bonding and local coordination. This leads to the charge on C atoms "adapting" to their environment. It has also been shown that domain size and composition in amorphous $(BN)_xC_y$ can have an effect on the charge distributions, which may in turn lead to variation in other properties, physical, chemical or otherwise.

9 | Utilizing the Fluctuating Charge Model to Investigate Applications of BN nanosheets

Contents

9.1 Mechanical Properties 160

9.1.1 Tension 161

9.1.2 Compression 170

9.2 Nanopores 172

9.3 Summary 179

In this chapter, results are discussed which show how the FCM may be applied to BN nanosheets to help understand some of their key applications. First, their mechanical properties and how the atomic charges change under strain were investigated. Secondly, the effect of pore shape and size on the charge distributions in ordered nanosheets was investigated as well as whether introducing pores into amorphous nanosheets affects them. The work studying these pores was carried out in collaboration with Luke Piggott [320] under my supervision and using the software developed in earlier parts of this thesis for generation of configurations and analysis.

9.1 Mechanical Properties

To measure the mechanical properties of boron nitride nanosheets, molecular dynamics simulations were used to place them under a constant controllable strain rate. Since these nanosheets are modelled using periodic boundary conditions, simply moving opposite ends of the sheets is not possible. Instead,

the strain is introduced by varying the periodic box length and scaling all atoms to the new box size. This process can be used to introduce a positive or negative uniaxial strain, resulting in the nanosheet being stretched or compressed. The strain is measured using a percentage change in the box length in the direction of strain compared to the box length at the energy minimum for the structure. A periodic box containing 800 atoms, 400 B and 400 N, was used to study the mechanical properties at 300K. A timestep of 1fs was used and all atomic interactions were modelled using the Tersoff potential, characterised for BN by Sevik *et al.* [166]. This potential was augmented with a electrostatic potential with atomic point charges modelled using the FCM as described in chapter 7.

9.1.1 Tension

The effect of varying two factors on the mechanical properties of nanosheets when positive strain was applied were investigated: strain rate and site disorder. Strain rate was controlled through the amount the periodic box was extended in each timestep whilst site disorder was introduced using the atomic label swapping Monte Carlo algorithm described in section 5.4.1.

9.1.1.1 Strain rate

Figure 9.1 shows how the stress-strain curves vary for a range of strain rates, applying strain along the zigzag edge. Strain rates were selected to be similar to those employed in other works investigating the mechanical properties of BN nanosheets [149, 175, 368, 369]. Stress values were calculated using a thickness for the monolayer of 0.333 nm, equal to the separation between layers of h-BN. From this figure a few main features can be identified. One of the most common methods of quantifying the mechanical properties of a

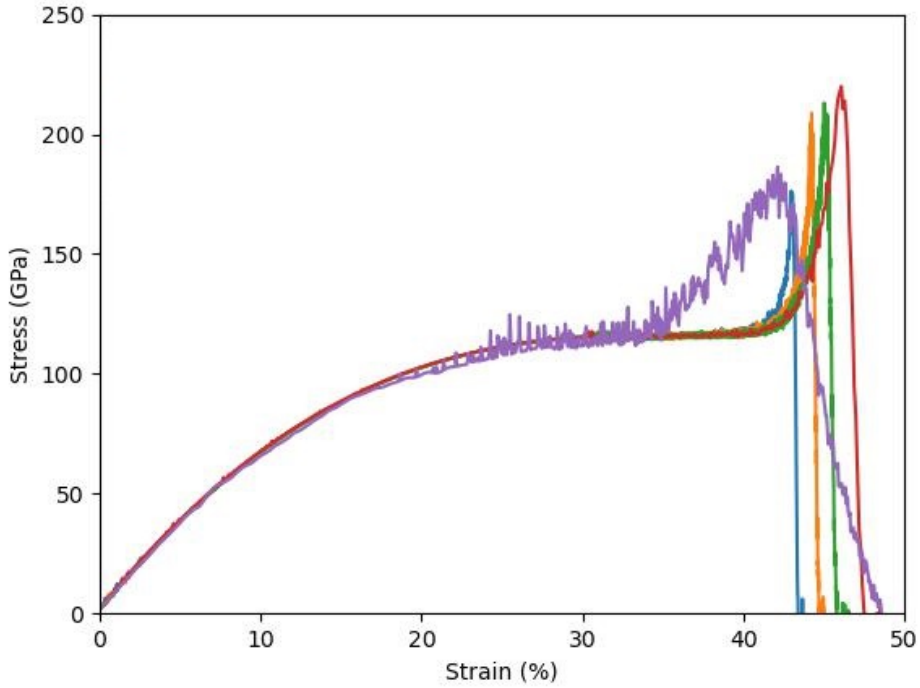
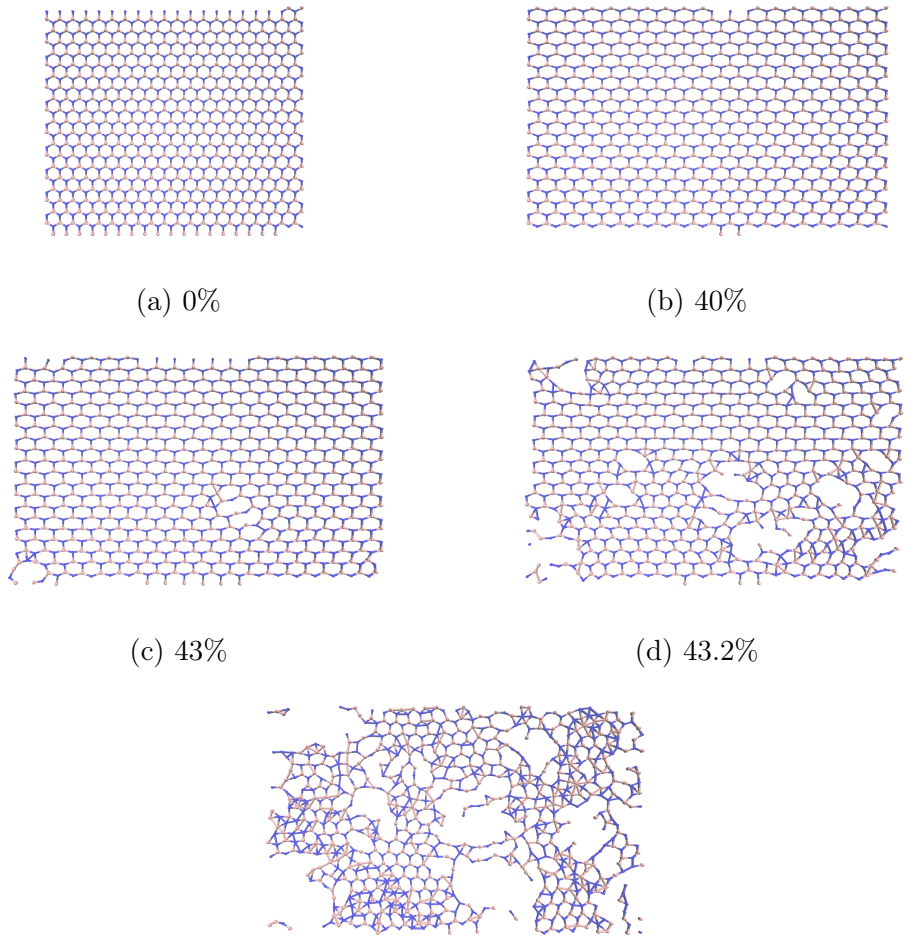


Figure 9.1: Stress-strain curves for BN nanosheets at a variety of strain rates, applying strain along the zigzag edge. Lines are coloured by strain rate: blue - $2 \times 10^{10}\text{s}^{-1}$, orange - $3 \times 10^{10}\text{s}^{-1}$, green - $5 \times 10^{10}\text{s}^{-1}$, red - $1 \times 10^{11}\text{s}^{-1}$ and purple - $5 \times 10^{11}\text{s}^{-1}$.

materials is the Young's modulus. This measures how stiff a material is under strain and is calculated by taking the gradient of a stress-strain curve in the linear region. The Young's modulus calculated for BN nanosheets stays at an approximately constant value of $\sim$ 752 GPa for all strain rates. This agrees with previously reported values for BN nanosheets along the zig-zag edge in the range of $\sim 690 - 840$ GPa [149, 175, 368, 369]. As the strain rate increases from $2 \times 10^{10}\text{s}^{-1}$ to $1 \times 10^{11}\text{s}^{-1}$, there is an increase in the fracture stress from $\sim$ 175 GPa to $\sim$ 220 GPa as well as an increase in fracture strain from $\sim$ 43% to $\sim$ 47%. However, these trends are caused by the appearance of a peak at high strain values. This peak is unphysical and characteristic of the Tersoff potential for BN, leading to it overestimating the fracture stress and strain [368, 370, 371]. It has been shown that this strain hardening is caused by the "soft" cut-off function of the Tersoff potential [307, 341]. This agrees with the peaks shown in figure 9.1 as they all start at the same point indicating that it is related to the potential and not the changing strain rate. The only strain rate which behaves differently is $5 \times 10^{11}\text{s}^{-1}$, which is significantly more noisy and has a much broader strain hardening peak. This is potentially evidence that this high strain rate is not possible to be accurately modelled using these methods at high strain values. Figure 9.2 shows snapshots of a BN nanosheet under tensile strain, demonstrating how little the structure changes to from 0 to 40% strain. However, once a fracture appears in the system it quickly spreads leading to a total mechanical failure.

Figure 9.3 shows how the average absolute charge changes as the strain is increased for a variety of strain rates. From this figure it can be seen that the strain rate has very little effect on how the charge evolves. From a strain of 0 to 40% the charges for all strain rates follow the same gradually decreasing curve. This shows that the charge in this region is only dependent on the



(a) 0%

(b) 40%

(c) 43%

(d) 43.2%

(e) 43.4%

Figure 9.2: Snapshots of a BN nanosheet under tensile strain with a strain rate of $2 \times 10^{10}\text{s}^{-1}$. Strain values of each panel are indicated in the caption. Atoms are coloured by their type: pink - boron and blue - nitrogen.

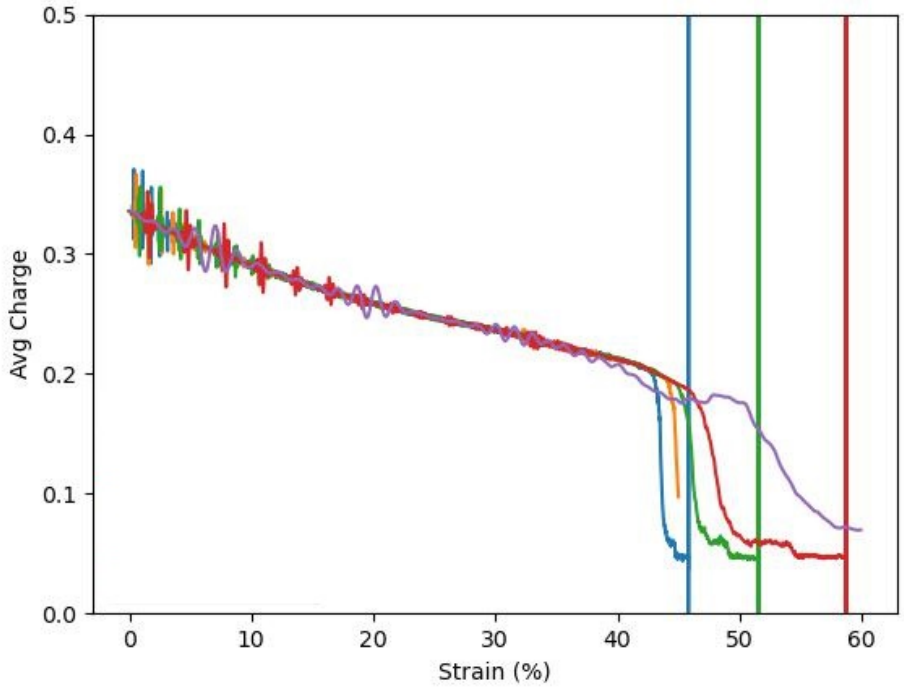


Figure 9.3: Average absolute charge-strain curves for BN nanosheets at a variety of strain rates. Lines are coloured by strain rate: blue - $2 \times 10^{10}s^{-1}$, orange - $3 \times 10^{10}s^{-1}$, green - $5 \times 10^{10}s^{-1}$, red - $1 \times 10^{11}s^{-1}$ and purple - $5 \times 10^{11}s^{-1}$.

distances between atoms and is correctly adjusting much faster than the nuclei. This gradual decrease shows the ionic nature of the bonds decreasing as the electron density becomes more equally located around each atom. In the high strain region, all strain rates result in a rapid reduction in charge as the material fails. This reduction does not reach an average charge of 0 as there are still fragments of the nanosheet present. Overall, both of these figures show that strain rate has little effect on the behaviour of the nanosheets in the low strain region and only slight changes at high strains.

9.1.1.2 Site Disorder

Figure 9.4 shows stress-strain curves for hexagonal BN nanosheets with a variety of levels of site disorder using a strain rate of 10^{11}s^{-1}. It can be seen that the curves are very similar across all levels of site disorder with only slight differences. At higher levels of site disorder there is a slightly shallower gradient at low strain values (0-10%). As the strain increases, the curves coalesce before again splitting at high strains with slightly decreasing fracture stress and strain, as the level of site disorder increases. As previously mentioned, the Tersoff potential without modification results in an unphysical strain hardening leading to over-prediction of the fracture stress and strain, as such the change in these values is less physically understandable.

Figure 9.5 shows how the Young's modulus of hexagonal BN nanosheets varies with the level of site disorder, measured using $\overline{n}_{\text{B}}^{\text{N}}$. From this figure, it can be seen that there is a clear trend between the two. This indicates that less force is required to stretch the nanosheet as disorder increases. This is expected as increased site disorder results in a greater number of weaker BB and NN bonds and a lesser number of stronger BN bonds. Since the Tersoff parametrisation used treats all of these bonds as equal, the reduction

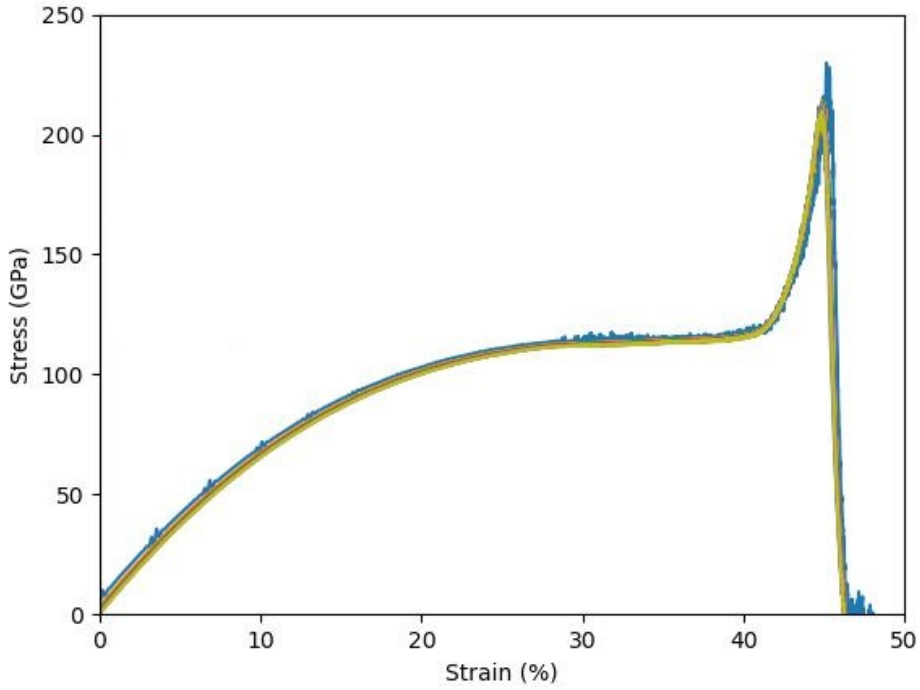


Figure 9.4: Stress-strain curves for BN nanosheets with a variety of levels of site disorder, at a strain rate of $10^{11}\mathrm{s}^{-1}$. Curves are coloured by level of site disorder, measured using the average number of N surrounding a B, $\overline{n}_{\mathrm{B}}^{\mathrm{N}}$. Key: blue - 3.000, orange - 2.406, green - 2.060, red - 1.815, purple - 1.707, brown - 1.623, pink - 1.598, grey - 1.550 and yellow - 1.507.

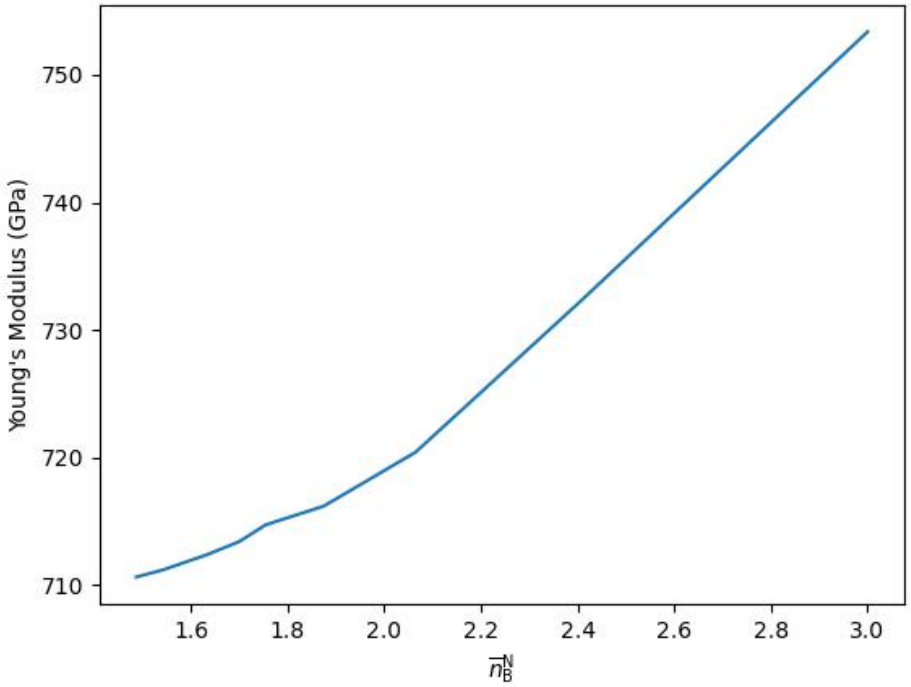


Figure 9.5: Young's modulus for a range of BN nanosheets shown as a function of the site disorder, measured using $\overline{n}_{\mathrm{B}}^{\mathrm{N}}$.

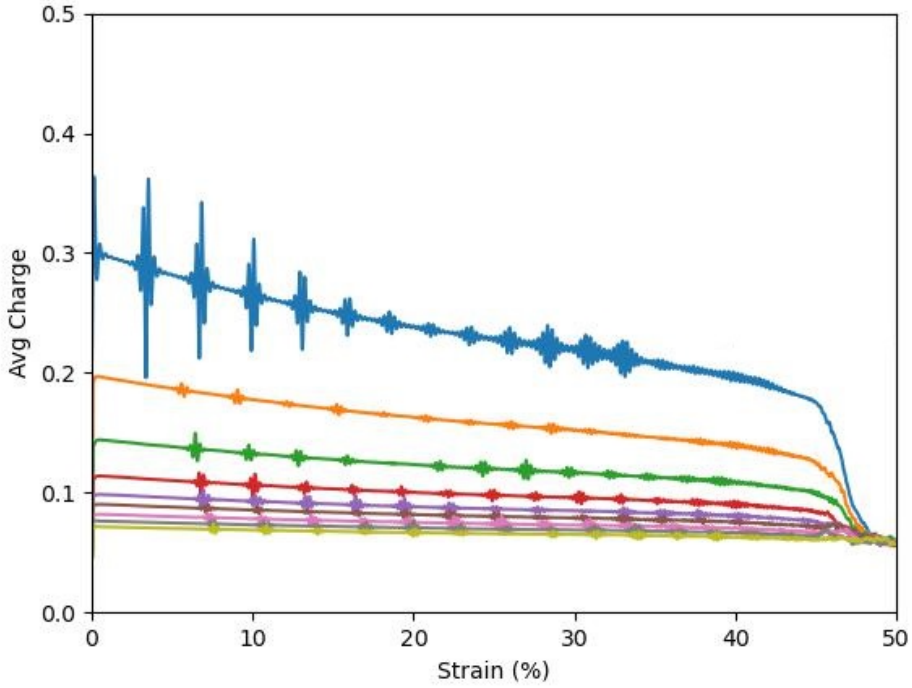


Figure 9.6: Average absolute charge-strain curves for BN nanosheets with a variety of levels of site disorder, at a strain rate of $10^{11}s^{-1}$. Curves are coloured by level of site disorder, measured using the average number of N round a B, $\overline{n}_{\mathrm{B}}^{\mathrm{N}}$. Key: blue - 3.000, orange - 2.406, green - 2.060, red - 1.815, purple - 1.707, brown - 1.623, pink - 1.598, grey - 1.550 and yellow - 1.507.

in strength must arise from the weaker electrostatic interaction.

Figure 9.6 shows how the average absolute charge of the system varies with strain for BN nanosheets with a variety of levels of site disorder. From this it can be seen that all levels of site disorder result in a gradual decrease as the strain increases, however the extent of this reduction is less as the site order increases, with the highest levels of site disorder having a practically constant level of charge. This is expected as at a $\overline{n}_{\mathrm{B}}^{\mathrm{N}}$ value of 1.5, homoatomic and heteroatomic bonds are present in equal amounts and so when these bonds are extended an equal amount of atoms with increase and decrease

in charge. The oscillations present in these lines are believed to be caused by the thermostat controlling the charge "temperature" as it begins to move away from is equilibrium values, as discussed in section 3.4.2. Adapting the charge thermostat parameters to reduce this effect is an area of potential further investigation.

9.1.2 Compression

Work was also carried out investigating the effect of compressive strain on BN nanosheets. A BN nanosheet contained within a periodic box was compressed along the zigzag edge. The armchair edges were clamped whilst the rest of the sheet was free to move. Strain was applied at a rate of $10^9 s^{-1}$. Soon after compression began the nanosheet began to buckle as shown in figure 9.7. Figure 9.7 shows how the buckling amplitude, measured as the furthest distance in the z direction from the clamped edges, changed as the strain on the nanosheet was increased, until mechanical failure occurred. There are two regions present in the figure where the buckling amplitude increases in different ways. First from a strain of 0 to $\sim$-2% there is a repeating pattern of sharp increase, followed by a very slight decrease. From a strain of $\sim$-2 to $\sim$-5.9% there is a much more steady and gradual increase in the buckling amplitude, until mechanical failure occurs. This process is demonstrated in figure 9.8, where it can be seen that the initial growth of the buckle involves multiple ripples in the sheet. These ripples potentially lead to the repeating pattern at low strain. Past this, only a single buckle is present leading to a smooth increase in amplitude as it grows. The eventual mechanical failure occurs where the buckle meets the clamped edges. This potential indicates that increasing the simulation box size would allow the investigation of even large buckles.

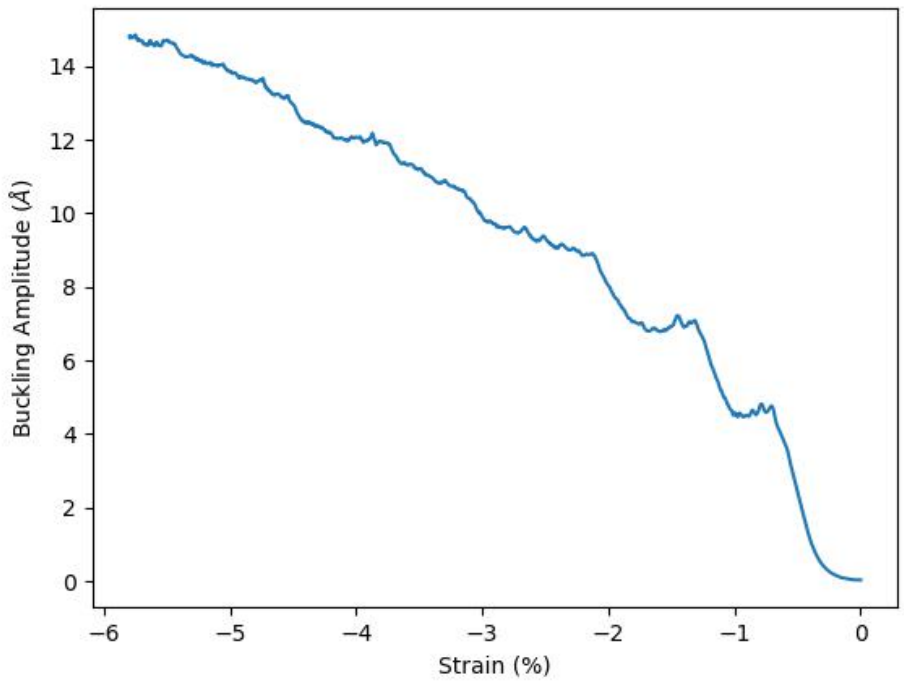
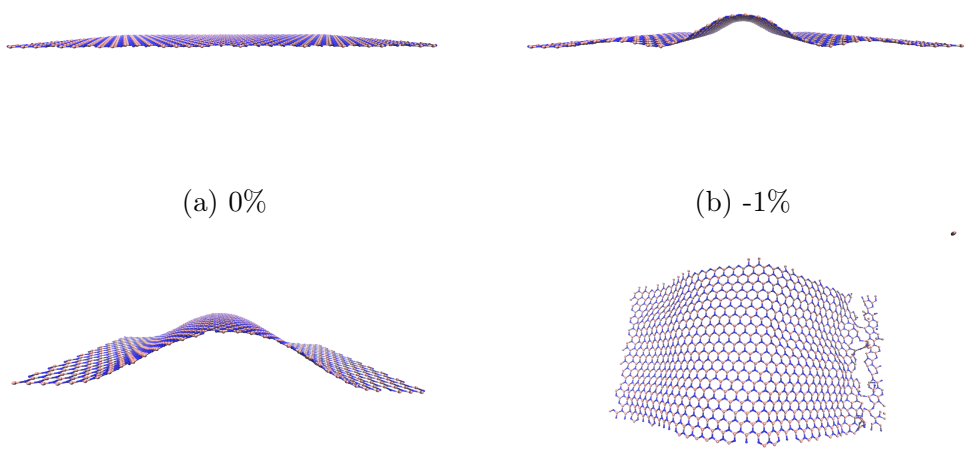


Figure 9.7: Change in buckling amplitude with increasing compressive strain for a h-BN nanosheet.

Unlike under stretching, the average absolute charge of the system under compression stayed at a constant value of $\sim$ 0.31e until mechanical failure occurred. This is due to the buckling allowing for a change in only the bond angles of the system rather than the bond lengths. Whilst this deviation from the optimal angle is still unfavourable for the Tersoff potential, the FCM treats the charges on atoms as point charges. As such only the distance between atoms affects their charges. This is a potential shortcoming of the FCM as changes in bond angles would likely result in a change in the bonding present and therefore a change in the charges on the atoms involved.



(a) 0%

(b) -1%

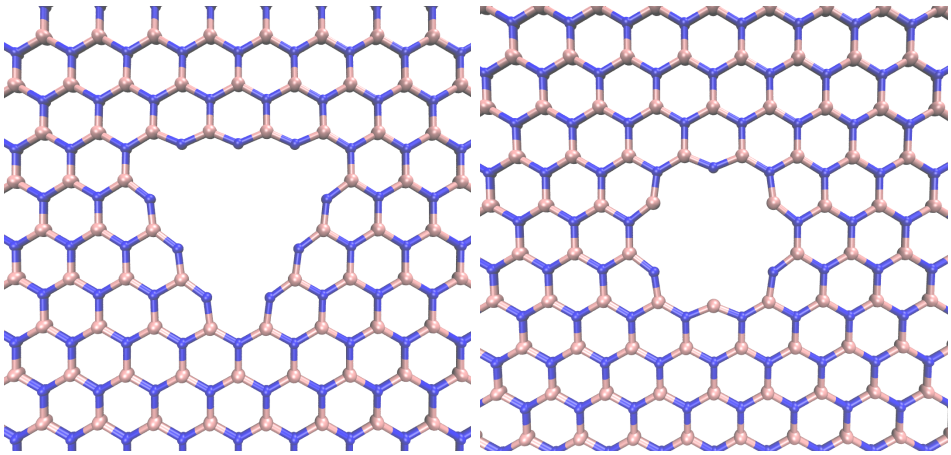
(c) -3%

(d) -5.8%

Figure 9.8: Snapshots of a BN nanosheet under compressive strain with a strain rate of $1 \times 10^{10} s^{-1}$. Strain values of each panel are indicated in the caption. Atoms are coloured by their type: pink - boron and blue - nitrogen.

9.2 Nanopores

As discussed in section 2.3, there are a wide range of chemical separation applications for which h-BN nanosheets have shown good potential [102–111]. These applications rely on species, often charged, moving through nanopores in these nanosheets. As such understanding how pores affect the charge distribution of these nanosheets is key in understanding and modelling this movement. Nanosheets containing pores of a variety of shapes and sizes were investigated using the fluctuating charge model. Figure 9.9 shows examples of the two main nanopore shapes formed in BN nanosheets. The key difference between these nanopores is the nature of the bonding and atom types along their edges. The edges of triangular pores are entirely zigzag bonded resulting in all the terminating atoms being the same type, most commonly

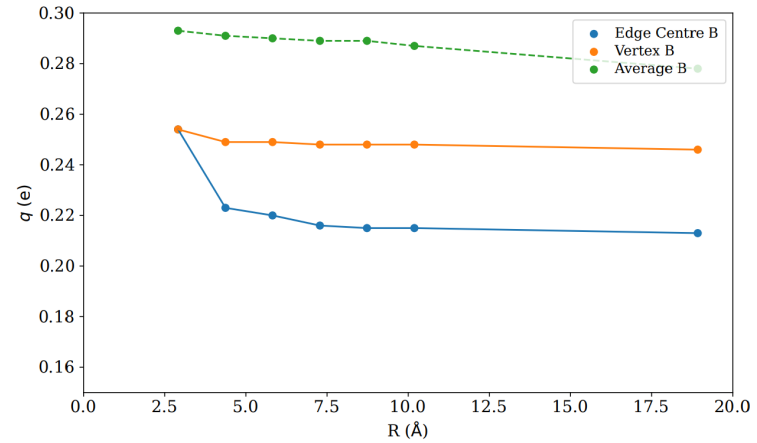


(a) (b)

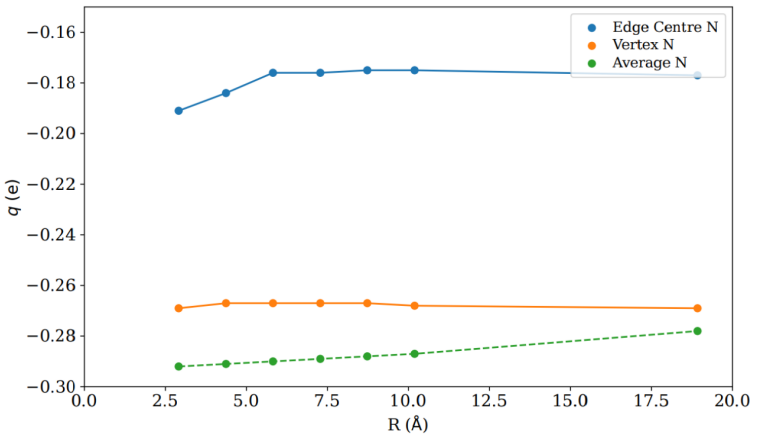
Figure 9.9: Example nanopore geometries in BN nanosheets. Panels (a) and (b) show a triangular and hexagonal pore respectively. Atoms are coloured by their type: pink - boron and blue - nitrogen.

N. Whereas, the edges of hexagonal pores have alternating section of zigzag and armchair bonding leading to a mixture of terminating B and N atoms.

Figure 9.10 shows how the charges on atoms surrounding N-terminated triangular pores are affected by the radii of said pores. From both panels, it can be seen that there is an initial reduction in the magnitude of charge as the pores increase in size, however once they reach a radius of ~ 7.5 Å this reduction plateaus. This trend is more prominent in the atoms located at the centre of the pore edges than the atoms at the vertices of the pores. The cause of this trend is the increase in the number of two-coordinate atoms along the edge of the pores, resulting in less polarised bonds. The trend plateaus as the atoms become far away enough from the vertices that greater charge caused by three-coordinate bonding has decayed away. The B atoms closest to the edge of the pore experience a weaker reduction in charge magnitude compared to the N atoms as the B atoms are all still three-coordinate. While the N atoms at the vertices have a greater charge magnitude than the B atoms as



(a)



(b)

Figure 9.10: Change in atomic charge surrounding N-terminated triangular pores in BN nanosheets with increasing pore radii. Panels (a) and (b) show charges on B and N atoms respectively.

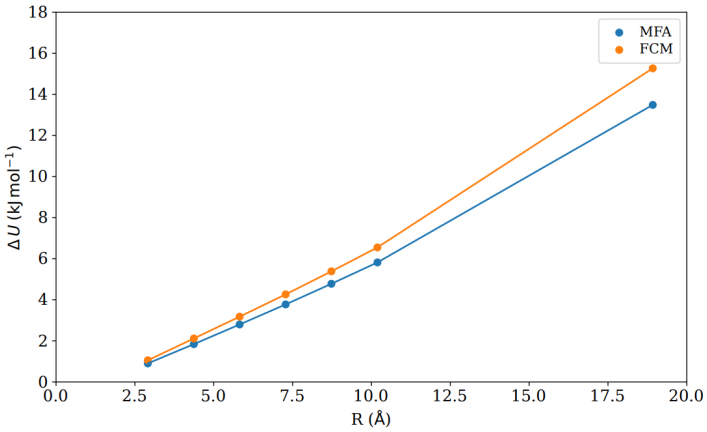
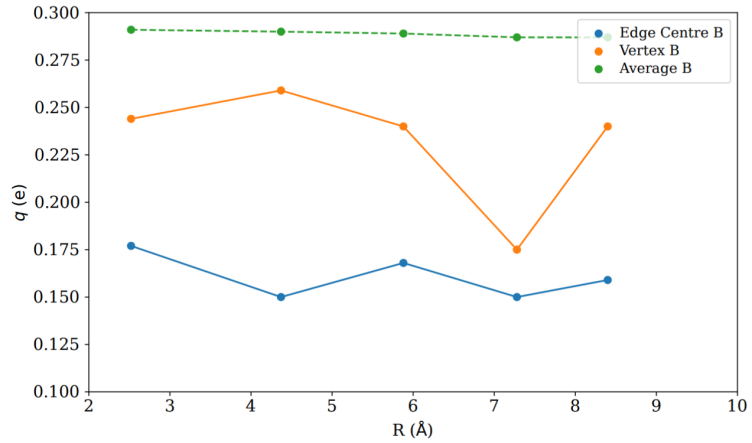


Figure 9.11: Comparison of energy difference compared to pristine nanosheet versus radius for a range of N-terminated triangular pore sizes for the mean field approximation (MFA) and the fluctuating charge model (FCM).

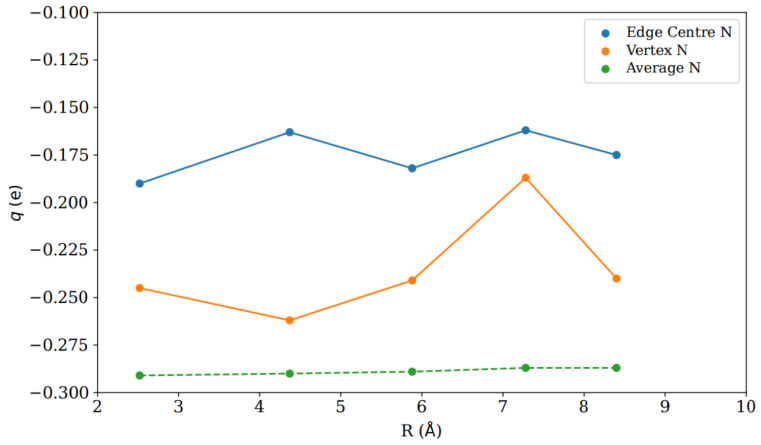
the N atoms are bonded to three three-coordinate atoms whilst the B atoms are bonded to two three-coordinate atoms and one two-coordinate atom.

Figure 9.11 shows how the difference in energy between a nanosheet containing pores and a pristine nanosheet of 800 atoms (ΔU) changes when they are modelled using a mean field approximation (MFA) and the FCM. Under the MFA, a fixed charge equal to the charge calculated for a pristine nanosheet using the FCM was employed. From this figure it can be seen that using the MFA results in underestimation of the energy required to introduce pores and that this error increases with the size of the pore. This is caused by the FCM predicting reduced charges in atoms close to the pores. This results in a weakening of the electrostatic component of the bonds these atoms make and therefore a increase in ΔU. For larger pore sizes the difference between the MFA and the FCM is more pronounced due to an increasing number bonds containing atoms with a reduced charge.

Figure 9.12 shows how the charges on atoms surrounding hexagonal pores



(a)



(b)

Figure 9.12: Change in atomic charge surrounding hexagonal pores in BN nanosheets with increasing pore radii. Panels (a) and (b) show charges on B and N atoms respectively.

are affected by the size of said pores. As previously discussed, one notable difference between hexagonal and triangular pores is bonding pattern on the pore edges, as shown in figure 9.9. In triangular pores, the edges are entirely zigzag, however, in hexagonal pores the edges of contain a mixture of the zigzag pattern and the armchair pattern. This also results in hexagonal pores not being entirely B- or N-terminated but a mixture of both. Therefore, the magnitude of the charges for B and N are much closer than in triangular holes. The multiple edge patterns also results in a very different trend in charges. As the pores increase in size, the patterns at the edges and vertices alternate between zigzag and armchair. While there is still a gradual decrease in charge as the pores grow, this alternating bonding pattern results in an oscillating behaviour in the charges. Along the edges, the armchair pattern results in two-coordinate atoms being bonded to each other resulting a lower charge magnitude. However, at the vertices, the armchair pattern allows for only three-coordinate atoms, increasing the charge. The second configuration ($R \approx$4.4 Å) is an anomaly to this trend as the zigzag pattern at the vertices is not wide enough for a two-coordinate atom resulting in a greater than expected magnitude of charge.

Introducing pores into amorphous sheets is more complex than into crystalline sheets. First, an amorphous configuration of 800 atoms was generated with a $p_6 \approx 0.55$ and $\overline{n}_{\mathrm{B}}^{\mathrm{N}} \approx 2.5$ using the methods described in section 5.4. Next, an atom is selected at random and the surrounding atoms are removed to forms a pore with radii r_c, where r_c is a integer multiple of r_{BN}. Due to the disordered nature of the nanosheets, the resulting pores are different shapes and involve removing different numbers of atoms depending on the initial atom choice. As such, 10 pores were generated for each value of r_c and averaged over. Figure 9.13 shows how introducing pores on increasing size

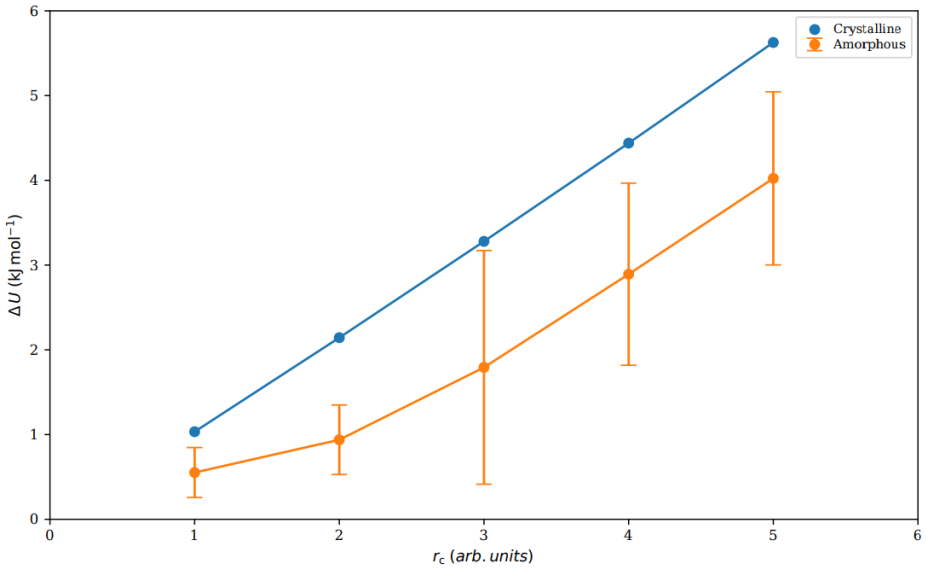


Figure 9.13: Comparison of energy difference compared to a nanosheet without pores for a range of pore sizes for the ordered and amorphous nanosheets.

affects the energy of both crystalline and amorphous BN nanosheets. The most notable difference is that ΔU is lower for amorphous configurations across all pores sizes, indicating it is easier to introduce pores to amorphous networks. This is likely due to amorphous networks containing a high concentration of less stable ring geometries and coordination environments. It should also be noted that for very small pores or holes, there is significantly less spread in the energy cost than for larger pores. This may be caused by the domains present in these configurations as discussed in chapter 7. These larger pores could remove large regions of low or high charge leading to a smaller or larger energy cost respectively.

9.3 Summary

In this chapter, we investigate how the fluctuating charge model can be applied to some key applications for BN nanosheets. First, mechanical properties were investigated. It was demonstrated that strain rate has little effect on how well the FCM performs at low strains and slight changes at high strains. It was also shown that site disorder can have an effect on the mechanical properties of BN nanosheets and change how charge decrease as nanosheets are stretched. It was also shown that charges calculated by the FCM are unaffected by mechanical buckling, indicating a potential downfall of the FCM.

Work was also carried out investigating how charge distributions are affected by nanopores of varying size and shape. It was noted that pores result in reduced charge surrounding atoms, which is potential important for separation applications. It was also shown that pores may be easier to form in amorphous nanosheets due to their high levels of disorder. This could be investigated further so determine if a balance between the favourable energy cost of forming pores in amorphous materials and the defined edge order of pores in crystalline materials can be achieved.

10 | Conclusions and Future Work

In conclusion, we have developed a potential model which can be applied to a wide range of boron nitride and borocarbonitride materials. This model is built on the Tersoff potential parametrised for BN and augmented with an electrostatic interaction which includes an implementation of the fluctuating charge model (FCM) to allow the atomic charges to vary and adapt to their environments. This is, to our knowledge, the first implementation of the FCM to network materials and required the implementation of a cutoff function to control the range of charge transfer. It was demonstrated that the FCM was required for these materials by modelling a variety of crystalline BN structures in two and three dimensions, as well as amorphous BN across a range of densities and fixed atomic charges. In the amorphous structures, it was shown that varying atomic charge has little effect on the topological order of the structure but a notable impact on the site ordering. This demonstrates that atomic charges can have a subtle but significant effect on the structure of these materials and therefore potentially their properties.

The new potential model was contrasted against independent density functional theory calculations for a range of BCN structures with the charge distributions showing excellent agreement for all structures. This agreement verifies that the parameters and cutoff range used accurately represent the charges in these BCN materials. The potential model was used to investigate a variety of network properties in BN nanosheets, including site disorder, defect types and topological disorder. It was shown that local coordination has the most significant effect on the atomic charges, an effect which would have not been accounted for using a fixed charge model. Next the FCM was used to model two-dimensional amorphous BN networks across a range of

levels of disorder. These configurations were generated using a Monte Carlo approach, allowing for control over the level of site and topological disorder independently. Within these networks it was shown that regions of high and low charge form, with the size of these domains being related to the level of topological disorder.

Next, BCN materials were studied in further detail. A Monte Carlo approach for generating amorphous BCN structures was developed. This method was used to generate structures which capture the formation of BN and C domains in these materials, as described by work employing simulations based on a higher level of theory. It was shown, by investigating C-substituted defects in h-BN, that C atoms are able to adopt a charge to "adapt" to their environment in these materials. It was also demonstrated that varying the domain size and composition in amorphous $(BN)_xC_y$ can have an effect on the charge distributions and therefore may lead to variations in the properties of these materials.

Finally, the FCM was employed to investigate some key applications of BN nanosheets, namely the mechanical properties and the nanopores for separation. Under tension, it was shown that strain rate has little effect on how the atomic charge decreases as the nanosheet is stretched. However, introducing increasing levels of site disorder results in an increasingly gradual decrease in atomic charge with all structures trending towards the same value. It was also shown that under compression, buckling of the BN nanosheet occurs. However, there was no change in atomic charge as the buckle grew, potentially indicating a downfall of the FCM. This is because a change in bonding angle should cause a change in the type of bonding and therefore lead to change in the atomic charge. The charge distributions around nanopores of varying size and shape were studied. It was noted that introducing these

pores results in an extended reduction of atomic charge which may be important for the movement of charge species through these pores. The cost of introducing pores to amorphous BN structures was also investigated. It was shown that pores are easier to form in these highly disordered structures but they have a less well-defined structure. This leads us to believe there maybe a level of disorder which can balance the reduced energy cost with the well-defined edge structure of pores in crystalline structures.

Future work for this research could move in one of three main directions: improving the current model, applying the current model to other applications of BCN materials and adapting the model to other network materials. Improving the potential model could involve refining the parameters currently employed by closely comparing the results to those of either experimental or theoretical *ab initio* results for a variety of properties or structural data. The model could also be improved by modifying it to work under a greater range of conditions such as layered van der Waals structures or those containing mechanical bending, such as nanotubes or fullerenes, both of which would require a more complex description of the bonding involved.

Further work on BCN materials could also progress in many different ways. This could involve further exploring the formation of nanopores for separation applications by investigating how other species interact with the nanopores. Work could also be carried out looking at how a variety of other dopant atoms, such as O, Si or S, affect the charge distributions of the structures or how a variety of ions adsorb on to the surface on h-BN and nanosheets. Further work investigating the generation of amorphous BN and BCN configurations could also be undertaken, such as generating an amorphous configuration containing only even-membered rings. This could allow for the investigation into how only topological disorder affects systems.

Finally, the framework of this research could be applied to a wide range of other network materials. This could include other amorphous III-V materials, GeS_2, SiO_2, MoS_2 and more.

Bibliography

(1) W. Balmain, *The London, Edinburgh, and Dublin Philosophical Magazine and Journal of Science*, 1842, **21**, 270–277.

(2) L. Vel, G. Demazeau and J. Etourneau, *Materials Science and Engineering: B*, 1991, **10**, 149–164.

(3) J. Wang, C. H. Lee and Y. K. Yap, *Nanoscale*, 2010, **2**, 2028–2034.

(4) S. Hong et al., *Nature*, 2020, **582**, 511–516.

(5) H. Xu, X. Tu, Q. Wang, X. Wang and X. Chu, *Journal of Molecular Liquids*, 2020, **318**, 114315.

(6) N. Metropolis, A. W. Rosenbluth, M. N. Rosenbluth, A. H. Teller and E. Teller, *The Journal of Chemical Physics*, 1953, **21**, 1087–1092.

(7) B. J. Alder and T. E. Wainwright, *The Journal of Chemical Physics*, 1957, **27**, 1208–1209.

(8) B. J. Alder and T. E. Wainwright, *The Journal of Chemical Physics*, 1959, **31**, 459–466.

(9) L. F. Dobrzhinetskaya, R. Wirth, J. Yang, H. W. Green, I. D. Hutcheon, P. K. Weber and E. S. Grew, *American Mineralogist*, 2014, **99**, 764–772.

(10) C. B. Samantaray and R. N. Singh, *International Materials Reviews*, 2005, **50**, 313–344.

(11) R. R. Wills, *Int. J. High Technology Ceramics*, 1985, **1**, 153.

(12) Z. Pan, H. Sun, Y. Zhang and C. Chen, *Physical Review Letters*, 2009, **102**, 055503.

(13) Y. Nikaido, T. Ichibha, K. Hongo, F. A. Reboredo, K. C. H. Kumar, P. Mahadevan, R. Maezono and K. Nakano, *J. Phys. Chem. C*, 2022, **126**, 6000–6007.

(14) N. Alem, R. Erni, C. Kisielowski, M. D. Rossell, W. Gannett and A. Zettl, *Physical Review B*, 2009, **80**, 155425.

(15) S. M. Kim, A. Hsu, M. H. Park, S. H. Chae, S. J. Yun, J. S. Lee, D. H. Cho, W. Fang, C. Lee, T. Palacios, M. Dresselhaus, K. K. Kim, Y. H. Lee and J. Kong, *Nature Communications*, 2015, **6**, 8662.

(16) L. Chen, J. Tai, D. Wang, S. Wang, H. Liang and H. Yin, *Applied Physics Letters*, 2024, **124**, 042102.

(17) M. Chubarov, H. Pedersen, H. Högberg, J. Jensen and A. Henry, *Crystal Growth and Design*, 2012, **12**, 3215–3220.

(18) A. Rousseau, M. Moret, P. Valvin, W. Desrat, J. Li, E. Janzen, L. Xue, J. H. Edgar, G. Cassabois and B. Gil, *Physical Review Materials*, 2021, **5**, 064602.

(19) L. Wang et al., *Nature*, 2024, **629**, 74–79.

(20) S. M. Gilbert, T. Pham, M. Dogan, S. Oh, B. Shevitski, G. Schumm, S. Liu, P. Ercius, S. Aloni, M. L. Cohen and A. Zettl, *2D Materials*, 2019, **6**, 021006.

(21) S. Li, A. Pershin, P. Li and A. Gali, *npj 2D Materials and Applications*, 2024, **8**, 16.

(22) D. Golberg, Y. Bando, O. Stéphan and K. Kurashima, *Applied Physics Letters*, 1998, **73**, 2441–2443.

(23) W. Han, P. Redlich, F. Ernst and M. Rühle, *Applied Physics Letters*, 1999, **75**, 1875–1877.

(24) N. G. Chopra, R. J. Luyken, K. Cherrey, V. H. Crespi, M. L. Cohen, S. G. Louie and A. Zettl, *Science*, 1995, **269**, 966–967.

(25) D. Bae, K.-H. Lee and M. J. Kim, *Nanoscale*, 2024, **16**, 3817.

(26) K. S. Novoselov, D. Jiang, F. Schedin, T. J. Booth, V. V. Khotkevich, S. V. Morozov and A. K. Geim, *Proceedings of the National Academy of Sciences*, 2005, **102**, 10451–10453.

(27) A. Pakdel, C. Zhi, Y. Bando and D. Golberg, *Materials Today*, 2012, **15**, 256–265.

(28) D. Paciĺ, J. C. Meyer, Ç. Girit and A. Zettl, *Applied Physics Letters*, 2008, **92**, 133107.

(29) J. C. Meyer, A. Chuvilin, G. Algara-Siller, J. Biskupek and U. Kaiser, *Nano Letters*, 2009, **9**, 2683–2689.

(30) L. H. Li, Y. Chen, G. Behan, H. Zhang, M. Petravic and A. M. Glushenkov, *Journal of Materials Chemistry*, 2011, **21**, 11862–11866.

(31) A. Deepika, L. H. Li, A. M. Glushenkov, S. K. Hait, P. Hodgson and Y. Chen, *Scientific Reports*, 2014, **4**, 7288.

(32) W. Q. Han, L. Wu, Y. Zhu, K. Watanabe and T. Taniguchi, *Applied Physics Letters*, 2008, **93**, 223103.

(33) C. Zhi, Y. Bando, C. Tang, H. Kuwahara and D. Golberg, *Advanced Materials*, 2009, **21**, 2889–2893.

(34) J. N. Coleman et al., *Science*, 2011, **331**, 568–571.

(35) X. Li, X. Hao, M. Zhao, Y. Wu, J. Yang, Y. Tian and G. Qian, *Advanced Materials*, 2013, **25**, 2200–2204.

(36) L. Cao, S. Emami and K. Lafdi, *Materials Express*, 2014, **4**, 165–171.

(37) Z. Rafiei-Sarmazdeh, S. H. Jafari, S. J. Ahmadi and S. M. Zahedi-Dizaji, *Journal of Materials Science*, 2016, **51**, 3162–3169.

(38) M. T. Paffett, R. J. Simonson, P. Papin and R. T. Paine, *Surface Science*, 1990, **232**, 286–296.

(39) A. Nagashima, N. Tejima, Y. Gamou, T. Kawai and C. Oshima, *Surface Science*, 1996, **357-358**, 307–311.

(40) R. Y. Tay, M. H. Griep, G. Mallick, S. H. Tsang, R. S. Singh, T. Tumlin, E. H. T. Teo and S. P. Karna, *Nano Letters*, 2014, **14**, 839–846.

(41) Y. Stehle, H. M. Meyer, R. R. Unocic, M. Kidder, G. Polizos, P. G. Datskos, R. Jackson, S. N. Smirnov and I. V. Vlassiouk, *Chemistry of Materials*, 2015, **27**, 8041–8047.

(42) J. S. Lee, S. H. Choi, S. J. Yun, Y. I. Kim, S. Boandoh, J.-H. Park, B. G. Shin, H. Ko, S. H. Lee, Y.-M. Kim, Y. H. Lee, K. K. Kim and S. M. Kim, *Science*, 2018, **362**, 817–821.

(43) M. Sajjad, G. Morell and P. Feng, *ACS Applied Materials and Interfaces*, 2013, **5**, 5051–5056.

(44) H. Wang, X. Zhang, H. Liu, Z. Yin, J. Meng, J. Xia, X. M. Meng, J. Wu and J. You, *Advanced Materials*, 2015, **27**, 8109–8115.

(45) J. H. Meng, X. W. Zhang, H. Liu, Z. G. Yin, D. G. Wang, Y. Wang, J. B. You and J. L. Wu, *Applied Physics Letters*, 2016, **109**.

(46) D. Velázquez, R. Seibert, H. Man, L. Spentzouris and J. Terry, *Journal of Applied Physics*, 2016, **119**, 095306.

(47) D. Q. Hoang, S. Korneychuk, K. J. Sankaran, P. Pobedinskas, S. Drijkoningen, S. Turner, M. K. V. Bael, J. Verbeeck, S. S. Nicley and K. Haenen, *Acta Materialia*, 2017, **127**, 17–24.

(48) M. Sajjad, V. Makarov, F. Mendoza, M. S. Sultan, A. Aldalbahi, P. X. Feng, W. M. Jadwisienczak, B. R. Weiner and G. Morell, *Nanomaterials*, 2019, **9**, 925.

(49) H. Park, T. K. Kim, S. W. Cho, H. S. Jang, S. I. Lee and S. Y. Choi, *Scientific Reports*, 2017, **7**, 40091.

(50) J. K. Sprenger, H. Sun, A. S. Cavanagh, A. Roshko, P. T. Blanchard and S. M. George, *Journal of Physical Chemistry C*, 2018, **122**, 9455–9464.

(51) S. Nakhaie, J. M. Wofford, T. Schumann, U. Jahn, M. Ramsteiner, M. Hanke, J. M. Lopes and H. Riechert, *Applied Physics Letters*, 2015, **106**, 213108.

(52) Y. J. Cho, A. Summerfield, A. Davies, T. S. Cheng, E. F. Smith, C. J. Mellor, A. N. Khlobystov, C. T. Foxon, L. Eaves, P. H. Beton and S. V. Novikov, *Scientific Reports*, 2016, **6**.

(53) A. A. Tonkikh, E. N. Voloshina, P. Werner, H. Blumtritt, B. Senkovskiy, G. Güntherodt, S. S. Parkin and Y. S. Dedkov, *Scientific Reports*, 2016, **6**, 23547.

(54) F. Liu, X. Rong, Y. Yu, T. Wang, B. W. Sheng, J. Q. Wei, S. F. Liu, J. J. Yang, F. Bertram, F. J. Xu, X. L. Yang, Z. H. Zhang, Z. X. Qin, Y. T. Zhang, B. Shen and X. Q. Wang, *Applied Physics Letters*, 2020, **116**, 142104.

(55) M. Moret, A. Rousseau, P. Valvin, S. Sharma, L. Souqui, H. Pedersen, H. HÃ¶gberg, G. Cassabois, J. Li, J. H. Edgar and B. Gil, *Applied Physics Letters*, 2021, **119**, 262102.

(56) T. Jähnichen, J. Hojak, C. Bläker, C. Pasel, V. Mauer, V. Zittel, R. Denecke, D. Bathen and D. Enke, *ACS Omega*, 2022, **7**, 33375–33384.

(57) N. R. Glavin, C. Muratore, M. L. Jespersen, J. Hu, P. T. Hagerty, A. M. Hilton, A. T. Blake, C. A. Grabowski, M. F. Durstock, M. E. McConney, D. M. Hilgefort, T. S. Fisher and A. A. Voevodin, *Advanced Functional Materials*, 2016, **26**, 2640–2647.

(58) Q. Abbas, H. Liang, J. Shi, Y. Chen, X. Xia, A. ul Ahmad, J. Liu and G. Du, *Materials Letters*, 2018, **227**, 284–288.

(59) R. Zedlitz, M. Heintze and M. B. Schubert, *Journal of Non-Crystalline Solids*, 1996, 403–406.

(60) W. H. Zachariasen, *Journal of the American Chemical Society*, 1932, **54**, 3841–3851.

(61) A. Lebedev, *Transactions of the Optical Institute in Petrograd*, 1921, **2**, 1–20.

(62) W. Ahn, S. Lee, J. Oh, H. Lee and S. Y. Choi, *Advanced Materials*, 2025, **37**, 2413640.

(63) H. Grigoriew and J. Leciejewicz, *Thin Solid Films*, 1989, **172**, L75–L79.

(64) Y. T. Zhang, Y. P. Wang, X. Zhang, Y. Y. Zhang, S. Du and S. T. Pantelides, *Nano Letters*, 2022, **22**, 8018–8024.

(65) X. Zhang, Y.-T. Zhang, Y.-P. Wang, S. Li, S. Du, Y.-Y. Zhang and S. T. Pantelides, *Physical Review B*, 2024, **109**, 174106.

(66) J. Kotakoski, A. V. Krasheninnikov, U. Kaiser and J. C. Meyer, *Physical Review Letters*, 2011, **106**.

(67) F. R. Eder, J. Kotakoski, U. Kaiser and J. C. Meyer, *Scientific Reports*, 2014, **4**, 4060.

(68) C. T. Toh, H. Zhang, J. Lin, A. S. Mayorov, Y. P. Wang, C. M. Orofeo, D. B. Ferry, H. Andersen, N. Kakenov, Z. Guo, I. H. Abidi, H. Sims, K. Suenaga, S. T. Pantelides and B. Özyilmaz, *Nature*, 2020, **577**, 199–203.

(69) M. He, Y. Ding and X. Liu, *Advanced Science*, 2024, **11**, 2308187.

(70) V. G. Akkili et al., *ACS Nano*, 2025, **19**, 1056–1069.

(71) H.-P. Komsa and A. V. Krasheninnikov, in *Defects in Two-Dimensional Materials*, ed. R. Addou and L. Colombo, Elsevier, 2022, pp. 7–41.

(72) Y. Han, S. Feng, K. Cao, Y. Wang, L. Gao, Z. Xu and Y. Lu, *Cell Reports Physical Science*, 2020, **1**, 100172.

(73) B. He, W. J. Zhang, Z. Q. Yao, Y. M. Chong, Y. Yang, Q. Ye, X. J. Pan, J. A. Zapien, I. Bello, S. T. Lee, I. Gerhards, H. Zutz and H. HofsÃ¤ss, *Applied Physics Letters*, 2009, **95**, 252106.

(74) Y. Lin, T. V. Williams, W. Cao, H. E. Elsayed-Ali and J. W. Connell, *Journal of Physical Chemistry C*, 2010, **114**, 17434–17439.

(75) A. L. Gibb, N. Alem, J. H. Chen, K. J. Erickson, J. Ciston, A. Gautam, M. Linck and A. Zettl, *Journal of the American Chemical Society*, 2013, **135**, 6758–6761.

(76) O. Cretu, Y. C. Lin and K. Suenaga, *Nano Letters*, 2014, **14**, 1064–1068.

(77) Q. Li, X. Zou, M. Liu, J. Sun, Y. Gao, Y. Qi, X. Zhou, B. I. Yakobson, Y. Zhang and Z. Liu, *Nano Letters*, 2015, **15**, 5804–5810.

(78) C. Jin, F. Lin, K. Suenaga and S. Iijima, *Physical Review Letters*, 2009, **102**, 195505.

(79) O. Cretu, Y. C. Lin, M. Koshino, L. H. G. Tizei, Z. Liu and K. Suenaga, *Physical Review Letters*, 2015, **114**, 075502.

(80) T. Pham, A. L. Gibb, Z. Li, S. M. Gilbert, C. Song, S. G. Louie and A. Zettl, *Nano Letters*, 2016, **16**, 7142–7147.

(81) Q. Wang, Q. Zhang, X. Zhao, X. Luo, C. P. Y. Wong, J. Wang, D. Wan, T. Venkatesan, S. J. Pennycook, K. P. Loh, G. Eda and A. T. Wee, *Nano Letters*, 2018, **18**, 6898–6905.

(82) J. Kotakoski, C. H. Jin, O. Lehtinen, K. Suenaga and A. V. Krasheninnikov, *Physical Review B*, 2010, **82**, 113404.

(83) O. L. Krivanek, M. F. Chisholm, V. Nicolosi, T. J. Pennycook, G. J. Corbin, N. Dellby, M. F. Murfitt, C. S. Own, Z. S. Szilagyi, M. P.

Oxley, S. T. Pantelides and S. J. Pennycook, *Nature*, 2010, **464**, 571–574.

(84) Y. Liu, X. Zou and B. I. Yakobson, *ACS Nano*, 2012, **6**, 7053–7058.

(85) M. Topsakal, E. Aktürk and S. Ciraci, *Physical Review B*, 2009, **79**, 115442.

(86) L. Weston, D. Wickramaratne, M. Mackoit, A. Alkauskas and C. G. V. D. Walle, *Physical Review B*, 2018, **97**, 214104.

(87) S. Azevedo, J. R. Kaschny, C. M. D. Castilho and F. D. B. Mota, *Nanotechnology*, 2007, **18**.

(88) M. Zhou, T. Liang, B. Wu, J. Liu and P. Zhang, *Journal of Applied Physics*, 2020, **128**, 234304.

(89) Y. Ding, J. Yang, H. Wang, Y. Ji, Q. Guo, W. Wang, X. Shen, Y. Yao and R. Yu, *Physica Status Solidi - Rapid Research Letters*, 2021, **15**, 2100216.

(90) S. Li, P. Li and A. Gali, *Applied Physics Letters*, 2025, **126**, 062104.

(91) A. J. Stone and D. J. Wales, *Chemical Physics Letters*, 1986, **128**, 501–503.

(92) W. Chen, Y. Li, G. Yu, Z. Zhou and Z. Chen, *Journal of Chemical Theory and Computation*, 2009, **5**, 3088–3095.

(93) H. Hamdi, G. Thiering, Z. Bodrog, V. Ivády and A. Gali, *npj Computational Materials*, 2020, **6**, 178.

(94) S. Ajori, A. Ameri and R. Ansari, *Superlattices and Microstructures*, 2020, **142**, 106526.

(95) R. Wang, J. Yang, X. Wu and S. Wang, *Nanoscale*, 2016, **8**, 8210.

(96) A. Sajid, J. R. Reimers and M. J. Ford, *Physical Review B*, 2018, **97**, 064101.

(97) S. A. Tawfik, S. Ali, M. Fronzi, M. Kianinia, T. T. Tran, C. Stampfl, I. Aharonovich, M. Toth and M. J. Ford, *Nanoscale*, 2017, **9**, 13575–13582.

(98) H. Park, Y. Wen, S. X. Li, W. Choi, G. D. Lee, M. Strano and J. H. Warner, *Small*, 2021, **17**, 2100693.

(99) V. V. Brazhkin, A. G. Lyapin and R. J. Hemley, *Philosophical Magazine A*, 2002, **82**, 231–253.

(100) S. N. Monteiro, A. L. D. Skury, M. G. de Azevedo and G. S. Bobrovnitchii, *Journal of Materials Research and Technology*, 2013, **2**, 68–74.

(101) Y. B. Li, S. Wang, L. Dong, X. Wang, J. Luo, R. Zhang, D. Gao and H. Yang, *Materials Today Communications*, 2023, **37**, 107291.

(102) W. Lei, D. Portehault, D. Liu, S. Qin and Y. Chen, *Nature Communications*, 2013, **4**, 1777.

(103) T. Liu, Y. Li, J. He, K. Zhang, Y. Hu, X. Chen, C. Wang, X. Huang, L. Kong and J. Liu, *Journal of Materials Science*, 2019, **54**, 5366–5380.

(104) P. Karthikeyan, S. S. Elanchezhiyan, J. Preethi, S. Meenakshi and C. M. Park, *Applied Surface Science*, 2020, **511**, 145543.

(105) L. Garnier, A. Szymczyk, P. Malfreyt and A. Ghoufi, *Journal of Physical Chemistry Letters*, 2016, **7**, 3371–3376.

(106) H. Gao, Q. Shi, D. Rao, Y. Zhang, J. Su, Y. Liu, Y. Wang, K. Deng and R. Lu, *Journal of Physical Chemistry C*, 2017, **121**, 22105–22113.

(107) L. Liu, Y. Liu, Y. Qi, M. Song, L. Jiang, G. Fu and J. Li, *Separation and Purification Technology*, 2020, **251**, 117409.

(108) B. B. Sharma and A. G. Rajan, *Journal of Physical Chemistry B*, 2022, **126**, 1284–1300.

(109) R. Jafarzadeh, J. Azamat, H. Erfan-Niya and M. Hosseini, *Applied Surface Science*, 2019, **471**, 921–928.

(110) Z. Zhou, Y. Hu, H. Wang, Z. Xu, W. Wang, X. Bai, X. Shan and X. Lu, *Scientific Reports*, 2013, **3**, 3287.

(111) S. Liu, B. Lu, Q. Zhao, J. Li, T. Gao, Y. Chen, Y. Zhang, Z. Liu, Z. Fan, F. Yang, L. You and D. Yu, *Advanced Materials*, 2013, **25**, 4549–4554.

(112) T. Li, X. Jiao, T. You, F. Dai, P. Zhang, F. Yu, L. Hu, L. Ding, L. Zhang, Z. Wen and Y. Wu, *Ceramics International*, 2019, **45**, 4283–4289.

(113) G. Babu, A. Sawas, N. K. Thangavel and L. M. R. Arava, *Journal of Physical Chemistry C*, 2018, **122**, 10765–10772.

(114) G. Deng, Y. Zhang, Y. Yu, X. Han, Y. Wang, Z. Shi, X. Dong, B. Zhang, G. Du and Y. Liu, *ACS Applied Materials and Interfaces*, 2020, **12**, 6788–6792.

(115) C. R. Dean, A. F. Young, I. Meric, C. Lee, L. Wang, S. Sorgenfrei, K. Watanabe, T. Taniguchi, P. Kim, K. L. Shepard and J. Hone, *Nature Nanotechnology*, 2010, **5**, 722–726.

(116) D. Liu, X. Chen, Y. Zhang, D. Wang, Y. Zhao, H. Peng, Y. Liu, X. Xu, A. T. S. Wee and D. Wei, *Advanced Electronic Materials*, 2020, **6**, 2000059.

(117) T. T. Tran, K. Bray, M. J. Ford, M. Toth and I. Aharonovich, *Nature Nanotechnology*, 2016, **11**, 37–41.

(118) M. Nguyen, S. Kim, T. T. Tran, Z. Q. Xu, M. Kianinia, M. Toth and I. Aharonovich, *Nanoscale*, 2018, **10**, 2267–2274.

(119) A. L. Exarhos, D. A. Hopper, R. N. Patel, M. W. Doherty and L. C. Bassett, *Nature Communications*, 2019, **10**, 222.

(120) M. A. Uddin, N. Glavin, A. Singh, R. Naguy, M. Jespersen, A. Voevodin and G. Koley, *Applied Physics Letters*, 2015, **107**, 203110.

(121) S. M. Sattari-Esfahlan, H. G. Kim, S. H. Hyun, J. H. Choi, H. S. Hwang, E. T. Kim, H. G. Park and J. H. Lee, *ACS Applied Materials and Interfaces*, 2023, **15**, 7274–7281.

(122) Z. Lu, M. Zhu, Y. Liu, G. Zhang, Z. Tan, X. Li, S. Xu, L. Wang, R. Dou, B. Wang, Y. Yao, Z. Zhang, J. Dong, Z. Cheng and S. Chen, *ACS Applied Materials and Interfaces*, 2022, **14**, 25984–25992.

(123) Y. Li, J. Guo, W. Zheng and F. Huang, *Applied Physics Letters*, 2020, **117**, 23504.

(124) C. Wu, P. Lv, Z. Zhu, J. Li, C. Tu, C. Chen, G. Lakshminarayana, H. Wang and Y. Wang, *Journal of Alloys and Compounds*, 2025, **1010**, 177635.

(125) Y. R. Jeon, Y. Abbas, A. S. Sokolov, S. Kim, B. Ku and C. Choi, *ACS Applied Materials and Interfaces*, 2019, **11**, 23329–23336.

(126) J. Lee, J. H. Ryu, B. Kim, F. Hussain, C. Mahata, E. Sim, M. Ismail, Y. Abbas, H. Abbas, D. K. Lee, M. H. Kim, Y. Kim, C. Choi, B. G. Park and S. Kim, *ACS Applied Materials and Interfaces*, 2020, **12**, 33908–33916.

(127) A. C. Khot, T. D. Dongale, K. A. Nirmal, J. H. Sung, H. J. Lee, R. D. Nikam and T. G. Kim, *ACS Applied Materials and Interfaces*, 2022, **14**, 56.

(128) Ǒ. Ç. Yıldırım, M. E. Arslan, S. Ǒner, I. Cacciatore, A. D. Stefano, A. Mardinoglu and H. Turkez, *International Journal of Molecular Sciences*, 2022, **23**.

(129) I. V. Sukhorukova, I. Y. Zhitnyak, A. M. Kovalskii, A. T. Matveev, O. I. Lebedev, X. Li, N. A. Gloushankova, D. Golberg and D. V.

Shtansky, *ACS Applied Materials and Interfaces*, 2015, **7**, 17217–17225.

(130) X. Li, X. Wang, J. Zhang, N. Hanagata, X. Wang, Q. Weng, A. Ito, Y. Bando and D. Golberg, *Nature Communications*, 2017, **8**, 13936.

(131) L. Li, J. Li, Y. Shi, P. Du, Z. Zhang, T. Liu, R. Zhang and Z. Liu, *ACS Nano*, 2019, **13**, 13843–13852.

(132) G. Lian, X. Zhang, S. Zhang, D. Liu, D. Cui and Q. Wang, *Energy and Environmental Science*, 2012, **5**, 7072–7080.

(133) R. Ma, Y. Bando, H. Zhu, T. Sato, C. Xu and D. Wu, *Journal of the American Chemical Society*, 2002, **124**, 7672–7673.

(134) C. Tang, Y. Bando, X. Ding, S. Qi and D. Golberg, *Journal of the American Chemical Society*, 2002, **124**, 14550–14551.

(135) G. Mpourmpakis and G. E. Froudakis, *Catalysis Today*, 2007, **120**, 341–345.

(136) A. L. M. Reddy, A. E. Tanur and G. C. Walker, *International Journal of Hydrogen Energy*, 2010, **35**, 4138–4143.

(137) T. Xu, K. Zhang, Q. Cai, N. Wang, L. Wu, Q. He, H. Wang, Y. Zhang, Y. Xie, Y. Yao and Y. Chen, *Chemical Engineering Journal*, 2022, **431**, 134118.

(138) W. Meng, Y. Huang, Y. Fu, Z. Wang and C. Zhi, *Journal of Materials Chemistry C*, 2014, **2**, 10049–10061.

(139) M. Yamaguchi, D. M. Tang, C. Zhi, Y. Bando, D. Shtansky and D. Golberg, *Acta Materialia*, 2012, **60**, 6213–6222.

(140) M. Antillon, P. Nautiyal, A. Loganathan, B. Boesl and A. Agarwal, *Advanced Engineering Materials*, 2018, **20**, 1800122.

(141) J. Bustillos, X. Lu, P. Nautiyal, C. Zhang, B. Boesl and A. Agarwal, *Advanced Engineering Materials*, 2020, **22**, 2000702.

(142) C. Gao, P. Feng, S. Peng and C. Shuai, *Acta Biomaterialia*, 2017, **61**, 1–20.

(143) B. Liu, Y. Gu, Y. Ji, G. Zheng, J. Wang, Y. Wu, F. Long and B. Zhou, *Journal of the Ceramic Society of Japan*, 2021, **129**, 187–194.

(144) N. P. Bansal, J. B. Hurst and S. R. Choi, *Journal of the American Ceramic Society*, 2006, **89**, 388–390.

(145) P. Tatarko, S. Grasso, H. Porwal, Z. Chlup, R. Saggar, I. Dlouhý and M. J. Reece, *Journal of the European Ceramic Society*, 2014, **34**, 3339–3349.

(146) W. Hao, C. Marichy and A. Brioude, *Environmental Science: Nano*, 2017, **4**, 2311–2320.

(147) H. Lim, B. L. Suh, M. J. Kim, H. Yun, J. Kim, B. J. Kim and S. G. Jang, *Journal of Membrane Science*, 2018, **551**, 172–179.

(148) A. Siria, P. Poncharal, A. L. Biance, R. Fulcrand, X. Blase, S. T. Purcell and L. Bocquet, *Nature*, 2013, **494**, 455–458.

(149) Q. Peng, W. Ji and S. De, *Computaional Materials Science*, 2012, **56**, 11–17.

(150) B. Grosjean, C. Pean, A. Siria, L. Bocquet, R. Vuilleumier and M. L. Bocquet, *Journal of Physical Chemistry Letters*, 2016, **7**, 4695–4700.

(151) B. Chettri, P. K. Patra, N. N. Hieu and D. P. Rai, *Surfaces and Interfaces*, 2021, **24**, 101043.

(152) A. R. Juárez, F. Ortíz-Chi, R. Pino-Ríos, G. Cárdenas-Jirón, M. S. Villanueva and E. C. Anota, *Chemical Physics Letters*, 2020, **741**, 137097.

(153) L.-C. Yin, H.-M. Cheng and R. Saito, *Physical Review B*, 2010, **81**, 153407.

(154) A. Malatesta, S. Fahy and G. B. Bachelet, *Physical Review B*, 1997, **56**.

(155) B. G. Brito, G. Q. Hai and L. Cândido, *Computational Condensed Matter*, 2022, **33**, e00759.

(156) B. G. Brito, L. C. DaSilva, G. Q. Hai and L. Cândido, *Physica Status Solidi (B)*, 2019, **256**, 1900164.

(157) R. J. Hunt, B. Monserrat, V. Zólyomi and N. D. Drummond, *Physical Review B*, 2020, **101**, 205115.

(158) B. G. Brito, L. Cândido, J. N. T. Rabelo and G. Q. Hai, *Computational Condensed Matter*, 2022, **31**, e00660.

(159) Y. Wu, L. K. Wagner and N. R. Aluru, *Journal of Chemical Physics*, 2016, **144**, 164118.

(160) S. Luo, R. P. Misra and D. Blankschtein, *ACS Nano*, 2024, **18**, 1629–1646.

(161) M. Szyniszewski, E. Mostaani, A. Knothe, V. Enaldiev, A. C. Ferrari, V. I. Falâko and N. D. Drummond, *ACS Nano*, 2025, **19**, 6014–6020.

(162) J. Tersoff, *Physical Review B*, 1988, **37**, 6991–7000.

(163) K. Albe, W. Möller and K.-H. Heinig, *Radiation Effects and Defects in Solids*, 1997, **141**, 85–97.

(164) W. Sekkal, B. Bouhafs, H. Aourag and M. Certier, *Journal of Physics Condensed Matter*, 1998, **10**, 4975–4984.

(165) K. Matsunaga, C. Fisher and H. Matsubara, *Japanese Journal of Applied Physics*, 2000, **39**, L48–L51.

(166) C. Sevik, A. Kınacı, J. B. Haskins and T. Çağın, *Physical Review B*, 2011, **84**, 85409.

(167) A. Kınacı, J. B. Haskins, C. Sevik and T. Çağın, *Physical Review B*, 2012, **86**, 115410.

(168) R. Jacobs et al., *Current Opinion in Solid State and Materials Science*, 2025, **35**, 101214.

(169) Y. Zhao, X. Peng, T. Fu, C. Huang, C. Feng, D. Yin and Z. Wang, *Applied Surface Science*, 2016, **382**, 309–315.

(170) L. Chen, K. Elibol, H. Cai, C. Jiang, W. Shi, C. Chen, H. S. Wang, X. Wang, X. Mu, C. Li, K. Watanabe, T. Taniguchi, Y. Guo, J. C. Meyer and H. Wang, *2D Materials*, 2021, **8**, 24001.

(171) P. Liu, Q. X. Pei and Y. W. Zhang, *Scientific Reports*, 2022, **12**, 11860.

(172) K. Wang, J. Huang, Y. Cai, Y. Liang and Q. Han, *Tribology International*, 2025, **204**, 110462.

(173) F. L. Thiemann, P. Rowe, E. A. Müller and A. Michaelides, *Journal of Physical Chemistry C*, 2020, **124**, 22278–22290.

(174) V. Choyal, M. Patil, N. Luhadiya and S. I. Kundalwal, *Journal of Physics: Materials*, 2025, **8**, 015003.

(175) T. Han, Y. Luo and C. Wang, *Journal of Physics D: Applied Physics*, 2014, **47**, 025303.

(176) N. Li, N. Ding, S. Qu, L. Liu, W. Guo and C. M. L. Wu, *Computational Materials Science*, 2017, **140**, 356–366.

(177) M. Salavati, A. Mojahedin and A. H. N. Shirazi, *Frontiers of Structural and Civil Engineering*, 2020, **14**, 623–631.

(178) B. Mortazavi and G. Cuniberti, *RSC Advances*, 2014, **4**, 19137–19143.

(179) Y. Liu, Y. Pan, D. Yin, S. Song, L. Lin, M. Zhang, X. Qi and J. Yao, *Computational Materials Science*, 2021, **186**, 110047.

(180) A. Chandra, P. K. Patra and B. Bhattacharya, *Materials Research Express*, 2016, **3**, 25005.

(181) H. Zeighampour and Y. T. Beni, *Molecular simulation*, 2019, **46**, 279–288.

(182) Y. Liu, Y. Pan, D. Yin, S. Song, L. Lin, X. Qi, M. Zhang and J. Yao, *Journal of Non-Crystalline Solids*, 2021, **558**, 120664.

(183) O. Kaya, L. Colombo, A. Antidormi, M. Lanza and S. Roche, *Nanoscale Horiz.*, 2023, **8**, 361.

(184) S. P. Ju, C. C. Huang and H. Y. Chen, *Computational Materials Science*, 2024, **232**, 112664.

(185) A. Seal and A. G. Rajan, *Nano Letters*, 2021, **21**, 8008–8016.

(186) Y. Wang, H. Luo, X. R. Advincula, Z. Zhao, A. Esfandiar, D. Wu, K. D. Fong, L. Gao, A. S. Hazrah, T. Taniguchi, C. Schran, Y. Nagata, L. Bocquet, M.-L. Bocquet, Y. Jiang, A. Michaelides and M. Bonn, *Journal of the American Chemical Society*, 2025, **147**, 30107–30116.

(187) M. Fischer, J. M. Caridad, A. Sajid, S. Ghaderzadeh, M. Ghorbani-Asl, L. Gammelgaard, P. BÃ‚ggild, K. S. Thygesen, A. V. Krasheninnikov, S. Xiao, M. Wubs and N. Stenger, *Sci. Adv*, 2021, **7**, 7138–7155.

(188) S. Ghosh, P. Nath, S. Moshat and D. Sanyal, *Physica Scripta*, 2024, **99**, 045913.

(189) S. J. Mahdizadeh and S. F. Tayyari, *Journal of Molecular Modeling*, 2012, **18**, 2699–2708.

(190) N. Ullah, A. Karim, M. Iqbal, R. E. Malekshah, S. Ali, J. Haribabu and S. C. Hsu, *Journal of Molecular Modeling*, 2025, **31**, 135.

(191) M. S. Kudinova, S. R. Odinaev, E. V. Boroznina and N. A. Stebenkova, *AIP Conference Proceedings*, 2020, **2313**, 030053.

(192) V. Caciuc, N. Atodiresei, M. Callsen, P. Lazić and S. Blügel, *Journal of Physics Condensed Matter*, 2012, **24**, 424214.

(193) A. Kinal and S. Sayhan, *International Journal of Hydrogen Energy*, 2016, **41**, 392–400.

(194) A. Zunger, *Journal of Physics C: Solid State Physics*, 1974, **7**, 96–106.

(195) M. Zhu, M. Matsubara and E. Bellotti, *Physical Review Applied*, 2023, **20**, 034055.

(196) J. Song, J. Wu, Y. Huang and K. C. Hwang, *Nanotechnology*, 2008, **19**, 445705.

(197) E. S. Oh, *Metals and Materials International*, 2011, **17**, 21–27.

(198) T. C. Theodosiou and D. A. Saravanos, *International Journal for Computational Methods in Engineering Science and Mechanics*, 2011, **12**, 203–211.

(199) J. W. Yan and K. M. Liew, *Composite Structures*, 2015, **125**, 489–498.

(200) A. Kia, F. Sadeghi and R. Ansari, *Bulletin of Materials Science*, 2024, **47**, 105.

(201) O. Hod, *Journal of Chemical Theory and Computation*, 2012, **8**, 1360–1369.

(202) D. A. Evans, A. G. McGlynn, B. M. Towlson, M. Gunn, D. Jones, T. E. Jenkins, R. Winter and N. R. Poolton, *Journal of Physics: Condensed Matter*, 2008, **20**, 075233.

(203) G. Cassabois, P. Valvin and B. Gil, *Nature Photonics*, 2016, **10**, 262–266.

(204) D. Wickramaratne, L. Weston and C. G. V. D. Walle, *Journal of Physical Chemistry C*, 2018, **122**, 25524–25529.

(205) C. Elias, P. Valvin, T. Pelini, A. Summerfield, C. J. Mellor, T. S. Cheng, L. Eaves, C. T. Foxon, P. H. Beton, S. V. Novikov, B. Gil and G. Cassabois, *Nature Communications*, 2019, **10**, 2639.

(206) K. S. Novoselov, A. K. Geim, S. V. Morozov, D. Jiang, Y. Zhang, S. V. Dubonos, I. V. Grigorieva and A. A. Firsov, *Science*, 2004, **306**, 3824.

(207) A. K. Geim and K. S. Novoselov, *Nature Materials*, 2007, **6**, 183–191.

(208) M. Terrones, W. Hsu, T. H, J. Zhang, S. Ramos, J. Hare, R. Castllo, K. Prassides, A. Cheetham, H. Kroto and D. Walton, *Chemical Physics Letters*, 1996, **259**, 568–573.

(209) A. Loiseau, F. Willaime, N. Demoncy, G. Hug and H. Pascard, *Physical Review Letters*, 1996, **76**, 4737.

(210) Y. Saito and M. Maida, *Journal of Physical Chemistry A*, 1999, **103**, 1291–1293.

(211) L. Xue, B. Lu, Z. S. Wu, C. Ge, P. Wang, R. Zhang and X. D. Zhang, *Chemical Engineering Journal*, 2014, **243**, 494–499.

(212) Y. Chao, J. Zhang, H. Li, P. Wu, X. Li, H. Chang, J. He, H. Wu, H. Li and W. Zhu, *Chemical Engineering Journal*, 2020, **387**, 124138.

(213) D. J. Joyner and D. M. Hercules, *Journal of Chemical Physics*, 1980, **72**, 1095–1108.

(214) Y.-N. Xu and W. Y. Ching, *Physical Review B: Condensed Matter*, 1991, **44**, 7787–7798.

(215) L. Chkhartishvili, S. Dekanosidze, N. Maisuradze, M. Beridze and R. Esiava, *Eastern-European Journal of Enterprise Technologies*, 2015, **3**, 50–57.

(216) T. Maaravi, I. Leven, I. Azuri, L. Kronik and O. Hod, *Journal of Physical Chemistry C*, 2017, **121**, 22826–22835.

(217) A. H. Silver and P. J. Bray, *Journal of Chemical Physics*, 1960, **32**, 288–292.

(218) P. J. Bray, *AIP Conf. Proc*, 1986, **140**, 142–167.

(219) L. Susana, A. Gloter, M. Tencé and A. Zobelli, *ACS Nano*, 2024, **18**, 7424–7432.

(220) D. Golze, J. Hutter and M. Iannuzzi, *Physical Chemistry Chemical Physics*, 2015, **17**, 14307–14316.

(221) A. K. Verma and B. B. Sharma, *Computational Materials Science*, 2024, **245**, 113323.

(222) K. Lawniczak-Jablonska, T. Suski, I. Gorczyca, N. E. Christensen, K. E. Attenkofer, R. C. C. Perera, E. M. Gullikson, J. H. Underwood, D. L. Ederer and Z. L. Weber, *Physical Review B*, 2000, **61**, 16623–16632.

(223) M. B. Khusidman and V. S. Neshpor, *Soviet Power Metallurgy and Metal Ceramics*, 1970, **9**, 672–675.

(224) A. G. Rajan, M. S. Strano and D. Blankschtein, *Journal of Physical Chemistry Letters*, 2018, **9**, 1584–1591.

(225) E. C. Anota, *SN Applied Sciences*, 2022, **4**, 295.

(226) S. Yamamurat, M. T. Ata and M. Sakata, *Journal of Physics and Chemistry of Solids*, 1997, **58**, 177–183.

(227) J. Robertson, *Materials Science and Engineering R*, 2002, **37**, 129–281.

(228) Y. Shang, Z. Liu, J. Dong, M. Yao, Z. Yang, Q. Li, C. Zhai, F. Shen, X. Hou, L. Wang, N. Zhang, W. Zhang, R. Fu, J. Ji, X. Zhang, H. Lin, Y. Fei, B. Sundqvist, W. Wang and B. Liu, *Nature*, 2021, **599**, 599–604.

(229) I. S. Kim, C. E. Shim, S. W. Kim, C. S. Lee, J. Kwon, K. E. Byun and U. Jeong, *Advanced Materials*, 2023, **35**, 2204912.

(230) A. Kumar, M. Wilson and M. F. Thorpe, *Journal of Physics: Condensed Matter*, 2012, **24**, 485003–485010.

(231) J. Joo, J.-H. Lee, Y. Jang, S.-G. Kang, Y.-N. Kwon, J. Chung, S. Lee, C. Kim, T.-H. Kim, C.-W. Yang, U. J. Kim, B. L. Choi, D. Whang and S.-W. Hwang, *Science Advances*, 2017, **3**, e1601821.

(232) L. Lichtenstein, M. Heyde and H. J. Freund, *Journal of Physical Chemistry C*, 2012, **116**, 20426–20432.

(233) P. Y. Huang, S. Kurasch, A. Srivastava, V. Skakalova, J. Kotakoski, A. V. Krasheninnikov, R. Hovden, Q. Mao, J. C. Meyer, J. Smet, D. A. Muller and U. Kaiser, *Nano Letters*, 2012, **12**, 1081–1086.

(234) A. Kumar, D. Sherrington, M. Wilson and M. F. Thorpe, *Journal of Physics: Condensed Matter*, 2014, **26**, 395401.

(235) E. Véron, M. N. Garaga, D. Pelloquin, S. Cadars, M. Suchomel, E. Suard, D. Massiot, V. Montouillout, G. Matzen and M. Allix, *Inorganic Chemistry*, 2013, **52**, 4250–4258.

(236) A. M. Lejus, N. Pelletier-Allard, R. Pelletier and D. Vivien, *Optical Materials*, 1996, **6**, 129–137.

(237) P. Florian, E. Veron, T. F. Green, J. R. Yates and D. Massiot, *Chemistry of Materials*, 2012, **24**, 4068–4079.

(238) J. Xiao, X. Chen, P. V. Sushko, M. L. Sushko, L. Kovarik, J. Feng, Z. Deng, J. Zheng, G. L. Graff, Z. Nie, D. Choi, J. Liu, J. G. Zhang and M. S. Whittingham, *Advanced Materials*, 2012, **24**, 2109–2116.

(239) A. Gautam, M. Sadowski, M. Ghidiu, N. Minafra, A. Senyshyn, K. Albe and W. G. Zeier, *Advanced Energy Materials*, 2021, **11**, 2003369.

(240) M. J. Fallon, V. Faka, M. A. Lange, M. A. Kraft, E. Suard, E. T. Connolly, B. E. Francisco, A. G. Squires and W. G. Zeier, *Journal of the American Chemical Society*, 2025, **147**, 10151–10159.

(241) D. Frenkel and B. Smit, *Understanding molecular simulation : from algorithms to applications*, Academic Press, Third edition, 2023, pp. 1–260.

(242) K. Binder and W. Kob, *Glassy materials and disordered solids: An introduction to their statistical mechanics*, World scientific, 2011, pp. 35–81.

(243) M. P. Allen and D. J. Tildesley, *Computer Simulations of Liquids*, Oxford University Press, 2nd edn., 2017, pp. 1–257.

(244) H. E. Fischer, A. C. Barnes and P. S. Salmon, *Reports on Progress in Physics*, 2006, **69**, 233–299.

(245) P. F. Peterson, D. Olds, M. T. Mcdonnell and K. Page, *Journal of Applied Crystallography*, 2021, **54**, 317–332.

(246) D. A. Keen, *Journal of Applied Crystallography*, 2001, **34**, 172–177.

(247) C. J. Gommes, S. Jaksch and H. Frielinghaus, *Journal of Applied Crystallography*, 2021, **54**, 1832–1843.

(248) W. Donner, S. Chamera, A. Rühm, H. Dosch, S. Ulrich and H. Ehrhardt, *MS No. APA616 Appl. Phys. A*, 1997, **65**, 1–4.

(249) T. E. Faber and J. M. Ziman, *Philosophical Magazine*, 1965, **11**, 153–173.

(250) A. B. Bhatia and D. E. Thornton, *Physical Review B*, 1970, **2**, 3004–3012.

(251) P. S. Salmon, *Proceedings of the Royal Society of London. Series A: Mathematical and Physical Sciences*, 1992, **437**, 591–606.

(252) P. S. Salmon, R. A. Martin, P. E. Mason and G. J. Cuello, *Nature*, 2005, **435**, 75–78.

(253) F. H. Stillinger and R. Lovett, *The Journal of Chemical Physics*, 1968, **48**, 3858–3868.

(254) A. Strihan, *Regional Studies*, 2008, **42**, 539–554.

(255) A. Sih, S. F. Hanser and K. A. McHugh, *Behavioral Ecology and Sociobiology*, 2009, **63**, 975–988.

(256) N. Trinajstic, *Chemical graph theory*, CRC press, 2018, pp. 1–3.

(257) M. Feinberg, *Foundations of chemical reaction network theory*, Springer, 2019, pp. 23–42.

(258) F. T. Lewis, *The Anatomical Record*, 1928, **38**, 341–376.

(259) D. O. Morley, A. L. Thorneywork, R. P. A. Dullens and M. Wilson, *Physical Review E*, 2020, **101**, 42309.

(260) D. A. Aboav, *Metallography*, 1970, **3**, 383–390.

(261) D. Weaire, *Metallography*, 1974, **7**, 157–160.

(262) R. Carter, Y. E. Sánchez-Corrales, M. Hartley, V. A. Grieneisen and A. F. Marée, *Development*, 2017, **144**, 4386–4397.

(263) M. C. Gibson, A. B. Patel, R. Nagpal and N. Perrimon, *Nature*, 2006, **442**, 1038–1041.

(264) C. Allain and L. Limat, *Physical Review Letters*, 1995, **74**, 2981–2985.

(265) M. Tong, K. Cole, P. R. Brito-Parada, S. Neethling and J. J. Cilliers, *Langmuir*, 2017, **33**, 3839–3846.

(266) X. Yuan and A. N. Cormack, *Computational Materials Science*, 2002, **24**, 343–360.

(267) M. C. C. Ribeiro and L. C. J. Almeida, *The Journal of Chemical Physics*, 2000, **113**, 4722–4731.

(268) P. L. Silvestrelli and M. Parrinello, *Physical Review Letters*, 1999, **82**, 3308.

(269) D. Kang, J. Dai and J. Yuan, *Journal of Chemical Physics*, 2011, **135**, 024505.

(270) M. K. Y. Chan, E. L. Shirley, N. K. Karan, M. Balasubramanian, Y. Ren, J. P. Greeley and T. T. Fister, *The Journal of Physical Chemistry Letters*, 2011, **2**, 2483–2486.

(271) X. Yang et al., *Advanced Materials*, 2019, **31**, 1901220.

(272) A. I. Boldyrev and J. Simons, *The Journal of Chemical Physics*, 1993, **98**, 4745–4752.

(273) A. K. Rappe and W. A. Goddard III, *The Journal of Chemical Physics*, 1991, **95**, 3358–3363.

(274) S. W. Rick, S. J. Stuart and B. J. Berne, *The Journal of Chemical Physics*, 1994, **101**, 6141–6156.

(275) M. C. Ribeiro and L. C. Almeida, *Journal of Chemical Physics*, 1999, **110**, 11445–11448.

(276) M. Wilson, M. C. Ribeiro, M. C. Wilding, C. Benmore, J. K. Weber, O. Alderman, A. Tamalonis and J. B. Parise, *Journal of Physical Chemistry A*, 2018, **122**, 1071–1076.

(277) M. C. Wilding, F. Demmel and M. Wilson, *Journal of Physical Chemistry A*, 2025, 1890–1895.

(278) P. Comba, B. Martin and A. Sanyal, *Journal of Computational Chemistry*, 2013, **34**, 1598–1608.

(279) L. Landry and P. Li, *Journal of Chemical Information and Modeling*, 2024, **64**, 812–824.

(280) L. Landry and P. Li, *J. Phys. Chem. B*, 2024, **128**, 10329–10338.

(281) M. Ambrosetti, S. Skoko, T. Giovannini and C. Cappelli, *Journal of Chemical Theory and Computation*, 2021, **17**, 7146–7156.

(282) R. S. Mulliken, *J. Chem. Phys*, 1934, **2**, 782–793.

(283) R. G. Parr and R. G. Pearson, *Journal of the American Chemical Society*, 1983, **105**, 7512–7516.

(284) S. Nosé, *The Journal of Chemical Physics*, 1984, **81**, 511–519.

(285) W. G. Hoover, *Physical Review A*, 1985, **31**, 1695–1697.

(286) N. Metropolis and S. Ulam, *Journal of the American Statistical Association*, 1949, **44**, 335–341.

(287) D. P. Kroese, T. Brereton, T. Taimre and Z. I. Botev, *Wiley Interdisciplinary Reviews: Computational Statistics*, 2014, **6**, 386–392.

(288) P. Ströker, R. Hellmann and K. Meier, *Physical Review E*, 2022, **105**, 064129.

(289) F. Wooten, K. Winer and D. Weaire, *Physical Review Letters*, 1985, **54**, 1392.

(290) O. Whitaker, D. O. Morley and M. Wilson, *The Journal of Chemical Physics*, 2025, **162**, 214506.

(291) S. Kirkpatrick, C. D. Gelatt and M. P. Vecchi, *Science*, 1983, **220**, 671–680.

(292) D. O. Morley, DPhil Thesis, University of Oxford, 2020.

(293) M. Karplus and J. A. McCammon, *Nature Structural Biology*, 2002, **9**, 646–652.

(294) J. L. Barrat, J. Baschnagel and A. Lyulin, *Soft Matter*, 2010, **6**, 3430–3446.

(295) D. Hinojosa-Romero, A. Valladares, R. M. Valladares, I. Rodríguez and A. A. Valladares, *Scientific Reports*, 2024, **14**, 7949.

(296) W. C. Swope, H. C. Andersen, P. H. Berens and K. R. Wilson, *The Journal of Chemical Physics*, 1982, **76**, 637–649.

(297) L. Verlet, *Physical Review*, 1967, **159**, 98.

(298) G. J. Martyna, M. L. Klein and M. Tuckerman, *The Journal of Chemical Physics*, 1992, **97**, 2635–2643.

(299) J. Nocedal and S. J. Wright, *Numerical optimization*, ed. S. J. Wright, Springer, 2nd ed., 2006.

(300) J. C. Meza, *Wiley Interdisciplinary Reviews: Computational Statistics*, 2010, **2**, 719–722.

(301) D. O. Morley and M. Wilson, *Journal of Physics: Condensed Matter*, 2018, **30**, 50LT02.

(302) J. Tersoff, *Physical Review Letters*, 1988, **61**, 2879–2882.

(303) J. Tersoff, *Physical Review B*, 1989, **39**, 5566–5568.

(304) K. Mohammadi, A. A. Madadi, Z. Bajalan and H. N. Pishkenari, *International Journal of Mechanical Sciences*, 2020, **187**.

(305) J. Luo, Q. Li, J. Pei, J. Huang, Z. Li and L. Liu, *Surface Science*, 2024, **742**, 122449.

(306) J. Wang, A. M. Rajendran and A. M. Dongare, *Journal of Materials Science*, 2015, **50**, 8128–8141.

(307) M.-Q. Le, *Journal of Mechanical Science and Technology*, 2014, **28**, 4173–4178.

(308) R. Kumar, G. Rajasekaran and A. Parashar, *Nanotechnology*, 2016, **27**, 085706.

(309) V. Vijayaraghavan and L. Zhang, *Nanomaterials*, 2018, **8**, 546.

(310) X. Wu and Q. Han, *Computational Materials Science*, 2020, **184**, 109938.

(311) J. H. Los, J. M. Kroes, K. Albe, R. M. Gordillo, M. I. Katsnelson and A. Fasolino, *Physical Review B*, 2017, **96**, 183108.

(312) M. Z. Dehaghani, F. Yousefi, S. M. Sajadi, M. T. Munir, O. Abida, S. Habibzadeh, A. H. Mashhadzadeh, N. Rabiee, E. Mostafavi and M. R. Saeb, *Molecules*, 2021, **26**, 4920.

(313) M. Corso, W. Auwärter, M. Muntwiler, A. Tamai, T. Greber and J. Osterwalder, *Science*, 2004, **303**, 217–220.

(314) H. Wang, Y. Zhao, Y. Xie, X. Ma and X. Zhang, *Journal of Semiconductors*, 2017, **38**.

(315) S. Roy et al., *Advanced Materials*, 2021, **33**, 2101589.

(316) A. E. Naclerio, P. R. Kidambi, A. E. Naclerio and P. R. Kidambi, *Advanced Materials*, 2023, **35**, 2207374.

(317) A. Valentin, J. Sée, S. Galdin-Retailleau and P. Dollfus, *Journal of Physics: Condensed Matter*, 2008, **20**, 145213.

(318) V. S. Harutyunyan, *Journal of Solid State Chemistry*, 2021, **296**, 121993.

(319) W. Vanhinsbergh, Master's Thesis, University of Oxford, 2024.

(320) L. Piggott, Master's Thesis, University of Oxford, 2025.

(321) V. L. Solozhenko, V. Z. Turkevich and W. B. Holzapfel, *Journal of Physical Chemistry B*, 1999, **103**, 2903–2905.

(322) A. Heafield and M. Wilson, *Journal of Physics: Condensed Matter*, 2024, **37**, 045101.

(323) A. Heafield and M. Wilson, *The Journal of Chemical Physics*, 2026, **164**, 24705.

(324) Z. Liu, L. Ma, G. Shi, W. Zhou, Y. Gong, S. Lei, X. Yang, J. Zhang, J. Yu, K. P. Hackenberg, A. Babakhani, J. C. Idrobo, R. Vajtai, J. Lou and P. M. Ajayan, *Nature Nanotechnology*, 2013, **8**, 119–124.

(325) M. Kaur, K. Singh, A. V. De and A. Kumar, *New Journal of Chemistry*, 2023, **47**, 2137.

(326) B. Xu, Y. Zhou, Y. She, Z. Ding, Y. Li, B. Yao, H. A. Ma, H. Li and Y. Lan, *Applied Physics Letters*, 2025, **126**, 071902.

(327) A. R. Badzian, *Materials Research Bulletin*, 1981, **16**, 1385–1393.

(328) X. Liu, X. Jia, Z. Zhang, M. Zhao, W. Guo, G. Huang and H. A. Ma, *Crystal Growth and Design*, 2011, **11**, 1006–1014.

(329) L. Ming-kai, Y. Li-jiang, Z. Zhong-lin and M. Teng-cai, *Chinese Physics Letters*, 1999, **16**, 71.

(330) Y. J. Tian, J. L. He, D. L. Yu, D. C. Li, G. T. Zou, X. P. Jia, L. X. Chen and O. Yanagisawa, *Radiation Effects and Defects in Solids*, 2002, **157**, 245–251.

(331) J. L. He, Z. Y. Liu, D. L. Yu, B. Xu and Y. J. Tian, *Frontiers of Physics in China*, 2007, **2**, 186–190.

(332) A. Castellanos-Gomez, X. Duan, Z. Fei, H. R. Gutierrez, Y. Huang, X. Huang, J. Quereda, Q. Qian, E. Sutter and P. Sutter, *Nature Reviews Methods Primers*, 2022, **2**, 58.

(333) R. Ribeiro-Palau, C. Zhang, K. Watanabe, T. Taniguchi, J. Hone and C. R. Dean, *Science*, 2018, **361**, 690–693.

(334) Y. Cao, V. Fatemi, S. Fang, K. Watanabe, T. Taniguchi, E. Kaxiras and P. Jarillo-Herrero, *Nature*, 2018, **556**, 43–50.

(335) S. Angizi, M. A. Akbar, M. Darestani-Farahani and P. Kruse, *ECS Journal of Solid State Science and Technology*, 2020, **9**, 083004.

(336) M. Li, Y. Sun, X. Xue, X. Lu, Z. Guo, Y. Han, J. Dong, D. Geng, L. Li and W. Yang, *ACS Applied Nano Materials*, 2022, **5**, 774–781.

(337) T. Gao, X. Song, H. Du, Y. Nie, Y. Chen, Q. Ji, J. Sun, Y. Yang, Y. Zhang and Z. Liu, *Nature Communications*, 2015, **6**, 6835.

(338) M. P. Levendorf, C. J. Kim, L. Brown, P. Y. Huang, R. W. Havener, D. A. Muller and J. Park, *Nature*, 2012, **488**, 627–632.

(339) S. Beniwal, J. Hooper, D. P. Miller, P. S. Costa, G. Chen, S. Y. Liu, P. A. Dowben, E. C. H. Sykes, E. Zurek and A. Enders, *ACS Nano*, 2017, **11**, 2486–2493.

(340) Y. Y. Zhang, Q. X. Pei, H. Y. Liu and N. Wei, *Physical Chemistry Chemical Physics*, 2017, **19**, 27326–27331.

(341) Y. Y. Zhang, Q. X. Pei, Z. D. Sha and Y. W. Zhang, *Physics Letters, Section A: General, Atomic and Solid State Physics*, 2019, **383**, 2821–2827.

(342) S. Thomas and S. U. Lee, *RSC Advances*, 2019, **9**, 1238.

(343) O. Farzadian, F. Yousefi, M. Shafiee, F. Khoeini, C. Spitas and K. V. Kostas, *Journal of Molecular Graphics and Modelling*, 2024, **129**.

(344) G. Zhang, Z. Liu, L. Zhang, L. Jing and K. Shi, *Journal of Chemical Sciences*, 2013, **125**, 1169–1176.

(345) R. S. Jones, B. Maciejewska and N. Grobert, *Nanoscale Advances*, 2020, **2**, 4996–5014.

(346) T. Liu, X. Yan, D. G. Hopkinson, C. S. Allen, B. M. Maciejewska, M. Wilson and N. Grobert, *Small*, 2026, **22**, e05371.

(347) E. Iyyamperumal, S. Wang and L. Dai, *ACS Nano*, 2012, **6**, 5259–5265.

(348) S. Z. Bai, B. Yao, G. Z. Xing, K. Zhang and W.-H. Su, *Physica B*, 2007, **396**, 214–219.

(349) M. Öz, *Chemical Papers*, 2024, **78**, 9591–9600.

(350) M. K. Lei, Q. Li, Z. F. Zhou, I. Bello, C. S. Lee and S. T. Lee, *Thin Solid Films*, 2001, **389**, 194–199.

(351) I. Caretti, I. Jiménez, R. Gago, D. Cáceres, B. Abendroth and J. M. Albella, *Diamond and Related Materials*, 2004, **13**, 1532–1537.

(352) S. Xu, X. Ma, G. Tang and Q. Zhang, *Surface Engineering*, 2015, **31**, 549–555.

(353) A. Essafti, E. Ech-Chamikh and M. Azizan, *Spectroscopy Letters*, 2008, **41**, 57–63.

(354) V. S. Sulyaeva, E. Y. Gatapova, A. K. Kozhevnikov, D. I. Rogilo, A. A. Saraev, I. V. Yushina, M. N. Khomyakov, A. A. Shapovalova, V. R. Shayapov, N. Bhaskar, R. Tu and M. L. Kosinova, *Journal of Structural Chemistry*, 2021, **62**, 1309–1324.

(355) Y. Hirata, R. Takeuchi, H. Taniguchi, M. Kawagoe, Y. Iwamoto, M. Yoshizato, H. Akasaka and N. Ohtake, *Materials*, 2021, **14**, 1–18.

(356) H. Kim, U. Kim, D. Hong, S. Kim, S. Han, Y. C. Joo and S. Y. Lee, *Carbon*, 2024, **226**, 119218.

(357) J. Huang, Y. T. Zhu and H. Mori, *Journal of Materials Research*, 2001, **16**, 1178–1184.

(358) R. Torres, I. Caretti, R. Gago, Z. Martín and I. Jiménez, *Diamond and Related Materials*, 2007, **16**, 1450–1454.

(359) M. Durandurdu, *Materials Chemistry and Physics*, 2025, **333**, 130393.

(360) M. Durandurdu, *Journal of Non-Crystalline Solids*, 2024, **639**, 123090.

(361) M. Durandurdu, *Journal of the American Ceramic Society*, 2025, **108**, e20493.

(362) V. I. Ivashchenko, P. E. Turchi, V. I. Shevchenko, L. Gorb and J. Leszczynski, *Journal of Non-Crystalline Solids*, 2025, **662**, 123542.

(363) R. Babar, Ã. Ganyecz, I. A. Abrikosov, G. Barcza and V. Ivády, *npj 2D Materials and Applications*, 2025, **9**, 33.

(364) E. M. O'Sullivan, N. Grobert and M. Swart, *Journal of Physical Chemistry C*, 2024, **129**, 638–647.

(365) K. Zhao, Y. Guo, Y. Shen, Q. Wang, Y. Kawazoe and P. Jena, *Journal of Physical Chemistry Letters*, 2020, **11**, 3501–3506.

(366) A. Bafekry, M. Naseri, M. M. Fadlallah, I. A. Sarsari, M. Faraji, A. B. Khatibani, M. Ghergherehchi and D. Gogova, *Journal of Applied Physics*, 2021, **130**, 114301.

(367) Y. Lu, Y. Yu, X. Zhu and M. Wang, *Physica E*, 2021, **125**, 114413.

(368) S. Zhao and J. Xue, *Journal of Physics D: Applied Physics*, 2013, **46**, 135303.

(369) J. Wu, B. Wang, Y. Wei, R. Yang and M. Dresselhaus, *Materials Research Letters*, 2013, **1**, 200–206.

(370) X. Qi-Lin, L. Zhen-Huan and T. Xiao-Geng, *Journal of Physics D: Applied Physics*, 2015, **48**, 375502.

(371) B. Mortazavi and Y. Rémond, *Physica E: Low-Dimensional Systems and Nanostructures*, 2012, **44**, 1846–1852.